Title
A unifying mechanism for activation and inhibition of the Integrated Stress Response and Aerosolized nanobodies for the treatment of SARS-CoV-2

Author
Schoof, Michael

Publication Date
2022

Peer reviewed|Thesis/dissertation

A unifying mechanism for activation and inhibition of the Integrated Stress Response

and

Aerosolized nanobodies for the treatment of SARS-CoV-2

by

Michael Schoof

DISSERTATION

Submitted in partial satisfaction of the requirements for degree of

DOCTOR OF PHILOSOPHY

in

Biochemistry and Molecular Biology

in the

GRADUATE DIVISION

of the

UNIVERSITY OF CALIFORNIA, SAN FRANCISCO

Approved:

DocuSigned by:
Martin Kampmann
03BA4012CC044AF...

Martin Kampmann

Chair

DocuSigned by:
Peter Walter

Peter Walter

DocuSigned by:
Stephen Floor

Stephen Floor

DocuSigned by:
Aashish Manglik
4C1E8A184D2E493...

Aashish Manglik

Committee Members

Acknowledgments

I suppose this is as good a space as any to put down in writing the long list of people who have been invaluable to me throughout my personal and professional life. I can pick a few times where it is reasonable to say ‘this is the start of my career in science.’ I did a Masters in Julie Ahringer’s lab that prepared me wonderfully for my time at UCSF. In undergrad I spent many years in Anne Brunet’s lab getting kind and rigorous guidance from Lauren Booth and Bethany Schaffer. And the summer in Rick Morimoto’s lab under John Labbadia’s mentorship was wonderful in so many ways. But there will always be a special place in my heart for the first lab I worked in when I was just a kid. Dr. Carrie Rinker-Schaeffer responded to an email and let me into her lab as a high school student. It was my first experience working in a real biology lab. I don’t think I would have gone to Stanford if I hadn’t been lucky enough to have that opportunity. And if that hadn’t happened, who knows where I would have ended up. Different friends. Different city. A whole different story for me. Still, I knew I wanted to be a scientist long before I emailed Carrie, and I don’t think that would be any different in this alternate universe.

My parents got me a subscription to *Nature* in middle school. I understood maybe a tenth of the sentences in those dense articles, but the lack of full comprehension made me want to learn more. And I am proud to say that I now understand at least a third of the sentences. More distant are the episodes of Star Trek I watched with my dad, episodes that made me dream of the future and what is possible – what is yet to be accomplished. I would insert myself into these ScFi worlds and imagine exploring the universe. Then there are the old home movies with timestamps and irrefutable proof of my proclivities. When all the kids on my fifth grade baseball team were interviewed about what they wanted to be when they grew up, I declared ‘a scientist.’ Further back in time, seven-year-old Michael proudly tells his mom that the mish mosh of tooth picks and marshmallows is ‘an atom silly, don’t you even know?’ Perhaps even earlier

still, when I first learned what it means to grow old, and how that scared me, is a sensible time to say that the path to where I am now had already begun.

When I graduate I will have spent almost five years at UCSF. For just being here I owe a profound debt of gratitude to Carol Gross. She has always advocated for me throughout my career here and is a truly special person. Peter Walter took me into his lab and has given me all the support a graduate student could ask for. Through our discussions of science to our shared time doing art to general perspectives on life, I have enjoyed it all. He is a kind and brilliant man who has shaped my life in ways he probably doesn't even realize. Carol and Peter have believed in me, both as a person and a scientist.

As my projects have progressed, many professors have provided critical advice. Aashish Manglik welcomed me into his lab early on to pursue collaborative work, and when the pandemic started was a tireless advocate of our new Covid project, providing both conceptual and hands-on guidance. Adam Frost has been a constant presence for the ISRIB team, helping parse our structural data and develop new models. Martin Kampmann and Stephen Floor have always been available to provide insight, either at thesis committee meetings or at random times when the project required it. Sandy Johnson has given honest assessments on projects and career questions, and is always a joy to chat with.

Within the lab I have a great many people to thank. Vlad Belyy was my rotation mentor, and working with him was an excellent experience that made me excited to join the lab. Morgane Boone has been a generous mentor and friend, always willing to help explain a new technique or discuss some data, especially when pastries are involved. Aditya Anand laid a strong foundation upon which we all are now able to work – solving the annoying little problems that hold projects up. Lan Wang is a structural biology wizard and an incredibly resilient person. She is an excellent bay mate and collaborator and we wouldn't have papers without her. Rosalie Lawrence is a thoughtful and skilled member of Team ISRIB who has always been there when we needed experimental support or a second pair of eyes to figure things out. I was lucky to

work with Zach Cogan when he was a rotation student and am proud of what he has accomplished since he joined the lab. As the next generation of Team ISRIB, I know the projects will be in good hands.

The Manglik lab contains a number of people who also served as excellent mentors and collaborators. Ben Barsi-Rhyne has been exceedingly generous with his time, introducing me to the nanobody display technology and serving as a one on one mentor when I know he had much of his own work to do. Bryan Faust helped power out all our structural work in the nanobody story, and was generous in his time when teaching SPR. Christian, Nick, Ishan and Jiahao have similarly been generous with their time, both before the pandemic and during our collaborative Covid work. Smriti Sangwan, though in the Walter lab, was also instrumental in the success of our Covid work. I owe everyone who contributed to this project a huge debt of gratitude.

A big thank you as well to everyone in the Tetrad program, particularly the administrators Toni, Billy, and Danny. And to my classmates who help keep me sane both in lab and outside of it. Reuben and Ben – you have both been excellent roommates and sounding boards for science and life. When the pandemic started, Reuben and I lived in Genentech hall, basically by ourselves, for a couple months in order to power out the nanobody project. And when we came home Emma had fresh bread waiting for us. Chris – our biochemistry chats and walks around the quad – both when things haven't been working and when science is sailing along nicely – have been essential throughout grad school. Hannah – you help make bay A fun. Melissa – you are a brilliant, wonderful, and thoughtful scientist and person.

Grad school is a stressful time. I have many friends outside of UCSF, and while they may not be there to help troubleshoot cloning, they are there to help when I am down. There are many who have been there for me over the years, but I must thank a few in particular. Ben – you are my oldest and dearest friend. Thank you for always being there whenever I need you.

Aarush, Dinislam, and Allan – we can always share anything with each other. Brian – love you bb. Melanie and Rae – you always bring a positive attitude and perspective to things.

I am the only child of Ellen Fishbein and Charles Schoof. My grandparents on my mother's side are Alene and Dick – on my father's side Dewey and Lou. My grandpa Dick would tell his kids that everything you do, you do for your children. My parents have embodied this advice – giving me a joyful childhood and teaching me important life lessons along the way. They have never doubted me or failed to encourage, support, and help actualize my dreams. I have never felt anything but loved by them. I love you both so much. My grandma Alene just turned 98 as I write this all – she is one of the strongest people I know and always there to help her grandkids. My grandpa Dick would come to all my baseball games and cheer me on. He would call me 'Michael the greatest' and always have a smile and a hug for me. I have never met a kinder man – I miss him.

Contributions

The work included in this dissertation was all performed under the guidance of Dr. Peter Walter. Dr. Aashish Manglik and Dr. Adam Frost were also instrumental in providing guidance for nanobody-related work and eIF2B Cryo-EM-related work, respectively. These were all highly collaborative projects, with many experiments done in conjunction with or fully by other members of the lab. On the eIF2B project, none of this work would have been possible without the contributions from Lan Wang, Morgane Boone, Rosalie Lawrence, and Zach Cogan. The nanobody work was a massive team effort, with key contributions from Bryan Faust, Reuben Saunders, Veronica Rezelj, Smriti Sangwan, Nick Hoppe, Christian Billesbølle, Ishan Deshpande, Ben Barsi-Rhyne and many more, particularly those participating in the QCRG Structural Biology Consortium. A full list of all contributors is detailed below for published manuscripts.

Chapter 1 contains work from a published manuscript:
Schoof M, Boone M, Wang L, Lawrence R, Frost A, Walter P. eIF2B conformation and assembly state regulate the integrated stress response. Elife. 2021 Mar 10;10:e65703. doi: 10.7554/eLife.65703.

Chapter 2 contains work from a published manuscript:
Schoof M, Wang L, Cogan JZ, Lawrence RE, Boone M, Wuerth JD, Frost A, Walter P. Viral evasion of the integrated stress response through antagonism of eIF2-P binding to eIF2B. Nat Commun. 2021 Dec 7;12(1):7103. doi: 10.1038/s41467-021-26164-4.

Chapter 3 contains work from a published manuscript:

Boone M, Wang L, Lawrence R, Frost A, Walter P, Schoof M. A point mutation in the nucleotide exchange factor eIF2B constitutively activates the integrated stress response by allosteric modulation. Elife. 2022 Apr 13;11:e76171. doi: 10.7554/eLife.76171.

Chapter 4 contains work from a published manuscript:
Schoof M, Faust B, Saunders RA, Sangwan S, Rezelj V, Hoppe N, Boone M, Billesbølle CB, Puchades C, Azumaya CM, Kratochvil HT, Zimanyi M, Deshpande I, Liang J, Dickinson S, Nguyen HC, Chio CM, Merz GE, Thompson MC, Diwanji D, Schaefer K, Anand AA, Dobzinski N, Zha BS, Simoneau CR, Leon K, White KM, Chio US, Gupta M, Jin M, Li F, Liu Y, Zhang K, Bulkley D, Sun M, Smith AM, Rizo AN, Moss F, Brilot AF, Pourmal S, Trenker R, Pospiech T, Gupta S, Barsi-Rhyne B, Belyy V, Barile-Hill AW, Nock S, Liu Y, Krogan NJ, Ralston CY, Swaney DL, García-Sastre A, Ott M, Vignuzzi M; QCRG Structural Biology Consortium, Walter P, Manglik A. An ultrapotent synthetic nanobody neutralizes SARS-CoV-2 by stabilizing inactive Spike. Science. 2020 Dec 18;370(6523):1473-1479. doi: 10.1126/science.abe3255.

A unifying mechanism for activation and inhibition of the Integrated Stress Response

and

Aerosolized nanobodies for the treatment of SARS-CoV-2

Michael Schoof

ABSTRACT

Coping with cellular stressors, manifesting as either intrinsic cues or environmental insults, is key to preserving cellular and organismal health. One strategy is to activate the Integrated Stress Response (ISR), a conserved eukaryotic signaling pathway that reprograms translation towards damage mitigation and recovery, or apoptosis when stress is irremediable. Although an inherently cytoprotective process, dysregulation of the ISR underlies a number of neurological disorders, and detailing its mechanism of action and precisely understanding modulators of the pathway is of critical importance. The ISR integrates diverse stresses through a set of stress-sensing kinases. Upon activation, they converge on a common task: the phosphorylation of a single serine in the translation initiation factor eIF2, the protein responsible for bringing the first amino acid to a translating ribosome. Phosphorylated eIF2 (eIF2-p), instead of acting as a substrate, inhibits its dedicated nucleotide exchange factor eIF2B, which is a two-fold symmetric heterodecameric complex. Inhibition of eIF2B by eIF2-p impairs the cycling of eIF2 from its inactive GDP-bound state to its active GTP-bound state, leading to diminished translation of most (and selective translation of a few) select mRNAs, the latter containing regulatory upstream open reading frames. Thus eIF2B serves as the central node regulating the critical first step of protein synthesis.

In Chapter 1 I will be describing how through a suite of *in vitro* and *in vivo* tools, we uncovered the mechanism by which eIF2B activity is modulated. We discovered that, contrary to prior hypotheses, eIF2B activity is regulated through its conformation. eIF2-p binding to eIF2B induces a conformational change in eIF2B that disfavors substrate (eIF2) engagement by pulling the two halves of the complex apart and disrupting the eIF2 binding site. eIF2-p therefore activates the ISR by shifting eIF2B from its enzymatically active 'A-State' towards a conformationally inhibited 'I-State' with diminished substrate binding and enzymatic activity. This conformational inhibition of eIF2B can be overcome by the small-molecule Integrated Stress Response Inhibitor (ISRIB) that our lab discovered. ISRIB binds across the symmetry interface of eIF2B and staples the complex into its active conformation, allosterically competing off the inhibitor eIF2-p.

We find orthogonal support for the A/I-State model of ISR activation through viral effector proteins and point mutations in eIF2B. In Chapter 2 I will describe how the NSs protein of Sandfly Fever Sicilian virus (SFSV) allows the virus to evade activation of the ISR. Mechanistically, NSs tightly binds to eIF2B and directly competes with inhibitory eIF2-p binding, restoring eIF2B's conformation to its active A-State. Having the opposite effect (and detailed in Chapter 3), a single histidine to aspartate point mutation at eIF2B's dimerization interface mimics the effects of eIF2-p binding by promoting an I-State like conformation. Through charge repulsion, this point mutation results in eIF2-p independent modulation of eIF2B's conformation and concomitant activation of the ISR *in vitro* and in cells. Collectively, these data establish that eIF2B is a highly dynamic complex through which protein translation and cellular functioning can be modulated by small molecules (ISRIB), endogenous binding partners (eIF2 and eIF2-P), evolved viral proteins, and point mutations.

My work on ISR regulation came to an abrupt halt when SARS-CoV-2 took over the world. During this involuntary pause, all non-Covid work stopped at UCSF. In an effort to address the global threat, I assembled and led an interdisciplinary team to develop agents that powerfully neutralize the virus (detailed in Chapter 4). In particular, we obtained single-domain antibodies

(nanobodies) by screening a yeast surface-displayed library of synthetic nanobodies. We identified nanobodies that bind to multiple epitopes on Spike and block ACE2 interaction. One exceptionally stable nanobody, Nb6, binds Spike in a fully inactive conformation with its receptor binding domains locked into their inaccessible down-state, incapable of binding ACE2. Affinity maturation and structure-guided design of multivalency yielded a humanized trivalent nanobody, mNb6-tri, with femtomolar affinity for Spike and picomolar neutralization of SARS-CoV-2 infection. mNb6-tri retains powerful binding and neutralization properties against the Delta-SARS-CoV-2. In hamster models of infection, mNb6-tri delivered via nasal-spray reduced the severity of infection in animals exposed to SARS-CoV-2, and served as a potent post-exposure prophylaxis in animals co-housed with infected individuals. Further, in initial safety trials in >200 human subjects after administration via a nasal spray, no safety concerns were observed. Most importantly mNb6-tri is fully resistant to aerosolization, lyophilization, and heat, and it can be readily and economically produced in yeast at industrial scale. These properties may allow these or similar agents to serve as a widely deployable, patient-friendly prophylactic and/or early infection therapeutic that can be self-administered directly to the initial sites of infection. Such a therapeutic is particularly needed in the developing world where vaccination levels remain low and access to expensive therapeutics is significantly limited.

Table of Contents

List of Figures

List of Tables

List of Abbreviations

ATF4	activation transcription factor 4
ATP	adenosine triphosphate
Cryo-EM	cryo-electron microscopy
eIF2	eukaryotic initiation factor 2
eIF2-P	phosphorylated eukaryotic initiation factor 2
eIF2B	translation initiation factor eIF-2B
ER	endoplasmic reticulum
FRET	Förster resonance energy transfer
GEF	guanine nucleotide exchange factor
GTP	guanosine triphosphate
IF	interface
IRES	internal ribosome entry site
ISR	integrated stress response
ISRIB	integrated stress response inhibitor
MM	Michaelis Menten
Nb	nanobody
RBD	receptor binding domain
RVFV	Rift Valley fever virus
SFSV	Sandfly Fever Sicilian virus
$tRNA_i$	initiator tRNA
uORF	upstream open reading frame
WT	wild type

Chapter 1

eIF2B Conformation and Assembly State Regulate the Integrated Stress Response

Summary

The integrated stress response (ISR) is activated by phosphorylation of the translation initiation factor eIF2 in response to various stress conditions. Phosphorylated eIF2 (eIF2-P) inhibits eIF2's nucleotide exchange factor eIF2B, a two-fold symmetric heterodecamer assembled from subcomplexes. Here, we monitor and manipulate eIF2B assembly *in vitro* and *in vivo.* In the absence of eIF2B's α-subunit, the ISR is induced because unassembled eIF2B tetramer subcomplexes accumulate in cells. Upon addition of the small-molecule ISR inhibitor ISRIB, eIF2B tetramers assemble into active octamers. Surprisingly, ISRIB inhibits the ISR even in the context of fully assembled eIF2B decamers, revealing allosteric communication between the physically distant eIF2, eIF2-P, and ISRIB binding sites. Cryo-EM structures suggest a rocking motion in eIF2B that couples these binding sites. eIF2-P binding converts eIF2B decamers into 'conjoined tetramers' with diminished substrate binding and enzymatic activity. Canonical eIF2-P-driven ISR activation thus arises due to this change in eIF2B's conformational state.

Introduction

All cells must cope with stress, ranging from nutrient deprivation to viral infection to protein misfolding. Cell stress may arise from cell-intrinsic, organismal, or environmental insults, yet often converges on common regulatory nodes. The integrated stress response (ISR) is a conserved eukaryotic stress response that senses and integrates diverse stressors and responds by reprogramming translation (Harding et al. 2003). ISR activation has been linked to numerous human diseases, including cancer and neurological diseases (reviewed in Costa-Mattioli and Walter, 2020). While acute ISR activation largely plays a cytoprotective role, its dysregulation (both aberrant activation and insufficient activation) can negatively affect disease progression. In many pathological conditions, for example, the ISR is constitutively activated and maladaptive effects arise that worsen the disease outcome. Many conditions of cognitive dysfunction, for example, have been linked causally to ISR activation in mouse models, including brain trauma resulting from physical brain injuries (Chou et al. 2017; Sen et al. 2017), familial conditions including Vanishing White Matter Disease and Down syndrome (Leegwater et al. 2001; van der Knaap et al. 2002; Zhu et al. 2019), neurodegenerative diseases such as Alzheimer's and ALS (Atkin et al. 2008; Ma et al. 2013), and even the cognitive decline associated with normal aging (Sharma et al. 2018; Krukowski et al. 2020). Our understanding of the molecular mechanism of ISR regulation therefore is of profound importance.

Translation reprogramming upon ISR induction results as a consequence of reduced ternary complex (TC) levels. The TC is composed of methionyl initiator tRNA (Met-tRNA^{i}), the general translation initiation factor eIF2, and GTP (Algire, Maag, and Lorsch 2005). At normal, saturating TC concentrations, translation initiates efficiently on most mRNAs containing AUG translation start sites; however, translation of some mRNAs is inhibited under these conditions by the presence of inhibitory small upstream open reading frames (uORF) in their 5'

untranslated regions (Hinnebusch, Ivanov, and Sonenberg 2016). When TC levels are sub-saturating, translation is repressed on most mRNAs. In contrast, some mRNAs that contain uORFs in their 5'UTRs are now preferentially translated, including mRNAs encoding stress-responsive transcription factors, such as ATF4 (Harding et al. 2000). Thus TC availability emerges as a prime factor in determining the translational and, consequentially, the transcriptional programs of the cell.

The central mechanism that regulates TC levels in response to stress conditions concerns the loading of eIF2's γ subunit with GTP. Without GTP, eIF2 cannot bind Met-tRNA^{i} and hence does not assemble the TC. Loading is catalyzed by the guanine nucleotide exchange factor (GEF) eIF2B, a large decameric and two-fold symmetric enzyme that is composed of two copies each of five different subunits, eIF2Bα, β, δ, γ, and ε (Kashiwagi et al. 2016; Tsai et al. 2018; Wortham et al. 2014; Zyryanova et al. 2018). Stress sensing is accomplished by four upstream kinases (PKR, PERK, GCN2, and HRI) that are activated by different stress conditions and, in turn, phosphorylate eIF2 as a common target (Hinnebusch 2005; Guo et al. 2020; Dey et al. 2005; Shi et al. 1998). Phosphorylation by each of these kinases converges on a single amino acid, S51, in eIF2's α subunit (eIF2α). As a profound consequence of eIF2α S51 phosphorylation, eIF2 converts from eIF2B's substrate for GTP exchange into a potent eIF2B inhibitor.

Cryo-EM studies of eIF2B•eIF2 complexes show that eIF2 snakes across the surface of eIF2B in an elongated conformation, contacting eIF2B at four discontinuous interfaces, which we here refer to as IF1 – IF4 (Figure 1.1 – figure supplement 1) (Kenner et al. 2019; Gordiyenko, Llácer, and Ramakrishnan 2019; Kashiwagi et al. 2019; Adomavicius et al. 2019). IF1 and IF2 engage eIF2γ (containing eIF2's GTPase domain) with eIF2Bε, sandwiching eIF2γ between eIF2Bε's catalytic and core-domain respectively. This interaction pries the GTP binding site open, thus

stabilizing the apo-state to catalyze nucleotide exchange. IF3 and IF4 engage eIF2 via its α subunit across eIF2B's two-fold symmetry interface, where two eIF2Bβδγε tetramer subcomplexes are joined. The eIF2α binding surfaces line a cleft between eIF2Bβ (IF3) and eIF2Bδ' (IF4) (the prime to indicate the subunit in the adjoining tetramer). Upon S51 phosphorylation, eIF2α adopts a new conformation that renders it incompatible with IF3/IF4 binding (Bogorad, Lin, and Marintchev 2017; Kenner et al. 2019; Zhu et al. 2019; Kashiwagi et al. 2019; Adomavicius et al. 2019; Gordiyenko, Llácer, and Ramakrishnan 2019). Rather, phosphorylation unlocks an entirely new binding mode on the opposite side of eIF2B, where eIF2α-P now binds to a site between eIF2Bα and eIF2Bδ. We and others previously proposed that, when bound to eIF2B in this way, the β and especially the γ subunits of eIF2-P could sterically block eIF2γ of a concomitantly bound unphosphorylated eIF2 substrate from engaging productively with eIF2Bε's active site (Kashiwagi et al. 2019; Kenner et al. 2019). Such a blockade could explain the inhibitory effect of eIF2-P, and this model predicts that GEF inhibition should depend on eIF2γ as the entity responsible for causing the proposed steric clash.

Both eIF2 and eIF2-P binding sites span interfaces between eIF2B subunits present in the decamer but not in the subcomplexes from which it is assembled. The eIF2B decamer is built from two eIF2Bβδγε tetramers and one eIF2Bα_2 homodimer (Wortham et al. 2014; Tsai et al. 2018). These subcomplexes are stable entities that, when mixed *in vitro,* readily assemble into decamers. The eIF2Bβδγε tetramer has a low, basal GEF activity, as it can only engage with eIF2 through IF1 - IF3 (Tsai et al. 2018; Craddock and Proud 1996). As expected, eIF2B decamer assembly results in a >20-fold rate enhancement of nucleotide exchange, presumably due to enhanced substrate binding caused by the completion of the eIF2α binding site through the addition of IF4 (Tsai et al. 2018; Craddock and Proud 1996). Assembly of the eIF2B decamer is driven by eIF2Bα_2, which acts as an assembly promoting factor. Thus, eIF2B

assembly into a decamer allows the modalities of i) full GEF activity on eIF2 and ii) inhibition by eIF2-P to manifest.

The activity of the ISR can be attenuated by ISRIB, a potent small drug-like molecule with dramatic effects (Sidrauski et al. 2013). In mice, ISRIB corrects with no overt toxicity the cognitive deficits caused by traumatic brain injury (Chou et al. 2017), Down syndrome (Zhu et al. 2019), normal aging (Krukowski et al. 2020), and other brain dysfunctions (Wong et al. 2018) with an extraordinary efficacy, indicating that the molecule reverses the detrimental effects of a persistent and maladaptive state of the ISR. ISRIB also kills metastatic prostate cancer cells (Nguyen et al. 2018). ISRIB's mechanistic target is eIF2B to which it binds in a binding groove that centrally bridges the symmetry interface between eIF2Bβδγε tetramers (Sekine et al. 2015; Tsai et al. 2018; Zyryanova et al. 2018; Sidrauski et al. 2015). As such, it acts as a "molecular staple", promoting assembly of two eIF2Bβδγε tetramers into an enzymatically active eIF2B$(\beta\delta\gamma\varepsilon)_2$ octamer. Here, we further interrogated the role of ISRIB by engineering cells that allow us to monitor and experimentally manipulate eIF2B's assembly state. These experiments led to the discovery of a conformational switch that negatively couples the eIF2 and eIF2-P binding sites and the ISRIB binding site by allosteric communication in the eIF2B complex. This conformational switch is the central mechanism by which ISR activation occurs.

Results

eIF2B assembly state modulates the ISR in cells.

To investigate the role of eIF2B's assembly state in controlling ISR activation, we developed ISR reporter cells that enable experimental modulation of the eIF2B decamer concentration. To this end, we tagged eIF2Bα with an FKBP12^{F36V} degron in human K562 cells (Figure 1.1 – figure supplement 2A and B), using CRISPR-Cas9 to edit the endogenous locus. The cell-permeable small molecule dTag13 induces selective degradation of the FKBP12^{F36V}-tagged eIF2Bα (Figure 1.1A) (Nabet et al. 2018). We also engineered a genomically integrated dual ISR reporter system into these cells. The reporter system consists of the mNeonGreen fluorescent protein placed under translational control of a uORF-containing 5' untranslated region (UTR) derived from ATF4 ("ATF4 reporter") and the mScarlet-i fluorescent protein containing a partial ATF4 5' UTR from which the uORFs have been removed ("general translation reporter"). To optimize the signal of these reporters, we fused both fluorescent proteins to the ecDHFR degron (Figure 1.1 – figure supplement 3). This degron drives the constitutive degradation of the fusion proteins unless the small molecule trimethoprim is added to stabilize them (Iwamoto et al. 2010). In this way, the reporters allow us to monitor only *de novo* translation. Unless otherwise stated, trimethoprim was added concurrently with other treatments.

Treating ISR reporter cells with the small molecule dTag13 led to rapid and complete degradation of FKBP12^{F36V}-tagged eIF2Bα (Figure 1.1B). As expected, eIF2Bα degradation was selective, as eIF2Bδ, which binds directly to eIF2Bα in the decamer, remained intact. dTag13 treatment also did not increase eIF2α phosphorylation, a hallmark of canonical ISR activation by ISR kinases (Figure 1.1B). Nevertheless, dTag13-induced eIF2Bα degradation led to increased translation of the ATF4 reporter and decreased translation of the general translation reporter (Figure 1.1C and Figure 1.1 – figure supplement 4A) in a concentration-dependent manner.

dTag13 treatment of cells lacking FKBP12^{F36V} degron-tagged eIF2Bα did not induce the ISR (Figure 1.1 – figure supplement 5). These results demonstrate that ISR-like translational reprogramming follows eIF2Bα depletion.

ISRIB resolves assembly-based stress.

As predicted from previous *in vitro* work, ISRIB entirely reversed the ISR translational reprogramming by eIF2Bα depletion (EC_{50} = 1.4 nM; Figure 1.1D and Figure 1.1 – figure supplement 4B) (Tsai et al. 2018). Thus, eIF2Bα can be quantitatively replaced by ISRIB, a small molecule that causes eIF2B$(\beta\delta\gamma\varepsilon)_2$ octamer assembly, rendering the eIF2B decamer and ISRIB-stabilized octamer functional equivalents in these cells. dTag13 treatment led to continued increases in ATF4 translation and decreased general translation over a 6-hour window (Figure 1.1E, Figure 1.1 – figure supplement 4C), and co-treatment with ISRIB completely reversed ISR activation.

By contrast, ISRIB inhibited eIF2-P-based stress induced by thapsigargin treatment only at early time points (1-3 hours), whereas at later time points, ISRIB showed greatly diminished effects in blocking ISR activation. These data distinguish eIF2B assembly-based stress and eIF2-P-based stress in their response to mitigation by ISRIB.

FRET reporters monitor eIF2B assembly state.

To directly measure eIF2B's assembly state, we tagged eIF2B subunits with fluorescent protein pairs and used Förster resonance energy transfer (FRET) as a readout of their molecular proximity. We tagged the C-terminus of eIF2Bβ with mNeonGreen as the FRET donor and the C-terminus of eIF2Bδ with mScarlet-i as the FRET acceptor. In this arrangement, donor and acceptor proteins would be in the range of 120-140 Å apart in the eIF2Bβδγε tetramer (expected negligible FRET efficiency) and become juxtaposed at a distance closer to 60-80 Å when two

eIF2B tetramers assemble into an octamer or a decamer (expected moderate FRET efficiency). Therefore, this genetically encodable system promised to provide us with a quantitative assay of eIF2B's assembly state.

To first characterize these tools *in vitro*, we co-expressed the fluorescently tagged eIF2Bβ and eIF2Bδ fusion proteins together with untagged eIF2Bγ and eIF2Bε in *E. coli* and purified the tetramer as previously described (Tsai et al. 2018). Analysis by analytical ultracentrifugation following absorbance at 280 nm demonstrated that the fluorescent protein tags do not interfere with tetramer stability (Figure 1.2 – figure supplement 1). Moreover, consistent with our previous work, addition of separately expressed eIF2Bα homodimers (eIF2Bα_2) readily assembled fluorescently-tagged eIF2Bβδγε tetramers (eIF2Bβδγε-F) into complete eIF2B decamers. Similarly, the addition of ISRIB caused the tagged tetramers to assemble into octamers.

Upon donor excitation at 470 nm, we next monitored the ratio of fluorescence at 516 nm (donor peak) and 592 nm (acceptor peak) as a function of eIF2Bα_2 and ISRIB concentrations. The results validated our system: in both cases, the FRET signal reliably reported on eIF2Bβδγε-F tetramer assembly into the respective larger complexes with half-maximal assembly (EC_{50}) at 250 nM of ISRIB and 20 nM of eIF2Bα_2 (Figure 1.2B and C). Kinetic analysis showed that eIF2Bα_2 drives assembly of eIF2Bβδγε-F tetramers into decamers with a $t_{1/2}$ of 7 min and that ISRIB drives eIF2Bβδγε-F tetramers into octamers with similar kinetics ($t_{1/2}$ = 5 min) (Figure 1.2D and E; 0-55 min time window). By contrast, the dissociation kinetics of eIF2Bα_2-stabilized decamers and ISRIB-stabilized octamers differed substantially. Spiking in an excess of unlabeled eIF2Bβδγε tetramers to trap dissociated eIF2Bβδγε-F tetramers into dark complexes revealed slow eIF2Bα_2-stabilized decamer dissociation kinetics ($t_{1/2}$ = 3 h), whereas ISRIB-stabilized octamers dissociated much faster ($t_{1/2}$ = 15 min) (Figure 2D and E; 55-150 min time window).

Still *in vitro*, as expected, co-treatment of ISRIB and eIF2Bα_2 did not induce greater complex assembly when eIF2Bα_2 was at saturating concentrations (Figure 1.2F). However, ISRIB substantially enhanced complex stability, slowing the dissociation rate of the ISRIB-stabilized decamer such that no discernible dissociation was observed. Critically, pre-addition of excess untagged eIF2B$\beta\delta\gamma\varepsilon$ and tetramer dimerizers (either eIF2Bα_2 or ISRIB) led to no change in FRET signal above baseline (Figure 1.2 – figure supplement 2A, B, and C). This observation confirms that the lack of signal loss in the ISRIB-stabilized decamer is indeed due to increased complex stability and not to sequestering of dimerizer by the untagged tetramer. Consistent with these observations, treatment with ISRIB at saturating eIF2Bα_2 concentrations did not lead to a further increase in eIF2B's nucleotide exchange activity as monitored by BODIPY-FL-GDP nucleotide exchange (Figure 1.2 – figure supplement 3).

eIF2B exists as a decamer in K562 cells.

Turning to live cells to monitor and modulate the assembly state of eIF2B, we engineered K562 cells to contain both the FRET reporters (eIF2Bβ-mNeonGreen-FLAG and eIF2Bδ-mScarlet-i-myc) and eIF2Bα-FKBP12^{F36V} (Figure 1.1 – figure supplement 2A and B). Consistent with our data on the ISR reporter in Figure 1.1, degradation of eIF2Bα led to translation of ATF4, whereas eIF2α-P and eIF2Bδ levels remain unchanged (Figure 1.3A).

Importantly, degradation of eIF2Bα via dTag13 treatment led to eIF2B complex disassembly, as monitored by FRET signal (Figure 1.3B), validating that our FRET system robustly reports on the eIF2B complex assembly state in living cells. At the 3-hour time point, the EC_{50} for eIF2B disassembly was 5 nM (Figure 1.3B), which mirrors the EC_{50} for ISR activation (15 nM, Figure 1.1B). These data indicate that eIF2B's assembly state is intimately linked to translational output.

ISRIB inhibits the ISR without impacting eIF2B's assembly state.

We next treated cells with a titration of ISRIB +/- the addition of optimal dTag13 concentration (83 nM, plateau from Figure 1.1B and 1.3B) for 3 hours (Figure 1.3C). ISRIB assembled tetramers into octamers when the eIF2Bα subunit was not present. Notably, in the presence of eIF2Bα, the FRET signal remained unchanged upon increasing ISRIB concentrations, indicating that the assembly state of eIF2B in K562 cells is largely decameric unless eIF2Bα is compromised.

As ISRIB's effect on translation is only noticeable upon cellular stress, we wondered whether the assembly state of eIF2B could be affected by stress. To this end, we treated cells with thapsigargin +/- ISRIB. We observed no decrease in FRET signal upon ER stress or ISRIB treatment, arguing that eIF2B exists as a fully assembled decamer in both stressed and unstressed cells (Figure 1.3D).

Nevertheless, ISRIB resolved both eIF2-P-based activation of the ISR induced by thapsigargin and assembly-based activation of the ISR induced by eIF2Bα depletion (Figure 1.3E, lanes 4 and 6), implying that while ISRIB does not alter eIF2B's assembly state in the thapsigargin-treated cells, it still impacts ISR signaling. Thus ISRIB must somehow overcome the inhibition of eIF2B's GEF activity asserted by eIF2-P binding.

ISRIB blocks eIF2-P binding to eIF2B.

To resolve this paradox, we immunoprecipitated eIF2B complexes, pulling on eIF2Bβ-mNeonGreen-FLAG, to assess whether eIF2-P binding changes upon ISRIB treatment in thapsigargin-stressed cells (Figure 1.4A). Consistent with canonical ISR activation, in total cell lysate eIF2α-P levels increased upon stress to a similar extent with and without ISRIB

treatment. At the same time, ATF4 translation occurred in stressed cells only, and ISRIB treatment inhibited ATF4 translation (Figure 1.4A, lanes 1-3).

Surprisingly, we found that the amount of eIF2α-P bound to eIF2B was dramatically reduced in the immunoprecipitations from ISRIB-treated cells (Figure 1.4A, lanes 4-6). Because the amount of total eIF2α bound by eIF2B is likewise reduced, this result suggests that under these stress conditions the majority of eIF2B-bound eIF2 still associated after immunoprecipitation is phosphorylated (note that the eIF2 antibody used in this analysis detects both eIF2α and eIF2α-P). Thus, ISRIB antagonizes eIF2-P binding to eIF2B. Because the binding sites for ISRIB and eIF2-P are ~50 Å apart, this result suggests an allosteric rather than an orthosteric interplay between ISRIB and eIF2-P binding.

eIF2α-P is sufficient to impair ISRIB binding to eIF2B.

To test this notion, we next examined whether, reciprocally, eIF2-P inhibits ISRIB binding *in vitro*. To this end, we used a fluorescent ISRIB analog (FAM-ISRIB) that emits light with a higher degree of polarization when bound to eIF2B compared to being free in solution (Zyryanova et al. 2018). As previously shown, ISRIB competed with FAM-ISRIB for eIF2B binding (Figure 1.4B) (Zyryanova et al. 2018). Indeed, our results show that eIF2-P, but not eIF2, competes with FAM-ISRIB binding (Figure 1.4C). In fact, eIF2α-P, that is, eIF2's phosphorylated α-subunit alone, but not eIF2α, its unphosphorylated form, suffices in this assay (Figure 1.4D). This observation defines eIF2α-P as the minimal unit needed to affect ISRIB release.

We confirmed this model with assays that used the eIF2 kinase PKR to phosphorylate eIF2α, thereby over time converting this previously inert component into eIF2α-P, the ISRIB-binding antagonist (Figure 1.4E). Conversely, dephosphorylation of eIF2α-P by λ phosphatase over time

destroyed its ability to dislodge FAM-ISRIB (Figure 1.4F). Together, these data show that ISRIB binding and eIF2α-P or eIF2-P binding are mutually exclusive events.

eIF2α-P is sufficient to inhibit eIF2B GEF activity.

We further extend these conclusions with activity-based assays. As previously shown, in nucleotide exchange assays that monitor eIF2B's GEF activity towards eIF2, eIF2-P inhibited eIF2B GEF activity in a concentration-dependent manner (Figure 1.5A) (Wong et al. 2018). ISRIB partially rescued the activity (Figure 1.5C). Remarkably, the phosphorylated α subunit alone (eIF2α-P) inhibited eIF2B GEF activity (Figure 1.5B), and ISRIB again partially rescued activity (Figure 1.5D). This observation is inconsistent with previous models that emphasized the potential for a steric clash between the γ subunit of eIF2-P and the γ subunit of the substrate eIF2 (Kenner et al. 2019; Kashiwagi et al. 2019). Therefore these data support the notion that the phosphorylated α subunit of eIF2 alone suffices to modulate eIF2B activity, i.e., that orthosteric competition cannot wholly explain eIF2-P's inhibitory properties and that the remaining eIF2 subunits are dispensable for this effect.

eIF2α-P decreases eIF2B's enzymatic activity and antagonizes eIF2 binding.

To explain how eIF2α-P alone could block GEF activity, we considered three principle options: i) eIF2α-P may decrease the rate of eIF2B's enzymatic activity, ii) it may allosterically inhibit eIF2 binding to eIF2B, or iii) it may perform some combination of those mechanisms. To investigate the relative contributions of these mechanisms, we employed multiple turnover kinetic measurements of eIF2B activity at varying eIF2 concentrations. We measured the initial velocity of this reaction and performed Michaelis Menten analysis to determine the V_{max} and the K_M of the GEF reaction at varying concentrations of eIF2α-P (Figure 1.6A and Figure 1.6 – figure supplement 1). Notably, with increasing concentrations of eIF2α-P, the V_{max} decreased while K_M increased, suggesting that both substrate affinity and eIF2B catalytic activity were affected by

eIF2α-P binding. We next examined how inhibited eIF2B decamers compared to tetramers. Intriguingly, at near-saturating eIF2α-P concentrations, the k_{cat} / K_M ratio, a measure of specific enzyme activity, approached that of the eIF2Bβδγε tetramer, suggesting that eIF2α-P inhibits the decamer by converting it to a tetramer-like state, rendering eIF2α-P-inhibited eIF2B decamers and eIF2B tetramers functionally equivalent (Figure 1.6B and Figure 1.6 – figure supplement 1).

To further examine whether eIF2 and eIF2α-P antagonize one another's binding, we immobilized eIF2B decamers on agarose beads and incubated with combinations of eIF2, eIF2α-P, and ISRIB (Figure 1.6C). eIF2 readily bound to eIF2B with and without ISRIB (lanes 1 and 2) but eIF2α-P addition reduced the amount of eIF2 recovered (lane 3). As expected, ISRIB inhibited eIF2α-P binding and restored normal eIF2 binding (lane 4). Additionally, we utilized FAM-ISRIB as a tool to read out the eIF2-bound active state of eIF2B. Consistent with the data shown in Figures 1.4E and 1.4F, eIF2B addition to FAM-ISRIB increased polarization (Figure 1.6D, black and red data points, respectively), and FAM-ISRIB binding was blocked by the addition of eIF2α-P (blue data point on the y-axis). A titration of eIF2 into this reaction allowed FAM-ISRIB polarization to recover, indicating that eIF2 binds and disrupts eIF2α-P's inhibitory binding, which restores FAM-ISRIB binding. This result reinforces the notion that eIF2 and ISRIB binding are synergistic, i.e., positively coupled.

eIF2α-P inhibits eIF2B by inducing a conformational change.

We next turned to structural studies to determine the basis of the decreased enzymatic activity and the apparent antagonism between eIF2α-P and both ISRIB and eIF2. First, we asked whether ISRIB binding alone causes a conformational change in decameric eIF2B. To this end, we prepared the apo-eIF2B decamer by combining eIF2Bβδγε tetramers and eIF2Bα_2 and subjected the sample to cryo-EM imaging. After 2D and 3D classification, we generated a single

consensus structure of the apo-eIF2B decamer at 2.8 Å resolution (Table 1.1, Figure 1.7 – figure supplement 1) with most side chains clearly resolved. This map allowed us to build an improved atomic model of the eIF2B decamer. This structure revealed that apo-eIF2B has an overall very similar structure as the ISRIB-bound decamer published previously (PDB ID: 6CAJ) (Tsai et al. 2018; Zyryanova et al. 2018). Closer inspection revealed that ISRIB slightly draws the decamer's two halves together by comparison with the apo state but does not induce marked changes in eIF2B's overall conformation (Figure 1.7 – figure supplement 2A).

We next examined the ISRIB-binding pocket. In the apo versus the ISRIB-bound state, eIF2Bδ L179 shifts slightly into the pocket, occupying a position where it would clash with ISRIB binding, and eIF2Bβ H188 (a key ISRIB interactor) adopts a different rotamer (Figure 1.7 – figure supplement 2B) (Tsai et al. 2018). Overall, however, we conclude that ISRIB binding to the eIF2B decamer correlates with slight rearrangements that are primarily confined to the ISRIB binding pocket. Overlay of the apo decamer with structures of eIF2B bound to one or two copies of its enzymatically-engaged substrate eIF2 also revealed unremarkable changes (Kashiwagi et al. 2019; Kenner et al. 2019; Gordiyenko, Llácer, and Ramakrishnan 2019; Adomavicius et al. 2019). We infer from these results that all of these structures represent, with the minor variations noted, the enzymatically active state of eIF2B, henceforth referred to as the "A-State" ("A" for active).

By contrast, overlaying the eIF2B-eIF2α-P structure (PDB ID: 6O9Z) with the A-State structures revealed significant changes in the overall architecture of eIF2B (Figure 1.7A), henceforth referred to as the "I-State" ("I" for inhibited) (Kenner et al. 2019). In the I-State, the two symmetrically opposed eIF2B tetramers have undergone a rocking motion that changes the angle between them by 7.5 degrees (Figure 1.7A). The ISRIB pocket, consequentially, is lengthened by ~2 Å (Figure 1.7B). Critically, the substrate-binding cleft between eIF2Bβ and

eIF2Bδ', where the N-terminal domain of the unphosphorylated eIF2α substrate binds, is widened by 2.6 Å, pulling IF4 away but leaving IF1 - IF3 as available binding surfaces (Figure 1.7C, Figure 1.7 – figure supplement 3). For both ISRIB and eIF2, these rearrangements break key anchoring interactions, providing a structural explanation why eIF2-P binding destabilizes ISRIB binding and compromises GEF activity. With only 3 of 4 interfaces available, eIF2 can still bind but would bind with lower affinity and may not necessarily be properly positioned, further explaining the reduced catalytic activity observed in Figure 1.6A. Conversely, in the A-State the cleft between eIF2Bα and eIF2Bδ' is widened by 5.5 Å (Figure 1.7D), disrupting the eIF2-P binding site and suggesting a possible mechanism for the antagonism between eIF2-P and eIF2/ISRIB.

Based on these structural comparisons, we conclude that eIF2B adopts at least two notably distinct conformational states, the A- and I-States. These two states are mutually exclusive (Figure 1.8). The A- and I-States, therefore, define an on-off switch of eIF2B's GEF activity and can be thought of as functional equivalents to the decamer and tetramer assembly states, respectively. The A- to I-State transition thus appears to be the central mechanism underlying ISR activation.

Discussion

As dysregulation of the ISR is increasingly implicated in numerous diseases with devastating consequences, understanding the mechanism of ISR signaling is of profound importance (Costa-Mattioli and Walter 2020). The central ISR regulatory hub is the decameric guanine nucleotide exchange complex eIF2B, which activates eIF2 by loading it with GTP. Upon ISR activation in response to a variety of stress conditions, eIF2 becomes phosphorylated, converting it from eIF2B's substrate into an eIF2B inhibitor. Both eIF2 and eIF2-P are elongated protein complexes that contact eIF2B through multi-subunit, composite interaction surfaces (Kenner et al. 2019; Kashiwagi et al. 2019). The binding mode appears to be determined mainly by eIF2's α subunit, which anchors eIF2 and eIF2-P to their respective binding sites. For the substrate eIF2, binding aligns eIF2γ with eIF2B's catalytic site via IF1 and IF2 for nucleotide exchange. By contrast, for the inhibitor eIF2-P, binding positions its γ-subunit such that it could orthosterically prevent nonphosphorylated eIF2 substrate from engaging the catalytic machinery in eIF2Bε (Kashiwagi et al. 2019; Kenner et al. 2019). While this model was appealing based on the cryo-EM structures of eIF2B•eIF2-P complexes (Kashiwagi et al. 2019), the eIF2α C-terminal domain may retain sufficient flexibility to allow eIF2γ to avert the proposed clash (Adomavicius et al. 2019; Ito, Marintchev, and Wagner 2004).

Expanding from this notion, in this work we show that allosteric rather than clash-based orthosteric competition contributes significantly to eIF2-P-mediated inhibition. We show that eIF2 and eIF2-P binding are negatively coupled, even when only the α subunit of eIF2-P is present. Thus, eIF2α-P binding impairs substrate binding even though the two binding sites are ~50 Å apart. Further, the phosphorylated form of eIF2's α subunit alone inhibits GEF activity both through reduced substrate affinity and reduced eIF2B catalytic efficiency. Indeed, depending on the concentration regime, this change in eIF2B's intrinsic catalytic activity may be the main driver of lowered TC levels. With these data, we demonstrate that the eIF2γ subunit,

which would be required for eIF2 inhibition via the clash-based orthosteric model, is mechanistically dispensable for eIF2-P's inhibitory role, although the added binding energy it contributes is certainly of importance in a cellular context.

Cryo-EM reconstructions support this model. They reveal a rocking motion of the two eIF2Bβδγε tetramers with eIF2Bα_2 acting as the fulcrum of the movement, akin to a butterfly raising and lowering its wings. These changes are induced by eIF2α-P alone. In the active or "wings-up" A-State, eIF2Bβ and eIF2Bδ' subunits are sufficiently close to fully shape the eIF2α binding site, thus allowing nonphosphorylated substrate engagement. The A-State also contains a properly sized ISRIB binding pocket, thus rendering eIF2 and ISRIB binding synergistic. In contrast, the eIF2α-P binding site is misshapen and lacking properly positioned sidechains critical for eIF2α-P binding. In the inhibited wings-down I-State, the eIF2α-P binding site is shaped correctly, while both the eIF2α (specifically IF4) and ISRIB binding sites are disrupted.

Prior to this work, models describing the molecular function of the drug-like small molecule ISRIB were exclusively focused on ISRIB's activity to promote eIF2B complex assembly. *In vitro* work from our and other labs demonstrated that eIF2Bβδγε tetramers assemble in the presence of ISRIB into eIF2B$(\beta\delta\gamma\varepsilon)_2$ octamers that approach the enzymatic activity of the eIF2B decamer, explaining how ISRIB could promote eIF2B assembly to restock the pool of active eIF2B when depleted by eIF2-P during ISR activation (Tsai et al. 2018; Zyryanova et al. 2018; Sekine et al. 2015; Sidrauski et al. 2015). However, because eIF2Bα_2 likewise has assembly-promoting activity, ISRIB can only exert this function when eIF2Bα_2 is limiting. We here validated this conjecture in living cells. Experimental depletion of eIF2Bα turned on ISR signaling in the absence of eIF2 phosphorylation, and ISRIB functionally substitutes for eIF2Bα_2. In the context of saturating eIF2Bα_2 we were thus left with a paradox regarding ISRIB's mechanism of action

which we resolve by showing that beyond a role in eIF2B assembly, ISRIB antagonizes eIF2-P binding.

Previous work investigating the effects of compromising eIF2Bα (deletion, mutation, knockdown) did not report on eIF2B complex assembly and were predominantly performed in non-human model systems (Pavitt, Yang, and Hinnebusch 1997; Hannig and Hinnebusch 1988; Elsby et al. 2011). Indeed, it is conceivable that eIF2B subcomplexes (and the role for these complexes in full heterodecamer assembly) are distinct between species. For example, in the fungus *Chaetomium thermophilum,* eIF2Bβ and eIF2Bδ appear to form heterotetrameric subcomplexes (Kuhle, Eulig, and Ficner 2015), whereas we see no evidence for such stable assemblies in our work with human eIF2B. Thus, in other organisms enzymatically active octamers may form, and eIF2Bα's role may thus be primarily to allow eIF2-P binding. Another intriguing possibility is that long-term, cells may enact mechanisms to compensate for the drop in TC levels that accompanies eIF2Bα depletion, consequent decamer disassembly, and decreased eIF2B GEF activity.

While our data clearly show that eIF2B is predominantly a decamer in K562 cells, this leaves open the possibility that the assembly state differs by cell type and/or is regulated physiologically. In principle, eIF2Bα could become limiting by regulation of its biosynthesis or degradation, by post-translational modification, and/or by sequestration into an unavailable pool. It is also important to note that an ISRIB-stabilized eIF2B$(\beta\delta\gamma\varepsilon)_2$ octamer is inert to inhibition by eIF2-P. Such inhibition would require eIF2α-P to bind at the eIF2Bα/eIF2Bδ interface, which does not exist in complexes lacking eIF2Bα. We speculate that endogenous eIF2B$(\beta\delta\gamma\varepsilon)_2$ octamers could be stabilized by putative alternate assembly factors, which could be metabolites or proteins that, like ISRIB, can substitute for eIF2Bα_2 in this regard.

In the course of this study, the demonstration that ISRIB still has a profound effect even in the context of fully assembled eIF2B led to the discovery of allosteric eIF2B regulation. While this manuscript was in preparation, a paper from Takuhiro Ito's and David Ron's laboratories was published that reached similar conclusions regarding ISRIB's effect on allosteric eIF2B regulation (Zyryanova et al. 2021). The work from these groups focuses almost exclusively on the allosteric effects promoted by the drug. Our results agree with their conclusions and demonstrate physiological significance. We show that substrate (eIF2) and inhibitor (eIF2-P) binding are negatively coupled. We additionally show that inhibitor binding reduces eIF2B's catalytic activity. Moreover, we show that by binding to the same binding site on eIF2B, ISRIB can affect the ISR in two modalities: i) by promoting eIF2B assembly under conditions where eIF2Bα_2 is limiting or decamer stability may be compromised, and ii) by biasing allosterically the conformational equilibrium of fully assembled decameric eIF2B towards the A-State, rendering inhibition by eIF2-P more difficult. Conceptually, these two modalities of ISRIB function are quite similar. In both cases, ISRIB promotes the completion of the eIF2α binding site by properly positioning IF4, so that it can cooperate with IF3 to anchor eIF2α. Indeed, in the I-State, the widening of the cleft between eIF2Bβ and eF2Bδ' effectively renders the available interaction surfaces on eIF2B equivalent to those on eIF2B$\beta\delta\gamma\varepsilon$ tetramers, limiting eIF2 engagement to IF1-IF3 as IF4 is pulled "out of reach" as it would be in fully dissociated tetramers. In this way, we can think of eIF2B's I-State as "conjoined tetramers" that remain tethered by eIF2Bα_2 but are functionally separate entities.

Considering the potential pharmacological applications of ISRIB, the relevant modality of ISRIB function may vary between different disease pathologies. In the case of Vanishing White Matter Disease, for example, point mutations destabilize the eIF2B complex and ISRIB therefore may provide primarily a stabilizing effect to recover eIF2B function (Wong et al. 2018). By contrast, in

traumatic brain injury, sustained cognitive dysfunction is caused by persistent canonical ISR activation through eIF2-P (Chou et al. 2017). Hence ISRIB would primarily counteract the aberrant ISR activation by predisposing eIF2B to the A-State. Other diseases are likely somewhere along the spectrum of purely assembly-based vs. purely eIF2-P-based ISR activation. Our illustration of the differences between ISRIB's ability to resolve assembly-based stress vs. eIF2-P-based stress should therefore inform how these different diseases are studied and ultimately treated.

The discovery of allosteric control of eIF2B activity raises intriguing possibilities. Indeed, we can envision that cell-endogenous modulators exist that work as activators (stabilizing the A-State) or inhibitors (stabilizing the I-State). Such putative ISR modulators could be small molecule metabolites or proteins and either bind to the ISRIB binding pocket or elsewhere on eIF2B to adjust the gain of ISR signaling to the physiological needs of the cell. Precedent for this notion comes from viruses that evolved proteins to counteract ISR mediated antiviral defenses. The AcP10 protein in the Bw-CoV SW1 virus, for example, interacts with eIF2B to exert an ISRIB-like effect, likely predisposing eIF2B to the A-state (Rabouw et al. 2020). Regarding the observed changes in the ISRIB binding pocket, the newly gained structural insights can be applied to engineer novel pharmacological ISR modulators that may be effective in opening new therapeutic opportunities in different diseases.

Figures

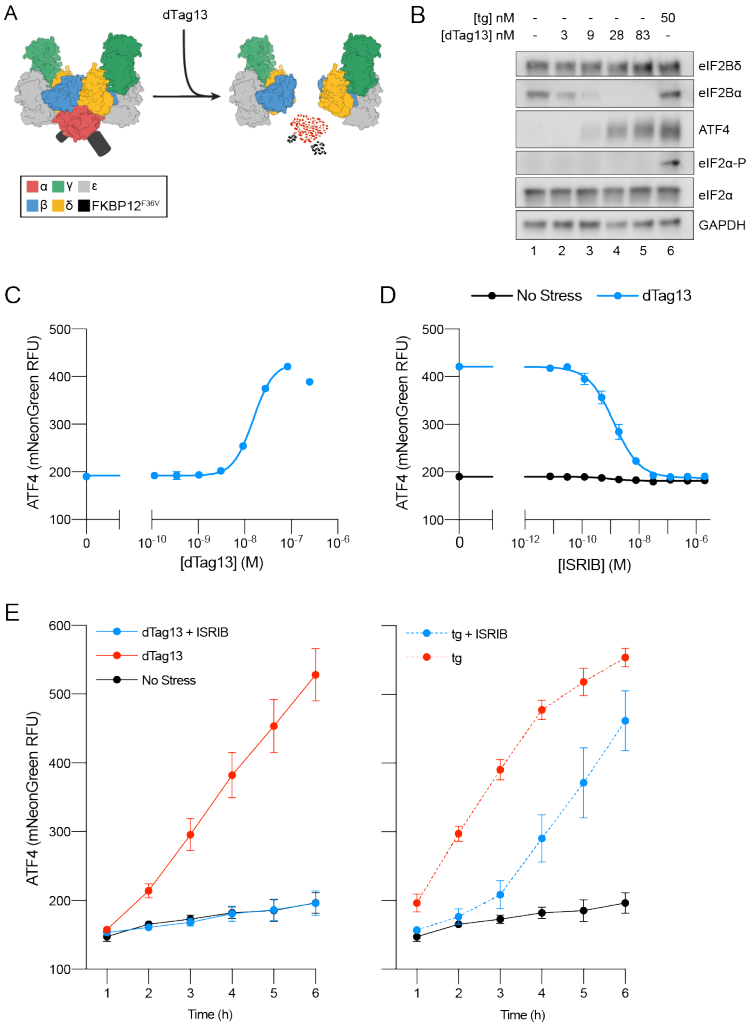

Figure 1.1: Cellular eIF2B assembly state in cells modulates the ISR.
(A) Schematic of eIF2B assembly state modulation via the FKBP12^{F36V} / dTag13 system used to induce degradation of eIF2Bα. **(B)** Western blot of K562 cell extracts after treatment with thapsigargin (tg) or dTag13 for 3 h as indicated. Thapsigargin induces the ISR by depleting Ca^{2+} levels in the endoplasmic reticulum. Loading of all lanes was normalized to total protein. **(C-E)** ATF4 reporter levels as monitored by flow cytometry. Trimethoprim was at 20 μM. (C) Samples after 3 h of dTag13 treatment (EC_{50} = 15 nM; s.e.m = 1 nM). (D) Samples after 3 h of ISRIB treatment +/- 83 nM dTag13 (EC_{50} = 1.4 nM; s.e.m = 0.3 nM). (E**)** Timecourse of tg treatment (dTag13 = 83 nM, tg = 100 nM, ISRIB = 2 μM).
For (B), eIF2Bδ, eIF2Bα, and GAPDH blots, and the ATF4 and eIF2α blots are from the same gels, respectively; the eIF2α-P blot is from its own gel. For (C-E), biological replicates: n = 3. All error bars represent s.e.m.

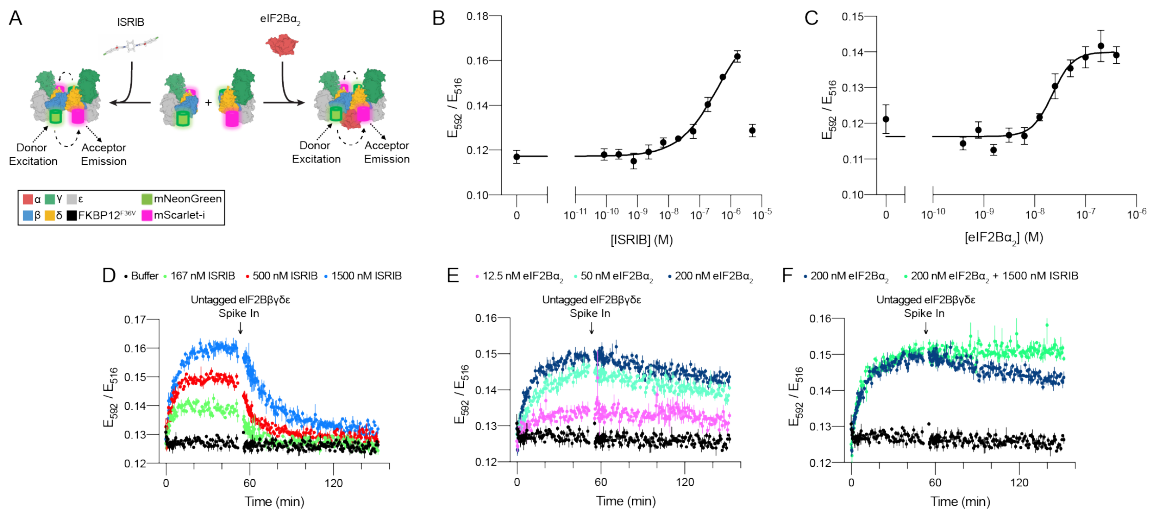

Figure 1.2: FRET system monitors eIF2B assembly state.
(A) Schematic depicting the principle of eIF2B assembly state modulation by ISRIB and eIF2Bα$_2$ and FRET readout. **(B-C)** FRET signal (E_{592}/E_{516}) measured after 1 h of incubation with (B) ISRIB (EC_{50} = 250 nM; s.e.m = 80 nM) or (C) eIF2Bα$_2$ (EC_{50} = 20 nM; s.e.m. = 4 nM) at 50 nM eIF2Bβδγε-F. **(D-F)** Timecourse monitoring FRET signal (E_{592}/E_{516}) after addition of (D) ISRIB (association $t_{1/2}$ = 5.1 min, s.e.m = 0.5 min; dissociation $t_{1/2}$ = 15 min, s.e.m. = 1 min), (E) eIF2Bα$_2$ (association $t_{1/2}$ = 7.3 min, s.e.m = 0.6 min; dissociation $t_{1/2}$ = 180 min, s.e.m. = 10 min), or (F) ISRIB + eIF2Bα$_2$ (association $t_{1/2}$ = 7 min, s.e.m = 1 min; dissociation $t_{1/2}$ = N/A) at 50 nM eIF2Bβδγε-F. At t = 52 min, unlabeled eIF2Bβδγε was added to a final concentration of 1 μM. For (B-C), representative replicate averaging four technical replicates are shown. For (D-F), representative replicate averaging three technical replicates are shown. For (B-F), biological replicates: n = 3. All error bars represent s.e.m.

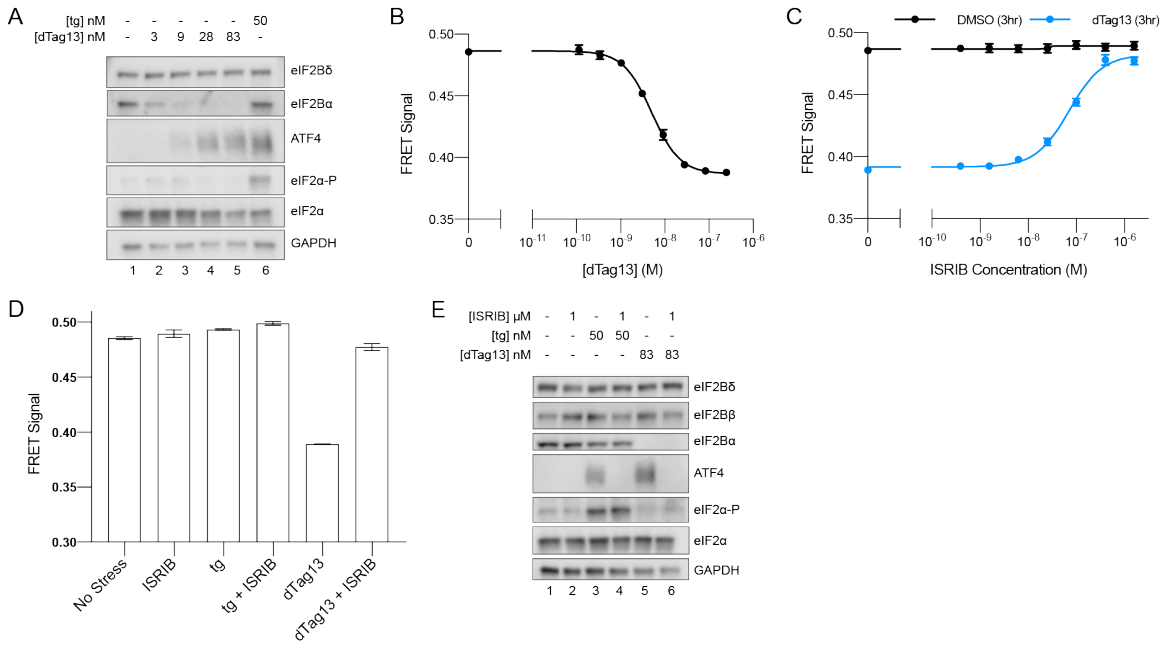

Figure 1.3: eIF2B is a decamer in both unstressed and stressed cells, and ISRIB blocks ISR activation.
(A) Western blot of K562 ISR reporter cell extracts after treatment with tg or dTag13 for 3 h as indicated. **(B-D)** FRET signal as monitored by flow cytometry after 3 h treatment with (B) dTag13 (EC_{50} = 5.1 nM; s.e.m = 0.2 nM), (C) ISRIB +/- 83 nM dTag13 (EC_{50} = 80 nM; s.e.m = 10 nM), (D) various stressors (83 nM dTag13, 50 nM tg, +/- 1.6 μM ISRIB). The ratio of mScarlet-i / mNeonGreen emission is presented. **(E)** Western blot of K562 ISR reporter cell extracts treated for 3 h with ISRIB, tg, and/or dTag13 as indicated.
All lanes across gels were loaded with equal total protein. For (A), eIF2Bδ, eIF2Bα, and GAPDH blots, and the ATF4 and eIF2α blots are from the same gels respectively; the eIF2α-P blot is from its own gel. For (E), eIF2Bδ, eIF2Bβ, and GAPDH blots, ATF4 and eIF2α blots, and eIF2Bα and eIF2α-P blots are from the same gels, respectively. For (B-D), biological replicates: n = 3. All error bars represent s.e.m.

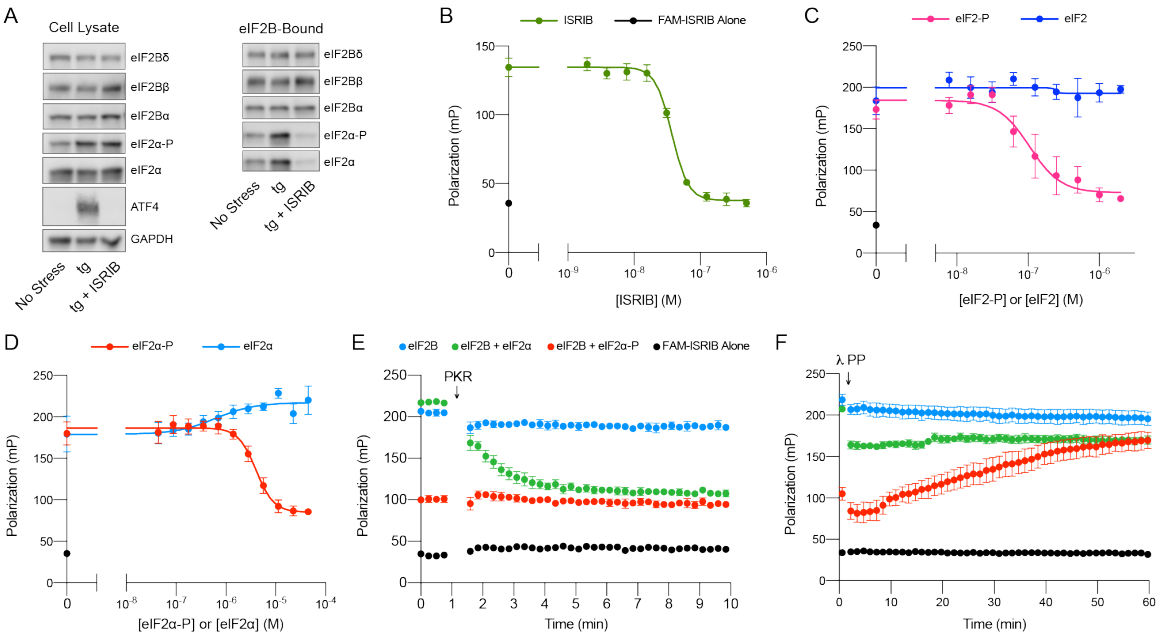

Figure 1.4: ISRIB and eIF2-P compete for eIF2B binding.
(A) Western blot of K562 ISR reporter cell extracts after treatment with tg +/- ISRIB as indicated (left panel) or of eIF2B-bound fraction isolated by anti-FLAG immunoprecipitation of the eIF2B-mNeonGreen-FLAG tagged subunit under native conditions (right panel). **(B-D)** Plot of fluorescence polarization signal after incubation of FAM-ISRIB (2.5 nM) with 100 nM eIF2B$(\alpha\beta\delta\gamma\varepsilon)_2$ and varying concentrations of (B) ISRIB (IC_{50} = 37 nM; s.e.m. = 1 nM), (C) eIF2 or eIF2-P (IC_{50} = 210 nM; s.e.m. = 120 nM), (D) eIF2α or eIF2α-P (IC_{50} = 4000 nM; s.e.m. = 200 nM). **(E-F)** Timecourse of fluorescence polarization signal after addition of (E) eIF2α kinase PKR and ATP or (F) λ phosphatase. FAM-ISRIB was at 2.5 nM. eIF2B$(\alpha\beta\delta\gamma\varepsilon)_2$ was at 100 nM. eIF2α and eIF2α-P were at 5.6 μM.
In (A), eIF2Bδ, eIF2Bα, and eIF2α blots, eIF2Bβ and eIF2α-P blots, and ATF4 and GAPDH blots are from the same gels, respectively. All cell lysate or eIF2B-bound lanes across all gels were loaded with equal total protein. Biological replicates: (B) n = 3; (C) n = 5 (n = 4 at 2 μM); (D-F) n =3. All error bars represent s.e.m.

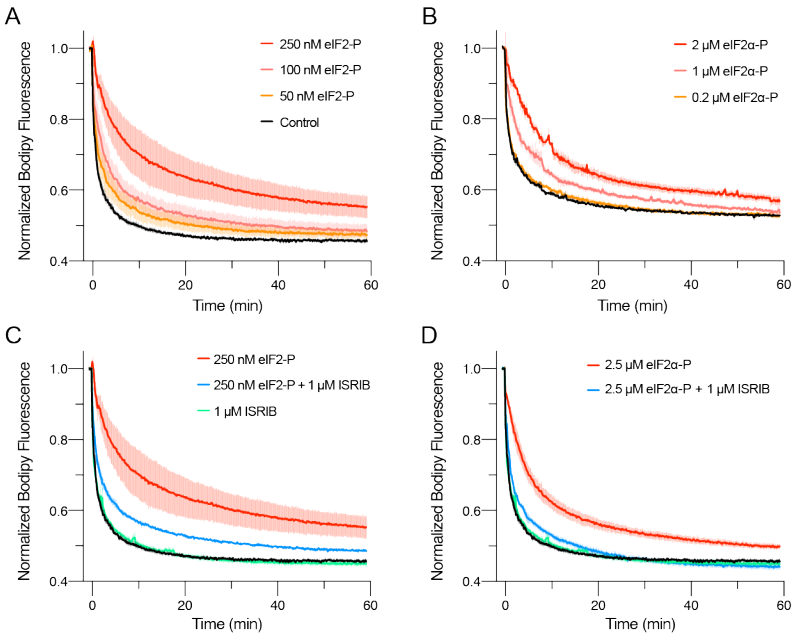

Figure 1.5: eIFα-P is the minimal unit needed to inhibit nucleotide exchange by eIF2B.
(A-D) GEF activity of eIF2B as assessed by BODIPY-FL-GDP exchange. eIF2B$(\alpha\beta\delta\gamma\varepsilon)_2$ was at 10 nM throughout. For (A) $t_{1/2}$ = 1.6 min (Control), 2.5 min (50 nM eIF2-P), 3.5 min (100 nM eIF2-P), and 7.2 min (250 nM eIF2-P). For (B) $t_{1/2}$ = 2.4 min (Control), 3.0 min (0.2 μM eIF2α-P), 5.0 min (1 μM eIF2α-P), and 6.7 min (2 μM eIF2α-P). For (C) $t_{1/2}$ = 1.6 min (Control), 1.9 min (1 μM ISRIB), 3.1 min (250 nM eIF2-P + 1 μM ISRIB), and 7.2 min (250 nM eIF2-P). For (D) $t_{1/2}$ = 1.6 min (Control), 1.9 min (1 μM ISRIB), 3.1 min (2.5 μM eIF2α-P + 1 μM ISRIB), and 5.3 min (2.5 μM eIF2α-P).
All error bars represent s.e.m. Biological replicates: (A-D) n = 3 except for the 100 and 50 nM eIF2-P conditions in (A) where n = 2.

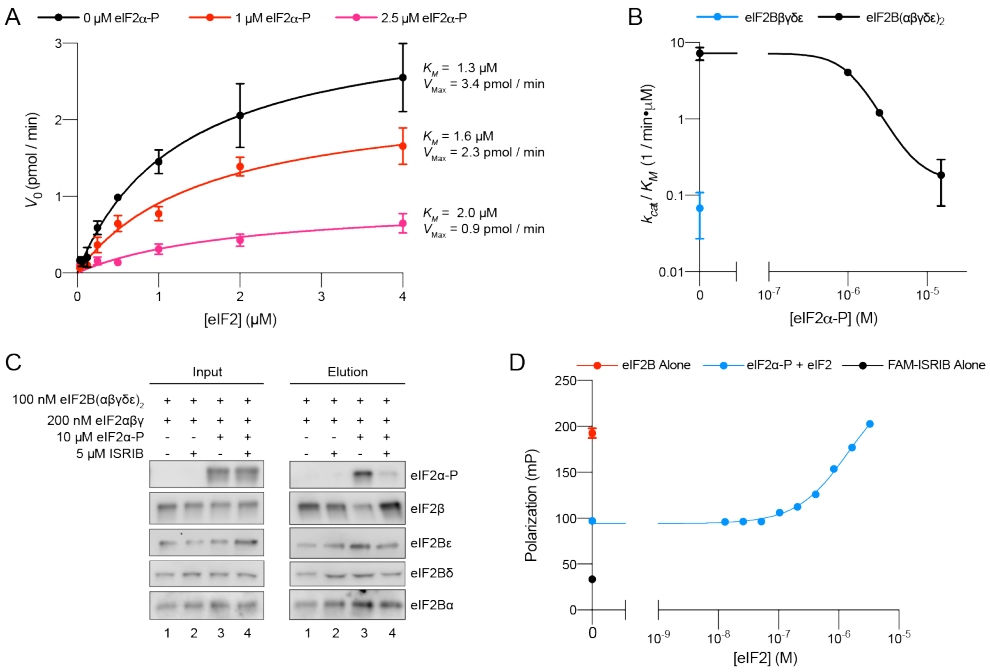

Figure 1.6: eIFα-P reduces eIF2B's catalytic activity and antagonizes eIF2 binding.
(A) Initial velocity of eIF2B-catalyzed nucleotide exchange as a function of eIF2 concentration. eIF2B(αβδγε)$_2$ concentration was 10 nM. **(B)** Plot of k_{cat} / K_M for tetramer and decamer at varying eIF2α-P concentrations, obtained by fitting the linear portion of the Michaelis Menten saturation curve. Keeping the number of eIF2 binding sites constant, the eIF2B(αβδγε)$_2$ concentration was 10 nM while eIF2Bβδγε was 20 nM. **(C)** Western blot of purified protein recovered after incubation with eIF2B(αβδγε)$_2$ immobilized on Anti-protein C antibody conjugated resin. eIF2Bα was protein C tagged. **(D)** Plot of fluorescence polarization signal before (*black*) and after incubation of FAM-ISRIB (2.5 nM) with 100 nM eIF2B(αβδγε)$_2$ (*red*) or 100 nM eIF2B(αβδγε)$_2$ + 6.0 μM eIF2α-P and varying concentrations of eIF2 (*blue*).
For elution samples In (C), eIF2β, eIF2Bε, and eIF2Bα, and the eIF2Bδ and eIF2α-P blots are from the same gels, respectively. For input samples eIF2β and eIF2Bα, and the eIF2Bδ and eIF2α-P blots are from the same gels, respectively; eIF2Bε is from its own gel. Biological replicates: (A-B) n = 2; (D) n = 3. All error bars represent s.e.m.

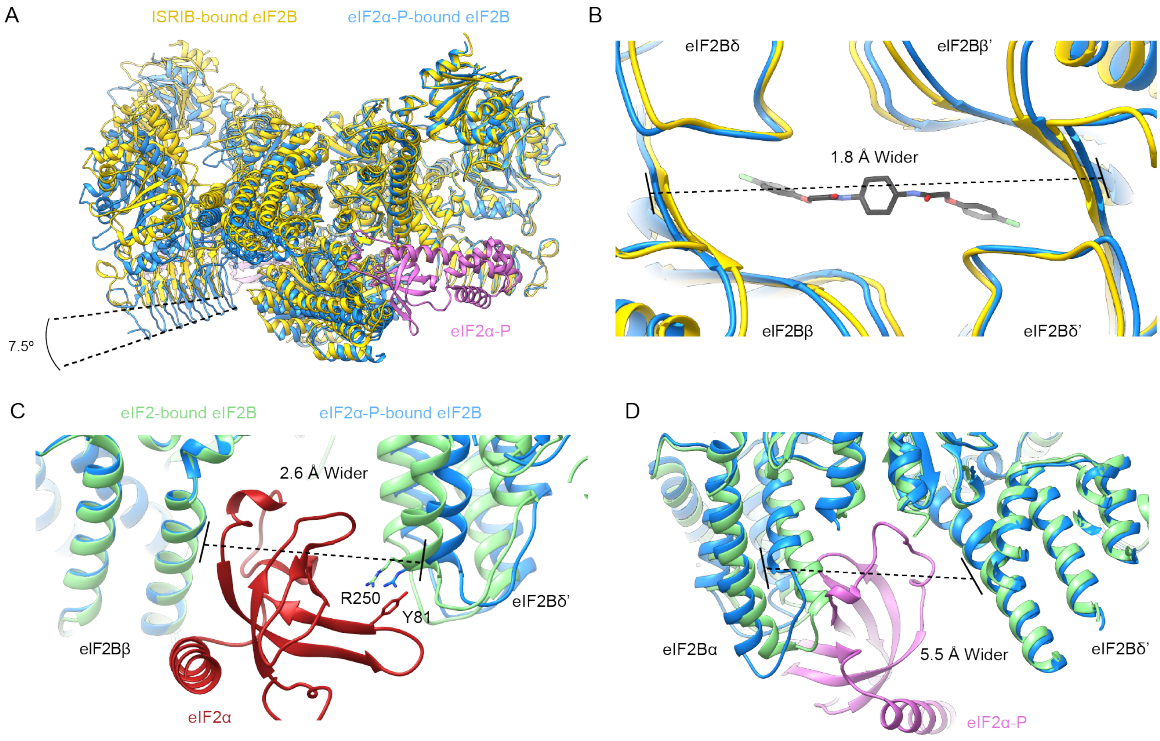

Figure 1.7: eIF2α-P binding conformationally inactivates eIF2B.
(A) Overlay of the ISRIB-bound eIF2B structure (PDB ID: 6CAJ) to the eIF2α-P-bound eIF2B structure (PDB ID: 6O9Z). The 7.5 degree hinge movement between the two eIF2B halves was measured between the lines connecting eIF2Bε H352 and P439 in the ISRIB-bound vs. eIF2α-P-bound structures. **(B)** Zoom-in view of the ISRIB binding pocket upon eIF2α-P binding. The ~2 Å pocket lengthening was measured between eIF2Bδ and eIF2Bδ' L482; the "prime" to indicate the subunit of the opposing tetramer. ISRIB is shown in stick representation. **(C)** Overlay of eIF2-bound eIF2B (PDB ID: 6O85) and eIF2α-P-bound eIF2B. The 2.6 Å widening of the eIF2 binding site induced by eIF2α-P binding was measured between E139 and R250 of eIF2Bβ and eIF2Bδ', respectively. The side chains involved in the key cation-π interaction between R250 in eIF2Bδ and Y81 in eIF2α that is lost due to pocket expansion are shown **(D)** Overlay of the eIF2-bound eIF2B to the eIF2α-P-bound eIF2B. The 5.5 Å narrowing of the eIF2α-P binding pocket causing a steric clash between eIF2Bα and eIF2α-P in the eIF2-bound state was measured between eIF2Bα S77 and eIF2Bδ L314. ISRIB-bound eIF2B is colored in *gold*, eIF2α-P-bound eIF2B in *blue* and eIF2-bound eIF2B in *light green*. eIF2α-P is shown in *pink* and eIF2α in *red*. ISRIB is colored in *CPK*.

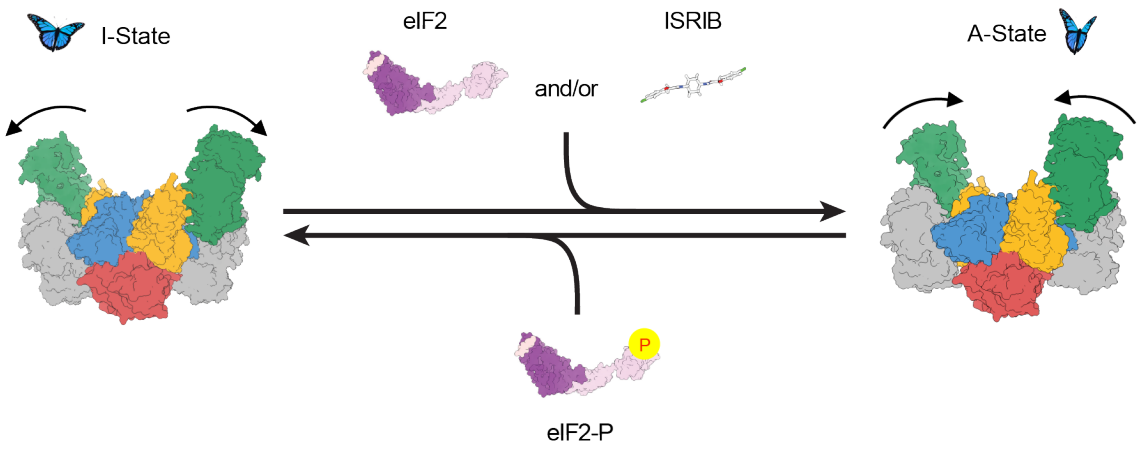

Figure 1.8: Model for modulation of eIF2B activity.
ISRIB and eIF2 binding to eIF2B stabilize the active, “wings up” conformation of eIF2B (A-State) while both eIF2-P (as well as eIF2α-P alone; not shown) stabilize the inactive “wings down” conformation of eIF2B (I-State), which cannot engage ISRIB and exhibits reduced enzymatic activity and eIF2 binding (akin to an eIF2Bβδγε tetramer). As indicated by the structure of the apo eIF2B decamer, the conformational equilibrium in the absence of ligand likely favors the A-State, which is further stabilized by substrate eIF2 and/or ISRIB binding but antagonized by eIF2-P binding.

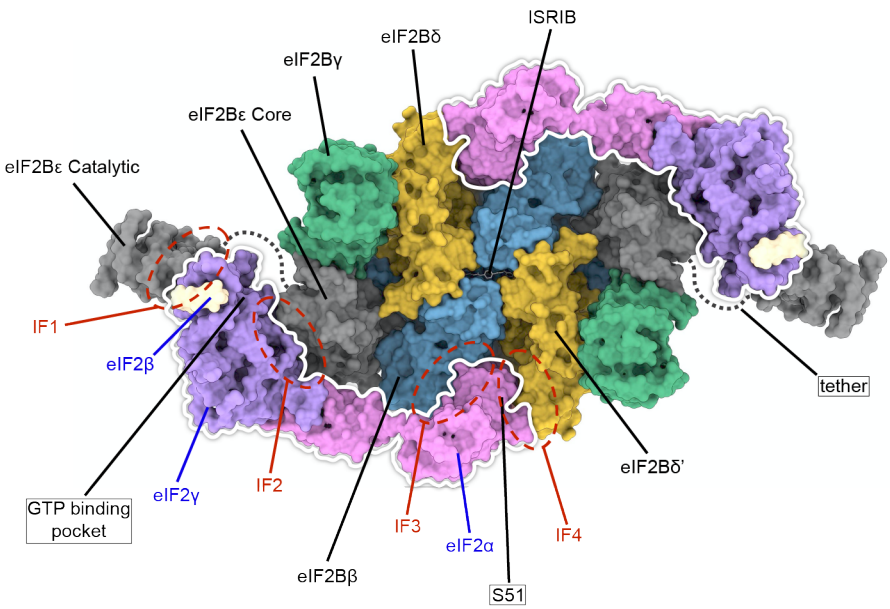

Figure 1.1 – figure supplement 1: Overview of key eIF2 and eIF2B interaction surfaces. A surface representation of a model of two eIF2 heterotrimers and ISRIB bound to an eIF2B decamer is shown (PDB ID: 6O85). Individual subunits of eIF2 and eIF2B are indicated. The eIF2 heterotrimers are outlined in white and the locations of interfaces IF1 - IF4 are indicated, as are the positions of eIF2α S51, the GTP binding pocket (empty in the structure), and ISRIB (shown in stick representation). The eIF2Bα_2 dimer is hidden in this orientation. eIF2Bε contains two domains linked by a flexible tether which was not resolved in the structure.

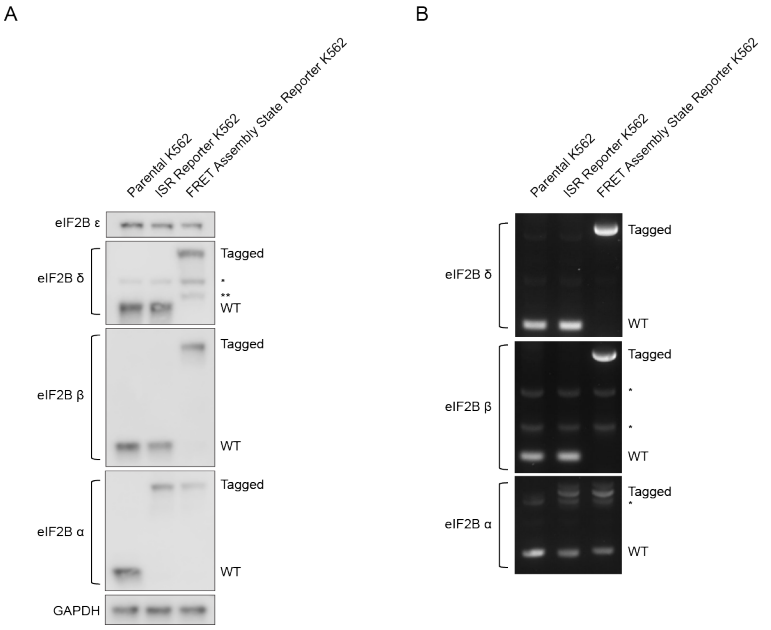

Figure 1.1 – figure supplement 2: Tagging of eIF2B subunits in K562 cells.
(A) Western blot of eIF2B subunits in parental and edited K562 cells. ISR Reporter cells and Assembly State Reporter cells were edited at the *EIF2B1* locus (eIF2Bα-FKBP12^{F36V} N-terminal fusion). No evidence of WT protein is observed in either cell line. Assembly State Reporter cells were edited at the *EIF2B2* locus (eIF2Bβ-mNeonGreen C-terminal fusion) and the *EIF2B4* locus (eIF2Bδ-mScarlet-i C-terminal fusion). No evidence of WT protein is observed in these cells. The asterisk denotes a non-specific band. The double asterisk denotes a minor eIF2Bδ species likely resulting from mScarlet-i / G/S linker proteolysis during sample preparation. eIF2Bδ and eIF2Bα blots and eIF2Bε and GAPDH blots are from the same gel, respectively; eIF2Bβ is from its own blot. **(B)** 1% agarose gel of PCR amplified eIF2Bα-, eIF2Bβ-, and eIF2Bδ-encoding loci from parental and edited cell line gDNA preps. The lengths of the eIF2Bβ and eIF2Bδ products demonstrate that no unedited alleles are present in the Assembly State reporter cells. The length of the eIF2Bα product demonstrates that some tagged as well as some untagged alleles are present in both cell lines. Based on the lack of WT length protein the remaining untagged alleles likely harbor deletions or frameshift mutations that prevent synthesis or destroy the protein product. The asterisk denotes a non-specific band.

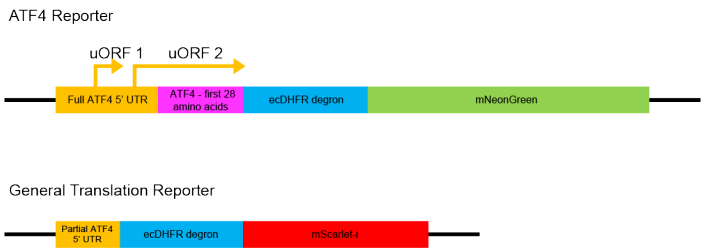

Figure 1.1 – figure supplement 3: ISR reporter design.
A schematic of the ATF4 Translation and General Translation reporters used to read out ISR activation.

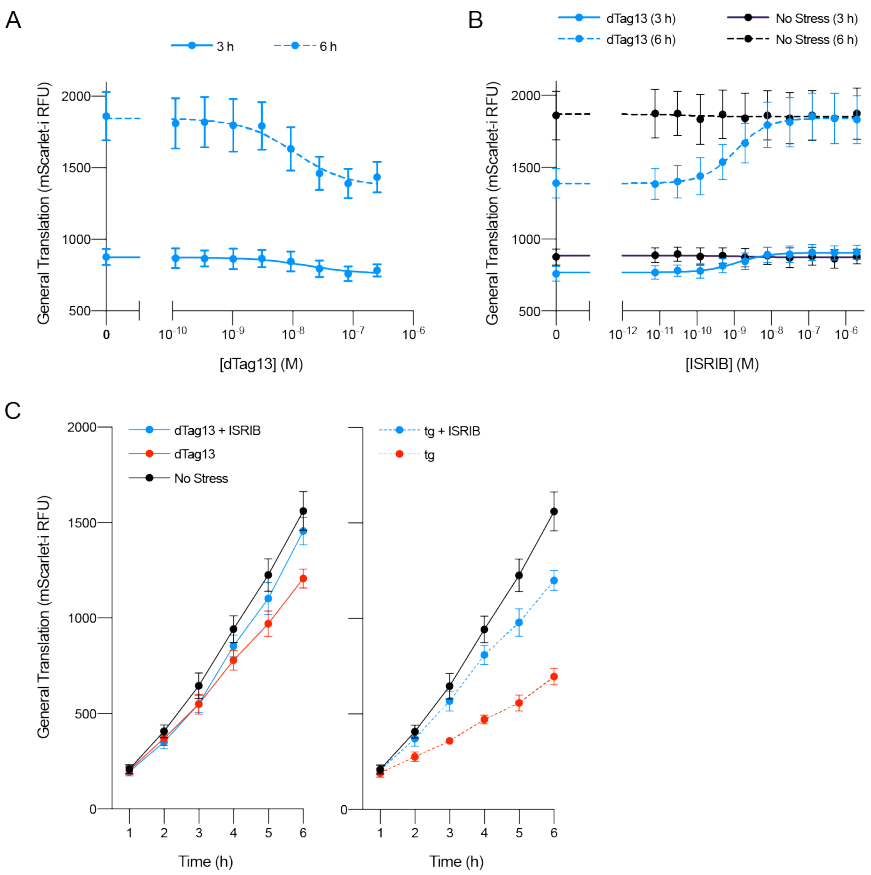

Figure 1.1 – figure supplement 4: Decreases in general translation after eIF2Bα depletion. **(A-C)** General translation reporter signal from the experiments shown in (A) Figure 1.1C, (B) Figure 1.1D, and (C) Figure 1.1E.

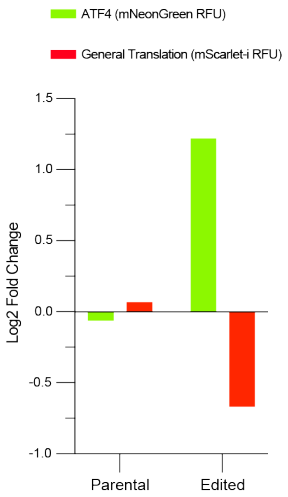

Figure 1.1 – figure supplement 5: dTag13 treatment alone does not activate the ISR. Parental cells containing the ATF4 and general translation reporters as well as the edited cells where eIF2Bα was tagged with an FKBP12^{F36V} degron were treated with 500 nM dTag13 or untreated (0.1% DMSO) for 24 h and then 20 μM trimethoprim for 3 h. ATF4 and General translation reporter levels were monitored by flow cytometry and the change in reporter signal between dTag13 treated and untreated conditions is shown. dTag13 only activates the ISR when eIF2Bα is endogenously tagged with the FKBP12^{F36V} degron.

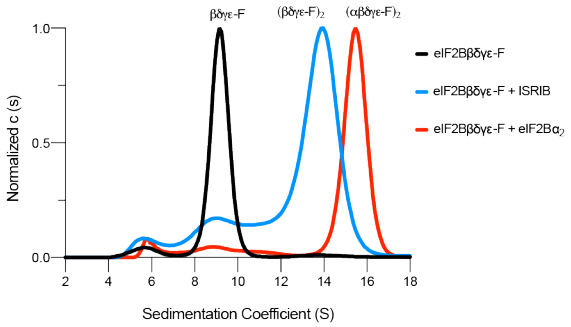

Figure 1.2 – figure supplement 1: eIF2Bβδγε-F can octamerize and decamerize**.** Analytical ultracentrifugation (sedimentation velocity) was used to determine eIF2B complex assembly state. Treatment with ISRIB induces octamerization of eIF2Bβδγε-F. Treatment with eIF2Bα_2 induces decamerization. 1 μM ISRIB, 1 μM eIF2Bβδγε-F, and 500 nM eIF2Bα_2 were used.

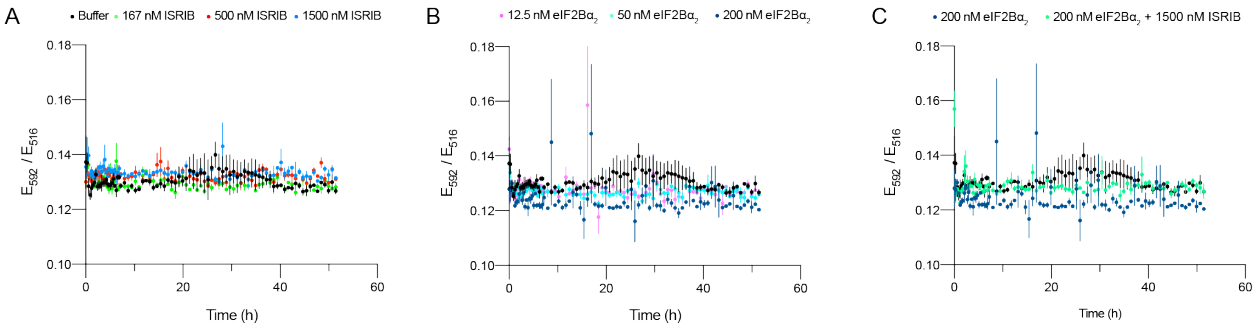

Figure 1.2 – figure supplement 2: Validation of eIF2Bβδγε-F kinetics.
(A-C) Treatment of 50 nM eIF2Bβδγε-F with ISRIB or eIF2Bα$_2$ led to no changes in FRET signal when simultaneously treated with excess of untagged eIF2Bβδγε (1 μM).
For (A-C), representative replicate averaging three technical replicates are shown. Biological replicates: n = 2. All error bars represent s.e.m.

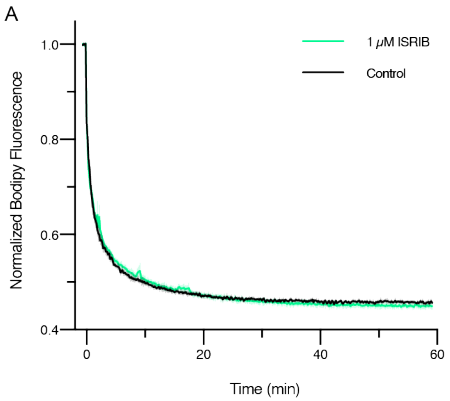

Figure 1.2 – figure supplement 3: ISRIB treatment does not impact GEF activity when eIF2Bα_2 is saturating.
GEF activity of eIF2B as assessed by BODIPY-FL-GDP exchange. BODIPY-FL-GDP fluorescence decreases when free in solution. $t_{1/2}$ = 1.6 min (Control) and 1.9 min (1 μM ISRIB). Biological replicates: n = 3.

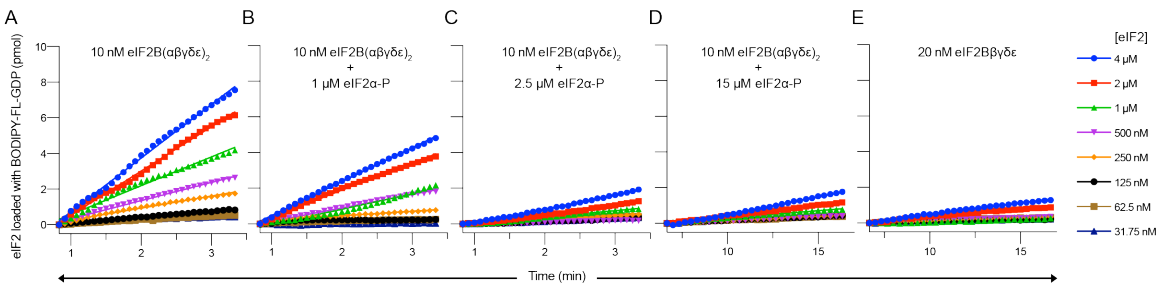

Figure 1.6 – figure supplement 1: eIF2α-P decreases the initial velocity of eIF2B's GEF activity.
(A-E) Initial velocity of the eIF2B GEF reaction under varying conditions. Initial velocity was determined by a linear fit to timepoints acquired from 50 – 200 seconds (panels A - C) or 400 - 1000 seconds (panels D - E) after addition of eIF2B. For panels A – E, representative replicates of n = 2 biological replicates are shown.

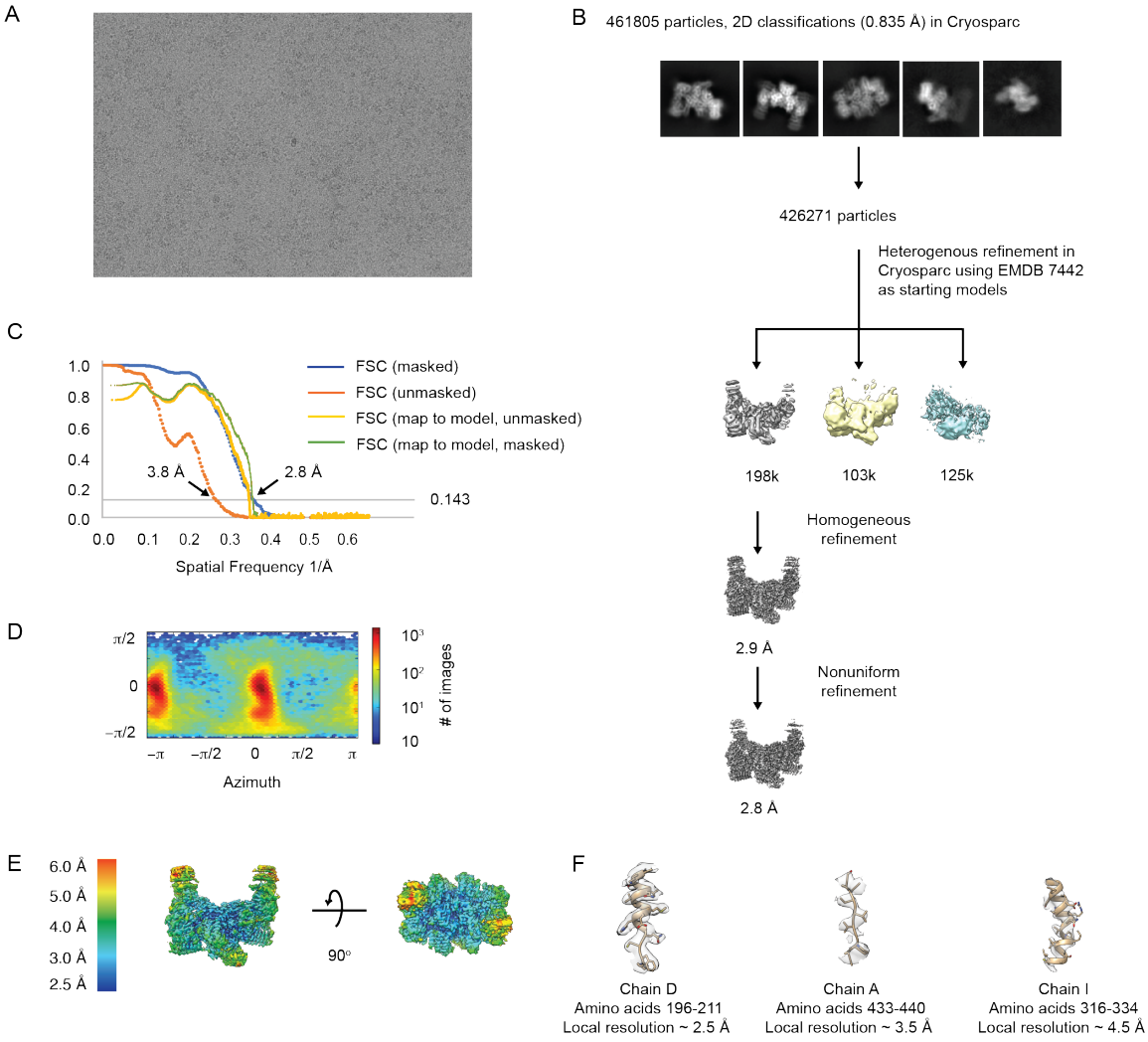

Figure 1.7 – figure supplement 1: Cryo-EM workflow for apo-eIF2B decamer. **(A)** Representative micrograph showing the quality of data used for the final reconstruction of the apo eIF2B structure. **(B)** Data processing scheme of the apo eIF2B. **(C)** Fourier Shell Correlation (FSC) plots of the 3D reconstructions of the apo eIF2B masked (dark blue), unmasked (orange) and map to model (yellow). **(D)** Orientation angle distribution of the apo eIF2B reconstruction. **(E)** Local resolution map of the apo eIF2B showing that the peripheral regions of the gamma and alpha subunits are dynamic. (**F**) EM maps of different regions of the apo eIF2B structure showing the quality of the data and the fit of the model. Regions close to the core (chain D, on the left) are well-resolved and have clear density for most side chains; regions close to the periphery of the molecule (chains A and I, middle and right) are less well-resolved due to higher flexibility.

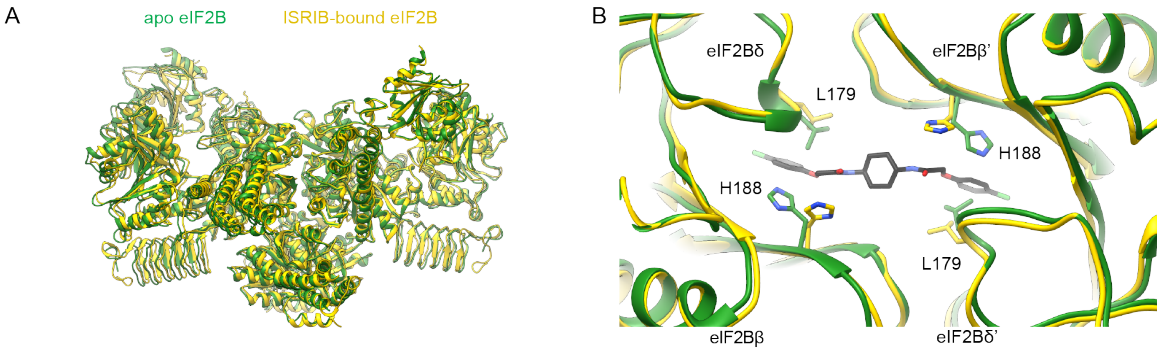

Figure 1.7 – figure supplement 2: ISRIB binding induces local pocket changes.
(A) Overlay of ISRIB-bound eIF2B (PDB ID: 6CAJ) to the apo eIF2B (PDB ID: 7L70) showing both structures share a similar global conformation. **(B)** Zoom-in view of the ISRIB-binding pocket showing that in the apo state L179 occupies a position in the ISRIB-binding pocket that would clash with ISRIB binding. H188 changes its rotameric conformation upon ISRIB binding. The apo eIF2B is shown in *green*, and the ISRIB-bound eIF2B in *gold*. ISRIB is shown in stick representation, colored in *CPK*.

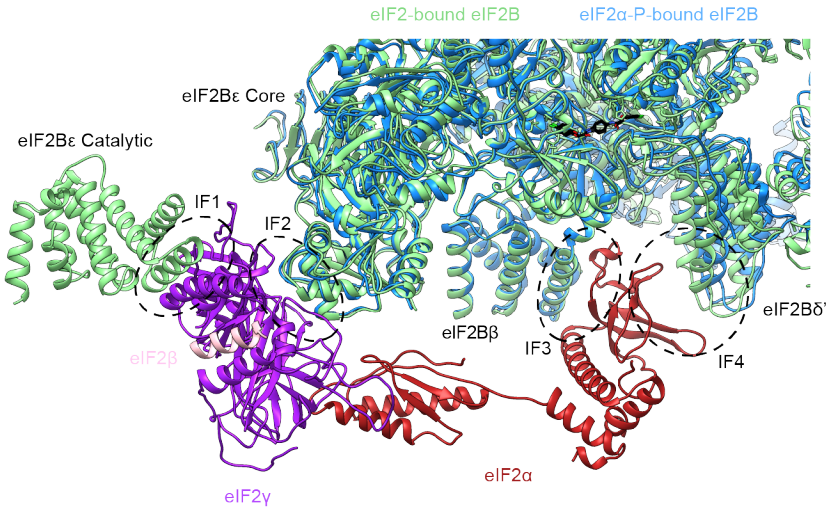

Figure 1.7 – figure supplement 3: eIF2-P binding pulls IF4 away but leaves IF1 - IF3
Overlay of eIF2-bound eIF2B (PDB ID: 6O85) and eIF2α-P-bound eIF2B (PDB ID: 6O9Z). IF4 is pulled away from IF3 by 2.6 Å but IF1 (eIF2Bε Catalytic and eIF2γ), IF2 (eIF2Bε Core and eIF2γ), and IF3 (eIF2Bβ and eIF2α) remain available for eIF2 binding. eIF2α-P-bound eIF2B in *blue* and eIF2-bound eIF2B in *light green*. eIF2γ is shown in *purple*, eIF2β in *pink,* and eIF2α in *red*. ISRIB is colored in *CPK*.

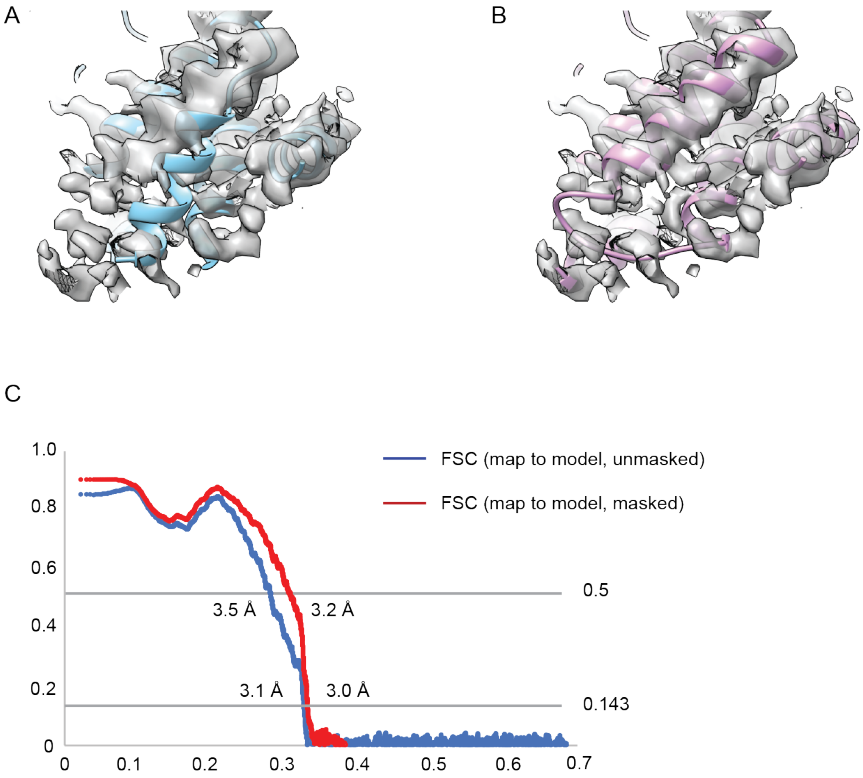

Figure 1.7 – figure supplement 4: Re-refinement of the ISRIB-bound eIF2B decamer. **(A)** The distal portion of the original model eIF2Bα from the ISRIB-bound eIF2B decamer placed within EMDB:7443 after lowpass filtering to 3.0Å resolution. There is a helix (amino acids 44-56) out of place. The average CC value for the chains belonging to eIF2Bα from this model is ~0.74. **(B)** After manual adjustments in Coot and re-refinement in phenix.real_space_refine, this short helix is placed inside the cryo-EM density with an average CC value for the chains belonging to eIF2Bα of ~0.77. **(C)** The map-to-model Fourier Shell Correlation plots of the updated model.

Table 1.1 Cryo-electron microscopy dataset for Apo eIF2B decamer

Structure	Apo eIF2B decamer (PDB ID: 7L70; EMD-23209)
Data collection	
Microscope	Titan Krios
Voltage (keV)	300
Nominal magnification	105000x
Exposure navigation	Image shift
Electron dose (e^{-}Å^{-2})	67
Dose rate (e^{-}/pixel/sec)	8
Detector	K3 summit
Pixel size (Å)	0.835
Defocus range (μm)	0.6-2.0
Micrographs	1699
Reconstruction	
Total extracted particles (no.)	461805
Final particles (no.)	198362
Symmetry imposed	C1
FSC average resolution, masked (Å)	3.8
FSC average resolution, unmasked (Å)	2.8
Applied B-factor (Å)	92.4
Reconstruction package	Cryosparc 2.15
Refinement	
Protein residues	3156
Ligands	0
RMSD Bond lengths (Å)	0.004
RMSD Bond angles (°)	0.978
Ramachandran outliers (%)	0.06
Ramachandran allowed (%)	3.81
Ramachandran favored (%)	96.13
Poor rotamers (%)	2.61
CaBLAM outliers (%)	2.00
Molprobity score	1.83
Clash score (all atoms)	4.77
B-factors (protein)	88.43
B-factors (ligands)	N/A
EMRinger Score	2.68
Refinement package	Phenix 1.17.1-3660-000

Data collection, reconstruction, and model refinement statistics for the apo eIF2B decamer

Table 1.2 Cryo-electron microscopy dataset for ISRIB-bound eIF2B decamer

Structure	ISRIB-bound eIF2B decamer from Janelia (PDB ID: 6CAJ) (Tsai et al. 2018)	ISRIB-bound eIF2B decamer from Berkeley (PDB ID: 6CAJ) (Tsai et al. 2018)
	Data collection	
Voltage (keV)	300	300
Nominal magnification	29000x	29000x
Per frame electron dose (e^{-}Å^{-2})	1.19	1.63
Spherical aberration (mm)	2.7	2.62
# of frames	67	27
Detector	K2 summit	K2 summit
Pixel size (Å)	1.02	0.838
Defocus range (μm)	-0.3 to -3.9	-0.3 to -3.9
Micrographs	1780	1515
Frame length (s)	0.15	0.18
Detector pixel size (μm)	5.0	5.0
Reconstruction Using Particles From Both Datasets After Magnification Rescaling		
Particles following 2D classification	202,125	
FSC average resolution unmasked (Å)	3.4	
FSC average resolution masked (Å)	3.0	
Map sharpening B-factor	-60	
Refinement		
PDB ID: 7L7G (Update to 6CAJ); EMD-7443		
Protein residues	3198	
Ligands	1	
RMSD Bond lengths (Å)	0.004	
RMSD Bond angles (°)	0.967	
Ramachandran outliers (%)	0.00	
Ramachandran allowed (%)	5.40	
Ramachandran favored (%)	94.60	
Poor rotamers (%)	1.00	
Molprobity score	1.81	
Clash score (all atoms)	7.95	
B-factors (protein)	65.93	
B-factors (ligands)	52.57	
EMRinger Score	2.37	
Refinement package	Phenix 1.17.1-3660-000	

Data collection, reconstruction and refinement statistics for the ISRIB-bound eIF2B decamer

Table 1.3 Antibodies and Western blotting conditions

Antibody Target	Host	Dilution	Manufacturer	Blocking Conditions
GAPDH	rabbit	1/2000	Abcam	TBS-T + 3% BSA
eIF2Bα	rabbit	1/1000	ProteinTech	TBS-T + 3% milk
eIF2Bβ	rabbit	1/1000	ProteinTech	TBS-T + 3% milk
eIF2Bδ	rabbit	1/1000	ProteinTech	TBS-T + 3% milk
eIF2Bε	mouse	1/1000	Santa Cruz Biotechnology	PBS-T + 3% milk
ATF4	rabbit	1/1000	Cell Signaling	PBS-T + 3% milk
eIF2α-P	rabbit	1/1000	Cell Signaling	PBS-T + 1% BSA
eIF2α	rabbit	1/1000	Cell Signaling	PBS-T + 3% milk
eIF2β	rabbit	1/1000	ProteinTech	PBS-T + 3% milk
eIF2γ	rabbit	1/500	ProteinTech	PBS-T + 3% milk

Table 1.4 Primers, oligos, and guide RNAs

Oligo	Sequence	Use
oMS266	/5InvddT/G*G*G*A*A*CCTCTTCT GTAACTCCTTAGC	Amplify HDR template
oMS267	/5InvddT/C*C*T*G*A*G*GGCAAA CAAGTGAGCAGG	Amplify HDR template
oMS269	TCGTGCCAGCCCCCTAATCT	Validate eIF2Bα tagging
oMS270	CTGAACGGCGCTGCTGTAGC	Validate eIF2Bα tagging
oMS256	AGTGAACTCTACCATCCTGA	Validate eIF2Bβ tagging
oMS258	TTAGGTGGACTCCTGTGC	Validate eIF2Bβ tagging
oMS096	CTGGCTAACTGGCAGAACC	Validate eIF2Bδ tagging
oMS268	AGAAACAAAGGCAGCAGAGT	Validate eIF2Bδ tagging
sgMS001	CAATCTGCTTAGGACACGTG	Target Cas9 to eIF2Bβ C-terminus
sgMS004	AGAGCAGTGACCAGTGACGG	Target Cas9 to eIF2Bδ C-terminus
sgMS006	GTGTGTGGTTGTCATTAGGG	Target Cas9 to eIF2$\alpha\beta$ N-terminus

Materials and Methods

Cloning of tagged human eIF2B expression plasmids

eIF2B2 (encoding eIF2Bβ) and *eIF2B4* (encoding eIF2Bδ) had previously been inserted into sites 1 and 2 of pACYCDuet-1, respectively (pJT073) (Tsai et al. 2018). In-Fusion HD cloning (Takarabio) was used to edit this plasmid further and insert mNeonGreen and a $(GS)_5$ linker at the C-terminus of *eIF2B2* and mScarlet-i and a $(GS)_5$ linker at the C-terminus of *eIF2B4* (pMS029). *eIF2B1* (encoding eIF2Bα) had previously been inserted into site 1 of pETDuet-1 (pJT075) (Tsai et al. 2018). In-Fusion HD cloning was used to edit this plasmid further and insert a protein C tag (EDQVDPRLIDGK) at the N-terminus of *eIF2B1*, immediately following the pre-existing 6x-His tag (pMS027).

Cloning of ATF4 and general translation reporter plasmids

The ATF4 translation reporter was generated using In-Fusion HD cloning. A gBlock containing the ATF4 UTR with both uORF1 and uORF2, ecDHFR, and mNeonGreen was inserted into the pHR vector backbone. The vector was additionally modified to contain a bGH poly(A) signal. The general translation reporter was similarly generated using a gBlock containing a modified ATF4 UTR with both uORF1 and uORF2 removed, ecDHFR, and mScarlet-i.

Cloning of eIF2B homology-directed recombination (HDR) template plasmids

HDR template plasmids were generated using Gibson Assembly (NEB) cloning. gBlocks containing mNeonGreen and flanking *eIF2B2* homology arms (pMS074), mScarlet-i and flanking *eIF2B4* homology arms (pMS075), and $FKBP12^{F36V}$ and flanking *eIF2B1* homology arms (pMS101) were inserted into the pUC19 vector. Homology arms were 300bp in all instances.

ISR reporter cell line generation

K562 cells expressing dCas9-KRAB as previously generated were used as the parental line (Gilbert et al. 2014). In the ISR reporter cell line, the general translation reporter and the ATF4 reporter were integrated sequentially using a lentiviral vector. Vesicular stomatitis virus (VSV)-G pseudotyped lentivirus was prepared using standard protocols and 293METR packaging cells. Viral supernatants were filtered through a 0.45 μm (low protein binding) filter unit (EMD Millipore). The filtered retroviral supernatant was then concentrated 20-fold using an Amicon Ultra-15 concentrator (EMD Millipore) with a 100,000-dalton molecular mass cutoff. Concentrated supernatant was then used the same day or frozen for future use. For spinfection, approximately 900,000 K562 cells were mixed with concentrated lentivirus + virus collection media (DMEM containing 4.5 g/l glucose supplemented with 10% FBS, 6 mM L-glutamine, 15 mM HEPES and penicillin/streptomycin), supplemented with polybrene to 8 μg/ml, brought to 1.5 mL in a 6-well plate, and centrifuged for 1.5 h at 1000 g. Cells were then allowed to recover and expand for ~1 week before sorting on a Sony SH800 cytometer to isolate cells that had integrated the reporter. Before sorting, cells were treated with 20 μM trimethoprim for 3 h to stabilize the general translation reporter product (ecDHFR-mScarlet-i). mScarlet-i positive cells (targeting a narrow window around median reporter fluorescence) were then sorted into a final pooled population.

Integration of the ATF4 reporter was performed as above, using the general translation reporter-containing cells as stock for spinfection. At the sorting stage, cells were again treated with 20 μM trimethoprim as well as 100 nM thapsigargin (tg) to allow ATF4 reporter translation to be monitored. The highest 3% of mNeonGreen-positive cells were sorted into a final pooled population.

The *eIF2B1* locus was endogenously edited using modifications to previous protocols (Leonetti et al. 2016). In brief, an HDR template was prepared by PCR amplifying from pMS101 using oligos oMS266 and oMS267 (Table 1.4). This product was then purified and concentrated to >1 µM using magnetic SPRI beads (Beckman Coulter). 2.2 µl Cas9 buffer (580 mM KCl, 40 mM Tris pH 7.5, 2 mM TCEP (tris(20carboxyethyl)phosphine)-HCl, 2 mM $MgCl_2$, and 20% v/v glycerol) was added to 1.3 µl of 100 µM sgRNA (sgMS006, purchased from Synthego) and 2.9 µl H_2O and incubated at 70 °C for 5 minutes. 1.6 µl of 62.5 µM Alt-R S.p Cas9 Nuclease V3 (IDT) was slowly added to the mix and incubated at 37 °C for 10 min. The donor template was then added to a final concentration of 0.5 µM, and final volume of 10 µl and the RNP mix was stored on ice.

ISR reporter cells were treated with 200 ng / mL nocodazole (Sigma Aldrich) to synchronize at G2 / M phase for 18 h. Approximately 200,000 cells were resuspended in a mixture of room temperature Amaxa solution (16.4 µl SF Solution, 3.6 µl Supplement (Lonza)). The cell / Amaxa solution mixture was added to the RNP mix and then pipetted into the bottom of a 96-well nucleofection plate (Lonza). This sample was then nucleofected using the 4D-Nucleofector Core unit and 96-well shuttle device (Lonza) with program FF-120. The cells were then returned to pre-warmed RPMI media in a 37 °C incubator and allowed to recover/expand for >1 week. Limiting dilutions of cells were then prepared and plated in individual wells of a 96-well plate and allowed to grow up to identify clonal cells. Identification of edited clones was performed by Western blotting for eIF2Bα and PCR amplification of the edited locus.

FRET assembly state reporter cell line generation

eIF2Bβ-mNeonGreen-Flag-tagged cells were generated as described above with pMS074 used to PCR amplify the HDR template and sgMS001 used as the sgRNA. After recovery and expansion, the edited cells were sorted on a Sony SH800 cytometer, and the top 0.1% of

mNeonGreen fluorescing cells were sorted into a polyclonal population. After expansion, recovery, and determining that the editing efficiency was over 90% in this population, the polyclonal cells were subjected to a second round of nucleofection using an HDR template amplified off of pMS075 to endogenously tag eIF2Bδ. sgMS004 was used to target the *eIF2B2* locus. Nucleofection conditions were as described above. After ~1 week of recovery and expansion, cells were again sorted as described above to isolate the highest mScarlet-i fluorescing cells. After ~1 week of recovery, limiting dilutions were prepared as described above to isolate and validate editing in individual clones. A fully *eIF2B2*-edited and *eIF2B4*-edited clone was then subjected to a third round of nucleofection to introduce the eIF2Bα-FKBP12^{F36V} fusion. This was performed under identical conditions to those described above for the ISR reporter cell line.

ATF4 / general translation reporter assays

ISR reporter cells (at ~500,000 / ml) were co-treated with varying combinations of drugs (trimethoprim, dTag13, thapsigargin, ISRIB) and incubated at 37 °C until the appropriate timepoint had been reached. At this time, the plate was removed from the incubator and samples were incubated on ice for 10 min. Then ATF4 (mNeonGreen) and General Translation (mScarlet-i) reporter levels were read out using a high throughput sampler (HTS) attached to a BD FACSCelesta cytometer. Data was analyzed in FlowJo version 10.6.1, and median fluorescence values for both reporters were exported and plotted in GraphPad Prism 8. Where appropriate curves were fit to log[inhibitor] versus response function with variable slope.

***In vivo* FRET assembly state reporter assays**

FRET assembly state reporter cells (at ~500,000 / ml) were dosed with varying combinations of drugs (dTag13, thapsigargin, ISRIB) and incubated at 37 °C until the appropriate timepoint had been reached. At this time, the plate was removed from the incubator, and samples were

transferred to 5 ml FACS tubes. Samples were kept on ice. FRET signal was measured on a BD FACSAria Fusion cytometer. Data were analyzed in FlowJo version 10.6.1 and median fluorescence values for both mNeonGreen and mScarlet-i emission after mNeonGreen excitation were calculated. The ratio of these two values (termed “FRET signal”) was plotted in GraphPad Prism 8. Where appropriate curves were fit to log[inhibitor] versus response function with variable slope.

Western Blotting

Approximately 1,000,000 cells of the appropriate cell type were drugged as described in individual assays and then pelleted (500x g for 4 min) at 4 °C, resuspended in ice cold PBS, pelleted again, and then resuspended in 150 µl lysis buffer (50 mM Tris-HCl pH 7.4, 150 mM NaCl, 1mM EDTA, 1% v/v Triton X-100, 10% v/v glycerol, 1x cOmplete protease inhibitor cocktail (Roche), and 1x PhosSTOP (Roche)). Cells were rotated for 30 min at 4 °C and then spun at 12,000 g for 20 min to pellet cell debris. The supernatant was removed to a fresh tube and protein concentration was measured using a bicinchoninic acid assay (BCA assay). Within an experiment, total protein concentration was normalized to the least concentrated sample (typically all values were within ~10% and in the 1 µg / µl range). 5x Laemmli loading buffer (250 mM Tris-HCl pH 6.8, 30% glycerol, 0.25% bromophenol blue, 10% SDS, 5% beta-mercaptoethanol) was added to each sample. Samples were placed in a 99 °C heat block for 10 min. Equal protein content for each condition (targeting 10 µg) was run on 10% Mini-PROTEAN TGX precast protein gels (Biorad). After electrophoresis, proteins were transferred onto a nitrocellulose membrane. Primary antibody / blocking conditions for each protein of interest are outlined in Table 1.3. Initial blocking is performed for 2 h. Primary antibody staining was performed with gentle agitation at 4 °C overnight. After washing 4 times in the appropriate blocking buffer, secondary antibody staining was performed for 1 h at room temperature and then membranes were washed 3x with the appropriate blocking buffer and then 1x with TBS-T

or PBS-T as appropriate. Membranes were developed with SuperSignal West Dura (Thermo Fisher Scientific). Developed membranes were imaged on a LI-COR Odyssey gel imager for 0.5-10 min depending on band intensity.

FLAG Immunoprecipitation

Approximately 25,000,000 cells were drugged as described, removed from the incubator after 3 h of treatment, and pelleted (3 min, 1000 x g) then resuspended in ice cold PBS then pelleted again. Cells were then resuspended in 200 µl Lysis Buffer (25 mM HEPES pH 7.4, 150 mM KCl, 1% NP-40, 1 mM EDTA, 2.5x cOmplete protease inhibitor cocktail (Roche), and 1x PhosSTOP (Roche)). Cells were vortexed for 3 s then incubated on ice for 3 min, with this process repeated 3 times. Cell debris was pelleted as described above, and the supernatant was removed to a new tube. A portion was retained as the Cell Lysate fraction. The remaining cell lysate was incubated at 4 °C overnight with M2 flag monoclonal antibody (Sigma Aldrich) conjugated to magnetic Protein G Dynabeads (Invitrogen). Beads were washed 3x with 500 µl of Sample Buffer (20 mM HEPES pH 7.4, 100 mM KCl, 5 mM $MgCl_2$, and 1 mM TCEP) and then eluted using FLAG peptide at 200 µg / ml (eIF2B Bound fraction). Both fractions were then treated as described above for Western blotting.

gDNA isolation, PCR, and DNA gel of edited loci

gDNA from parental and edited cells was isolated using the PureLink Genomic DNA Mini Kit (Invitrogen) as per manufacturer instructions. The targeted *EIF2B1*, *EIF2B2*, and *EIF2B4* loci were amplified with the primer pairs detailed in Table 1.4 and run on a 1% agarose gel and imaged using a ChemiDoc XRS+ imaging system (Biorad). The expected WT fragment length for the *EIF2B1*, *EIF2B2*, and *EIF2B4* products are 256, 151, and 224 bp, respectively, while the edited products are expected at 643, 955, and 997 bp, respectively.

Purification of human eIF2B subcomplexes

Human eIFBα_2 (pJT075 or pMS027), eIF2B$\beta\gamma\delta\varepsilon$ (pJT073 and pJT074 co-expression), and eIF2B$\beta\gamma\delta\varepsilon$-F (pMS029 and pJT074 co-expression) were purified as previously described (Tsai et al. 2018). All eIF2B$(\alpha\beta\gamma\delta\varepsilon)_2$ used throughout was assembled by mixing purified eIF2B$\beta\gamma\delta\varepsilon$ and eIF2Bα_2 at the appropriate molar ratios.

Purification of human eIF2α and eIF2α-P

The purification of human eIF2α was modified from a previous protocol (Kenner et al. 2019). Briefly, the expression plasmid for N-terminally 6x-His-tagged human eIF2α, pAA007, was heat-transformed into One Shot BL21 Star (DE3) chemically competent *E. coli* cells (Invitrogen), along with the tetracycline-inducible, chloramphenicol-resistant plasmid, pG-Tf2, containing the chaperones groES, groEL, and Tig (Takara Bio). Transformed cells were selected for in LB with kanamycin and chloramphenicol. When the culture reached an OD600 of ~0.2, 1 ng / ml, tetracycline was added to induce expression of chaperones. At an OD_{600} of ~0.8, the culture was cooled to room temperature, eIF2α expression was induced with 1 mM IPTG (Gold Biotechnology) and the culture was grown for 16 hours at 16 °C. Cells were harvested and lysed through 3 cycles of high-pressure homogenization using the EmulsiFlex-C3 (Avestin) in a buffer containing 100 mM HEPES-KOH, pH 7.5, 300 mM KCl, 2 mM dithiothreitol (DTT), 5 mM $MgCl_2$, 5 mM imidazole, 10% glycerol, 0.1% IGEPAL CA-630, and cOmplete EDTA-free protease inhibitor cocktail (Roche). The lysate was clarified at 30,000 x g for 30 min at 4 °C. Subsequent purification steps were conducted on the ÄKTA Pure (GE Healthcare) system at 4 °C. Clarified lysate was loaded onto a 5 ml HisTrap FF Crude column (GE Healthcare), washed in a buffer containing 20 mM HEPES-KOH, pH 7.5, 100 mM KCl, 5% glycerol, 1 mM DTT, 5 mM $MgCl_2$, 0.1% IGEPAL CA-630, and 20 mM imidazole, and eluted with 75 ml linear gradient of 20 to 500 mM imidazole. The eIF2α-containing fractions were collected and applied to a MonoQ HR 10/100 GL column (GE Healthcare) equilibrated in a buffer containing 20 mM HEPES-KOH pH

7.5, 100 mM KCl, 1 mM DTT, 5% glycerol, and 5 mM $MgCl_2$ for anion exchange. The column was washed in the same buffer, and the protein was eluted with an 80 ml linear gradient of 100 mM to 1 M KCl. eIF2α containing fractions were collected and concentrated with an Amicon Ultra-15 concentrator (EMD Millipore) with a 30,000-dalton molecular mass cutoff, spun down for 10 min at 10,000 g to remove aggregates. The supernatant was then chromatographed on a Superdex 75 10/300 GL (GE Healthcare) column equilibrated in a buffer containing 20 mM HEPES-KOH pH 7.5, 100 mM KCl, 1 mM DTT, 5 mM $MgCl_2$, and 5% glycerol, and concentrated using Amicon Ultra-15 concentrators (EMD Millipore) with a 10,000-dalton molecular mass cutoff.

For the purification of human phosphorylated eIF2α (eIF2α-P) the protein was expressed and purified as described above for eIF2α, except that before size exclusion on the Superdex 75, the pooled anion exchange fractions were phosphorylated *in vitro* overnight at 4 °C with 1 mM ATP and 1 µg of $PKR_{(252-551)}$-GST enzyme (Thermo Scientific) per mg of eIF2α. Complete phosphorylation was confirmed by running the samples on a 12.5% Super-Sep PhosTag gel (Wako Chemicals).

Purification of heterotrimeric human eIF2 and eIF2-P

Human eIF2 was prepared from an established recombinant *S. cerevisiae* expression protocol (de Almeida et al. 2013). In brief, the yeast strain GP6452 (gift from the Pavitt lab, University of Manchester) containing yeast expression plasmids for human eIF2 subunits and a deletion of GCN2 encoding the only eIF2 kinase in yeast, was grown to saturation in synthetic complete media (Sunrise Science Products) with auxotrophic markers (-Trp, -Leu, -Ura) in 2% dextrose. The β and α subunits of eIF2 were tagged with 6x-His and FLAG epitopes, respectively. A 12 liter yeast culture was grown in rich expression media containing yeast extract, peptone, 2% galactose, and 0.2% dextrose. Cells were harvested and resuspended in lysis buffer (100 mM

Tris, pH 8.5, 300 mM KCl, 5 mM $MgCl_2$, 0.1% NP-40, 5 mM imidazole, 10% glycerol (Thermo Fisher Scientific), 1 mM TCEP, 1x cOmplete protease inhibitor cocktail (Sigma Aldrich), 1 μg / ml each aprotinin (Sigma Aldrich), leupeptin (Sigma Aldrich), pepstatin A (Sigma Aldrich)). Cells were lysed in liquid nitrogen using a steel blender. The lysate was centrifuged at 30,000 x g for 30 min at 4 °C. Subsequent purification steps were conducted on the ÄKTA Pure (GE Healthcare) system at 4 °C. Lysate was applied to a 5 ml HisTrap FF Crude column (GE Healthcare) equilibrated in buffer (100 mM HEPES-KOH, pH 7.5, 100 mM KCl, 5 mM $MgCl_2$, 0.1% NP-40, 5% glycerol, 1 mM TCEP, 0.5x cOmplete protease inhibitor cocktail, 1 μg/ml each aprotinin, leupeptin, pepstatin A). eIF2 bound to the column was washed with equilibration buffer and eluted using a 50 ml linear gradient of 5 mM to 500 mM imidazole. Eluted eIF2 was incubated with FLAG M2 magnetic affinity beads, washed with FLAG wash buffer (100 mM HEPES-KOH, pH 7.5, 100 mM KCl, 5 mM $MgCl_2$, 0.1% NP-40, 5% glycerol, 1 mM TCEP, 1x cOmplete protease inhibitor cocktail, 1 μg/ml each aprotinin, leupeptin, pepstatin A) and eluted with FLAG elution buffer [identical to FLAG wash buffer but also containing 3x FLAG peptide (100 μg/ml, Sigma Aldrich)]. Protein was flash-frozen in liquid nitrogen and stored in elution buffer at -80 °C.

For the purification of eIF2-P the protein was purified as above, except that a final concentration of 10 nM recombinant PKR (Life Technologies # PV4821) and 1 mM ATP was added during incubation with FLAG M2 magnetic beads. These components were removed during the wash steps described above. Phosphorylation of the final product was verified by 12.5% SuperSep PhosTag gel (Wako Chemical Corporation).

Additional human eIF2 was purified as previously described with the only modification in one purification being an additional Avi-Tag on the eIF2α subunit (Wong et al. 2018). This material was a generous gift of Carmela Sidrauski and Calico Life Sciences.

In vitro eIF2/eIF2α-P immunoprecipitation

eIF2B$(\alpha\beta\delta\gamma\varepsilon)_2$ decamers were assembled by mixing eIF2Bβγδε and protein C-tagged eIF2Bα_2 in a 2:1 molar ratio and incubating at room temperature for at least 1 hour. Varying combinations of purified eIF2, eIF2α-P, eIF2B$(\alpha\beta\delta\gamma\varepsilon)_2$, and ISRIB were incubated (with gentle rocking) with Anti-protein C antibody conjugated resin (generous gift from Aashish Manglik) in Assay Buffer (20 mM HEPES-KOH, pH 7.5, 150 mM KCl, 5 mM $MgCl_2$, 1mM TCEP, 1 mg/ml bovine serum albumin (BSA), 5mM $CaCl_2$). After 1.5 hours the resin was pelleted by benchtop centrifugation and the supernatant was removed. Resin was washed 3x with 1 mL of ice cold Assay Buffer before resin was resuspended in Elution Buffer (Assay Buffer with 5 mM EDTA and 0.5 mg/mL protein C peptide added) and incubated with gentle rocking for 1 hour. The resin was then pelleted and the supernatant was removed. Samples were analyzed by Western Blotting as previously described

Analytical ultracentrifugation

Analytical ultracentrifugation sedimentation velocity experiments were performed as previously described (Tsai et al. 2018).

In vitro FRET assays

Equilibrium measurements of eIF2B assembly state were performed in 20 µl reactions with 50 nM eIF2Bβγδε-F + ISRIB or eIF2Bα_2 titrations in FP buffer (20 mM HEPES-KOH pH 7.5, 100 mM KCl, 5 mM $MgCl_2$, 1 mM TCEP) and measured in 384 square-well black-walled, clear-bottom polystyrene assay plates (Corning). Measurements were taken using the ClarioStar PLUS plate reader (BMG LabTech) at room temperature. mNeonGreen was excited (470 nm, 8 nm bandwidth) and mNeonGreen (516 nm, 8 nm bandwidth) and mScarlet-i (592 nm, 8 nm bandwidth) emission were monitored. FRET signal (E_{592}/E_{516}) is the ratio of mScarlet-i emission after mNeonGreen excitation and mNeonGreen emission after mNeonGreen excitation. All

reactions were performed in a final 0.5% DMSO content. Samples were incubated for 1 h before measurement. Data were plotted in GraphPad Prism 8 and curves were fit to log(inhibitor) versus response function with variable slope.

Kinetic measurements of eIF2B assembly were performed in the same final volume and buffer as above. 10 µl of 2x ISRIB, eIF2Bα_2, or ISRIB + eIF2Bα_2 stocks were placed in wells of the above-described assay plate. 10 µl of 100 nM (2x) eIF2Bβγδε-F was then added and mixed with the contents of each well using a 20 µl 12-channel multichannel pipette. Measurements were taken using the above instrument every 18 s for the first 24 cycles and then every 45 s for the next 60 cycles. mNeonGreen was excited (470 nm, 16 nm bandwidth), and mNeonGreen (516 nm, 16 nm bandwidth) and mScarlet-i (592 nm, 16 nm bandwidth) emission were monitored. After this association phase 18 μl were removed from each well using a multichannel pipette and mixed with 1 µl of 20 µM (20x) untagged eIF2Bβγδε pre-loaded into PCR strips. The material was then returned to the original wells and measurement of dissociation began. Measurements were taken every 18 s for the first 24 cycles and then every 45 s for the next 120 cycles. Data were plotted in GraphPad Prism 8. Association and dissociation phases were fit separately using the One-phase association and Dissociation – One phase exponential decay models, respectively. Global fits were performed on the ISRIB titrations or eIF2Bα_2 titrations. When modeling dissociation, the median buffer signal at assay completion was used to set the bottom baseline for conditions where full dissociation was not observed (eIF2Bα_2 and eIF2Bα_2 + ISRIB conditions).

GDP exchange assay

in vitro detection of GDP binding to eIF2 was adapted from a published protocol for a fluorescence intensity–based assay describing dissociation of eIF2 and nucleotide (Sekine et al. 2015). We first performed a loading assay for fluorescent BODIPY-FL-GDP as described (Tsai et al. 2018). Purified eIF2 (100 nM) was incubated with 100 nM BODIPY-FL-GDP (Thermo

Fisher Scientific) in assay buffer (20 mM HEPES-KOH, pH 7.5, 100 mM KCl, 5 mM $MgCl_2$, 1 mM TCEP, and 1 mg/ml BSA) to a volume of 18 µl in 384 square-well black-walled, clear-bottom polystyrene assay plates (Corning). The GEF mix was prepared by incubating a 10x solution of eIF2B$(\alpha\beta\gamma\delta\varepsilon)_2$ with 10x solutions of eIF2-P or eIF2α-P. For analyzing the effect of ISRIB, the 10x GEF mixes were pre-incubated with 2% NMP or 10 µM ISRIB in N-Methyl-2-Pyrrolidone (NMP), such that the final NMP and ISRIB concentration was 1 µM and the final NMP concentration was 0.2%. To compare nucleotide exchange rates, the 10x GEF mixes were spiked into the 384-well plate wells with a multi-channel pipette, such that the resulting final concentration of eIF2B$(\alpha\beta\gamma\delta\varepsilon)_2$ was 10 nM and the final concentration of other proteins and drugs are as indicated in the figures. Subsequently, in the same wells, we performed a "GDP unloading assay," as indicated in the figures. After completion of the loading reaction, wells were next spiked with 1 mM GDP to start the unloading reaction at t = 0. Fluorescence intensity was recorded every 10 s for 60 min using a Clariostar PLUS (BMG LabTech) plate reader (excitation wavelength: 497 nm, bandwidth 14 nm, emission wavelength: 525 nm, bandwidth: 30 nm). Data collected were fit to a first-order exponential.

Michaelis Menten kinetics

BODIPY-FL-GDP loading assays were performed as described above, varying substrate concentration in 2-fold increments from 31.25 nM to 4 µM while eIF2B decamer concentration was held constant at 10 nM. Experiments containing tetramer were performed at 20 nM, such that the number of active sites was held constant. For conditions reported in Figure 1.6A, initial velocity was determined by a linear fit to timepoints acquired at 5 second intervals from 50 – 200 seconds after addition of GEF. For eIF2B tetramer and eIF2B decamer + 15 µM eIF2α-P conditions, timepoints were acquired at 20 second intervals and initial velocity was determined by a linear fit to timepoints 400 - 1000 seconds. k_{cat} and K_M were determined by fitting the saturation curves shown in Figure 1.6A to the Michaelis Menten equation. Data collected for

tetramer and decamer + 15 μM eIF2α-P conditions fell within the linear portion of the Michaelis Menten saturation curve, and thus the linear portion of each curve was fit to determine the k_{cat} / K_M values reported in Figure 1.6B.

FAM-ISRIB binding assay

All fluorescence polarization measurements were performed in 20 μl reactions with 100 nM eIF2B$(\alpha\beta\gamma\delta\varepsilon)_2$ + 2.5 nM FAM-ISRIB (Praxis Bioresearch) in FP buffer (20 mM HEPES-KOH pH 7.5, 100 mM KCl, 5 mM $MgCl_2$, 1 mM TCEP) and measured in 384-well non-stick black plates (Corning 3820) using the ClarioStar PLUS (BMG LabTech) at room temperature. Prior to reaction setup, eIF2B$(\alpha\beta\gamma\delta\varepsilon)_2$ was assembled in FP buffer using eIF2Bβγδε and eIF2Bα_2 in 2:1 molar ratio for at least 15 min at room temperature. FAM-ISRIB was always first diluted to 2.5 μM in 100% NMP prior to dilution to 50 nM in 2% NMP and then added to the reaction. For titrations with eIF2, eIF2-P, eIF2α, and eIF2α-P, dilutions were again made in FP buffer, and the reactions with eIF2B, FAM-ISRIB, and these dilutions were incubated at 22 °C for 30 min prior to measurement of parallel and perpendicular intensities (excitation: 482 nm, emission: 530 nm). To measure the effect of phosphorylated eIF2 on FAM-ISRIB binding to eIF2B, we additionally added 1 μl (0.21 μg) of $PKR_{(252\text{-}551)}$-GST enzyme (Thermo Scientific) and 1 mM ATP to the reaction with eIF2B, FAM-ISRIB and eIF2 before incubation at 22 °C for 30 min. For the measurement of eIF2 and eIF2α-P competition, 19 μl reactions of 100 nM eIF2B$(\alpha\beta\gamma\delta\varepsilon)_2$, 2.5 nM FAM-ISRIB, and 6 μM eIF2α-P were incubated with titrations of eIF2 for 30 min before polarization was measured. To confirm that FAM-ISRIB binding was specific to eIF2B, after each measurement, ISRIB was spiked to 1 μM into each reaction (from a 40 μM stock in 100% NMP), reactions were incubated for 15 min at 22 °C, and polarization was measured again using the same gain settings. Data were plotted in GraphPad Prism 8, and where appropriate, curves were fit to log[inhibitor] vs response function with variable slope.

The kinetic characterization of FAM-ISRIB binding during eIF2α phosphorylation was assayed in 19 µl reactions of 100 nM eIF2B$(\alpha\beta\gamma\delta\varepsilon)_2$, 2.5 nM FAM-ISRIB, 1 mM ATP, and 5.6 µM eIF2α / eIF2α-P in FP buffer. These solutions were pre-incubated at 22 °C for 30 min before polarization was measured every 15 s (30 flashes / s). After 4 cycles, 1 µl (0.21 µg) of $PKR_{(252-551)}$-GST enzyme (Thermo Scientific) was added, and measurement was resumed. Dephosphorylation reactions were set up in an analogous way, but instead of ATP 1 mM $MnCl_2$ was added and 1 µl (400 U) of λ phosphatase (NEB) was used instead of PKR.

Sample preparation for cryo-electron microscopy

Decameric eIF2B$(\alpha\beta\gamma\delta\varepsilon)_2$ was prepared by incubating 20 µM eIF2Bβγδε with 11 µM eIF2Bα_2 in a final solution containing 20 mM HEPES-KOH, 200 mM KCl, 5 mM $MgCl_2$, and 1 mM TCEP. This 10 µM eIF2B$(\alpha\beta\gamma\delta\varepsilon)_2$ sample was further diluted to 750 nM and incubated on ice for 1 h before plunge freezing. A 3 µl aliquot of the sample was applied onto the Quantifoil R 1.2/1/3 400 mesh Gold grid and waited for 30 s. A 0.5 µl aliquot of 0.1-0.2% Nonidet P-40 substitute was added immediately before blotting. The entire blotting procedure was performed using Vitrobot (FEI) at 10ºC and 100% humidity.

Electron microscopy data collection

Cryo-EM data for the *apo* decamer of eIF2B was collected on a Titan Krios transmission electron microscope operating at 300 keV, and micrographs were acquired using a Gatan K3 direct electron detector. The total dose was 67 $e^-/ Å^2$, and 117 frames were recorded during a 5.9 s exposure. Data was collected at 105,000 x nominal magnification (0.835 Å/pixel at the specimen level), and nominal defocus range of -0.6 to -2.0 µm. Cryo-EM data for the ISRIB-bound eIF2B decamer (EMDB:7442, 7443, and 7444) (Tsai et al. 2018) and the eIF2-bound eIF2B decamer were collected as described previously (EMDB:0651) (Kenner et al. 2019).

Image processing

For the apo decamer, the micrograph frames were aligned using MotionCorr2 (Zheng et al. 2017). The contrast transfer function (CTF) parameters were estimated with GCTF (Zhang 2016). Particles were automatically picked using Gautomatch and extracted in RELION using a 400-pixel box size (Scheres 2012). Particles were classified in 2D in Cryosparc (Punjani et al. 2017). Classes that showed clear protein features were selected and extracted for heterogeneous refinement using the ISRIB-bound decamer as a starting model (EMDB ID: 7442) (Tsai et al. 2018). Homogeneous refinement was performed on the best model to yield a reconstruction of 2.89 Å. Nonuniform refinement was then performed to yield a final reconstruction of 2.83 Å. For the ISRIB-bound eIF2B decamer (EMDB:7442, 7443, and 7444) (Tsai et al. 2018), and the eIF2-bound eIF2B decamer (EMDB:0651) (Kenner et al. 2019), the published maps were used for further model refinement.

Atomic model building, refinement, and visualization

For all models, previously determined structures of the human eIF2B complex [PDB: 6CAJ] (Tsai et al. 2018), human eIF2α [PDBs: 1Q8K (Ito, Marintchev, and Wagner 2004) and 1KL9 (Nonato, Widom, and Clardy 2002)], the C-terminal HEAT domain of eIF2Bε [PDB: 3JUI (Wei et al. 2010)], and mammalian eIF2γ [PDB: 5K0Y (Esser et al. 2017)] were used for initial atomic interpretation. The models were manually adjusted in Coot (Emsley and Cowtan 2004) or ISOLDE (Croll 2018) and then refined in phenix.real_space_refine (Adams et al. 2010) using global minimization, secondary structure restraints, Ramachandran restraints, and local grid search. Then iterative cycles of manually rebuilding in Coot and phenix.real_space_refine with additional B-factor refinement were performed. The final model statistics were tabulated using Molprobity (Table 1.1 and 1.2) (Chen et al. 2010). Map versus atomic model FSC plots were computed after masking using Phenix validation tools. Distances and rotations were calculated from the atomic models using UCSF Chimera. Final atomic models have been deposited at the

PDB with the following accession codes: ISRIB-bound eIF2B (6caj, updated), eIF2•eIF2B•ISRIB (6o85); and apo eIF2B (7L70). Molecular graphics and analyses were performed with the UCSF Chimera package (Pettersen et al. 2004). UCSF Chimera is developed by the Resource for Biocomputing, Visualization, and Informatics and supported by NIGMS P41-GM103311.

References

Adams, P. D., P. V. Afonine, G. Bunkóczi, V. B. Chen, I. W. Davis, N. Echols, J. J. Headd, L. W. Hung, G. J. Kapral, R. W. Grosse-Kunstleve, A. J. McCoy, N. W. Moriarty, R. Oeffner, R. J. Read, D. C. Richardson, J. S. Richardson, T. C. Terwilliger, and P. H. Zwart. 2010. 'PHENIX: a comprehensive Python-based system for macromolecular structure solution', *Acta Crystallogr D Biol Crystallogr*, 66: 213-21.

Adomavicius, T., M. Guaita, Y. Zhou, M. D. Jennings, Z. Latif, A. M. Roseman, and G. D. Pavitt. 2019. 'The structural basis of translational control by eIF2 phosphorylation', *Nat Commun*, 10: 2136.

Algire, M. A., D. Maag, and J. R. Lorsch. 2005. 'Pi release from eIF2, not GTP hydrolysis, is the step controlled by start-site selection during eukaryotic translation initiation', *Mol Cell*, 20: 251-62.

Atkin, J. D., M. A. Farg, A. K. Walker, C. McLean, D. Tomas, and M. K. Horne. 2008. 'Endoplasmic reticulum stress and induction of the unfolded protein response in human sporadic amyotrophic lateral sclerosis', *Neurobiol Dis*, 30: 400-7.

Bogorad, A. M., K. Y. Lin, and A. Marintchev. 2017. 'Novel mechanisms of eIF2B action and regulation by eIF2α phosphorylation', *Nucleic Acids Res*, 45: 11962-79.

Chen, V. B., W. B. Arendall, 3rd, J. J. Headd, D. A. Keedy, R. M. Immormino, G. J. Kapral, L. W. Murray, J. S. Richardson, and D. C. Richardson. 2010. 'MolProbity: all-atom structure validation for macromolecular crystallography', *Acta Crystallogr D Biol Crystallogr*, 66: 12-21.

Chou, A., K. Krukowski, T. Jopson, P. J. Zhu, M. Costa-Mattioli, P. Walter, and S. Rosi. 2017. 'Inhibition of the integrated stress response reverses cognitive deficits after traumatic brain injury', *Proc Natl Acad Sci U S A*, 114: E6420-e26.

Costa-Mattioli, M., and P. Walter. 2020. 'The integrated stress response: From mechanism to disease', *Science*, 368.

Craddock, B. L., and C. G. Proud. 1996. 'The alpha-subunit of the mammalian guanine nucleotide-exchange factor eIF-2B is essential for catalytic activity in vitro', *Biochem Biophys Res Commun*, 220: 843-7.

Croll, T. I. 2018. 'ISOLDE: a physically realistic environment for model building into low-resolution electron-density maps', *Acta Crystallogr D Struct Biol*, 74: 519-30.

de Almeida, R. A., A. Fogli, M. Gaillard, G. C. Scheper, O. Boesflug-Tanguy, and G. D. Pavitt. 2013. 'A yeast purification system for human translation initiation factors eIF2 and eIF2Bε and their use in the diagnosis of CACH/VWM disease', *PLoS One*, 8: e53958.

Dey, M., C. Cao, A. C. Dar, T. Tamura, K. Ozato, F. Sicheri, and T. E. Dever. 2005. 'Mechanistic link between PKR dimerization, autophosphorylation, and eIF2alpha substrate recognition', *Cell*, 122: 901-13.

Elsby, R., J. F. Heiber, P. Reid, S. R. Kimball, G. D. Pavitt, and G. N. Barber. 2011. 'The alpha subunit of eukaryotic initiation factor 2B (eIF2B) is required for eIF2-mediated translational suppression of vesicular stomatitis virus', *J Virol*, 85: 9716-25.

Emsley, P., and K. Cowtan. 2004. 'Coot: model-building tools for molecular graphics', *Acta Crystallogr D Biol Crystallogr*, 60: 2126-32.

Esser, L., F. Zhou, K. M. Pluchino, J. Shiloach, J. Ma, W. K. Tang, C. Gutierrez, A. Zhang, S. Shukla, J. P. Madigan, T. Zhou, P. D. Kwong, S. V. Ambudkar, M. M. Gottesman, and D. Xia. 2017. 'Structures of the Multidrug Transporter P-glycoprotein Reveal Asymmetric ATP Binding and the Mechanism of Polyspecificity', *J Biol Chem*, 292: 446-61.

Gilbert, L. A., M. A. Horlbeck, B. Adamson, J. E. Villalta, Y. Chen, E. H. Whitehead, C. Guimaraes, B. Panning, H. L. Ploegh, M. C. Bassik, L. S. Qi, M. Kampmann, and J. S. Weissman. 2014. 'Genome-Scale CRISPR-Mediated Control of Gene Repression and Activation', *Cell*, 159: 647-61.

Gordiyenko, Y., J. L. Llácer, and V. Ramakrishnan. 2019. 'Structural basis for the inhibition of translation through eIF2α phosphorylation', *Nat Commun*, 10: 2640.

Guo, X., G. Aviles, Y. Liu, R. Tian, B. A. Unger, Y. T. Lin, A. P. Wiita, K. Xu, M. A. Correia, and M. Kampmann. 2020. 'Mitochondrial stress is relayed to the cytosol by an OMA1-DELE1-HRI pathway', *Nature*, 579: 427-32.

Hannig, E. M., and A. G. Hinnebusch. 1988. 'Molecular analysis of GCN3, a translational activator of GCN4: evidence for posttranslational control of GCN3 regulatory function', *Mol Cell Biol*, 8: 4808-20.

Harding, H. P., I. Novoa, Y. Zhang, H. Zeng, R. Wek, M. Schapira, and D. Ron. 2000. 'Regulated translation initiation controls stress-induced gene expression in mammalian cells', *Mol Cell*, 6: 1099-108.

Harding, H. P., Y. Zhang, H. Zeng, I. Novoa, P. D. Lu, M. Calfon, N. Sadri, C. Yun, B. Popko, R. Paules, D. F. Stojdl, J. C. Bell, T. Hettmann, J. M. Leiden, and D. Ron. 2003. 'An integrated

stress response regulates amino acid metabolism and resistance to oxidative stress', *Mol Cell*, 11: 619-33.

Hinnebusch, A. G. 2005. 'Translational regulation of GCN4 and the general amino acid control of yeast', *Annu Rev Microbiol*, 59: 407-50.

Hinnebusch, A. G., I. P. Ivanov, and N. Sonenberg. 2016. 'Translational control by 5'-untranslated regions of eukaryotic mRNAs', *Science*, 352: 1413-6.

Ito, T., A. Marintchev, and G. Wagner. 2004. 'Solution structure of human initiation factor eIF2alpha reveals homology to the elongation factor eEF1B', *Structure*, 12: 1693-704.

Iwamoto, M., T. Björklund, C. Lundberg, D. Kirik, and T. J. Wandless. 2010. 'A general chemical method to regulate protein stability in the mammalian central nervous system', *Chem Biol*, 17: 981-8.

Kashiwagi, K., M. Takahashi, M. Nishimoto, T. B. Hiyama, T. Higo, T. Umehara, K. Sakamoto, T. Ito, and S. Yokoyama. 2016. 'Crystal structure of eukaryotic translation initiation factor 2B', *Nature*, 531: 122-5.

Kashiwagi, K., T. Yokoyama, M. Nishimoto, M. Takahashi, A. Sakamoto, M. Yonemochi, M. Shirouzu, and T. Ito. 2019. 'Structural basis for eIF2B inhibition in integrated stress response', *Science*, 364: 495-99.

Kenner, L. R., A. A. Anand, H. C. Nguyen, A. G. Myasnikov, C. J. Klose, L. A. McGeever, J. C. Tsai, L. E. Miller-Vedam, P. Walter, and A. Frost. 2019. 'eIF2B-catalyzed nucleotide exchange and phosphoregulation by the integrated stress response', *Science*, 364: 491-95.

Krukowski, K., A. Nolan, E. S. Frias, M. Boone, G. Ureta, K. Grue, M. S. Paladini, E. Elizarraras, L. Delgado, S. Bernales, P. Walter, and S. Rosi. 2020. 'Small molecule cognitive enhancer reverses age-related memory decline in mice', *Elife*, 9.

Kuhle, B., N. K. Eulig, and R. Ficner. 2015. 'Architecture of the eIF2B regulatory subcomplex and its implications for the regulation of guanine nucleotide exchange on eIF2', *Nucleic Acids Res*, 43: 9994-10014.

Leegwater, P. A., G. Vermeulen, A. A. Könst, S. Naidu, J. Mulders, A. Visser, P. Kersbergen, D. Mobach, D. Fonds, C. G. van Berkel, R. J. Lemmers, R. R. Frants, C. B. Oudejans, R. B. Schutgens, J. C. Pronk, and M. S. van der Knaap. 2001. 'Subunits of the translation initiation factor eIF2B are mutant in leukoencephalopathy with vanishing white matter', *Nat Genet*, 29: 383-8.

Leonetti, M. D., S. Sekine, D. Kamiyama, J. S. Weissman, and B. Huang. 2016. 'A scalable strategy for high-throughput GFP tagging of endogenous human proteins', *Proc Natl Acad Sci U S A*, 113: E3501-8.

Ma, T., M. A. Trinh, A. J. Wexler, C. Bourbon, E. Gatti, P. Pierre, D. R. Cavener, and E. Klann. 2013. 'Suppression of eIF2α kinases alleviates Alzheimer's disease-related plasticity and memory deficits', *Nat Neurosci*, 16: 1299-305.

Nabet, B., J. M. Roberts, D. L. Buckley, J. Paulk, S. Dastjerdi, A. Yang, A. L. Leggett, M. A. Erb, M. A. Lawlor, A. Souza, T. G. Scott, S. Vittori, J. A. Perry, J. Qi, G. E. Winter, K. K. Wong, N. S. Gray, and J. E. Bradner. 2018. 'The dTAG system for immediate and target-specific protein degradation', *Nat Chem Biol*, 14: 431-41.

Nguyen, H. G., C. S. Conn, Y. Kye, L. Xue, C. M. Forester, J. E. Cowan, A. C. Hsieh, J. T. Cunningham, C. Truillet, F. Tameire, M. J. Evans, C. P. Evans, J. C. Yang, B. Hann, C. Koumenis, P. Walter, P. R. Carroll, and D. Ruggero. 2018. 'Development of a stress response therapy targeting aggressive prostate cancer', *Sci Transl Med*, 10.

Nonato, M. C., J. Widom, and J. Clardy. 2002. 'Crystal structure of the N-terminal segment of human eukaryotic translation initiation factor 2alpha', *J Biol Chem*, 277: 17057-61.

Pavitt, G. D., W. Yang, and A. G. Hinnebusch. 1997. 'Homologous segments in three subunits of the guanine nucleotide exchange factor eIF2B mediate translational regulation by phosphorylation of eIF2', *Mol Cell Biol*, 17: 1298-313.

Pettersen, E. F., T. D. Goddard, C. C. Huang, G. S. Couch, D. M. Greenblatt, E. C. Meng, and T. E. Ferrin. 2004. 'UCSF Chimera--a visualization system for exploratory research and analysis', *J Comput Chem*, 25: 1605-12.

Punjani, A., J. L. Rubinstein, D. J. Fleet, and M. A. Brubaker. 2017. 'cryoSPARC: algorithms for rapid unsupervised cryo-EM structure determination', *Nat Methods*, 14: 290-96.

Rabouw, H. H., L. J. Visser, T. C. Passchier, M. A. Langereis, F. Liu, P. Giansanti, A. L. W. van Vliet, J. G. Dekker, S. G. van der Grein, J. G. Saucedo, A. A. Anand, M. E. Trellet, Amjj Bonvin, P. Walter, A. J. R. Heck, R. J. de Groot, and F. J. M. van Kuppeveld. 2020. 'Inhibition of the integrated stress response by viral proteins that block p-eIF2-eIF2B association', *Nat Microbiol*, 5: 1361-73.

Scheres, S. H. 2012. 'RELION: implementation of a Bayesian approach to cryo-EM structure determination', *J Struct Biol*, 180: 519-30.

Sekine, Y., A. Zyryanova, A. Crespillo-Casado, P. M. Fischer, H. P. Harding, and D. Ron. 2015. 'Stress responses. Mutations in a translation initiation factor identify the target of a memory-enhancing compound', *Science*, 348: 1027-30.

Sen, T., R. Gupta, H. Kaiser, and N. Sen. 2017. 'Activation of PERK Elicits Memory Impairment through Inactivation of CREB and Downregulation of PSD95 After Traumatic Brain Injury', *J Neurosci*, 37: 5900-11.

Sharma, V., H. Ounallah-Saad, D. Chakraborty, M. Hleihil, R. Sood, I. Barrera, E. Edry, S. Kolatt Chandran, S. Ben Tabou de Leon, H. Kaphzan, and K. Rosenblum. 2018. 'Local Inhibition of PERK Enhances Memory and Reverses Age-Related Deterioration of Cognitive and Neuronal Properties', *J Neurosci*, 38: 648-58.

Shi, Y., K. M. Vattem, R. Sood, J. An, J. Liang, L. Stramm, and R. C. Wek. 1998. 'Identification and characterization of pancreatic eukaryotic initiation factor 2 alpha-subunit kinase, PEK, involved in translational control', *Mol Cell Biol*, 18: 7499-509.

Sidrauski, C., D. Acosta-Alvear, A. Khoutorsky, P. Vedantham, B. R. Hearn, H. Li, K. Gamache, C. M. Gallagher, K. K. Ang, C. Wilson, V. Okreglak, A. Ashkenazi, B. Hann, K. Nader, M. R. Arkin, A. R. Renslo, N. Sonenberg, and P. Walter. 2013. 'Pharmacological brake-release of mRNA translation enhances cognitive memory', *Elife*, 2: e00498.

Sidrauski, C., J. C. Tsai, M. Kampmann, B. R. Hearn, P. Vedantham, P. Jaishankar, M. Sokabe, A. S. Mendez, B. W. Newton, E. L. Tang, E. Verschueren, J. R. Johnson, N. J. Krogan, C. S. Fraser, J. S. Weissman, A. R. Renslo, and P. Walter. 2015. 'Pharmacological dimerization and activation of the exchange factor eIF2B antagonizes the integrated stress response', *Elife*, 4: e07314.

Tsai, J. C., L. E. Miller-Vedam, A. A. Anand, P. Jaishankar, H. C. Nguyen, A. R. Renslo, A. Frost, and P. Walter. 2018. 'Structure of the nucleotide exchange factor eIF2B reveals mechanism of memory-enhancing molecule', *Science*, 359.

van der Knaap, M. S., P. A. Leegwater, A. A. Könst, A. Visser, S. Naidu, C. B. Oudejans, R. B. Schutgens, and J. C. Pronk. 2002. 'Mutations in each of the five subunits of translation initiation factor eIF2B can cause leukoencephalopathy with vanishing white matter', *Ann Neurol*, 51: 264-70.

Wei, J., M. Jia, C. Zhang, M. Wang, F. Gao, H. Xu, and W. Gong. 2010. 'Crystal structure of the C-terminal domain of the ε subunit of human translation initiation factor eIF2B', *Protein Cell*, 1: 595-603.

Wong, Y. L., L. LeBon, R. Edalji, H. B. Lim, C. Sun, and C. Sidrauski. 2018. 'The small molecule ISRIB rescues the stability and activity of Vanishing White Matter Disease eIF2B mutant complexes', *Elife*, 7.

Wortham, N. C., M. Martinez, Y. Gordiyenko, C. V. Robinson, and C. G. Proud. 2014. 'Analysis of the subunit organization of the eIF2B complex reveals new insights into its structure and regulation', *Faseb j*, 28: 2225-37.

Zhang, K. 2016. 'Gctf: Real-time CTF determination and correction', *J Struct Biol*, 193: 1-12.

Zheng, S. Q., E. Palovcak, J. P. Armache, K. A. Verba, Y. Cheng, and D. A. Agard. 2017. 'MotionCor2: anisotropic correction of beam-induced motion for improved cryo-electron microscopy', *Nat Methods*, 14: 331-32.

Zhu, P. J., S. Khatiwada, Y. Cui, L. C. Reineke, S. W. Dooling, J. J. Kim, W. Li, P. Walter, and M. Costa-Mattioli. 2019. 'Activation of the ISR mediates the behavioral and neurophysiological abnormalities in Down syndrome', *Science*, 366: 843-49.

Zyryanova, A. F., K. Kashiwagi, C. Rato, H. P. Harding, A. Crespillo-Casado, L. A. Perera, A. Sakamoto, M. Nishimoto, M. Yonemochi, M. Shirouzu, T. Ito, and D. Ron. 2021. 'ISRIB Blunts the Integrated Stress Response by Allosterically Antagonising the Inhibitory Effect of Phosphorylated eIF2 on eIF2B', *Mol Cell*, 81: 88-103.e6.

Zyryanova, A. F., F. Weis, A. Faille, A. A. Alard, A. Crespillo-Casado, Y. Sekine, H. P. Harding, F. Allen, L. Parts, C. Fromont, P. M. Fischer, A. J. Warren, and D. Ron. 2018. 'Binding of ISRIB reveals a regulatory site in the nucleotide exchange factor eIF2B', *Science*, 359: 1533-36.

Chapter 2

Viral Evasion of the Integrated Stress Response Through Antagonism of eIF2-P binding to eIF2B

Summary

Viral infection triggers activation of the integrated stress response (ISR). In response to viral double-stranded RNA (dsRNA), RNA-activated protein kinase (PKR) phosphorylates the translation initiation factor eIF2, converting it from a translation initiator into a potent translation inhibitor and this restricts the synthesis of viral proteins. Phosphorylated eIF2 (eIF2-P) inhibits translation by binding to eIF2's dedicated, heterodecameric nucleotide exchange factor eIF2B and conformationally inactivating it. We show that the NSs protein of Sandfly Fever Sicilian virus (SFSV) allows the virus to evade the ISR. Mechanistically, NSs tightly binds to eIF2B (K_D = 30 nM), blocks eIF2-P binding, and rescues eIF2B GEF activity. Cryo-EM structures demonstrate that SFSV NSs and eIF2-P directly compete, with the primary NSs contacts to eIF2Bα mediated by five 'aromatic fingies'. NSs binding preserves eIF2B activity by maintaining eIF2B's conformation in its active A-State.

Introduction

The Integrated Stress Response (ISR) is a conserved eukaryotic stress response network that, upon activation by a diverse set of stressors, profoundly reprograms translation. It is coordinated by at least four stress-responsive kinases: PERK (responsive to protein misfolding in the endoplasmic reticulum), PKR (responsive to viral infection), HRI (responsive to heme deficiency and oxidative and mitochondrial stresses), and GCN2 (responsive to nutrient deprivation) (Hinnebusch 2005; Guo et al. 2020; Dey et al. 2005; Shi et al. 1998). All four known ISR kinases converge on the phosphorylation of a single serine (S51) of the α subunit of the general translation initiation factor eIF2. Under non-stress conditions, eIF2 forms a ternary complex (TC) with methionyl initiator tRNA (Met-tRNA^{i}) and GTP. This complex performs the critical task of delivering the first amino acid to ribosomes at AUG initiation codons. Upon S51 phosphorylation, eIF2 is converted from a substrate to an inhibitor of its dedicated nucleotide exchange factor (GEF) eIF2B. GEF inhibition results from binding of eIF2-P in a new, inhibitory binding orientation on eIF2B, where it elicits allosteric changes to antagonize eIF2 binding and additionally compromise eIF2B's intrinsic enzymatic activity (Schoof et al. 2021; Zyryanova et al. 2021).

eIF2B is a two-fold symmetric heterodecamer composed of 2 copies each of α, β, δ, γ, and ε subunits (Kashiwagi et al. 2016; Tsai et al. 2018; Wortham et al. 2014; Zyryanova et al. 2018). eIF2B can exist in a range of stable subcomplexes (eIF2Bβδγε tetramers and eIF2Bα_2 dimers) if the concentrations of its constituent subunits are altered (Wortham et al. 2014; Tsai et al. 2018; Craddock and Proud 1996; Schoof et al. 2021). While earlier models suggested eIF2B assembly to be rate-limiting and a potential regulatory step, recent work by us and others show that eIF2B in cells primarily exists in its fully assembled decameric, enzymatically active state (Schoof et al. 2021; Zyryanova et al. 2021). Cryo-EM studies of various eIF2B complexes

elucidated the mechanisms of nucleotide exchange and ISR inhibition through eIF2-P binding (Kenner et al. 2019; Gordiyenko, Llácer, and Ramakrishnan 2019; Kashiwagi et al. 2019; Adomavicius et al. 2019; Schoof et al. 2021; Zyryanova et al. 2021). Under non-stress conditions, eIF2 engages eIF2B through multiple interfaces along a path spanning the heterodecamer. In this arrangement, eIF2α binding to eIF2B critically positions the GTPase domain in eIF2's γ subunit, allowing for efficient catalysis of nucleotide exchange (Kenner et al. 2019; Kashiwagi et al. 2019). eIF2B's catalytically active conformation ('A-State') becomes switched to an inactive conformation upon eIF2-P binding (Inhibited or 'I-State'), which displays altered substrate-binding interfaces (Schoof et al. 2021; Zyryanova et al. 2021). I-State eIF2B$(\alpha\beta\delta\gamma\varepsilon)_2$ exhibits enzymatic activity and substrate engagement akin to the tetrameric eIF2Bβδγε subcomplex, hence eIF2-P inhibition of eIF2B converts the decamer into conjoined tetramers, which reduces its GEF activity, lowers the cell's TC concentration, and results in ISR-dependent translational reprogramming (Schoof et al. 2021; Zyryanova et al. 2021).

Viruses hijack the host cell's protein synthesis machinery to produce viral proteins and package new viral particles. Numerous host countermeasures have evolved. In the context of the ISR, double-stranded RNA (dsRNA), a by-product of viral replication, triggers dimerization and autophosphorylation of PKR (Dey et al. 2005; Galabru and Hovanessian 1987). In this activated state PKR phosphorylates eIF2, which then binds to and inhibits eIF2B. As such, cells downregulate mRNA translation as a strategy to slow the production of virions. Viruses, in turn, enact strategies of evasion. Indeed, viral evasion strategies acting at each step of ISR activation have been observed. Influenza virus, for example, masks its dsRNA (Rosário-Ferreira et al. 2020; Stasakova et al. 2005). Rift Valley Fever virus (RVFV) encodes an effector protein that degrades PKR (Habjan et al. 2009). Hepatitis C virus blocks PKR dimerization (Gale, Korth, and Katze 1998). Vaccinia virus encodes a pseudosubstrate as a PKR decoy (Kawagishi-Kobayashi et al. 1997). Herpes simplex virus can dephosphorylate eIF2-P (Li et al. 2011). And some

coronavirus and picornavirus proteins appear to block the eIF2B-eIF2-P interaction (Rabouw et al. 2020). This evolutionary arms race between host and pathogen can provide invaluable tools and insights into the critical mechanisms of the ISR, as well as other cellular stress responses.

Here, we investigated the previously unknown mechanism by which Sandfly Fever Sicilian virus (SFSV) evades the ISR. SFSV and RVFV are both members of the genus *Phlebovirus* (order *Bunyavirales*) which encode an evolutionarily related non-structural protein (NSs) (Hedil and Kormelink 2016; Ly and Ikegami 2016; Wuerth and Weber 2016). Across the phleboviruses, NSs serves to counteract the antiviral interferon response, but NSs proteins perform other functions as well (Wuerth et al. 2018; Billecocq et al. 2004). Unlike the RVFV NSs which degrades PKR, SFSV NSs does not impact the levels or phosphorylation status of PKR or eIF2 (Habjan et al. 2009; Wuerth et al. 2020). Instead, it binds to eIF2B, inhibiting the ISR. The mechanistic basis of this inhibition was previously unclear. We here provide cellular, biochemical, and structural insight into this question, showing that the SFSV NSs evades all branches of the ISR by binding to eIF2B and selectively blocking eIF2-P binding, thereby maintaining eIF2B in its active A-State.

Results

The SFSV NSs is a pan ISR inhibitor

To dissect the role of the SFSV NSs (henceforth referred to as NSs) in ISR modulation, we engineered cells stably expressing either an empty vector, a functional NSs (NSs::FLAG), or a non-functional NSs (FLAG::NSs) (Figure 2.1 – figure supplement 1). As previously reported, the NSs with a C-terminal FLAG tag (NSs::FLAG) should retain its PKR-evading properties while tagging at the N-terminus (FLAG::NSs) blocks this functionality (Wuerth et al. 2020). These constructs were genomically integrated into our previously generated ISR reporter system, in which both changes in ATF4 translation and general translation can be monitored (Schoof et al. 2021). Both NSs::FLAG and FLAG::NSs were stably expressed in these cells without impacting the levels of key ISR components (eIF2B, eIF2, PKR, PERK) (Figure 2.1A). The apparent differences in band intensity between NSs::FLAG and FLAG::NSs may reflect differences in protein stability or, perhaps more likely, differences in antibody affinity for the FLAG epitope at the respective C- and N-terminal tagging locations.

To ask whether NSs is a pan-ISR inhibitor capable of dampening ISR activation irrespective of any particular ISR activating kinase, we chemically activated PERK, HRI, and GCN2 with thapsigargin, oligomycin, and glutamine deprivation / synthetase inhibition through L-methionine sulfoximine, respectively. NSs::FLAG expression dampened the increases in ATF4 translation brought about by activation of any of the kinases (Figure 2.1B-D). NSs::FLAG also maintained general translation levels in the thapsigargin and oligomycin treated cells (Figure 2.1B,C). Notably, in the context of GCN2 activation, general translation comparably decreased at the highest levels of stress regardless of NSs status (Figure 2.1D). This observation likely reflects the additional stress responses that react to reduced amino acid levels, as well as the fact that while the ISR controls translation initiation, ribosome-engaged mRNAs still need sufficient levels

of amino acids to be successfully translated. On the whole, these data therefore show that the NSs is a pan-ISR inhibitor akin to the small molecule ISRIB, which binds to eIF2B and counteracts the ISR by allosterically blocking eIF2-P binding and promoting eIF2B complex assembly when eIF2B's decameric state is compromised (Sidrauski et al. 2013; Schoof et al. 2021; Zyryanova et al. 2021).

NSs binds decameric eIF2B exclusively

To explain the mechanism by which NSs inhibits the ISR, we purified NSs expressed in mammalian cells (Figure 2.2A,B). We next validated that NSs binds to eIF2B *in vitro* by immobilizing distinct eIF2B complexes on agarose beads and incubating them with an excess of NSs (Figure 2.2C). As expected, NSs binds to the fully assembled eIF2B$(\alpha\beta\delta\gamma\varepsilon)_2$ decamers (Lane 4). Notably, it did not bind to eIF2B$\beta\delta\gamma\varepsilon$ tetramers (Lane 5) or to eIF2Bα_2 dimers (Lane 6). The NSs interaction with eIF2B thus either spans multiple interfaces that are only completed in the fully assembled complex or interacts with a region of eIF2B that undergoes a conformational change when in the fully assembled state.

To quantitatively assess NSs binding to eIF2B, we employed surface plasmon resonance (SPR) experiments to determine the affinity of NSs for the various eIF2B complexes (Figure 2.2D-F). The NSs interaction with decameric eIF2B could be modeled using one-phase association and dissociation kinetics. NSs binds to decameric eIF2B with a K_D of 30 nM (k_a = 3.0 x 10^5 $M^{-1}s^{-1}$, k_d = 8.9 x 10^{-3} s^{-1}) (Figure 2.2D). This affinity is comparable to the low nanomolar affinity of ISRIB for decameric eIF2B (Figure 2.2 – figure supplement 1) (Zyryanova et al. 2018). In this orthogonal approach, we again observed no detectable binding of NSs to eIF2B$\beta\delta\gamma\varepsilon$ tetramers or eIF2Bα_2 dimers (Figure 2.2E,F).

NSs rescues eIF2B activity by blocking eIF2-P binding

We next sought to explain the mechanism of NSs inhibition of the ISR using our established *in vitro* systems for studying eIF2B. As is the case with the small molecule ISRIB, NSs did not impact the intrinsic nucleotide exchange activity of eIF2B as monitored by a fluorescent BODIPY-FL-GDP loading assay (Figure 2.3 – figure supplement 1). To mimic the conditions during ISR activation, we repeated our nucleotide exchange assay in the presence of the inhibitory eIF2α-P (Figure 2.3A). As expected, eIF2α-P inhibited eIF2B GEF activity ($t_{1/2}$ = 13.4 min, s.e.m. = 1.5 min), but increasing concentrations of NSs (25 nM: $t_{1/2}$ = 9.2 min, s.e.m. = 1.2 min; 100 nM: $t_{1/2}$ = 6.2 min, s.e.m. = 0.5 min) overcame the inhibitory effects of eIF2α-P and fully rescued eIF2B GEF activity (uninhibited $t_{1/2}$ = 6.3 min, s.e.m. = 0.6 min).

As NSs' ability to affect eIF2B activity markedly manifests in the presence of eIF2α-P, we wondered whether NSs blocks eIF2α-P binding to eIF2B. To test this notion, we utilized a fluorescent ISRIB analog (FAM-ISRIB) that emits light with a higher degree of polarization when bound to eIF2B, compared to being free in solution (Figure 2.3B, black and red dots on the Y axis, respectively). It has been previously shown that eIF2α-P binding to eIF2B antagonizes FAM-ISRIB binding by shifting eIF2B into a conformation incapable of binding ISRIB or its analogs (Figure 2.3B, blue dot on the Y axis) (Schoof et al. 2021; Zyryanova et al. 2021). A titration of NSs into this reaction recovered FAM-ISRIB polarization (EC_{50} = 72 nM, s.e.m. = 9 nM), indicating that NSs engages eIF2B and disrupts eIF2α-P's inhibitory binding. To directly show this antagonism, we immobilized eIF2B decamers on agarose beads and incubated with combinations of NSs and eIF2α-P (Figure 2.3C). While individually, both eIF2α-P and NSs bound to eIF2B (Figure 2.3C, lanes 4 and 5, respectively), in the presence of saturating NSs, eIF2α-P no longer bound eIF2B (Figure 2.3C, lane 6). We next sought to analyze the impact of NSs binding on full-length substrate (eIF2) and inhibitor (eIF2-P) binding through SPR experiments. In this assay we first flowed one analyte over immobilized eIF2B (to saturate the

binding site) immediately followed by a mixture of both analytes (to assess whether the second analyte could co-bind elsewhere). Consistent with the nucleotide exchange assay in Figure 2.3A, eIF2 and NSs co-bound eIF2B (Figure 2.3D,F, increases in RU at 60 s). However, as with the phosphorylated eIF2α subunit alone, the full phosphorylated heterotrimer (eIF2-P) and NSs did not co-bind (Figure 2.3E,G, no increases in RU at 60 s). Together, these results demonstrate that the NSs is a potent inhibitor of eIF2-P binding while preserving eIF2 binding.

NSs binds to eIF2B at the eIF2α-P binding site and keeps eIF2B in the active A-State

Having established that the NSs blocks eIF2-P binding to eIF2B, we next assessed whether NSs is an allosteric regulator of eIF2-P binding (as is the case with ISRIB) or, alternatively, whether it directly competes with eIF2-P binding. To answer this question and to rigorously determine NSs' interactions with eIF2B, we turned to cryoEM. To obtain a homogeneous sample suitable for structural studies, we mixed full-length NSs with decameric eIF2B at a 3:1 molar ratio. We then prepared the sample for cryo-EM imaging and determined the structure of the eIF2B-NSs complex.

3D classification with no symmetry assumptions yielded a distinct class of 137,093 particles. Refinement of this class resulted in a map with an average resolution of 2.6 Å (Figure 2.4 – figure supplement 1). After docking the individual eIF2B subunits into the recorded density, we observed significant extra density next to both eIF2Bα subunits, indicating that two copies of NSs are bound to each eIF2B decamer (Figure 2.4A). The local resolution of the NSs ranges from 2.5 Å (regions close to eIF2B) to >4.0 Å (periphery), with most of the side chain densities clearly visible (Figure 2.4 – figure supplement 1). To build the molecular model for NSs, we split the protein into two domains. The C-terminal domain was built using the crystal structure of the C-terminal domain of the RVFV NSs (PDB ID: 5OOO) as a homology model (43.8% sequence similarity with the C-terminal domain of the SFSV NSs (residues 85-261)) (Figure 2.4 – figure

supplement 2) (Barski et al. 2017). The N-terminal domain of the NSs (residues 1-84) was built *de novo* (Table 2.1). The high resolution map allowed us to build a model for the majority of NSs. The map quality of both NSs molecules are comparable, and their molecular models are nearly identical (root mean square deviation (RMSD) ≈ 0.2 Å). We henceforth focus our analysis on one of them (chain K).

Two copies of NSs bind to one decameric eIF2B in a symmetric manner (Figure 2.4A). An overlay of the NSs-bound eIF2B and the eIF2α-P-bound eIF2B structures (PDB ID: 6O9Z) shows a significant clash between the NSs and eIF2-αP, indicating that, unlike the allosteric regulator ISRIB, NSs binds in direct competition with eIF2α-P (Figure 2.4D-F). Interestingly, whereas eIF2α-P forms extensive interactions with both the α and the δ subunits of eIF2B, the NSs mainly interacts with the eIF2Bα subunit. The expansive interactions between eIF2α-P and both eIF2Bα and eIF2Bδ mediate a shift in eIF2B's conformation from eIF2B's enzymatically active A-state to its inhibited I-state (Zyryanova et al. 2021; Schoof et al. 2021). Thus, despite binding to a region known to influence eIF2B's conformation, an overlay of the NSs-bound eIF2B and apo-eIF2B shows that the overall conformation of eIF2B in the two structures are virtually identical (Figure 2.4B). By contrast, the eIF2B-NSs and eIF2B-eIF2α-P overlay shows major conformational differences (Figure 2.4C). Together, these structural data, paired with our *in vitro* assays, show that the NSs grants SFSV evasion of the ISR by directly competing off eIF2-P and restoring eIF2B to its enzymatically active A-State.

NSs uses a novel protein fold containing aromatic fingies to bind eIF2B

Next, we sought to interrogate the molecular details of the NSs-eIF2B interaction. As mentioned above, NSs consists of two domains. Its N-terminal domain (amino acids 1-84) consists of six β strands and interacts directly with eIF2B. A search in the DALI protein structure comparison server did not reveal any hits, suggesting a novel protein fold. β strands 1 and 2 and β strands 3

and 4 form two antiparallel β sheets and fold on top of the C-terminal domain (Figure 2.4 – figure supplement 3). The C-terminal domain (amino acids 85-261) is largely α-helical and presumably supports the folding of the N-terminal domain, as truncating the C-terminal domain results in the complete loss of NSs activity in terms of ISR evasion (Figure 2.4 – figure supplement 4). Also, despite the moderate sequence conservation of the C-terminal domain of the SFSV NSs and the RVFV NSs, their structures overlay extensively (RMSD ≈ 0.2 Å, Figure 2.4 – figure supplement 3).

The surface of the N-terminal domain forms a hand shape that grips the alpha helices of eIF2Bα, akin to a koala grabbing a eucalyptus branch (Figure 2.5A, Figure 2.6 – figure supplement 4). In this arrangement, the N-terminal domain extends three loops that contact eIF2Bα. The first two loops sit in a groove between helices α3 and α4 and the third loop just below helix α3, effectively sandwiching helix α3 (Figure 2.5B). Together, the three loops extend five aromatic amino acids to contact eIF2Bα. We refer to these aromatic amino acids as "aromatic fingies". On the top side of helix α3, the side chain of NSs Y5 forms a cation-π interaction with eIF2Bα R74 and its backbone carbonyl forms a hydrogen bond with eIF2Bα R46 (Figure 2.5D). NSs F7 forms a cation-π interaction with eIF2Bα R46, and hydrophobic stacking with eIF2Bα I42. NSs F33 stacks against the backbone of eIF2Bα Y304 and L305, as well as the aliphatic region of eIF2Bα R74. On the bottom side of helix α3, NSs F80 stacks against a hydrophobic groove formed by eIF2Bα I7, F33 and A52 (Figure 2.5E). NSs Y79 forms a polar interaction with eIF2Bα D37, completing the extensive interaction network of the NSs' aromatic fingies with the α helices in eIF2Bα. In addition, the side chain of NSs H36 and the backbone carbonyl of NSs T35 both contact eIF2Bδ R321. The side chain of NSs D37 also forms an ionic interaction with eIF2Bδ R321, although the distance is close to 4.0 Å, suggesting a weak interaction. These three amino acids account for the only interactions with eIF2Bδ (Figure 2.5C).

To validate the functional importance of the eIF2Bα-facing aromatic fingies, we mutated them in pairs or singly to alanines (Y5A/F7A, Y79A/F80A, and F33A) and stably expressed these NSs variants in the dual ISR reporter cells. The point mutations did not compromise NSs stability and, as with WT NSs, did not affect eIF2 or eIF2B subunit levels (Figure 2.6A). Upon stress, eIF2α became phosphorylated in all cell lines, but only in cells expressing WT NSs::FLAG was ATF4 translation blunted (Figure 2.6A). A similar picture emerged from analysis of the fluorescent ISR reporter signals. Whereas WT NSs inhibited the translation of ATF4 and maintained general translation at roughly normal levels, all the point mutants tested broke the NSs' function as an ISR evader (Figure 2.6B). All 5 eIF2Bα-facing aromatic fingies thus appear critical for NSs modulation of the ISR, likely through reducing the binding affinity of NSs for eIF2B. Indeed, alanine substitutions of the aromatic fingies was independently shown to reduce NSs binding affinity to eIF2B (Kashiwagi et al. 2021).

We additionally assessed the importance of the eIF2Bδ-facing residues – generating stable lines with alanine mutations (H36A and D37A). As we saw with mutation of the aromatic fingies, neither H36A nor D37A impaired NSs translation or impacted eIF2 or eIF2B subunit levels, but ISR evasion as monitored by ATF4 translation became compromised (Figure 2.6C). Notably, NSs::FLAG (H36A) displayed an intermediate phenotype in the ATF4 and general translation reporter assays, suggesting that while this mutation compromises NSs binding it does not appear to entirely break the interaction (Figure 2.6D). In contrast, NSs::FLAG (D37A) expressing cells appear unable to resist ISR activation. Although the structure suggests only a mild ionic interaction between NSs D37 and eIF2Bδ R321, we reason the D37A mutation might not only break the ionic interaction, but also potentially alter the conformation of the loop. As a result, V38 would move, disrupting its stacking with M6, an amino acid next to two aromatic fingies (Y5 and F7) (Figure 2.6 – figure supplement 2). Thus, changes to D37 and H36 could

result in the repositioning of the eIF2Bα-facing aromatic fingies, leading to a complete loss of NSs interaction with eIF2B. Together, these data provide a rationale for NSs' potent and selective binding to only fully assembled eIF2B$(\alpha\beta\delta\gamma\varepsilon)_2$ decamers.

Discussion

As one of the strategies in the evolutionary arms race between viruses and the host cells they infect, mammalian cells activate the ISR to temporarily shut down translation, thus preventing the synthesis of viral proteins. Viruses, in turn, have evolved ways to evade the ISR, typically by disarming the PKR branch through countermeasures that lead to decreased levels of eIF2-P, thus allowing translation to continue. In this study, we show that SFSV expresses a protein (NSs) that allows it to evade not just PKR-mediated ISR activation, but all four branches of the ISR, through a mechanism that exploits the conformational flexibility of eIF2B. NSs is an antagonistic of eIF2B's inhibitor eIF2-P, deploying an overlapping binding site. Whereas eIF2-P shifts eIF2B to its inactive I-State conformation by closing the angle between the eIF2Bα and eIF2Bδ subunits, NSs engages the enzyme to opposite effect, binding to an overlapping site with eIF2-P but preserving the angle between eIF2Bα and eIF2Bδ and locking it into its active A-State conformation.

Previously, we and others showed that the GEF activity of eIF2B is modulated conformationally: eIF2B's substrate (eIF2) binding stabilizes it in the A-State, whereas its inhibitor (eIF2-P) binding induces a hinge motion between the two tetrameric halves, resulting in a conformation that cannot engage the substrate optimally (I-state) (Schoof et al. 2021; Zyryanova et al. 2021). Our structure shows that NSs antagonizes the endogenous inhibitor (eIF2-P) by directly competing it off and stabilizing eIF2B in the active conformation. Owing to the reported single digit nM affinity of eIF2-P for eIF2B, this likely entails a cellular excess of NSs relative to eIF2-P (which should be expected given the high levels at which viral proteins are typically expressed) (Bogorad, Lin, and Marintchev 2018; Soday et al. 2019; Weekes et al. 2014). While NSs binds to the inhibitor-binding site, it does not induce the conformational change that the inhibitor binding induces. This mechanism is reminiscent of the antagonistic inhibition of GPCRs, such

as the β adrenergic receptors, where binding of an agonist ligand shifts the receptor to its active conformation, whereas binding of an antagonist ligand occupies an overlapping but not identical binding site that lacks contacts required to induce the activating conformational change (Kobilka 2011; Rasmussen, Choi, et al. 2011; Rasmussen, DeVree, et al. 2011; Staus et al. 2016). NSs, however, is an antagonist of an inhibitor (eIF2-P). Thus, by inhibiting an inhibition, it actually works as an eIF2B activator under conditions where eIF2-P is present and the ISR is induced.

In its ability to modulate eIF2B, NSs is not unique among viral proteins. The beluga whale coronavirus (Bw-CoV) protein AcP10 likewise allows evasion of the host cell ISR by interacting with eIF2B, as does the picornavirus AiVL protein (Rabouw et al. 2020). It was suggested that AcP10 makes contacts with eIF2Bα and eIF2Bδ, akin to NSs, and hence may act through a similar mechanism by antagonizing eIF2-P, although no structural information is yet available. By primary sequence comparison, AcP10, AiVL, and NSs show no recognizable homology with one another, indicating that viruses have evolved at least three – and likely more – different ways to exploit the eIF2α-P binding site on eIF2B to shut off the ISR. Therefore, inhibiting the eIF2B-eIF2-P interaction through the antagonism of eIF2-P binding could also be a general strategy used by many viruses.

Our structure and mutational analysis suggest that the binding of different parts of NSs to eIF2B occurs in a highly synergistic manner. While the amino acids facing eIF2Bδ do not seem to make sufficiently intimate contacts to provide a significant contribution to the enthalpic binding energy, changing them disrupts binding. It is plausible that the contacts of NSs with eIF2Bδ allow the optimal positioning of the aromatic fingies through allosteric communications between the loops and thus license NSs for tight binding.

The structure of the eIF2B-NSs complex reveals a previously unknown site on eIF2B that is potentially druggable. Unlike ISRIB, which stabilizes eIF2B's A-State through binding to a narrow pocket at the center of eIF2B and stapling the two tetrameric halves together at a precise distance and angle, NSs binds to a different interface on the opposite side of the protein. With ISRIB-derivatives showing extreme promise to alleviate cognitive dysfunction in animal studies of various neurological disorders and recently progressing into the clinic for Phase I human trials, developing therapeutics that modulate the ISR has never been more relevant (Chou et al. 2017).

Across phleboviruses, all characterized members of the family of related NSs proteins also counteract the host's interferon response (Wuerth and Weber 2016; Ly and Ikegami 2016). For RVFV, this functionality is contained within the structurally conserved C-terminal domain, which nonetheless varies quite heavily in sequence space (Wuerth et al. 2018; Billecocq et al. 2004; Cyr et al. 2015; Sall et al. 1997). A strict functional conservation does not appear to be the case for the N-terminal domain. Although this domain serves to evade PKR in some phleboviruses such as RVFV and SFSV, it accomplishes it through entirely different means: degradation of PKR in RVFV and antagonism of eIF2-P binding to eIF2B in SFSV (Habjan et al. 2009; Wuerth et al. 2020). The NSs is thus a bispecific molecule – a multitool of sorts. The C-terminal domain may serve as a scaffold containing a core functionality upon which the N-terminal domain may be free to evolve, exploring diverse functionalities and mechanisms. It is exciting to speculate whether anti-PKR properties of the N-terminal domain, as we identified for SFSV NSs, are commonly found across phleboviruses and whether still other PKR evasion strategies can be found.

Aberrant ISR activation underlies many neurological disorders (Traumatic Brain Injury, Down's Syndrome, Alzheimer's Disease, Amyotrophic Lateral Sclerosis), as well as certain cancers

(metastatic prostate cancer) (Zhu et al. 2019; Chou et al. 2017; Ma et al. 2013; Atkin et al. 2008; Nguyen et al. 2018; Costa-Mattioli and Walter 2020). Virotherapy, where viruses are used as a therapeutic agent for particular diseases, has seen the most success in the realm of cancer treatment where the infection either directly attacks cancer cells (oncolytic virotherapy) or serves to activate host defenses which target virus and cancer alike (Harrington et al. 2019; Russell 2002). Indeed, decades of evidence have shown that cancer patients that experience an unrelated viral infection can show signs of improvement, paving the way for the generation of genetically engineered oncolytic viruses that have only just received FDA approval in the last decade (Pelner, Fowler, and Nauts 1958; Kelly and Russell 2007). With our ever-growing understanding of diverse host-virus interactions, a whole host of new virotherapies are imaginable that can exploit the evolved functionalities of viral proteins such as the NSs.

Figures

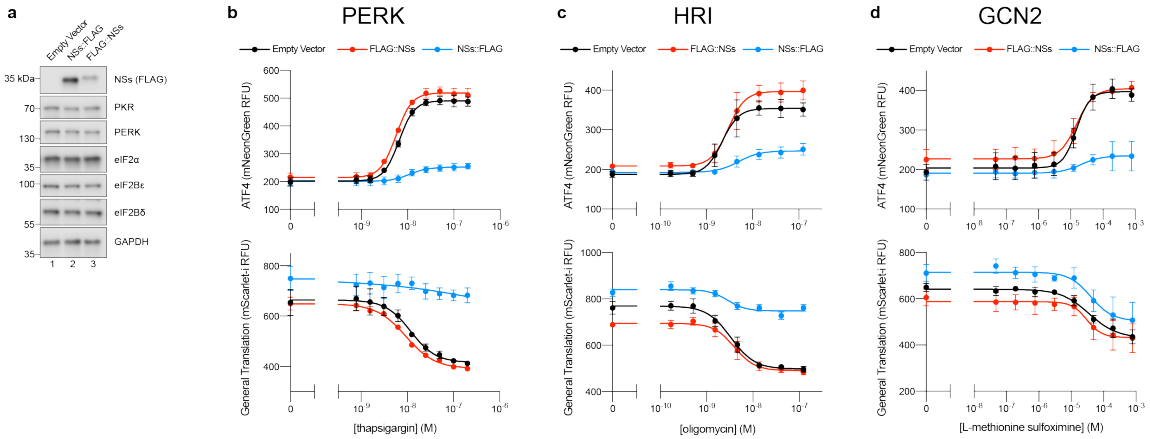

Figure 2.1: The SFSV NSs is a pan-ISR inhibitor
(a) Western blot of K562 cell extracts. Loading of all lanes was normalized to total protein. **(b-d)** ATF4 and General Translation reporter levels as monitored by flow cytometry. Trimethoprim, which is necessary to stabilize the ecDHFR::mScarlet-i and ecDHFR::mNeonGreen translation reporters, was at 20 μM for all conditions. (b) Samples after 3 h of thapsigargin and trimethoprim treatment. (c) Samples after 3 h of oligomycin and trimethoprim treatment. (d) Samples after 4 h of glutamine deprivation, L-methionine sulfoximine, and trimethoprim treatment.
For (a), PERK and GAPDH, PKR and eIF2α, and eIF2Bε and NSs (FLAG) are from the same gels, respectively. eIF2Bδ is from its own gel. For (b-d), biological replicates: n = 3. All error bars represent s.e.m. Source data are provided as a Source Data file.

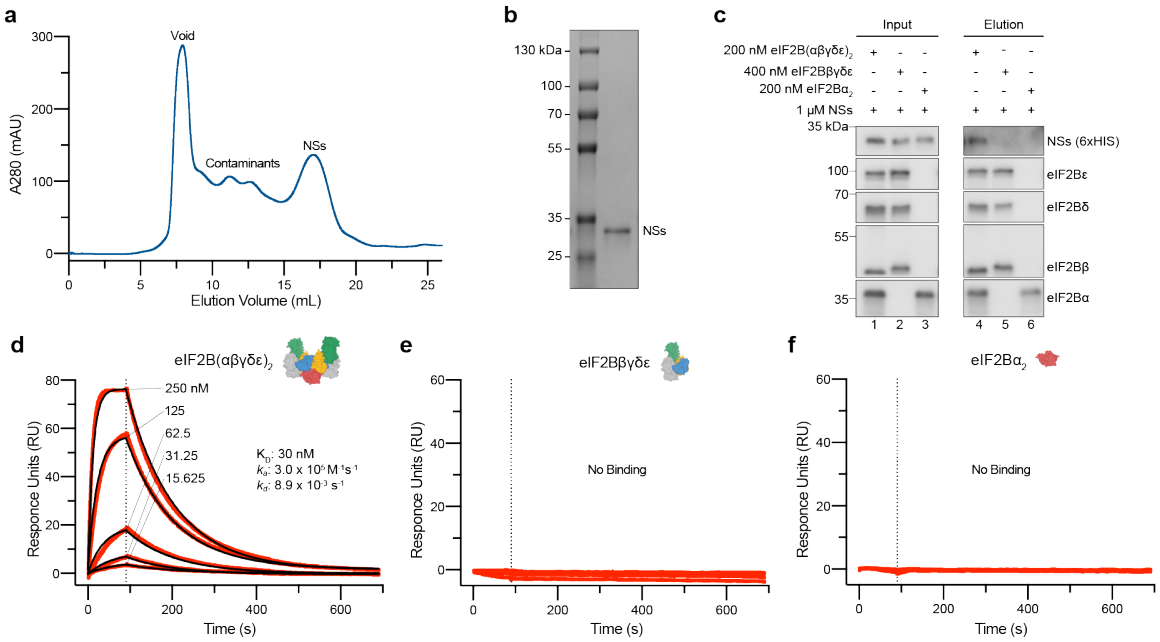

Figure 2.2: NSs specifically binds to eIF2B(αβδγε)$_2$ decamers
(a) Size exclusion chromatogram (Superdex 200 Increase 10/300 GL) during NSs purification from Expi293 cells. **(b)** Coomassie Blue staining of purified NSs. **(c)** Western blot of purified protein recovered after incubation with eIF2B(αβδγε)$_2$, eIF2Bβδγε, or eIF2Bα$_2$ immobilized on Anti-protein C antibody conjugated resin. For eIF2B(αβδγε)$_2$ and eIF2Bα$_2$, eIF2Bα was protein C tagged. eIF2Bβ was protein C tagged for eIF2Bβδγε. **(d-f)** SPR of immobilized (d) eIF2B(αβδγε)$_2$, (e) eIF2Bβδγε, and (f) eIF2Bα$_2$ binding to NSs. For eIF2B(αβδγε)$_2$ and eIF2Bβδγε, eIF2Bβ was Avi-tagged and biotinylated. For eIF2Bα$_2$, eIF2Bα was Avi-tagged and biotinylated. For (d), concentration series: (250 nM - 15.625 nM) For (e-f), concentration series: (125 nM – 15.625 nM). For (c), eIF2Bβ and eIF2Bα, and eIF2Bδ and NSs (6xHIS) are from the same gels, respectively. eIF2Bε is from its own gel. For (b-f), a single biological replicates. Source data are provided as a Source Data file.

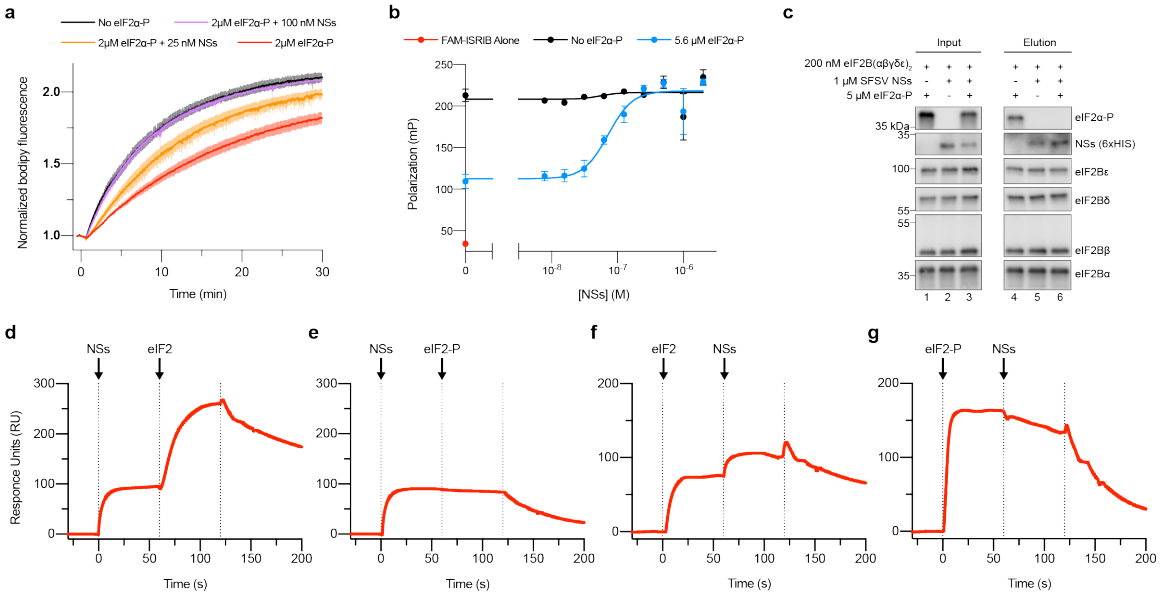

Figure 2.3: NSs grants ISR evasion by antagonizing eIF2α-P binding to eIF2B
(a) GEF activity of eIF2B as assessed by BODIPY-FL-GDP exchange. eIF2B$(\alpha\beta\delta\gamma\varepsilon)_2$ at 10 nM throughout. $t_{1/2}$ = 6.3 min (No eIF2α-P), 6.2 min (2 μM eIF2α-P + 100 nM NSs), 9.2 min (2 μM eIF2α-P + 25 nM NSs), and 13.4 min (2 μM eIF2α-P). **(b)** Plot of fluorescence polarization signal before (*red*) and after incubation of FAM-ISRIB (2.5 nM) with 100 nM eIF2B$(\alpha\beta\delta\gamma\varepsilon)_2$ (*black*) or 100 nM eIF2B$(\alpha\beta\delta\gamma\varepsilon)_2$ + 5.6 μM eIF2α-P (*blue*) and varying concentrations of NSs. **(c)** Western blot of purified protein recovered after incubation with eIF2B$(\alpha\beta\delta\gamma\varepsilon)_2$ immobilized on Anti-protein C antibody conjugated resin. eIF2Bα was protein C tagged. **(d-g)** SPR of immobilized eIF2B$(\alpha\beta\delta\gamma\varepsilon)_2$ binding to saturating (d-e) 500 nM NSs, (f) 125 nM eIF2, or (g) 125 nM eIF2-P followed by (d) 125 nM eIF2, (e) 125 nM eIF2-P, or (f-g) 500 nM NSs. eIF2Bα was Avi-tagged and biotinylated.
For (c), eIF2Bε and eIF2α-P, eIF2Bβ and eIF2Bα, and eIF2Bδ and NSs (6xHIS) are from the same gels, respectively. For (a-b), biological replicates: n = 3. For (c-g), a single biological replicate. All error bars represent s.e.m. Source data are provided as a Source Data file.

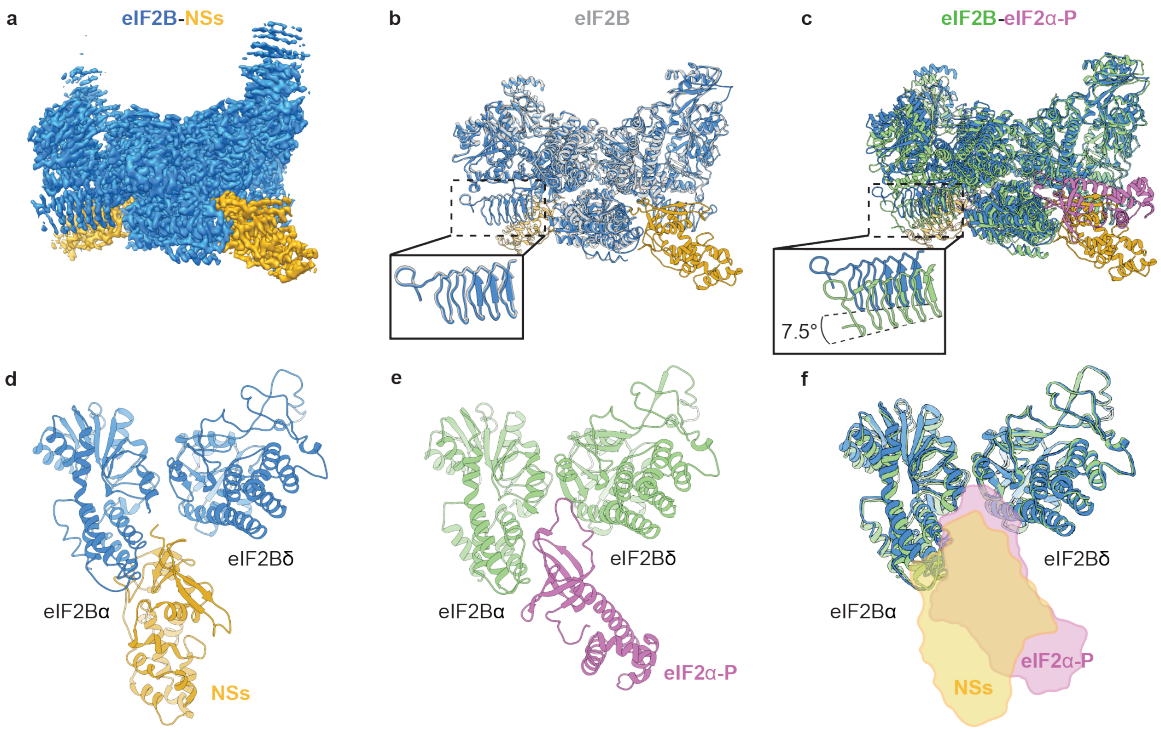

Figure 2.4: Overall architecture of the eIF2B-NSs complex
(a) Cryo-EM map of the eIF2B-NSs complex. **(b)** Overlay of the apo eIF2B structure (PDB ID: 7L70) and the eIF2B-NSs structure shows that the overall conformation of eIF2B is nearly identical between the NSs-bound state and the apo state. **(c)** Overlay of the eIF2B-eIF2α-P complex structure (PDB ID: 6O9Z) and the eIF2B-NSs structure shows a 7.5° hinge movement between the two eIF2B halves. **(d)** and **(e)** Both NSs and eIF2α-P bind to eIF2B at the cleft between eIF2Bα and eIF2Bδ. **(d)** NSs mainly contacts eIF2Bα, whereas **(e)** eIF2α-P makes extensive contacts to both eIF2Bα and eIF2Bδ. **(f)** Comparison between the surfaces of NSs and eIF2α-P showing a significant overlay between the two. eIF2B in the eIF2B-NSs complex is colored in blue and NSs in gold. eIF2B in its apo form is colored white. eIF2B in the eIF2α-P-bound complex is colored in green, and eIF2α-P in pink.

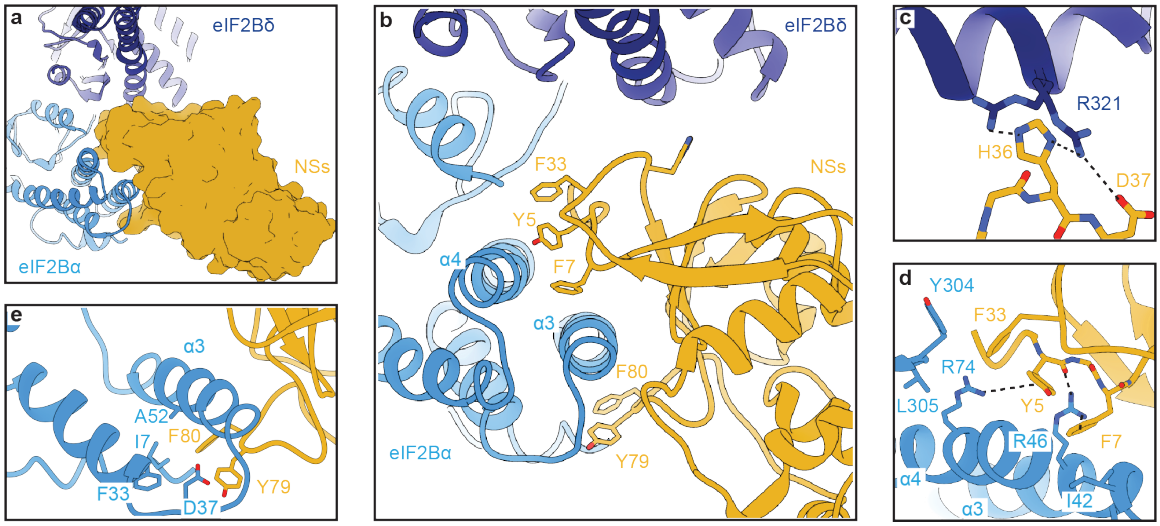

Figure 2.5: NSs latches on to eIF2B with its aromatic fingies
(a) Surface representation of NSs showing that it grips the alpha helices of eIF2Bα. **(b)** NSs extends five aromatic amino acids in three short loops to contact eIF2Bα. They contact helices α3 and α4 of eIF2Bα. The backbone of T35 and the side chains of H36 and D37 of NSs make contact with eIF2Bδ **(c)** Zoomed in view of panel b showing the interaction between H36 and D37 with eIF2Bδ. **(d)** and **(e)** Zoomed-in view of panel b showing the detailed interactions between the five main aromatic amino acids and eIF2Bα. Each polar-polar or cation-π interaction is denoted by a dashed line. NSs is colored in gold, eIF2Bα in blue, and eIF2Bδ in purple.

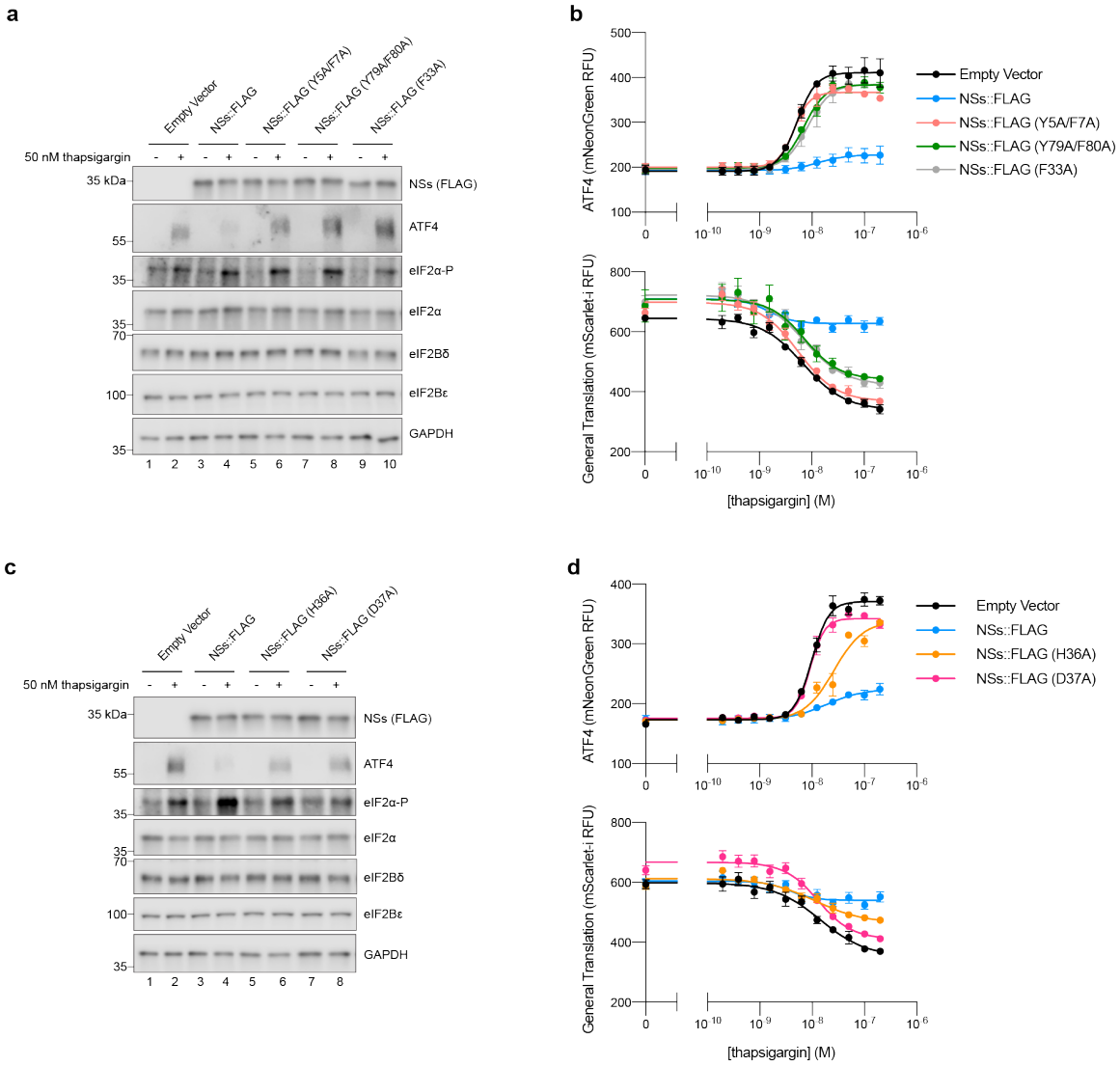

Figure 2.6: All 5 aromatic fingies are required for NSs evasion of the ISR
(a and c) Western blot of K562 cell extracts 3 h after treatment with 50 nM thapsigargin. Loading of all lanes was normalized to total protein. **(b and d)** ATF4 and General Translation reporter levels as monitored by flow cytometry after 3 h of thapsigargin and trimethoprim (20 μM) treatment.
For (a), ATF4 and eIF2α, eIF2Bε and NSs (FLAG), and eIF2Bδ and eIF2α-P are from the same gels, respectively. GAPDH is from its own gel. For (c), ATF4 and GAPDH, eIF2Bε and NSs (FLAG), and eIF2Bδ and eIF2α-P are from the same gels, respectively. eIF2α is from its own gel. For (b), biological replicates: n = 3. For (d), biological replicates: n = 4. All error bars represent s.e.m. Source data are provided as a Source Data file.

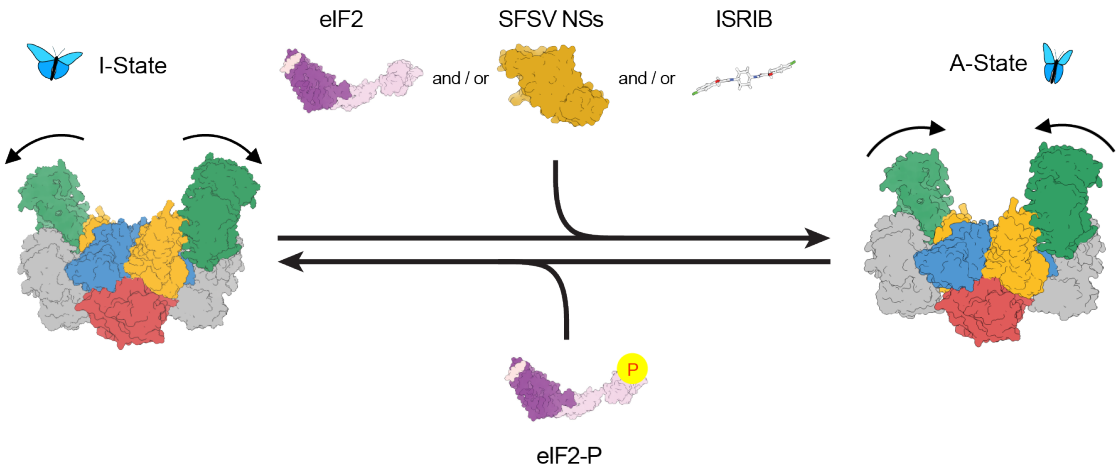

Figure 2.7: Model for regulation of eIF2B activity.
Like the small molecule ISRIB and the substrate eIF2, NSs binds to and stabilizes the active, "wings up" conformation of eIF2B (A-State). eIF2-P induces the inhibited "wings down" conformation of eIF2B (I-State).

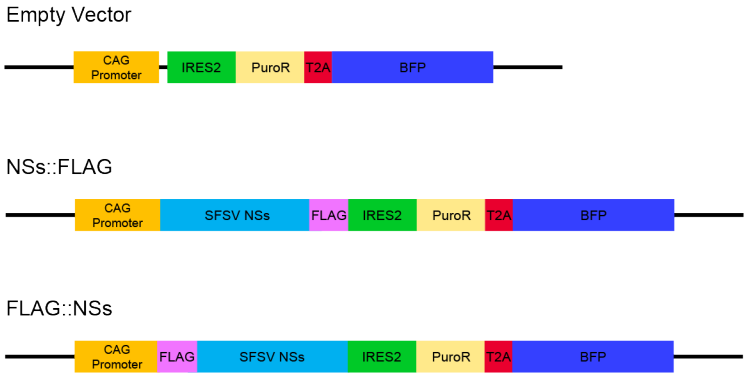

Figure 2.1 – figure supplement 1: Design of NSs expression constructs
A schematic of the NSs expression constructs stably integrated (lentivirus) into the genome.

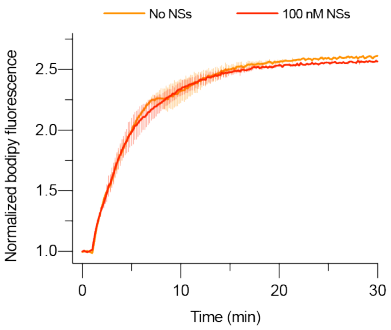

Figure 2.2 – figure supplement 1: Effect of NSs alone on eIF2B nucleotide exchange
GEF activity of eIF2B as assessed by BODIPY-FL-GDP exchange. BODIPY-FL-GDP fluorescence increases when bound to protein. $t_{1/2}$ = 3.6 min, s.e.m. = 0.5 min (No NSs) and 3.4 min, s.e.m. = 0.5 min (100 nM NSs). eIF2B$(\alpha\beta\delta\gamma\varepsilon)_2$ at 10 nM throughout. Biological replicates: n = 2. Source data are provided as a Source Data file.

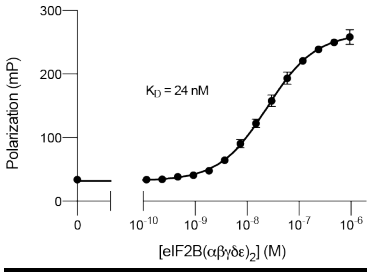

Figure 2.3 – figure supplement 1: Binding affinity of ISRIB for decameric eIF2B
Plot of fluorescence polarization signal after incubation of FAM-ISRIB (2.5 nM) with a titration of eIF2B(αβδγε)$_2$. Biological replicates: n = 3. All error bars represent s.e.m. Source data are provided as a Source Data file.

A

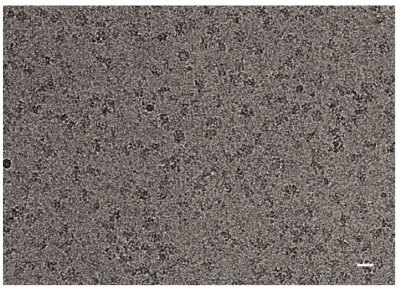

C

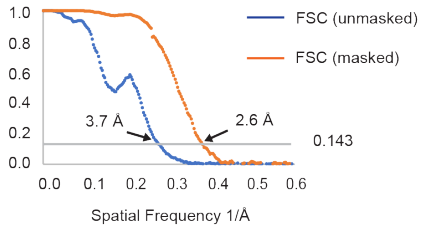
1.0
0.8
0.6
0.4
0.2
0.0
FSC (unmasked)
FSC (masked)
3.7 Å
2.6 Å
0.143
0.0 0.1 0.2 0.3 0.4 0.5 0.6
Spatial Frequency 1/Å

D

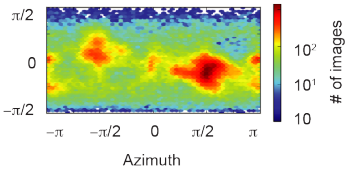
π/2
0
−π/2
−π −π/2 0 π/2 π
Azimuth
# of images

E

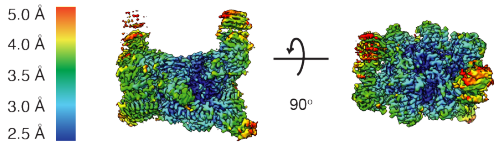
5.0 Å
4.0 Å
3.5 Å
3.0 Å
2.5 Å
90°

F

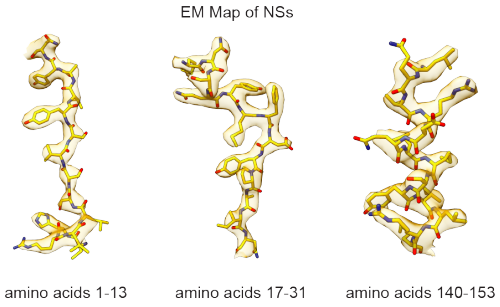
EM Map of NSs
amino acids 1-13
amino acids 17-31
amino acids 140-153

B

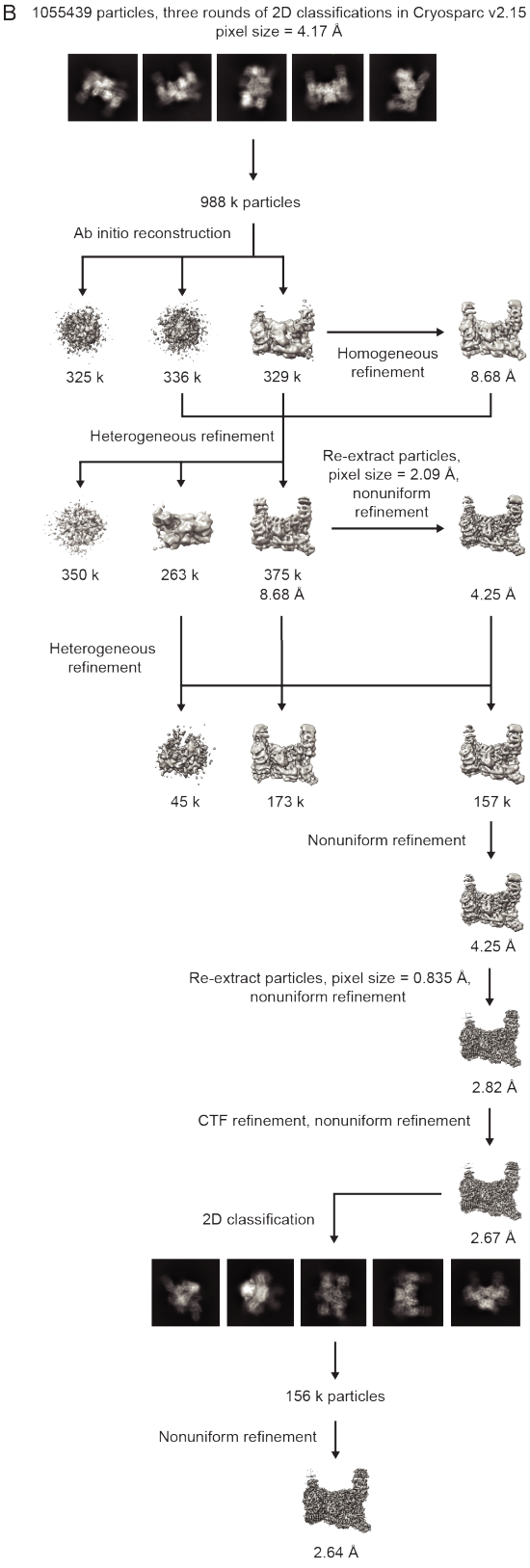
1055439 particles, three rounds of 2D classifications in Cryosparc v2.15
pixel size = 4.17 Å
988 k particles
Ab initio reconstruction
325 k
336 k
329 k
Homogeneous refinement
8.68 Å
Heterogeneous refinement
Re-extract particles, pixel size = 2.09 Å, nonuniform refinement
350 k
263 k
375 k
8.68 Å
4.25 Å
Heterogeneous refinement
45 k
173 k
157 k
Nonuniform refinement
4.25 Å
Re-extract particles, pixel size = 0.835 Å, nonuniform refinement
2.82 Å
CTF refinement, nonuniform refinement
2D classification
2.67 Å
156 k particles
Nonuniform refinement
2.64 Å

Figure 2.4 – figure supplement 1: Cryo-EM data analysis flow
(**a**) Representative micrograph of a total of 2143 micrographs collected for the eIF2B-NSs sample. The scale bar shown in white at the bottom-right is 200 Å. (**b**) Data processing scheme for reconstruction of eIF2B-NSs assembly. (**c**) Fourier shell correlation (FSC) plots of the 3D reconstructions of the eIF2B-NSs complex masked (orange), unmasked (blue) (**d**) Orientation angle distribution of the eIF2B-NSs complex reconstruction. (**e**) Local resolution map of the eIF2B-NSs complex showing that the N-terminal region of NSs that contacts eIF2B is well-resolved, and the C-terminal region of NSs that faces the solution is more dynamic. (**f**) Electron microscopy maps of different regions of the NSs structure in the eIF2B-NSs complex showing the quality of the data and the fit of the model.

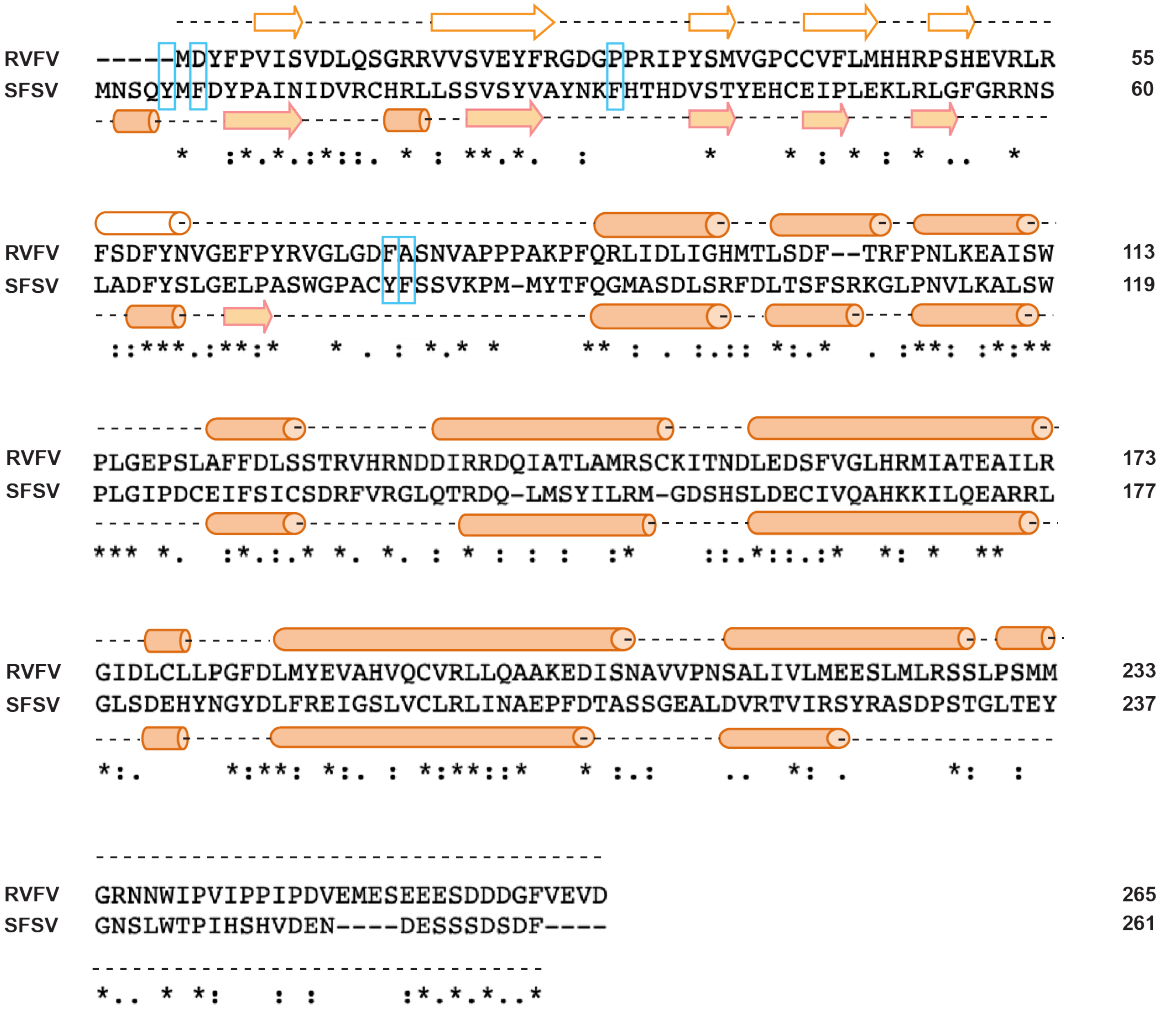

Figure 2.4 – figure supplement 2: Primary sequence alignment of the SFSV NSs and the RVFV NSs

Alignment shows that the primary sequence between the two NSs shares 43.2% similarity and most of the aromatic finger amino acids (in cyan boxes) in the SFSV NSs are not conserved in the RVFV NSs. Secondary structures are shown in arrows (beta strands) and cylinders (helices). The secondary structure of the SFSV NSs is assigned based on the experimental structure. The secondary structure of the C-terminal domain of the RVFV NSs is assigned based on PDB ID: 5OOO, and the N-terminal domain based on predictions (shown as hollow arrows or cylinders (Barski et al. 2017).

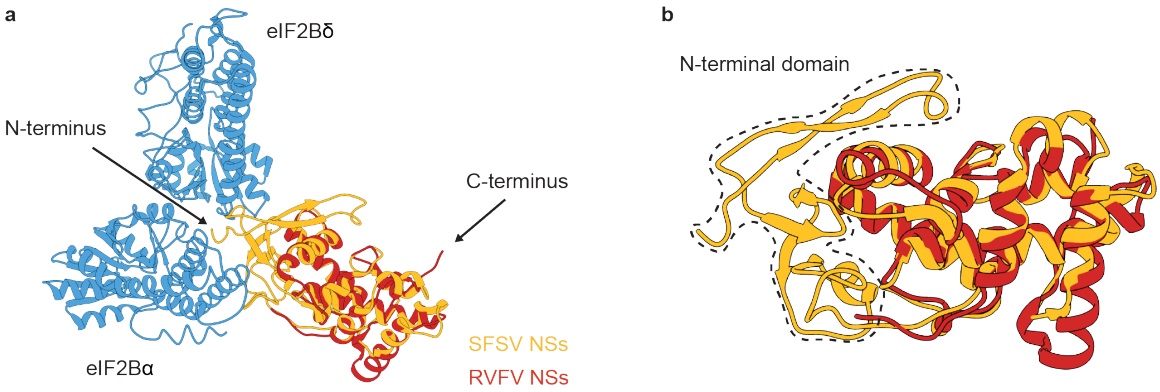

Figure 2.4 – figure supplement 3: Structural comparision between the SFSV NSs and the RVFV NSs
(a) Overlay of the RVFV NSs C-terminal domain structure (PDB ID: 5OOO, chain A) to the SFSV NSs showing that the C-terminal domain of the two NSs share similar overal structures. However, it is the N-terminal domain that forms direct contact with eIF2B. **(b)** Zoomed in view of panel a showing the structural similarity between the C-terminal domains fo the two NSs. eIF2B is colored blue, the SFSV NSs in gold and the RVFV NSs in red.

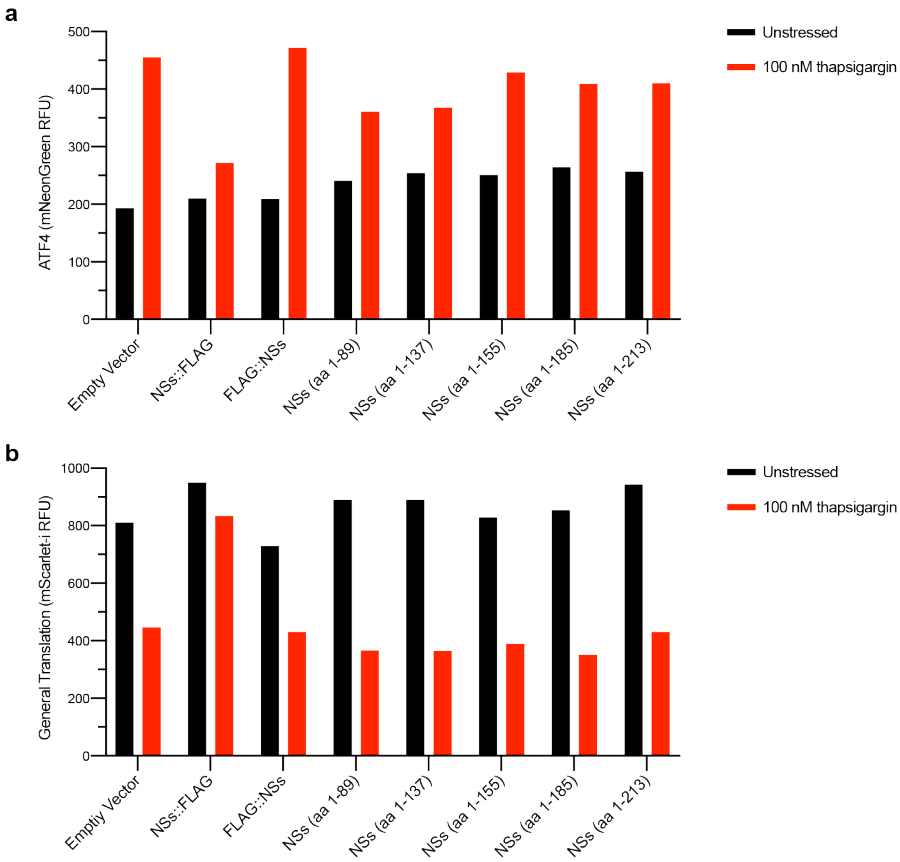

Figure 2.4 – figure supplement 4: Effect of NSs truncations on protein function
(a) ATF4 and **(b)** General Translation reporter levels as monitored by flow cytometry after 3 h of thapsigargin (100 nM) and trimethoprim (20 μM) treatment. ATF4 and General Translation reporter levels are show for the population of BFP+ cells (that is, cells that have stably integrated the NSs expression constructs). NSs truncation abolishes its ISR evasion functionality, either by destabilizing protein synthesis or, more specifically, the interaction with eIF2B. Source data are provided as a Source Data file.

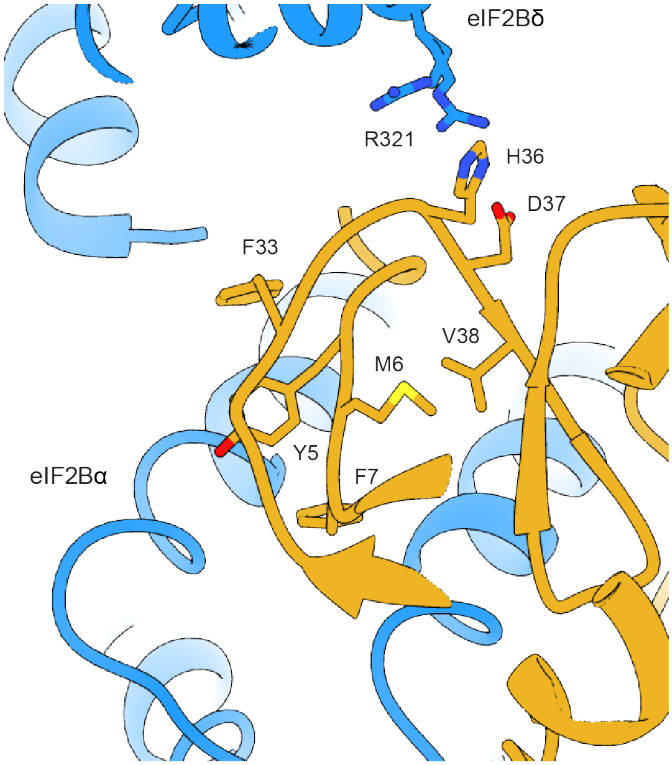

Figure 2.6 – figure supplement 1: Synergistic binding of NSs loops
Zoomed in view of the NSs loops interaction with eIF2B. The conformation of the eIF2Bδ-facing amino acids (H36 and D37) could affect the positioning of V38, which forms hydrophobic stacking with M6. This stacking interaction may be important for the optimal positioning of Y5 and F7, the two main aromatic fingies facing eIF2Bα, thus contributing to NSs-eIF2B binding. eIF2B is colored in blue and NSs in gold.

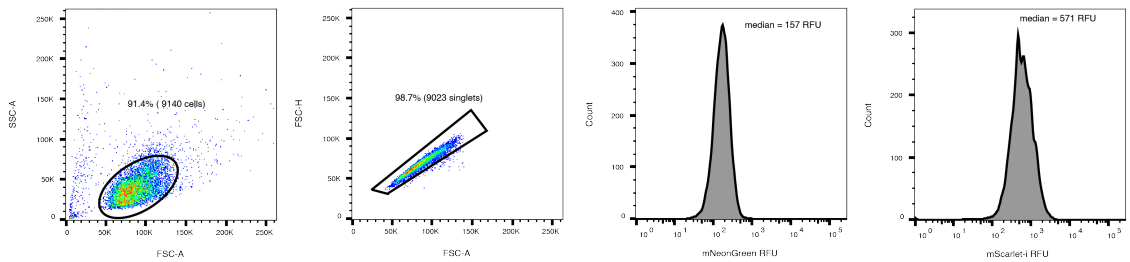

Figure 2.6 – figure supplement 2: Representative gating strategy for flow cytometry experiments
An example of how flow cytometry data is analyzed. From 10,000 events collected the vast majority pass filtering and are included in median reporter signal calculations.

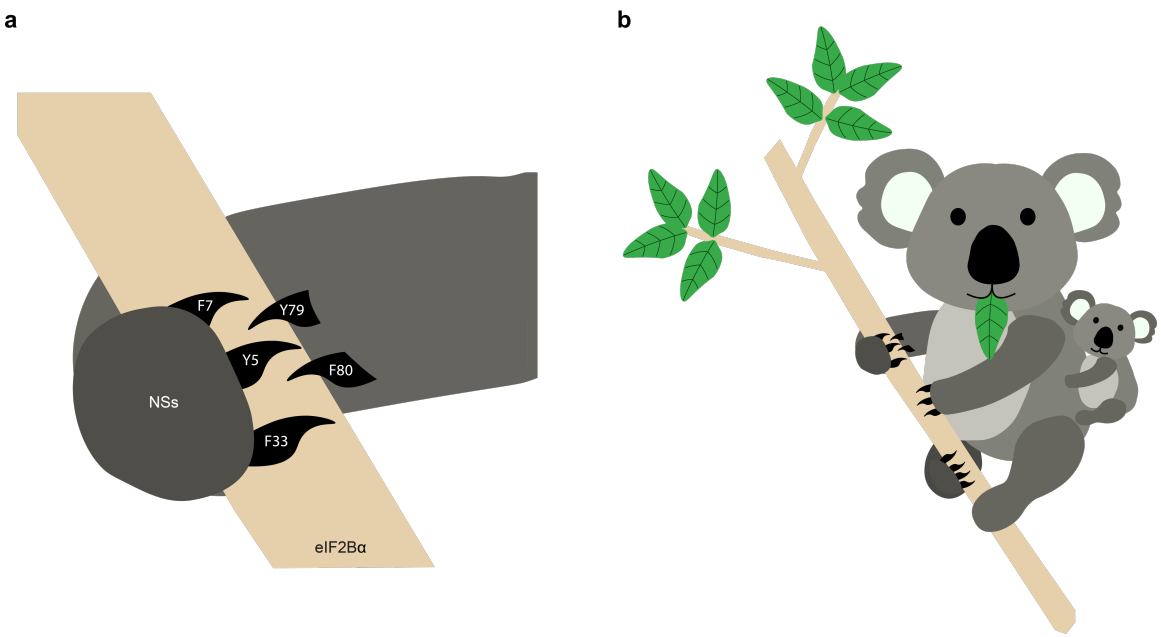

Figure 2.6 – figure supplement 3: Schematic overview of the aromatic fingies
(a) Cartoon representation of the NSs aromatic fingies interacting with eIF2Bα. A koala was chosen to illustrate this interaction as their hands have three fingies and two opposable thumbs that grab onto branches from opposite sides in a geometry similar to how NSs grabs onto eIF2Bα **(b)** Zoomed out view of panel a.

Table 2.1 Cryo-electron microscopy dataset for eIF2B-NSs complex

Structure	eIF2B-NSs complex (PDB ID: 7RLO)
Data collection	
Microscope	Titan Krios
Voltage (keV)	300
Nominal magnification	105000x
Exposure navigation	Image shift
Electron dose (e^{-}Å^{-2})	67
Dose rate (e^{-}/pixel/sec)	8
Detector	K3 summit
Pixel size (Å)	0.835
Defocus range (μm)	0.6-2.0
Micrographs	2143
Reconstruction	
Total extracted particles (no.)	1055439
Final particles (no.)	137093
Symmetry imposed	C1
FSC average resolution, masked (Å)	2.6
FSC average resolution, unmasked (Å)	3.7
Applied B-factor (Å)	76.2
Reconstruction package	Cryosparc 2.15
Refinement	
Protein residues	3670
Ligands	0
RMSD Bond lengths (Å)	0.002
RMSD Bond angles (°)	0.530
Ramachandran outliers (%)	0.08
Ramachandran allowed (%)	4.55
Ramachandran favored (%)	95.37
Poor rotamers (%)	3.20
CaBLAM outliers (%)	2.57
Molprobity score	2.08 (96th percentile)
Clash score (all atoms)	6.8 (99th percentile)
B-factors (protein)	102.73
B-factors (ligands)	N/A
EMRinger Score	2.77
Refinement package	Phenix 1.17.1-3660-000

Table 2.2 List of plasmids

Plasmid	Description	Antibiotic
pMS113	NSs::6xHIS for Expi293 expression / purification	Ampicillin
pMS085	Empty Vector for lentiviral integration	Ampicillin
pMS110	NSs::FLAG for lentiviral integration	Ampicillin
pMS111	FLAG::NSs for lentiviral integration	Ampicillin
pMS119	Truncated NSs (aa 1-89) for lentiviral integration	Ampicillin
pMS120	Truncated NSs (aa 1-137) for lentiviral integration	Ampicillin
pMS121	Truncated NSs (aa 1-155) for lentiviral integration	Ampicillin
pMS122	Truncated NSs (aa 1-185) for lentiviral integration	Ampicillin
pMS123	Truncated NSs (aa 1-213) for lentiviral integration	Ampicillin
pMS127	NSs::FLAG (Y5A/F7A) for lentiviral integration	Ampicillin
pMS128	NSs::FLAG (Y79A/F80A) for lentiviral integration	Ampicillin
pMS129	NSs::FLAG (F33A) for lentiviral integration	Ampicillin
pMS132	NSs::FLAG (H36A) for lentiviral integration	Ampicillin
pMS134	NSs::FLAG (D37A) for lentiviral integration	Ampicillin
pMS001	*E. coli* expression plasmid for eIF2Bδ and Avi-tagged eIF2Bβ	Chloramphenicol
pMS003	*E. coli* expression plasmid for eIF2Bδ and Protein C-tagged eIF2Bβ	Chloramphenicol
pMS026	*E. coli* expression plasmid for Avi-tagged eIF2Bα	Ampicillin

Table 2.3 Antibodies and Western blotting conditions

Antibody Target	Host	Dilution	Manufacturer / Catalog #	Blocking Conditions
GAPDH	Rabbit	1/2000	Abcam / ab9485	TBS-T + 3% BSA
eIF2Bα	Rabbit	1/1000	ProteinTech / 18010-1-AP	TBS-T + 3% milk
eIF2Bβ	Rabbit	1/1000	ProteinTech / 11034-1-AP	TBS-T + 3% milk
eIF2Bδ	Rabbit	1/1000	ProteinTech / 11332-1-AP	TBS-T + 3% milk
eIF2Bε	Mouse	1/1000	Santa Cruz Biotechnology / sc-55558	PBS-T + 3% milk
ATF4	Rabbit	1/1000	Cell Signaling / 11815S	PBS-T + 3% milk
eIF2α-P	Rabbit	1/1000	Cell Signaling / 9721S	PBS-T + 1% BSA
eIF2α	Rabbit	1/1000	Cell Signaling / 5324S	PBS-T + 3% milk
6xHIS	Goat (directly conjugated to HRP)	1/1000	Abcam / ab1269	TBS-T + 5% milk
FLAG	Mouse	1/1000	Sigma / F1804-1MG	PBS-T + 3% milk
PKR	Mouse	1/1000	BD Transduction Laboratories / 610764	TBS-T + 3% milk
PERK	Rabbit	1/1000	Cell Signaling / 3192S	TBS-T + 3% milk

Material and Methods

Cloning of NSs expression plasmids

The NSs::6xHIS Expi293 expression plasmid for transient transfection was generated using In-Fusion HD cloning. The SFSV NSs sequence (Wuerth et al. 2020) was inserted into the pXSN vector backbone and a 6xHIS tag was added at the C-terminus. The various NSs overexpression plasmids for stable lentiviral integration were generated using In-Fusion HD cloning. The SFSV NSs sequence was inserted into the pDBR vector backbone and a FLAG tag was added at the C-terminus (pMS110, pMS127, pMS128, pMS129, pMS130, pMS131, pMS132, pMS133) or N-terminus (pMS111). The various NSs truncations did not have a FLAG tag (pMS119, pMS120, pMS121, pMS122, pMS123). An empty vector control plasmid with no NSs insertion was also generated (pMS085). An IRES followed by the puromycin resistance gene, a T2A self-cleaving peptide, and the BFP sequence allows for selection based on antibiotic resistance or BFP signal (what was used in this study) (Figure 2.1 – figure supplement 1). Full plasmid details are shown in Table 2.2.

Cloning of tagged human eIF2B expression plasmids

eIF2B2 (encoding eIF2Bβ) and *eIF2B4* (encoding eIF2Bδ) had previously been inserted into sites 1 and 2 of pACYCDuet-1, respectively (pJT073) (Tsai et al. 2018). In-Fusion HD cloning (Takarabio) was used to edit this plasmid further and insert an Avi tag (GLNDIFEAQKIEWHE) or a Protein C tag (EDQVDPRLIDGK) at the N-terminus of *eIF2B2,* immediately following the pre-existing 6xHIS tag (pMS001 and pMS003). *eIF2B1* (encoding eIF2Bα) had previously been inserted into site 1 of pETDuet-1 (pJT075) (Tsai et al. 2018). In-Fusion HD cloning was used to edit this plasmid further and insert an Avi tag at the N-terminus of *eIF2B1*, immediately following the pre-existing 6xHIS tag (pMS026). The Avi tag allows selective, single, and complete biotinylation of the tagged protein.

Generation of stable NSs-expressing cells in an ISR reporter cell line

Our previously generated dual ISR reporter K562 cells expressing a stably integrated ATF4 reporter (pMS086), general translation reporter (pMS078), and dCas9-KRAB was used as the parental line (Schoof et al. 2021). The various NSs overexpression constructs (Table 2.2) were integrated using a lentiviral vector. Vesicular stomatitis virus (VSV)-G pseudotyped lentivirus was prepared using standard protocols and 293METR packaging cells. Viral supernatants were filtered (0.45 μm low protein binding filter unit (EMD Millipore)) and concentrated 10-20-fold (Amicon Ultra-15 concentrator with a 100,000-dalton molecular mass cutoff). Concentrated supernatant was then used the same day or frozen for future use. For spinfection, approximately 1,000,000 K562 cells were mixed with concentrated lentivirus and fresh media (RPMI containing 4.5 g/l glucose and 25 mM HEPES supplemented with 10% FBS, 2 mM L-alanyl-L-glutamine (Gibco GlutaMAX), and penicillin/streptomycin), supplemented with polybrene to 8 μg/ml, brought to 1.5 mL in a 6-well plate, and centrifuged for 1.5 h at 1000 g. Cells were then allowed to recover and expand for ~1 week before sorting on a Sony SH800 cytometer to isolate cells that had integrated the reporter. Roughly 100,000 BFP positive cells (targeting the highest 1-3% of expressers) were then sorted into a final pooled population and allowed to recover and expand. Cells expressing NSs truncations (pMS119-pMS123) were not sorted and instead analyzed as a polyclonal population, gating for BFP positive cells during data analysis.

Western Blotting

Western blotting was performed as previously described (Schoof et al. 2021). In brief, approximately 1,000,000 cells of the appropriate cell type were drugged as described in individual assays and then pelleted, washed, pelleted again, and resuspended in lysis buffer. Cells were then rotated for 30 min at 4 °C and then spun at 12,000 g for 20 min to pellet cell debris. Protein concentration was measured using a bicinchoninic acid assay (BCA assay) and

within an experiment, total protein concentration was normalized to the least concentrated sample. Equal protein content for each condition (targeting 10 µg) was run on 10% Mini-PROTEAN TGX precast protein gels (Biorad). After electrophoresis, samples were transferred onto a nitrocellulose membrane. Primary antibody / blocking conditions for each protein of interest are outlined in Table 2.3. Membranes were developed with SuperSignal West Dura (Thermo Fisher Scientific). Developed membranes were imaged on a LI-COR Odyssey gel imager for 0.5-10 min depending on band intensity.

ATF4 / general translation reporter assays

ISR reporter cells (at ~500,000 / ml) were co-treated with varying combinations of drugs (20 µM trimethoprim plus one of the following: thapsigargin, oligomycin, or glutamine deprivation (and no FBS) + L-methionine sulfoximine) and incubated at 37 °C until the appropriate timepoint had been reached. At this time, the plate was removed from the incubator and samples were incubated on ice for 10 min. Then ATF4 (mNeonGreen) and General Translation (mScarlet-i) reporter levels were monitored using a high throughput sampler (HTS) attached to a BD FACSCelesta cytometer running BD FACSDiva v9.0. Data was analyzed in FlowJo version 10.6.1, and median fluorescence values for both reporters were exported and plotted in GraphPad Prism 8 (Figure 2.6 – figure supplement 2). No BFP positive sorting was performed on the lines expressing NSs truncations. For analysis of these samples, BFP positive cells were gated in FlowJo and analysis performed on this population. Where appropriate, curves were fit to log[inhibitor] versus response function with variable slope.

Purification of human eIF2B subcomplexes

Human eIFBα$_2$ (pJT075), Avi-tagged eIFBα$_2$ (pMS026), protein C-tagged eIFBα$_2$ (pMS027), eIF2Bβγδε (pJT073 and pJT074 co-expression), Avi-tagged eIF2Bβγδε (pMS001 and pJT074 co-expression), and ProteinC-tagged eIF2Bβγδε (pMS003 and pJT074 co-expression) were

purified as previously described with a minor modification for purification of the Avi-tagged species (Tsai et al. 2018). One Shot BL21 Star (DE3) chemically competent *E. coli* cells (Invitrogen) were transformed with the requisite expression plasmids and grown in LB with kanamycin and chloramphenicol (eIF2B tetramer preps) or ampicillin (eIF2Bα_2 preps). At an OD_{600} of ~0.8 1 mM IPTG (Gold Biotechnology) was added and the culture was grown overnight at 16 °C. Using the EmulsiFlex-C3 (Avestin), Cells were harvested and lysed through 3 cycles of high-pressure homogenization in lysis buffer (20 mM HEPES-KOH, pH 7.5, 250 mM KCl, 1 mM dithiothreitol (DTT), 5 mM $MgCl_2$, 15 mM imidazole, and cOmplete EDTA-free protease inhibitor cocktail (Roche)). For eIF2Bα_2 preps 20 mM imidazole was used.The lysate was clarified at 30,000 g for 30 min at 4 °C. Lysate was then clarified at 30,000 g for 60 min at 4 °C.

All following purification steps were conducted on the ÄKTA Pure (GE Healthcare) system at 4 °C. Clarified lysate was loaded onto a 5 ml HisTrap HP column (GE Healthcare). For eIF2B tetramer preps the column was then washed in a buffer containing 20 mM HEPES-KOH, pH 7.5, 200 mM KCl, 1 mM DTT, 5 mM $MgCl_2$, and 15 mM imidazole. For eIF2Bα_2 preps 30 mM KCl and 20 mM imidazole were used. The sample was then eluted with a linear gradient up to 300 mM imidazole. eIF2B containing fractions were collected and applied to a MonoQ HR 10/100 GL column (GE Healthcare) equilibrated in 20 mM HEPES-KOH pH 7.5, 200 mM KCl, 1 mM DTT, and 5 mM $MgCl_2$. For eIF2Bα_2 preps 30 mM KCl was used. The column was washed in the same buffer, and the protein was eluted with a linear gradient up to 500 mM KCl. eIF2B containing fractions were collected and concentrated with an Amicon Ultra-15 concentrator (EMD Millipore) with a 30 kDa (tetramer preps) or 10 kDa (eIF2Bα_2 preps) molecular mass cutoff and spun down for 10 min at 10,000 g to remove aggregates. The supernatant was then injected onto a Superdex 200 10/300 GL (GE Healthcare) column equilibrated in a buffer containing 20 mM HEPES-KOH pH 7.5, 200 mM KCl, 1 mM DTT, 5 mM $MgCl_2$, and 5%

glycerol, and concentrated using the appropriate Amicon Ultra-15 concentrators (EMD Millipore).

For Avi-tagged species, after running samples over a MonoQ HR 10/10 column the eluted fractions were combined and concentrated to a target concentration of 40 μM. The sample was then incubated at 4 °C overnight according to manufacturer's instructions with 2.5 μg BirA for every 10 nmol substrate, 10mM ATP, 50 μM d-biotin, and 100mM $Mg(OAc)^2$ in a 50 mM bicine buffer, pH 8.3 (Avidity BirA biotin-protein ligase standard reaction kit). Incubation with BirA yields selective and efficient biotinylation of Avi-tagged species. After the biotinylation reaction, purification of biotinylated species proceeded as described above.

All eIF2B$(\alpha\beta\gamma\delta\varepsilon)_2$ used throughout was assembled by mixing purified eIF2B$\beta\gamma\delta\varepsilon$ and eIF2Bα_2 (either tagged or untagged versions as needed) at the appropriate molar ratios.

Purification of human eIF2αβγ heterotrimer and eIF2α-P

Human eIF2 was purified as previously described (Wong et al. 2018). This material was a generous gift of Calico Life Sciences LLC. eIF2-P was prepared by mixing eIF2 in 50-fold excess with PERK kinase and 1 mM ATP. The mixture was incubated at room temperature for 60 min before incubation on ice until use. The purification of human eIF2α-P was performed as previously described (Schoof et al. 2021). One Shot BL21 Star (DE3) chemically competent *E. coli* cells (Invitrogen) were transformed with the expression plasmid for N-terminally 6x-His-tagged human eIF2α, (pAA007) along with a tetracycline-inducible, chloramphenicol-resistant plasmid (pG-Tf2) containing the chaperones groES, groEL, and Tig (Takara Bio). Transformed cells were grown in LB with kanamycin and chloramphenicol for selection. Chaperone expression was induced at an OD600 of ~0.2, by addition of tetracycline (1 ng/ml). At an OD_{600} of ~0.8 the culture was cooled to room temperature and eIF2α expression was induced with 1

mM IPTG (Gold Biotechnology) and the culture was grown for at least 16 h more at 16 °C. Using the EmulsiFlex-C3 (Avestin), Cells were harvested and lysed through 3 cycles of high-pressure homogenization in lysis buffer (100 mM HEPES-KOH, pH 7.5, 300 mM KCl, 2 mM dithiothreitol (DTT), 5 mM $MgCl_2$, 5 mM imidazole, 10% glycerol, 0.1% IGEPAL CA-630, and cOmplete EDTA-free protease inhibitor cocktail (Roche)). The lysate was clarified at 30,000 g for 30 min at 4 °C.

Subsequent purification steps were conducted on the ÄKTA Pure (GE Healthcare) system at 4 °C. Clarified lysate was loaded onto a 5 ml HisTrap FF Crude column (GE Healthcare), washed in a buffer containing 20 mM HEPES-KOH, pH 7.5, 100 mM KCl, 5% glycerol, 1 mM DTT, 5 mM $MgCl_2$, 0.1% IGEPAL CA-630, and 20 mM imidazole, and eluted with 75 ml linear gradient of 20 to 500 mM imidazole. The eIF2α-containing fractions were collected and applied to a MonoQ HR 10/100 GL column (GE Healthcare) equilibrated in anion exchange buffer (20 mM HEPES-KOH pH 7.5, 100 mM KCl, 1 mM DTT, 5% glycerol, and 5 mM $MgCl_2$). The column was washed in the same buffer, and the protein was eluted with a linear gradient of 100 mM to 1 M KCl. eIF2α containing fractions were collected and concentrated with an Amicon Ultra-15 concentrator (EMD Millipore) with a 30 kDa molecular mass cutoff and spun down for 10 min at 10,000 g to remove aggregates. Before size exclusion, the pooled anion exchange fractions were phosphorylated *in vitro* overnight at 4 °C with 1 mM ATP and 1 µg of $PKR_{(252-551)}$-GST enzyme (Thermo Scientific) per mg of eIF2α. The supernatant was then injected onto a Superdex 75 10/300 GL (GE Healthcare) column equilibrated in a buffer containing 20 mM HEPES-KOH pH 7.5, 100 mM KCl, 1 mM DTT, 5 mM $MgCl_2$, and 5% glycerol, and concentrated using Amicon Ultra-15 concentrators (EMD Millipore) with a 10 kDa molecular mass cutoff. Complete phosphorylation was confirmed by running the samples on a 12.5% Super-Sep PhosTag gel (Wako Chemicals).

Purification of NSs::6xHIS

We used the pMS113 construct to express and purify NSs::6xHIS. Expi293T cells (ThermoFisher) were transfected with the NSs construct per the manufacturer's instructions for the MaxTiter protocol and harvested 5 days after transfection. Cells were pelleted (1000 g, 4 min) and resuspended in Lysis Buffer (130 mM KCl, 2.5 mM $MgCl_2$, 25 mM HEPES-KOH pH 7.4, 2 mM EGTA ,1% triton, 1mM TCEP, 1x cOmplete protease inhibitor cocktail (Roche)). Cells were then incubated for 30 min at 4 °C and then spun at 30,000 g for 1 h to pellet cell debris. Lysate was applied to a 5 ml HisTrap HP column (GE Healthcare) equilibrated in Buffer A (20 mM HEPES-KOH, pH 7.5, 200 mM KCl, 5 mM $MgCl_2$, 15mM imidazole) and then eluted using a gradient of Buffer B (20 mM HEPES-KOH, pH 7.5, 200 mM KCl, 5 mM $MgCl_2$, 300mM imidazole). NSs::6xHIS was concentrated using a 10 kDa MWCO spin concentrator (Amicon) and further purified by size exclusion chromatography over a Superdex 200 Increase 10/300 GL column (GE Healthcare) in Elution Buffer (20 mM HEPES, pH 7.5, 200 mM KCl, 5mM $MgCl_2$, 1mM TCEP, and 5% Glycerol). The resulting fractions were pooled and flash frozen in liquid nitrogen.

***In vitro* NSs/eIF2α-P immunoprecipitation**

Varying combinations of purified eIF2α-P, NSs::6xHIS, $eIF2B(\alpha\beta\delta\gamma\varepsilon)_2$, eIF2Bβδγε, and $eIF2B\alpha_2$ were incubated (with gentle rocking) with Anti-protein C antibody conjugated resin (generous gift from Aashish Manglik) in Assay Buffer (20 mM HEPES-KOH, pH 7.5, 150 mM KCl, 5 mM $MgCl_2$, 1mM TCEP, 1 mg/ml bovine serum albumin (BSA), 5mM $CaCl_2$). After 1.5 h the resin was pelleted by benchtop centrifugation and the supernatant was removed. Resin was washed 3x with 1 mL of ice cold Assay Buffer before resin was resuspended in Elution Buffer (Assay Buffer with 5 mM EDTA and 0.5 mg/mL protein C peptide added) and incubated with gentle rocking for 1 h. The resin was then pelleted and the supernatant was removed. Samples were analyzed by Western Blotting as described above.

GDP exchange assay

in vitro detection of GDP binding to eIF2 was performed as previously described (Schoof et al. 2021; Tsai et al. 2018). The only modification was addition of NSs in certain conditions as indicated. In brief, purified eIF2 (100 nM) was incubated with 100 nM BODIPY-FL-GDP (Thermo Fisher Scientific) in assay buffer (20 mM HEPES-KOH, pH 7.5, 100 mM KCl, 5 mM $MgCl_2$, 1 mM TCEP, and 1 mg / ml BSA) to a volume of 18 µl in 384 square-well black-walled, clear-bottom polystyrene assay plates (Corning). The GEF mix was prepared by incubating a 10x solution of eIF2B$(\alpha\beta\gamma\delta\varepsilon)_2$ with or without 10x solutions of eIF2α-P and / or NSs. To compare nucleotide exchange rates, the 10x GEF mixes were spiked into the 384-well plate wells with a multi-channel pipette, such that the resulting final concentration of eIF2B$(\alpha\beta\gamma\delta\varepsilon)_2$ was 10 nM and the final concentration of other proteins and drugs are as indicated in the figures. Fluorescence intensity was recorded every 10 s for 30-60 min using a Clariostar PLUS (BMG LabTech) plate reader (excitation wavelength: 497 nm, bandwidth 14 nm, emission wavelength: 525 nm, bandwidth: 30 nm). Data were fit to a first-order exponential and plotted in GraphPad Prism 8.

FAM-ISRIB binding assay

All fluorescence polarization measurements were performed as previously described (Schoof et al. 2021). In brief, 20 µl reactions were set up with 100 nM eIF2B$(\alpha\beta\gamma\delta\varepsilon)_2$ + 2.5 nM FAM-ISRIB (Praxis Bioresearch) in FP buffer (20 mM HEPES-KOH pH 7.5, 100 mM KCl, 5 mM $MgCl_2$, 1 mM TCEP) and measured in 384-well non-stick black plates (Corning 3820) using the ClarioStar PLUS (BMG LabTech) at room temperature. Prior to reaction setup, eIF2B$(\alpha\beta\gamma\delta\varepsilon)_2$ was assembled in FP buffer using eIF2B$\beta\gamma\delta\varepsilon$ and eIF2Bα_2 in 2:1 molar ratio for 1 h at room temperature. FAM-ISRIB was first diluted to 2.5 µM in 100% NMP prior to dilution to 50 nM in 2% NMP and then added to the reaction. For titrations with NSs, dilutions were again made in

FP buffer, and the reactions with eIF2B, FAM-ISRIB, and these dilutions +/- eIF2α-P were incubated at 22 °C for 30 min prior to measurement of parallel and perpendicular intensities (excitation: 482 nm, emission: 530 nm). Data were plotted in GraphPad Prism 8, and where appropriate, curves were fit to log[inhibitor] vs response function with variable slope.

Affinity determination and competition analysis by surface plasmon resonance

NSs affinity determination experiments were performed on a Biacore T200 instrument (Cytiva Life Sciences) by capturing the biotinylated eIF2B$(\alpha\beta\gamma\delta\varepsilon)_2$, eIF2B$\beta\gamma\delta\varepsilon$, and eIF2B$\alpha_2$ at ~100nM on a Biotin CAPture Series S sensor chip (Cytiva Life Sciences) to achieve maximum response (Rmax) of <100 response units (RUs) upon NSs binding. A molar equivalent of each eIF2B species was immobilized. 2-fold serial dilutions of purified NSs were flowed over the captured eIF2B complexes at 30 µL / min for 90 seconds followed by 600 seconds of dissociation flow. Following each cycle, the chip surface was regenerated with 3 M guanidine hydrochloride. A running buffer of 20 mM HEPES-KOH, pH 7.5, 100 mM KCl, 5 mM $MgCl_2$, and 1 mM TCEP was used throughout. The resulting sensorgrams were fit to a 1:1 Langmuir binding model using the association then dissociation model in GraphPad Prism 8.0.

For NSs and eIF2/eIF2-P competition experiments, eIF2B$(\alpha\beta\gamma\delta\varepsilon)_2$ was immobilized as described above. A solution containing 500 nM NSs, 125 nM eIF2, or 125 nM eIF2-P was flowed over the captured eIF2B for 60 s at 30 µL / min to achieve saturation. Following this binding reaction, a second injection of 500 nM NSs and either 125 nM eIF2 or 125 nM eIF2-P was performed.

Sample preparation for cryo-electron microscopy

Decameric eIF2B$(\alpha\beta\gamma\delta\varepsilon)_2$ was prepared by incubating 20 µM eIF2B$\beta\gamma\delta\varepsilon$ with 11 µM eIF2Bα_2 in a final solution containing 20 mM HEPES-KOH, pH 7.5, 200 mM KCl, 5 mM $MgCl_2$, and 1 mM TCEP. This 10 µM eIF2B$(\alpha\beta\gamma\delta\varepsilon)_2$ sample was further diluted to 750 nM and incubated with 2.25

µM NSs::6xHIS on ice for 1 h before plunge freezing. A 3 µl aliquot of the sample was applied onto the Quantifoil R 1.2/1/3 400 mesh Gold grid and we waited for 30 s. A 0.5 µl aliquot of 0.1-0.2% Nonidet P-40 substitute was added immediately before blotting. The entire blotting procedure was performed using Vitrobot (FEI) at 10 ºC and 100% humidity.

Electron microscopy data collection

Cryo-EM data for the eIF2B-NSs complex was collected on a Titan Krios transmission electron microscope operating at 300 keV, and micrographs were acquired using a Gatan K3 direct electron detector. Serial EM was used to collect the EM data (Mastronarde 2003). The total dose was 67 $e^-/ Å^2$, and 117 frames were recorded during a 5.9 s exposure. Data was collected at 105,000 x nominal magnification (0.835 Å/pixel at the specimen level), and nominal defocus range of -0.6 to -2.0 µm.

Image processing

The micrograph frames were aligned using MotionCorr2 (Zheng et al. 2017). The contrast transfer function (CTF) parameters were estimated with GCTF (Zhang 2016). Particles were picked in Cryosparc v2.15 using the apo eIF2B (EMDB: 23209) as a template. Particles were extracted using a 80-pixel box size (Scheres 2012), and classified in 2D (Punjani et al. 2017). Classes that showed clear protein features were selected and extracted for ab initio reconstruction followed by homogenous and heterogeneous refinement. Particles belonging to the best class were then re-extracted with a pixel size of 2.09 Å, and then subjected to nonuniform refinement, yielding a reconstruction of 4.25 Å. These particles were subjected to another round of heterogeneous refinement followed by nonuniform refinement to generate a consensus reconstruction consisting of the best particles. These particles were re-extracted at a pixel size of 0.835 Å. Then, CTF refinement was performed to correct for the per-particle CTF

as well as beam tilt. A final round of 2D classification followed by nonuniform refinement was performed to yield the final structure of 2.6 Å.

Atomic model building, refinement, and visualization

To build models for the eIF2B-NSs complex, the previously determined structures of the human eIF2B in its apo form (PDB ID: 7L70) was used as the starting model for the eIF2B part (Schoof et al. 2021). To build the NSs model, we first ran the structure prediction program RaptorX using the full-length NSs sequence (Xu, McPartlon, and Li 2021). The predicted structure is divided into two parts: the C-terminal domain predicted based on the structure of the RVFV NSs (PDB ID: 5OOO), and the N-terminal domain is predicted without a known PDB structure as a template (Barski et al. 2017). The predicted full-length structure was docked into the EM density corresponding to the NSs in UCSF Chimera (Pettersen et al. 2004), and then subjected to rigid body refinement in Phenix (Adams et al. 2010). The models were then manually adjusted in Coot (Emsley and Cowtan 2004) and then refined in phenix.real_space_refine (Adams et al. 2010) using global minimization, secondary structure restraints, Ramachandran restraints, and local grid search. Then iterative cycles of manual rebuilding in Coot and phenix.real_space_refine were performed. The final model statistics were tabulated using Molprobity (Chen et al. 2010). Distances were calculated from the atomic models using UCSF Chimera. Molecular graphics and analyses were performed with the UCSF Chimera package (Pettersen et al. 2004). UCSF Chimera is developed by the Resource for Biocomputing, Visualization, and Informatics and supported by NIGMS P41-GM103311. The atomic model is deposited in the PDB under accession code 7RLO. The EM map is deposited into EMDB under accession code EMD-24535.

References

Adams, P. D., P. V. Afonine, G. Bunkóczi, V. B. Chen, I. W. Davis, N. Echols, J. J. Headd, L. W. Hung, G. J. Kapral, R. W. Grosse-Kunstleve, A. J. McCoy, N. W. Moriarty, R. Oeffner, R. J. Read, D. C. Richardson, J. S. Richardson, T. C. Terwilliger, and P. H. Zwart. 2010. 'PHENIX: a comprehensive Python-based system for macromolecular structure solution', *Acta Crystallogr D Biol Crystallogr*, 66: 213-21.

Adomavicius, T., M. Guaita, Y. Zhou, M. D. Jennings, Z. Latif, A. M. Roseman, and G. D. Pavitt. 2019. 'The structural basis of translational control by eIF2 phosphorylation', *Nat Commun*, 10: 2136.

Atkin, J. D., M. A. Farg, A. K. Walker, C. McLean, D. Tomas, and M. K. Horne. 2008. 'Endoplasmic reticulum stress and induction of the unfolded protein response in human sporadic amyotrophic lateral sclerosis', *Neurobiol Dis*, 30: 400-7.

Barski, M., B. Brennan, O. K. Miller, J. A. Potter, S. Vijayakrishnan, D. Bhella, J. H. Naismith, R. M. Elliott, and U. Schwarz-Linek. 2017. 'Rift Valley fever phlebovirus NSs protein core domain structure suggests molecular basis for nuclear filaments', *Elife*, 6.

Billecocq, A., M. Spiegel, P. Vialat, A. Kohl, F. Weber, M. Bouloy, and O. Haller. 2004. 'NSs protein of Rift Valley fever virus blocks interferon production by inhibiting host gene transcription', *J Virol*, 78: 9798-806.

Bogorad, A. M., K. Y. Lin, and A. Marintchev. 2018. 'eIF2B Mechanisms of Action and Regulation: A Thermodynamic View', *Biochemistry*, 57: 1426-35.

Chen, V. B., W. B. Arendall, 3rd, J. J. Headd, D. A. Keedy, R. M. Immormino, G. J. Kapral, L. W. Murray, J. S. Richardson, and D. C. Richardson. 2010. 'MolProbity: all-atom structure validation for macromolecular crystallography', *Acta Crystallogr D Biol Crystallogr*, 66: 12-21.

Chou, A., K. Krukowski, T. Jopson, P. J. Zhu, M. Costa-Mattioli, P. Walter, and S. Rosi. 2017. 'Inhibition of the integrated stress response reverses cognitive deficits after traumatic brain injury', *Proc Natl Acad Sci U S A*, 114: E6420-e26.

Costa-Mattioli, M., and P. Walter. 2020. 'The integrated stress response: From mechanism to disease', *Science*, 368.

Craddock, B. L., and C. G. Proud. 1996. 'The alpha-subunit of the mammalian guanine nucleotide-exchange factor eIF-2B is essential for catalytic activity in vitro', *Biochem Biophys Res Commun*, 220: 843-7.

Cyr, N., C. de la Fuente, L. Lecoq, I. Guendel, P. R. Chabot, K. Kehn-Hall, and J. G. Omichinski. 2015. 'A ΩXaV motif in the Rift Valley fever virus NSs protein is essential for degrading p62, forming nuclear filaments and virulence', *Proc Natl Acad Sci U S A*, 112: 6021-6.

Dey, M., C. Cao, A. C. Dar, T. Tamura, K. Ozato, F. Sicheri, and T. E. Dever. 2005. 'Mechanistic link between PKR dimerization, autophosphorylation, and eIF2alpha substrate recognition', *Cell*, 122: 901-13.

Emsley, P., and K. Cowtan. 2004. 'Coot: model-building tools for molecular graphics', *Acta Crystallogr D Biol Crystallogr*, 60: 2126-32.

Galabru, J., and A. Hovanessian. 1987. 'Autophosphorylation of the protein kinase dependent on double-stranded RNA', *J Biol Chem*, 262: 15538-44.

Gale, M. J., Jr., M. J. Korth, and M. G. Katze. 1998. 'Repression of the PKR protein kinase by the hepatitis C virus NS5A protein: a potential mechanism of interferon resistance', *Clin Diagn Virol*, 10: 157-62.

Gordiyenko, Y., J. L. Llácer, and V. Ramakrishnan. 2019. 'Structural basis for the inhibition of translation through eIF2α phosphorylation', *Nat Commun*, 10: 2640.

Guo, X., G. Aviles, Y. Liu, R. Tian, B. A. Unger, Y. T. Lin, A. P. Wiita, K. Xu, M. A. Correia, and M. Kampmann. 2020. 'Mitochondrial stress is relayed to the cytosol by an OMA1-DELE1-HRI pathway', *Nature*, 579: 427-32.

Habjan, M., A. Pichlmair, R. M. Elliott, A. K. Overby, T. Glatter, M. Gstaiger, G. Superti-Furga, H. Unger, and F. Weber. 2009. 'NSs protein of rift valley fever virus induces the specific degradation of the double-stranded RNA-dependent protein kinase', *J Virol*, 83: 4365-75.

Harrington, K., D. J. Freeman, B. Kelly, J. Harper, and J. C. Soria. 2019. 'Optimizing oncolytic virotherapy in cancer treatment', *Nat Rev Drug Discov*, 18: 689-706.

Hedil, M., and R. Kormelink. 2016. 'Viral RNA Silencing Suppression: The Enigma of Bunyavirus NSs Proteins', *Viruses*, 8.

Hinnebusch, A. G. 2005. 'Translational regulation of GCN4 and the general amino acid control of yeast', *Annu Rev Microbiol*, 59: 407-50.

Kashiwagi, K., M. Takahashi, M. Nishimoto, T. B. Hiyama, T. Higo, T. Umehara, K. Sakamoto, T. Ito, and S. Yokoyama. 2016. 'Crystal structure of eukaryotic translation initiation factor 2B', *Nature*, 531: 122-5.

Kashiwagi, K., T. Yokoyama, M. Nishimoto, M. Takahashi, A. Sakamoto, M. Yonemochi, M. Shirouzu, and T. Ito. 2019. 'Structural basis for eIF2B inhibition in integrated stress response', *Science*, 364: 495-99.

Kashiwagi, Kazuhiro, Yuichi Shichino, Tatsuya Osaki, Ayako Sakamoto, Madoka Nishimoto, Mari Takahashi, Mari Mito, Friedemann Weber, Yoshiho Ikeuchi, Shintaro Iwasaki, and Takuhiro Ito. 2021. 'eIF2B-capturing viral protein NSs suppresses the integrated stress response', *bioRxiv*: 2021.06.07.447466.

Kawagishi-Kobayashi, M., J. B. Silverman, T. L. Ung, and T. E. Dever. 1997. 'Regulation of the protein kinase PKR by the vaccinia virus pseudosubstrate inhibitor K3L is dependent on residues conserved between the K3L protein and the PKR substrate eIF2alpha', *Mol Cell Biol*, 17: 4146-58.

Kelly, E., and S. J. Russell. 2007. 'History of oncolytic viruses: genesis to genetic engineering', *Mol Ther*, 15: 651-9.

Kenner, L. R., A. A. Anand, H. C. Nguyen, A. G. Myasnikov, C. J. Klose, L. A. McGeever, J. C. Tsai, L. E. Miller-Vedam, P. Walter, and A. Frost. 2019. 'eIF2B-catalyzed nucleotide exchange and phosphoregulation by the integrated stress response', *Science*, 364: 491-95.

Kobilka, B. K. 2011. 'Structural insights into adrenergic receptor function and pharmacology', *Trends Pharmacol Sci*, 32: 213-8.

Li, Y., C. Zhang, X. Chen, J. Yu, Y. Wang, Y. Yang, M. Du, H. Jin, Y. Ma, B. He, and Y. Cao. 2011. 'ICP34.5 protein of herpes simplex virus facilitates the initiation of protein translation by bridging eukaryotic initiation factor 2alpha (eIF2alpha) and protein phosphatase 1', *J Biol Chem*, 286: 24785-92.

Ly, H. J., and T. Ikegami. 2016. 'Rift Valley fever virus NSs protein functions and the similarity to other bunyavirus NSs proteins', *Virol J*, 13: 118.

Ma, T., M. A. Trinh, A. J. Wexler, C. Bourbon, E. Gatti, P. Pierre, D. R. Cavener, and E. Klann. 2013. 'Suppression of eIF2α kinases alleviates Alzheimer's disease-related plasticity and memory deficits', *Nat Neurosci*, 16: 1299-305.

Mastronarde, David N. 2003. 'SerialEM: A Program for Automated Tilt Series Acquisition on Tecnai Microscopes Using Prediction of Specimen Position', *Microscopy and Microanalysis*, 9: 1182-83.

Nguyen, H. G., C. S. Conn, Y. Kye, L. Xue, C. M. Forester, J. E. Cowan, A. C. Hsieh, J. T. Cunningham, C. Truillet, F. Tameire, M. J. Evans, C. P. Evans, J. C. Yang, B. Hann, C. Koumenis, P. Walter, P. R. Carroll, and D. Ruggero. 2018. 'Development of a stress response therapy targeting aggressive prostate cancer', *Sci Transl Med*, 10.

Pelner, Louis, George A. Fowler, and Helen C. Nauts. 1958. 'EFFECT OF CONCURRENT INFECTIONS AND THEIR TOXINS ON THE COURSE OF LEUKEMIA', *Acta Medica Scandinavica*, 162: 5-24.

Pettersen, E. F., T. D. Goddard, C. C. Huang, G. S. Couch, D. M. Greenblatt, E. C. Meng, and T. E. Ferrin. 2004. 'UCSF Chimera--a visualization system for exploratory research and analysis', *J Comput Chem*, 25: 1605-12.

Punjani, A., J. L. Rubinstein, D. J. Fleet, and M. A. Brubaker. 2017. 'cryoSPARC: algorithms for rapid unsupervised cryo-EM structure determination', *Nat Methods*, 14: 290-96.

Rabouw, H. H., L. J. Visser, T. C. Passchier, M. A. Langereis, F. Liu, P. Giansanti, A. L. W. van Vliet, J. G. Dekker, S. G. van der Grein, J. G. Saucedo, A. A. Anand, M. E. Trellet, Amjj Bonvin, P.

Walter, A. J. R. Heck, R. J. de Groot, and F. J. M. van Kuppeveld. 2020. 'Inhibition of the integrated stress response by viral proteins that block p-eIF2-eIF2B association', *Nat Microbiol*, 5: 1361-73.

Rasmussen, S. G., H. J. Choi, J. J. Fung, E. Pardon, P. Casarosa, P. S. Chae, B. T. Devree, D. M. Rosenbaum, F. S. Thian, T. S. Kobilka, A. Schnapp, I. Konetzki, R. K. Sunahara, S. H. Gellman, A. Pautsch, J. Steyaert, W. I. Weis, and B. K. Kobilka. 2011. 'Structure of a nanobody-stabilized active state of the β(2) adrenoceptor', *Nature*, 469: 175-80.

Rasmussen, S. G., B. T. DeVree, Y. Zou, A. C. Kruse, K. Y. Chung, T. S. Kobilka, F. S. Thian, P. S. Chae, E. Pardon, D. Calinski, J. M. Mathiesen, S. T. Shah, J. A. Lyons, M. Caffrey, S. H. Gellman, J. Steyaert, G. Skiniotis, W. I. Weis, R. K. Sunahara, and B. K. Kobilka. 2011. 'Crystal structure of the β2 adrenergic receptor-Gs protein complex', *Nature*, 477: 549-55.

Rosário-Ferreira, N., A. J. Preto, R. Melo, I. S. Moreira, and R. M. M. Brito. 2020. 'The Central Role of Non-Structural Protein 1 (NS1) in Influenza Biology and Infection', *Int J Mol Sci*, 21.

Russell, S. J. 2002. 'RNA viruses as virotherapy agents', *Cancer Gene Ther*, 9: 961-6.

Sall, A. A., A. Zanotto P. M. de, H. G. Zeller, J. P. Digoutte, Y. Thiongane, and M. Bouloy. 1997. 'Variability of the NS(S) protein among Rift Valley fever virus isolates', *J Gen Virol*, 78 (Pt 11): 2853-8.

Scheres, S. H. 2012. 'RELION: implementation of a Bayesian approach to cryo-EM structure determination', *J Struct Biol*, 180: 519-30.

Schoof, M., M. Boone, L. Wang, R. Lawrence, A. Frost, and P. Walter. 2021. 'eIF2B conformation and assembly state regulate the integrated stress response', *Elife*, 10.

Shi, Y., K. M. Vattem, R. Sood, J. An, J. Liang, L. Stramm, and R. C. Wek. 1998. 'Identification and characterization of pancreatic eukaryotic initiation factor 2 alpha-subunit kinase, PEK, involved in translational control', *Mol Cell Biol*, 18: 7499-509.

Sidrauski, C., D. Acosta-Alvear, A. Khoutorsky, P. Vedantham, B. R. Hearn, H. Li, K. Gamache, C. M. Gallagher, K. K. Ang, C. Wilson, V. Okreglak, A. Ashkenazi, B. Hann, K. Nader, M. R. Arkin, A. R. Renslo, N. Sonenberg, and P. Walter. 2013. 'Pharmacological brake-release of mRNA translation enhances cognitive memory', *Elife*, 2: e00498.

Soday, Lior, Yongxu Lu, Jonas D. Albarnaz, Colin T. R. Davies, Robin Antrobus, Geoffrey L. Smith, and Michael P. Weekes. 2019. 'Quantitative Temporal Proteomic Analysis of Vaccinia Virus Infection Reveals Regulation of Histone Deacetylases by an Interferon Antagonist', *Cell Reports*, 27: 1920-33.e7.

Stasakova, J., B. Ferko, C. Kittel, S. Sereinig, J. Romanova, H. Katinger, and A. Egorov. 2005. 'Influenza A mutant viruses with altered NS1 protein function provoke caspase-1 activation in primary human macrophages, resulting in fast apoptosis and release of high levels of interleukins 1beta and 18', *J Gen Virol*, 86: 185-95.

Staus, D. P., R. T. Strachan, A. Manglik, B. Pani, A. W. Kahsai, T. H. Kim, L. M. Wingler, S. Ahn, A. Chatterjee, A. Masoudi, A. C. Kruse, E. Pardon, J. Steyaert, W. I. Weis, R. S. Prosser, B. K. Kobilka, T. Costa, and R. J. Lefkowitz. 2016. 'Allosteric nanobodies reveal the dynamic range and diverse mechanisms of G-protein-coupled receptor activation', *Nature*, 535: 448-52.

Tsai, J. C., L. E. Miller-Vedam, A. A. Anand, P. Jaishankar, H. C. Nguyen, A. R. Renslo, A. Frost, and P. Walter. 2018. 'Structure of the nucleotide exchange factor eIF2B reveals mechanism of memory-enhancing molecule', *Science*, 359.

Weekes, Michael P, Peter Tomasec, Edward L Huttlin, Ceri A Fielding, David Nusinow, Richard J Stanton, Eddie C Y. Wang, Rebecca Aicheler, Isa Murrell, Gavin W G. Wilkinson, Paul J Lehner, and Steven P Gygi. 2014. 'Quantitative Temporal Viromics: An Approach to Investigate Host-Pathogen Interaction', *Cell*, 157: 1460-72.

Wong, Y. L., L. LeBon, R. Edalji, H. B. Lim, C. Sun, and C. Sidrauski. 2018. 'The small molecule ISRIB rescues the stability and activity of Vanishing White Matter Disease eIF2B mutant complexes', *Elife*, 7.

Wortham, N. C., M. Martinez, Y. Gordiyenko, C. V. Robinson, and C. G. Proud. 2014. 'Analysis of the subunit organization of the eIF2B complex reveals new insights into its structure and regulation', *Faseb j*, 28: 2225-37.

Wuerth, J. D., M. Habjan, M. Kainulainen, B. Berisha, D. Bertheloot, G. Superti-Furga, A. Pichlmair, and F. Weber. 2020. 'eIF2B as a Target for Viral Evasion of PKR-Mediated Translation Inhibition', *mBio*, 11.

Wuerth, J. D., M. Habjan, J. Wulle, G. Superti-Furga, A. Pichlmair, and F. Weber. 2018. 'NSs Protein of Sandfly Fever Sicilian Phlebovirus Counteracts Interferon (IFN) Induction by Masking the DNA-Binding Domain of IFN Regulatory Factor 3', *J Virol*, 92.

Wuerth, J. D., and F. Weber. 2016. 'Phleboviruses and the Type I Interferon Response', *Viruses*, 8.

Xu, Jinbo, Matthew McPartlon, and Jin Li. 2021. 'Improved protein structure prediction by deep learning irrespective of co-evolution information', *Nature Machine Intelligence*.

Zhang, K. 2016. 'Gctf: Real-time CTF determination and correction', *J Struct Biol*, 193: 1-12.

Zheng, S. Q., E. Palovcak, J. P. Armache, K. A. Verba, Y. Cheng, and D. A. Agard. 2017. 'MotionCor2: anisotropic correction of beam-induced motion for improved cryo-electron microscopy', *Nat Methods*, 14: 331-32.

Zhu, P. J., S. Khatiwada, Y. Cui, L. C. Reineke, S. W. Dooling, J. J. Kim, W. Li, P. Walter, and M. Costa-Mattioli. 2019. 'Activation of the ISR mediates the behavioral and neurophysiological abnormalities in Down syndrome', *Science*, 366: 843-49.

Zyryanova, A. F., K. Kashiwagi, C. Rato, H. P. Harding, A. Crespillo-Casado, L. A. Perera, A. Sakamoto, M. Nishimoto, M. Yonemochi, M. Shirouzu, T. Ito, and D. Ron. 2021. 'ISRIB Blunts the Integrated Stress Response by Allosterically Antagonising the Inhibitory Effect of Phosphorylated eIF2 on eIF2B', *Mol Cell*, 81: 88-103.e6.

Zyryanova, A. F., F. Weis, A. Faille, A. A. Alard, A. Crespillo-Casado, Y. Sekine, H. P. Harding, F. Allen, L. Parts, C. Fromont, P. M. Fischer, A. J. Warren, and D. Ron. 2018. 'Binding of ISRIB reveals a regulatory site in the nucleotide exchange factor eIF2B', *Science*, 359: 1533-36.

Chapter 3

A point mutation in the nucleotide exchange factor eIF2B constitutively activates the integrated stress response by allosteric modulation

Summary

In eukaryotic cells, stressors reprogram the cellular proteome by activating the integrated stress response (ISR). In its canonical form, stress-sensing kinases phosphorylate the eukaryotic translation initiation factor eIF2 (eIF2-P), which ultimately leads to reduced levels of ternary complex required for initiation of mRNA translation. Previously we showed that translational control is primarily exerted through a conformational switch in eIF2's nucleotide exchange factor, eIF2B, which shifts from its active A-State conformation to its inhibited I-State conformation upon eIF2-P binding, resulting in reduced nucleotide exchange on eIF2 (Schoof et al. 2021). Here, we show functionally and structurally how a single histidine to aspartate point mutation in eIF2B's β subunit (H160D) mimics the effects of eIF2-P binding by promoting an I-State like conformation, resulting in eIF2-P independent activation of the ISR. These findings corroborate our previously proposed A/I-State model of allosteric ISR regulation.

Introduction

Coping with cellular stressors, manifesting as either intrinsic cues or environmental insults, is key to preserving cellular and organismal health. One strategy is to activate the integrated stress response (ISR), a conserved eukaryotic signaling network that reprograms translation towards damage mitigation and recovery, or apoptosis when stress is irremediable (Costa-Mattioli and Walter 2020). The ISR integrates diverse stresses through at least four stress-sensing kinases – PERK, HRI, GCN2, PKR, and perhaps MARK2, via phosphorylation of a single serine, S51 of the α subunit of the translation initiation factor eIF2 (Hinnebusch 2005; Guo et al. 2020; Dey et al. 2005; Shi et al. 1998; Lu et al. 2021). eIF2 is a central player in translation initiation, mediating start codon recognition on the mRNA and delivery of the initiator methionine tRNA. Phosphorylation of eIF2 disrupts this process and leads to a precipitous drop in global protein synthesis. Conversely, the translation of a subset of stress-responsive mRNAs, such as *ATF4*, generally repressed by the presence of 5' UTR upstream open reading frames (uORFs), is induced (Harding et al. 2000). The alternative translation program that is thus set in motion drives the cell's return to homeostasis. While the ISR is inherently cytoprotective, its dysregulation has been documented in multiple disease states. Specifically, the ISR has been linked to neurodegenerative diseases (Ma et al. 2013), brain-injury induced dementia (Chou et al. 2017; Sen et al. 2017), aging (Krukowski et al. 2020), diabetes (Abdulkarim et al. 2015; Harding et al. 2001), and cancer (Nguyen et al. 2018; Koromilas et al. 1992).

Mechanistically, it is the level of ternary complex (TC) that determines the regulation of translation initiation by the ISR. The TC consists of eIF2 (heterotrimer composed of an α, β, and γ subunit, containing a GTPase domain in its γ subunit), the initiator tRNA loaded with methionine (Met-tRNA^{i}), and GTP (Algire, Maag, and Lorsch 2005). Once the TC associates with the 40S ribosomal subunit, additional initiation factors, and the 5' methylguanine cap of the

mRNA, the pre-initiation complex scans the mRNA for a start codon. Recognition of the start codon leads to GTP hydrolysis and triggers the release of eIF2 now bound to GDP (as reviewed in (Hinnebusch, Ivanov, and Sonenberg 2016)). The large ribosomal subunit joins and the assembled 80S ribosome proceeds with elongation of the polypeptide chain. Crucially, for every round of cap-dependent translation initiation, eIF2 requires GDP-to-GTP exchange, catalyzed by its dedicated guanine nucleotide exchange factor (GEF), eIF2B. Failure to complete this step impacts the cellular concentration of the TC, which impairs the translation of most mRNAs. At the same time, lower TC concentrations can induce the translation of specific stress-responsive ORFs, some of which are regulated by uORFs (Harding et al. 2000; Lu, Harding, and Ron 2004; Vattem and Wek 2004). Thus, the ISR regulates translation by tuning the available pool of TC.

Given its central role in controlling TC levels and mRNA translation, many eIF2B mutations result in an aberrant ISR and severe disease, such as Vanishing White Matter Disease (VWMD) (Leegwater et al. 2001; van der Knaap et al. 2002). Molecularly, eIF2B is a large, heterodecameric complex composed of two copies each of an α, β, γ, δ, and ε subunit (Kashiwagi et al. 2016; Tsai et al. 2018; Zyryanova et al. 2018; Wortham et al. 2014; Gordiyenko et al. 2014). It has long been established that phosphorylation of eIF2 (eIF2-P) converts eIF2 from an eIF2B substrate to an eIF2B inhibitor, leading to a reduction in GEF activity and ISR activation (Siekierka, Mauser, and Ochoa 1982; Matts, Levin, and London 1983; Konieczny and Safer 1983; Salimans et al. 1984; Rowlands, Panniers, and Henshaw 1988). Earlier atomic-resolution snapshots of the eIF2-bound and eIF2-P-bound human eIF2B complexes suggested steric hindrance to be the predominant mechanism for inhibition, given the proposed overlap of binding sites (Kenner et al. 2019; Kashiwagi et al. 2019; Adomavicius et al. 2019; Gordiyenko, Llácer, and Ramakrishnan 2019; Bogorad, Lin, and Marintchev 2017). However, we and others recently discovered that binding of the inhibitor eIF2-P to a distinct binding site — located on the face of the eIF2B complex opposite of the substrate-binding site

— allosterically switches eIF2B from its active ‘A-State’ (which can readily engage eIF2 and catalyze nucleotide exchange) to an inhibited ‘I-State’ (Schoof et al. 2021; Zyryanova et al. 2021).

The multi-subunit composition of eIF2B also lends itself to regulation at the level of complex assembly. The decameric holoenzyme is built from two eIF2Bβγδε tetramers and one eIF2Bα_2 dimer (Tsai et al. 2018). The eIF2Bε subunit harbors the enzyme’s catalytic center but only contains a small part of the binding surface of eIF2. Two of four interfaces between eIF2 and eIF2B (IF1 and IF2) reside in eIF2Bε. Thus, poor substrate-binding severely limits eIF2Bε’s catalytic activity. The substrate-binding surface is increased upon addition of more subunits (a third interface, IF3 in eIF2Bβ). Yet, even when embedded in the eIF2Bβγδε tetramer subcomplex, the specific enzyme activity (k_{cat}/K_M) of eIF2Bε is ~100-fold lower compared to the fully assembled eIF2B$(\alpha\beta\gamma\delta\varepsilon)_2$ decamer (tetramer k_{cat}/K_M = 0.07 $min^{-1}\mu M^{-1}$, decamer k_{cat}/K_M = 7.24 $min^{-1}\mu M^{-1}$), in which the substrate-interacting surface is further extended by bridging the two-fold symmetric interface formed between the two tetrameric subcomplexes (a fourth interface, IF4 in eIF2Bδ’) (Schoof et al. 2021; Kenner et al. 2019; Kashiwagi et al. 2019).

eIF2B activity, assembly-state, and conformation are all modulated by the ISR inhibitor, ISRIB. This small molecule binds in a deep groove spanning across the symmetry interface of the two eIF2B tetramers and enhances its GEF activity (Sekine et al. 2015; Sidrauski et al. 2013; Sidrauski et al. 2015; Tsai et al. 2018; Zyryanova et al. 2018). ISRIB exerts these effects by acting on both eIF2B assembly and conformation (Schoof et al. 2021). When eIF2Bα_2 levels are low, pharmacological dimerization of tetrameric subcomplexes by ISRIB rescues eIF2B function (Schoof et al. 2021). When eIF2Bα_2 levels are saturating and eIF2B decamers are therefore fully assembled, ISRIB binding stabilizes eIF2B in the active ‘A-State’, reducing its affinity for the inhibitor eIF2-P (Schoof et al. 2021; Zyryanova et al. 2021).

Given these insights, we here revisit previous observations concerning a histidine to aspartate point mutation in eIF2Bβ (βH160D) that straddles the junction of the β-β'and β-δ' interface (the ' notation indicates that the subunit resides in the adjoining, second tetramer in eIF2B) (Tsai et al. 2018). We formerly observed that this missense mutation blocked ISRIB-driven assembly of eIF2B tetramers into octamers *in vitro*, underlining the importance of the H160 residue in stabilizing the octamer (Tsai et al. 2018). However, whether the change to aspartic acid, predicted to be repulsed by the apposed D450 in δ', precluded decameric assembly or activated the ISR, remained unknown. Here, we show that the βH160D mutation does not affect decameric holoenzyme formation when all subunits are present. However, this mutation stabilizes eIF2B in an inactive conformation reminiscent of the inhibited 'I-State', normally promoted by eIF2-P binding. Concomitantly, cells with this mutation constitutively activate the ISR, even in absence of stress and eIF2-P. These results validate the A/I-State model of eIF2B and ISR regulation by showing that a conformational change in eIF2B is sufficient to impair its enzymatic function and activate the ISR.

Results

The eIF2B βH160D mutation does not block decamer assembly *in vitro*

To dissect the regulation of eIF2B assembly and activity, we purified human eIF2Bβδγε tetramers both with and without the βH160D mutation (Figure 3.1 – figure supplement 1). We first performed sedimentation velocity experiments to assess the assembly state of eIF2B. Consistent with our previous observations (Tsai et al. 2018), WT eIF2B tetramers readily assembled into octamers in the presence of ISRIB, whereas βH160D tetramers did not (Figure 3.1A-B). In contrast, we found that assembly into the fully decameric holoenzyme by addition of the eIF2Bα_2 dimer was not compromised (Figure 3.1C-D).

To confirm that the βH160D mutation does not impair decamer assembly, we utilized an orthogonal, previously established Förster resonance energy transfer (FRET) assay to assess eIF2B's assembly state (Schoof et al. 2021). In this system, the C-terminus of eIF2Bβ is tagged with mNeonGreen as the FRET donor and the C-terminus of eIF2Bδ with mScarlet-i as the FRET acceptor. Both WT and βH160D tetramers were purified with these fluorescent tags (and hereafter are denoted eIF2Bβδγε-F). A titration of ISRIB readily assembled WT eIF2Bβδγε-F tetramers into octamers (EC_{50} = 170 ± 25 nM) but did not promote βH160D eIF2Bβδγε-F assembly into octamers , even at the highest concentrations tested (Figure 3.1E). By contrast and in agreement with the analytical ultracentrifugation data in Figure 3.1A-D, titration of eIF2Bα_2 assembled both WT (EC_{50} = 29 ± 3 nM) and βH160D (EC_{50} = 33 ± 3 nM) eIF2Bβδγε-F tetramers into decamers with comparable efficiency (Figure 3.1F).

The eIF2B βH160D decamer is impaired in GEF activity

These properties are reminiscent of eIF2B's behavior in the presence of its inhibitor eIF2-P. In the inhibited decameric conformation (I-State) induced by eIF2-P binding, ISRIB binding to

eIF2B is impaired (Schoof et al. 2021; Zyryanova et al. 2021). We next asked whether the βH160D mutation impacts eIF2B's enzymatic activity. To this end, we monitored eIF2B's GEF activity using a BODIPY-FL-GDP nucleotide exchange assay. Both WT and βH160D tetramers exhibited comparably low enzymatic activity. The activity was robustly enhanced in WT octamers assembled from tetramers with ISRIB but, as expected, ISRIB had no impact on βH160D tetramer activity (Figure 3.2A). Intriguingly, βH160D decamers were less active than WT decamers ($t_{1/2}$ = 23.6 ± 0.8 min vs. 9.3 ± 1.0 min, respectively) (Figure 3.2B). To understand how the βH160D mutation impaired eIF2B's GEF activity, we next performed nucleotide exchange assays of WT and βH160D decamer activity at varying eIF2 concentrations. We measured the initial velocity of these reactions and fit the data to the Michaelis-Menten model of enzyme kinetics to determine the V_{max} and the K_M of the nucleotide loading reaction (Figure 3.2C, Figure 3.2 – figure supplement 1). The V_{max} (and consequently also the k_{cat}) was significantly diminished by ~three-fold for βH160D decamers when compared to WT decamers (WT V_{max} = 1.86 ± 0.13 pmol / min; βH160D V_{max} = 0.66 ± 0.03 pmol / min, two-sided t-test p = 0.0045) suggesting that the βH160D mutation limits the intrinsic enzymatic activity of eIF2B (Figure 3.2D). In contrast, we could not detect a significant difference in measured K_M (WT K_M = 0.36 ± 0.06 μM, βH160D K_M = 0.19 ± 0.04 μM, two-sided t-test p = 0.07).

Impaired substrate binding in decameric eIF2B results from the βH160D mutation

The absence of a clear difference in K_M was puzzling, as we suspected the βH160D decamer to adopt an inhibited conformation reminiscent of the I-State, where both intrinsic enzymatic activity and binding of eIF2 are compromised (Schoof et al. 2021). We therefore directly assessed binding affinities of eIF2B's substrate (eIF2) and inhibitor (eIF2-P), using surface plasmon resonance (SPR) to measure binding to WT decamers, βH160D decamers, and WT tetramers. eIF2 association with WT and βH160D decamers was monophasic, but dissociation was notably biphasic irrespective of eIF2 concentration, with a fast phase and a slow phase

(Figure 3.3A-B). Although the rate constants k_a, $k_{d\ fast}$, and $k_{d\ slow}$ were broadly comparable, eIF2 binding to WT vs. βH160D decamers differed in the percentage of fast phase dissociation events (WT = 29%; βH160D = 67%) (Figure 3.3A-B, Table 3.1). Thus, a larger fraction of substrate molecules dissociates rapidly from βH160D compared to WT decamers. Since the K_M is only equal to the K_D when the dissociation rate constant k_d is much larger than the k_{cat}, this measurement can resolve the paradox of a similar K_M but different dissociation behavior.

In contrast to eIF2's interaction with decameric eIF2B, binding to WT tetramers could be modeled using one phase association and dissociation. Indeed, eIF2 dissociation from tetrameric eIF2B can be thought of as being 100% fast phase as the dissociation constant was indistinguishable from the fast phase dissociation constant for both WT and βH160D (k_d = 0.12 s^{-1}) (Figure 3.3C). The fraction of eIF2 molecules that dissociate from decamers with fast phase kinetics may therefore only be engaging eIF2B through interfaces 1-3 (interfaces 1 and 2 in eIF2Bε and interface 3 in eIF2Bβ). In contrast, the eIF2 molecules that dissociate with slow phase kinetics may additionally contact interface 4 in eIF2Bδ', reaching across the central symmetry interface (Schoof et al. 2021). This explanation would be consistent with identical dissociation constants for tetramer dissociation and fast phase dissociation from the decamers. For eIF2-binding, the βH160D decamers can therefore be thought of as more like isolated tetramers. That is, eIF2 readily associates but then is likely to dissociate too rapidly for efficient catalysis.

We further interrogated the biphasic dissociation behavior of eIF2 from WT and βH160D decamers by varying the time allowed for eIF2 binding to eIF2B (Figure 3.3 – figure supplement 1A-B). For both WT and βH160D we observed an exponential decrease in the percentage of fast phase dissociation, which within two minutes plateaued at ~11% fast phase dissociation for eIF2 binding to WT and at ~55% fast phase dissociation for eIF2 binding to βH160D decamers

(Figure 3.3G). These data argue that at equilibrium the fast phase dissociation plays a small part in the engagement between eIF2 and WT eIF2B but plays a significant part in substrate engagement with βH160D decamers. This kinetic behavior can be explained by a model proposing stepwise engagement between eIF2 and eIF2B in a process that first entails engagement of 3 interaction interfaces (IF1-3), followed by a second, slower step that engages the fourth interaction interface (IF4; Figure 3.3H-I). In this model, the βH160D mutation does not affect the on/off rates of eIF2 engagement with eIF2B through interfaces 1-3, but slows the on-rate (k_2 in Figure 3.3H-I) of converting from 3 interface engagement to 4 interface engagement. Such a mechanism can explain the accumulation of the "intermediate" fast phase dissociation species.

We next assessed eIF2-P binding to the immobilized eIF2B species. For both WT and βH160D decamer binding, this interaction could be modeled using one-phase association and dissociation kinetics. The overall affinity of eIF2-P for both species was largely comparable (WT K_D = 14 nM; βH160D K_D = 8.1 nM) (Figure 3.3D-E). As expected owing to the absence of the dimeric eIF2Bα subunit, which constitutes part of the eIF2-P binding site, we observed no noticeable eIF2-P binding to WT tetramers (Figure 3.3F).

From these results, we conclude that the βH160D decamer shares a number of properties with the eIF2-P-bound decamer: 1) reduced intrinsic GEF activity, 2) impaired substrate binding, and 3) insensitivity to ISRIB. Owing to these similarities, we wondered whether the βH160D mutation mimics eIF2-P binding and shifts eIF2B into an I-State or 'I-State like' conformation. To assess this notion, we determined the structure of the βH160D eIF2B decamer using single-particle cryo-EM.

The βH160D mutation shifts eIF2B into an inhibited conformation

We prepared the βH160D decamer by combining βH160D tetramers and eIF2Bα_2, and subjected the sample to cryo-EM imaging. After 2D and 3D classification, we generated a single consensus structure of the βH160D decamer at 2.8 Å resolution (Table 3.2, Figure 3.4 – figure supplement 1) with most side chains clearly resolved (Figure 3.4A, Figure 3.4 – figure supplement 1E-F). This map allowed us to build an atomic model of how the βH160D substitution alters the conformation of the eIF2B decamer. By superimposing the βH160D decamer structure and our previously published A-State structure (eIF2B-eIF2 complex, PDB ID: 6O81), we observed a significant difference in their overall architecture: the two tetramer halves of the βH160D decamer underwent a rocking motion that changed the angle between them by approximately 3.5° (Figure 3.4B). This rocking motion repositions the two tetramer halves in an orientation comparable to the I-State structure (eIF2B-eIF2αP complex, PDB ID: 6O9Z), although not reaching the 6° angle observed for the eIF2-P-inhibited decamer (Figure 3.4 – figure supplement 2). To further understand how the βH160D mutation affects the conformation and dynamics of the decamer, we performed additional cryo-EM analysis of both the WT and the βH160D decamer particles (Figure 3.4 – figure supplement 3-5). We found the following: 1) in both the WT and the mutant, the two tetrameric halves can undergo rocking motions around the central axis; 2) the βH160D mutation shifts the mean conformation of the decamer towards the I-State; and 3) the βH160D dataset likely represents particles that follow a continuous conformation distribution, rather than a mixture of distinct A and I-State populations. These observations validate our hypothesis that the βH160D mutation shifts eIF2B from the active conformation towards an inhibited conformation.

We next examined changes to the ISRIB-binding pocket. Comparing the βH160D decamer to A-State (eIF2-bound eIF2B) and I-State (eIF2α-P-bound eIF2B) structures, we noticed that its ISRIB binding pocket was 3.3 Å wider in its long dimension than that of the A-State (Figure

3.5A), again reminiscent of the I-State (Figure 3.5C). The widening of the binding pocket can explain why ISRIB fails to assemble βH160D tetramers into octamers or affect GEF activity.

Zooming in on the tetramer-tetramer interface, we examined the interactions in the WT eIF2B A-State decamer that stabilize the dimerization interface (Figure 3.5B). In the WT decamer, βH160 forms a π-π stacking interaction with δ'F452, which is lost in the βH160D eIF2B decamer and leads to the retraction of the short loop bearing this residue (Figure 3.5B and Figure 3.5 – figure supplement 1). Other interactions in WT decamer include an ionic interaction between β'R228 and δ'D450, as well as a cation-π interaction between β'R228 and δ'F452. In the βH160D decamer, β'R228 repositions itself within the network of three negative charges (βE163, βD160 and δ'D450) and one aromatic amino acid (δ'F452) to reach a new stable state locally. The loop movement caused by the mutation propagates across the entire tetramer, resulting in the rocking motion observed in Figure 3.4B. This explains how the βH160D amino acid change in eIF2B remodels the dimerization interface to widen the ISRIB binding pocket and induce an I-State like conformation.

To further examine the long-range effect of this interface mutation, we looked at the critical interfaces for substrate (eIF2) binding provided by eIF2Bβ and eIF2Bδ. An overlay of the βH160D decamer structure with the eIF2B-eIF2 complex structure revealed that the substrate eIF2α binding pocket was widened by 2.9 Å (Figure 3.5F). As established before (Schoof et al. 2021), a similar pocket widening is observed in the I-State structure of eIF2B (2.6 Å induced by eIF2α-P binding). This widening is predicted to prevent eIF2 from properly engaging the fourth binding site on eIF2Bδ' and hence turns the decameric eIF2B into conjoined tetramers such that only three of the four eIF2-eIF2B binding interfaces remain readily accessible to eIF2 binding. Our structural observations, therefore, explain the decrease in eIF2 binding and reduction in GEF activity of the βH160D decamer. The remaining portion of slow phase dissociation of eIF2

from βH160D decamers, though, indicates that engagement with all 4 interfaces, while disfavored, is not impossible as is the case with the pure tetrameric species). By contrast, the inhibitor (eIF2α-P) binding site (Figure 3.5G) was not changed significantly compared to the eIF2B-eIF2α-P complex structure. This observation is consistent with the similar binding affinities measured for eIF2-P towards the βH160D decamer and the WT decamer. We conclude that the βH160D mutation shifts the eIF2B decamer into a conformation closely resembling the I-State.

eIF2B βH160D mutation leads to stress-independent ISR activation

Given that the eIF2B βH160D mutation biases eIF2B's conformation towards an I-State like conformation, reducing its GEF activity, we predicted that expression of eIF2B βH160D in cells would lead to constitutive ISR activation. To test this notion, we introduced the βH160D mutation into the genome of HEK293FTR cells by editing the endogenous eIF2Bβ gene (*EIF2B2*) (Figure 3.6 – figure supplement 1A). Using CRISPR/Cas9 technology, we obtained two such lines. One cell line yielded a homozygous clone in which all alleles were edited (line βH160D #1) (Figure 3.6 – figure supplement 1B-C). The other was a heterozygous clone containing one edited allele while the remaining alleles were knocked out through CRISPR/Cas9-induced frameshift mutations (line βH160D #2). Critically, both βH160D cell lines showed eIF2Bβ and eIF2Bε protein levels comparable to the unedited parental cells, demonstrating that the mutation does not destabilize eIF2Bβ or other complex members and that compensatory mechanisms must normalize the gene dosage imbalance in clone #2 (Figure 3.6A) (Wortham et al. 2016). We observed constitutive, low-level activation of the ISR in both clones, exemplified by elevated levels of ATF4 protein in the absence of stress (Figure 3.6A, lanes 5 and 9 vs lane 1). ATF4 induction was still responsive to induced stress with thapsigargin (lanes 7 and 11) but could not be alleviated by ISRIB treatment in the βH160D lines, both in the absence or presence of stressor (Figure 3.6A). ATF4 is translationally upregulated during the

ISR and, accordingly, ATF4 mRNA levels remained unchanged between WT and the two βH160D clones (Figure 3.6B). However, as expected, key ATF4 transcriptional targets (such as *DDIT3, ASNS, and CARS*) were upregulated in βH160D cells, confirming that increased ATF4 mRNA translation leads to production of active ATF4, which in turn activates transcription of its downstream stress-responsive genes (Figure 3.6B).

The second hallmark of an active ISR is the general inhibition of translation initiation and, hence, a reduction in protein synthesis. To monitor protein synthesis, we treated WT and βH160D cells with puromycin and assessed puromycin incorporation in nascent polypeptide chains by immunoblotting. Both βH160D cell lines displayed significantly reduced levels of basal protein synthesis (βH160D #1 cells: 47 ± 9.0%; βH160D #2 cells: 69% ± 7.3%, both compared to WT), again consistent with constitutive activation of the ISR (Figure 3.6C, Figure 3.6 – figure supplement 2). WT and βH160D cells did not differ in eIF2α phosphorylation levels, underlining the observation that the impairment of eIF2B GEF activity caused by this mutation is sufficient to induce a constitutive ISR (Figure 3.6C, Figure 3.6 – figure supplement 3A-B).

Phenotypically, the constitutive ISR activation was accompanied by slow cell growth: cell doubling time increased from 25.7 ± 3.6 h for WT cells to 38.4 ± 3.5 h for βH160D (#1) cells and could not be rescued by ISRIB treatment (Figure 3.6D, Figure 3.6 – figure supplement 3C) .

Discussion

Here, we show that a single engineered H to D mutation in eIF2Bβ alters the conformation of the eIF2B decamer, resulting in altered dissociation kinetics of substrate eIF2, a ~three-fold reduction of intrinsic enzymatic activity, and resistance to ISRIB rescue. In cells, this hypomorphic mutation culminates in a constitutively activated low-level ISR. The structural, biochemical, and cellular changes resulting from the βH160D mutation are evocative of the Inhibitor (eIF2-P) bound state of eIF2B ('I-State'). In conjunction with our prior assessment of changes in eIF2B induced by eIF2α-P binding, these orthogonal data underscore how the conformational changes brought about by eIF2α-P binding govern ISR activation (A/I-State model) and that even the presence of eIF2α-P is dispensable as long as an I-State or I-State like conformation is maintained.

eIF2B is a far more dynamic complex than we realized just a year ago. Small molecules (ISRIB and its derivatives), the natural substrate (eIF2), and viral proteins (SFSV NSs) can stabilize eIF2B in its active A-State (Kashiwagi et al. 2021; Schoof, Wang, et al. 2021; Schoof et al. 2021; Zyryanova et al. 2021). Conversely, binding of the inhibitor (eIF2-P) can compete with these molecules by shifting the decamer to the inhibited I-State (Schoof et al. 2021; Zyryanova et al. 2021). Although the conformational displacements induced by βH160D are in many aspects similar to those of the eIF2-P bound I-State when compared to the A-State, they are not identical. While the cryo-EM data show a comparable widening of the eIF2α binding pocket, the movement of the β-solenoid in eIF2Bε is less pronounced in βH160D decamers than in the eIF2-P bound I-State (Figure 3.4 – figure supplement 2), likely because the rocking motion induced by βH160D originates near the ISRIB pocket, not from the eIF2-P binding site. In addition, despite extensive classification calculations, we did not recover single-particle images of the βH160D complex belonging to the A-State, arguing against the idea that the βH160D structure is a mixture of A-State and I-State structures. The βH160D decamer rather represents

a continuous distribution of conformations with a more restricted range of motion compared to the WT decamer, and for which the average converges to an I-State like model. Hence, acknowledging both similarities and differences to the I-State, we refer to the conformation induced by βH160D as 'I-State like'.

The conformational changes brought about by eIF2-P binding result in a specific enzymatic activity (quantified in the specificity constant k_{cat}/K_M) that is approximately 2 orders of magnitude reduced from that of the A-State (Schoof et al. 2021). By comparison, the βH160D mutation causes the specificity constant to drop by only ~2 fold (Figure 3.2). Nevertheless, despite the comparatively small change in eIF2B activity, the mutation induces constitutive ISR activation, suggesting that cells are sensitive to small fluctuations in eIF2B GEF activity. These numbers also tell us that there is still potential for more robust ISR activation. Indeed, treating βH160D cells with relatively low amounts (10 nM) of an eIF2-P inducing stressor like thapsigargin further enhances ATF4 translation (Figure 3.6A). The latter result also suggests that the mutation is compatible with even more potent inhibition mediated by eIF2-P binding. This conclusion is further supported by our 3D reconstructions and the SPR studies, which show that the βH160D mutation does not appreciably affect eIF2-P binding.

We demonstrate that both intrinsic enzymatic activity and substrate (eIF2) binding are affected in the I-State like βH160D decamer. It remains unclear how the conformational changes in either this structure or that in the eIF2-P bound I-State (Schoof et al. 2021) engender a reduced k_{cat}, especially given that βH160 is located far from the catalytic center. Non-ideal positioning of substrate molecules that still engage an I-State or I-State like decamer may explain the reduced rate of nucleotide exchange. Further speculation regarding the mechanism is limited by a lack of structural data for certain critical regions. The eIF2Bε catalytic domain is absent from all but the substrate (eIF2) bound structures. The eIF2Bε linker, a known regulatory region connecting the

catalytic domain to the core of eIF2Bε, is similarly unresolved, as are the poorly understood C-terminal solenoid “ear domains” of eIF2Bγ (Welsh and Proud 1993). The conformation and positioning of these and other regions may be affected during the ISR and play roles in regulation of eIF2B’s activity that warrant further examination. With the recent discovery that eIF2B can directly read out and respond to sugar phosphate levels, there may be a host of functions and mechanisms of regulation for eIF2B still to be uncovered (Hao et al. 2021).

Our SPR data (Figure 3.3) demonstrate that the effects of the βH160D mutation on substrate (eIF2) binding result from changes to the relative proportion of rapidly dissociating eIF2 molecules. Substrate association, however, remains unaffected. The biphasic dissociation behavior, usually observed for multivalent ligands due to avidity effects, is not entirely unexpected. Substrate-bound structures of eIF2B decamer previously revealed four binding interfaces (IF1-IF4) between eIF2 and eIF2B. Hence, it is possible that stochastic partial binding occurs for a fraction of substrate molecules when the IF4 interface is too distant from IF3 for both to be engaged by eIF2. eIF2α-P binding (or the βH160D mutation) pulls IF4 away from IF3, increasing the probability of this partially engaged binding mode, thus reducing the substrate binding affinity. Notably, though, the biphasic dissociation is not observed for inhibitor (eIF2-P) binding, where both association and dissociation can be fit to monophasic models. This observation suggests greater conformational flexibility along the combinatorial eIF2 binding surfaces than along the eIF2-P binding surfaces.

The βH160 residue is highly conserved amongst eukaryotes. To date, no variation has been reported at this position in the human genome. However, the mechanism by which the βH160D mutation impacts eIF2B activity raises the possibility that certain VWMD mutations may likewise compromise eIF2B function through alteration of conformational state. The disease-associated βE213G mutation (ClinVar VCV000004336), for example, localized near the ISRIB pocket and

far away from the catalytic center, reportedly does not affect complex association but substantially reduces GEF activity (Li et al. 2004). Understanding the precise mechanism of eIF2B inactivation in individual VWMD patients may be critical for patient stratification and proper treatment. Although ISRIB is unable to rescue the βH160D defect, it is plausible that other analogs (or molecules acting at a different site) with higher affinities than ISRIB may be able to overcome the charge repulsion and restore the A-State conformation, demonstrating the importance of continued endeavors to uncover molecules and strategies to inhibit or activate the ISR orthogonally.

Figures

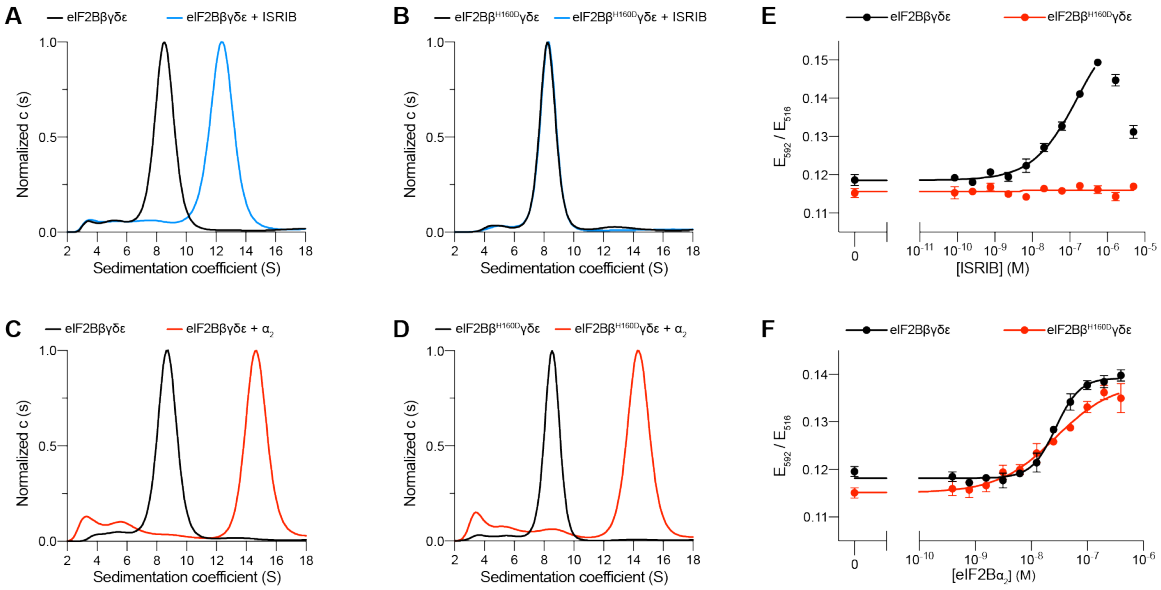

Figure 3.1: The eIF2B βH160D mutation prevents octamer assembly but not decamer assembly.
(A-D) Characterization by analytical ultracentrifugation (sedimentation velocity) of (A) 500 nM eIF2Bβδγε +/- 1 μM ISRIB, (B) 500 nM eIF2Bβ^{H160D}δγε +/- 1 μM ISRIB, (C) 500 nM eIF2Bβδγε +/- 500 nM eIF2Bα_2, and (D) 500 nM eIF2Bβ^{H160D}δγε +/- 500 nM eIF2Bα_2. The eIF2Bβδγε tetramer sediments with a sedimentation coefficient of ~8 S, the eIF2B$(\beta\delta\gamma\varepsilon)_2$ octamer at ~12 S, and the eIF2B$(\alpha\beta\delta\gamma\varepsilon)_2$ decamer at ~14 S. **(E-F)** FRET signal (E_{592}/E_{516}) measured after 1 h of eIF2Bβδγε-F tetramers incubation with (E) ISRIB or (F) eIF2Bα_2. For assembly by ISRIB, WT EC_{50} = 170 ± 25 nM. For assembly by eIF2Bα_2, WT EC_{50} = 29 ± 3 nM and βH160D EC_{50} = 33 ± 3 nM. WT and βH160D eIF2Bβδγε-F tetramers at 50 nM throughout. For (E-F), representative replicate averaging four technical replicates are shown. Biological replicates: n = 3. All error bars and '±' designations are s.e.m.

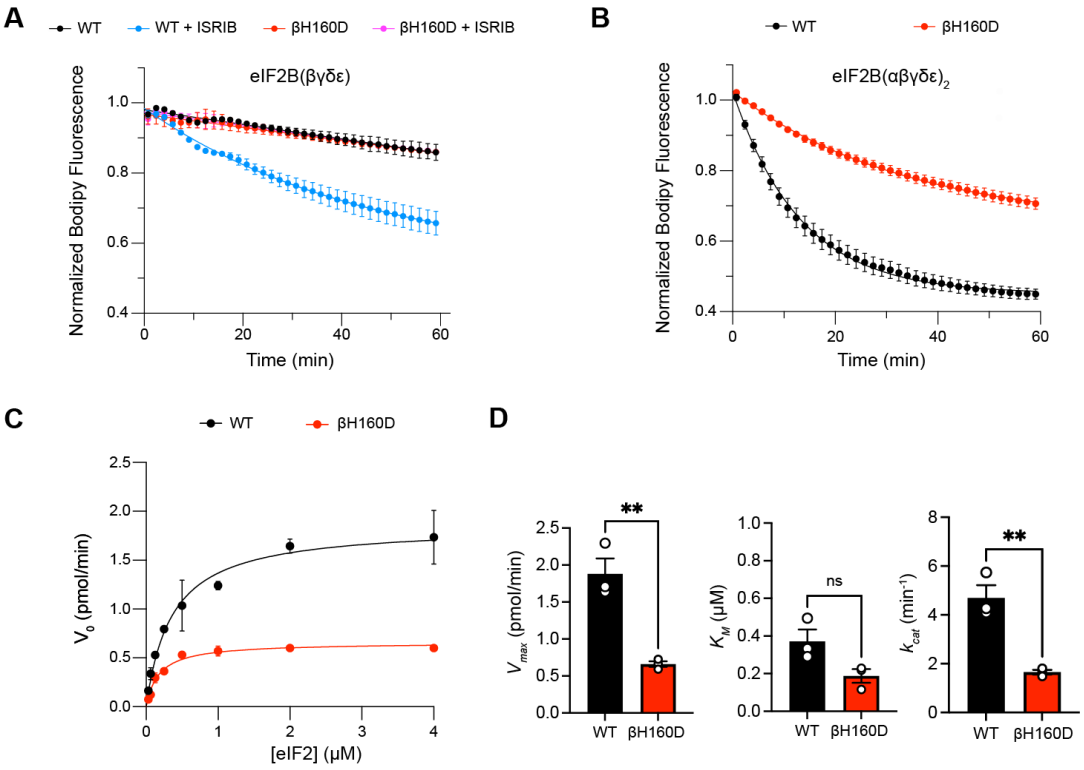

Figure 3.2: The βH160D mutation impairs nucleotide exchange by the eIF2B holoenzyme. (**A-B**) GEF activity of eIF2B as assessed by BODIPY-FL-GDP exchange on eIF2 using (A) eIF2B tetramer (100 nM) and (B) eIF2B decamer (10 nM). For (A), ISRIB only stimulates eIF2B guanine nucleotide exchange (GEF) activity for the WT tetramer ($t_{1/2}$ = 31.1 ±1.47 min). In (B), the βH160D decamer has lower GEF activity ($t_{1/2}$ = 23.57 ± 0.82 min) than WT decamer ($t_{1/2}$ = 9.28 ± 0.96 min)). (**C**) Michaelis-Menten fit of the initial velocity of eIF2B-catalyzed nucleotide exchange as a function of eIF2 concentration (10 nM eIF2B decamer throughout). **(D)** Kinetic parameters of the Michaelis-Menten fit. βH160D decamers have ~3-fold reduced intrinsic enzymatic activity (WT V_{max} = 1.86 ± 0.13 pmol/min; βH160D V_{max} = 0.66 ± 0.03 pmol/min; two-sided t-test p = 0.0045) and turnover number (WT k_{cat} = 4.70 ± 0.52 min^{-1}; βH160D k_{cat} = 1.65 ± 0.10 min^{-1}; two-sided t-test p = 0.0045). The K_M is not significantly different (WT K_M = 0.36 μM ± 0.09 μM; βH160D K_M = 0.18 ± 0.03 μM; two-sided t-test p = 0.07). Biological replicates: n = 2 for (A), and n = 3 for (B-D). All error bars and '±' designations are s.e.m.

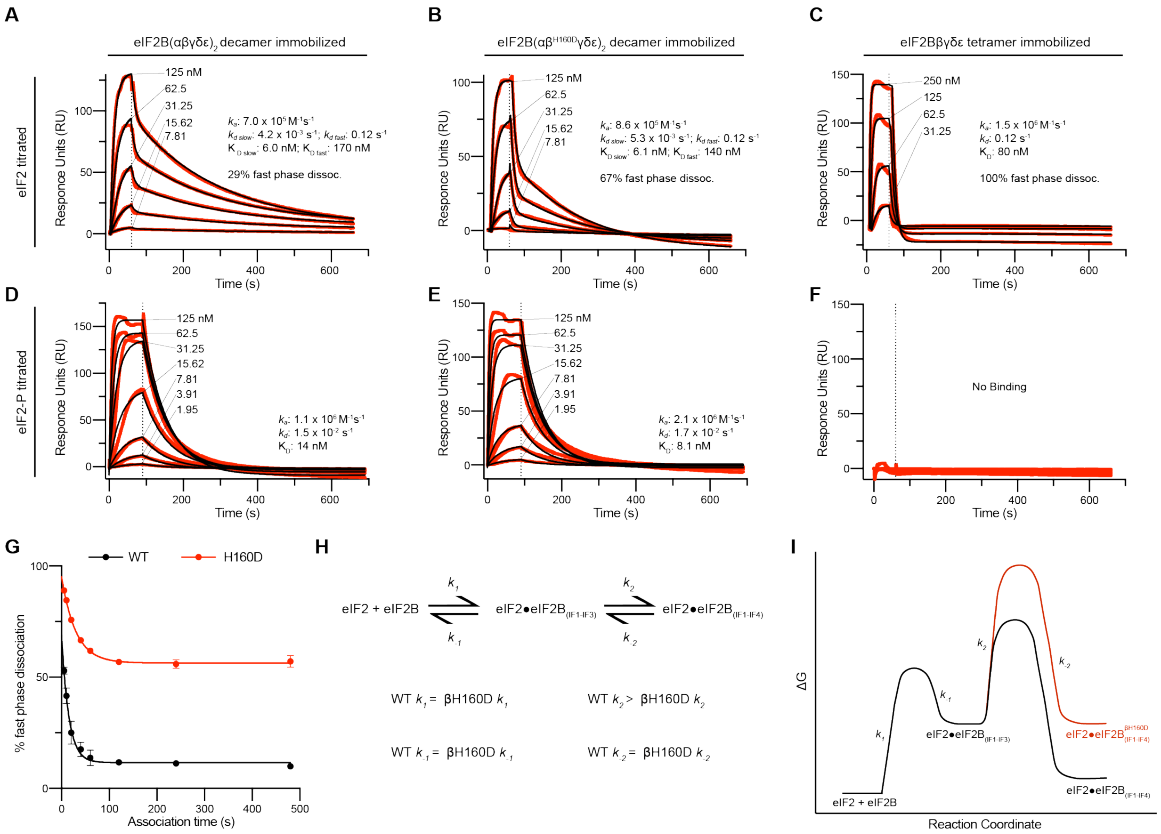

Figure 3.3: Substrate (eIF2) binding to eIF2B is compromised by the βH160D mutation. (**A-F**) SPR of immobilized (A and D) WT eIF2B decamer, (B and E) βH160D eIF2B decamer, and (C and F) WT eIF2B tetramer binding to 2-fold titrations of (A-C) eIF2 or (D-F) eIF2-P. For WT eIF2B decamer and βH160D eIF2B decamer, eIF2Bα was Avi-tagged and biotinylated. For WT eIF2B tetramer, eIF2Bβ was Avi-tagged and biotinylated. Binding was modeled as one-phase association for (A-E), two-phase dissociation for (A-B), and one-phase dissociation for (C-E). **(G)** SPR of immobilized WT eIF2B decamer and βH160D eIF2B decamer was performed with eIF2 at 62.5 nM throughout and varied association time from 5-480 s. The dissociation kinetics were then modeled (individual traces shown in Figure 3 – figure supplement 1) and from this data percent fast phase dissociation was plotted as a function of association time with a single exponential fit. WT $t_{1/2}$ = 10.4 s; βH160D $t_{1/2}$ = 20.7 s. Percent fast phase dissociation is always higher for βH160D decamers vs. WT decamers and reaches an equilibrium at ~55% fast phase dissociation for βH160D decamers and ~11% fast phase dissociation for WT decamers. **(H)** Model reaction scheme of eIF2 engagement with eIF2B. k_1, k_{-1}, and k_{-2} each are comparable for WT and βH160D decamers but WT k_2 > βH160D k_2. Based on the SPR data in Figure 3 A-C, k_1 ~ 7.0 x 10^5 $M^{-1}s^{-1}$ and k_{-1} ~ 0.12 s^{-1}. k_{-2} is calculated under the assumption that slow phase dissociation represents the combination of k_{-1} and k_{-2} dissociation. k_{-1} is fast phase dissociation, so k_{-1} = $k_{d\ fast}$. Hence from k_{-1} * k_{-2} = $k_{d\ slow}$ we get that 0.12 s^{-1} * k_{-2} = 5.3 x 10^{-3} s^{-1}. Therefore k_{-2} ~ 0.044 s^{-1}. **(I)** Free energy profile of eIF2 engagement with eIF2B either in the WT (black) or βH160D (black then red) context. Initial 3 interface engagement is energetically the same for either WT or βH160D, but engagement with the 4th interface is disfavored in the βH160D mutant. The free energy profile is drawn at sub saturating conditions. Given the percent fast phase vs slow phase dissociation at equilibrium in Figure 1G we know that for WT, [eIF2•eIF2B$_{(IF1-IF4)}$] / [eIF2•eIF2B$_{(IF1-IF3)}$] ~8 while for βH160D [eIF2•eIF2B$_{(IF1-IF4)}$] /

[eIF2•eIF2B$_{(IF1\text{-}IF3)}$] ~1. For (G), n = 3 biological replicates. All error bars and '±' designations are s.e.m.

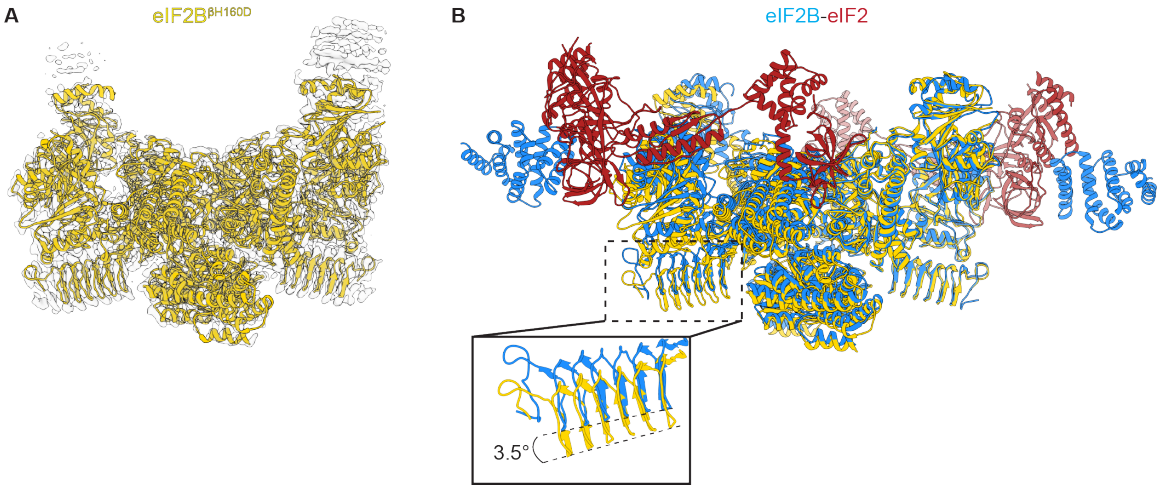

Figure 3.4: Overall architecture of eIF2B$^{\beta H160D}$.
(A) Atomic model of eIF2B$^{\beta H160D}$ decamer (yellow) superimposed into the cryo-EM map (grey), showing the overall structure of the molecule. **(B)** Overlay of the eIF2B$^{\beta H160D}$ structure to the eIF2B-eIF2 structure (PDB ID: 6O81) shows a 3.5° hinge movement between the two eIF2B halves. eIF2B$^{\beta H160D}$ is shown in gold; eIF2B in the eIF2B-eIF2 structure in blue; eIF2 in red.

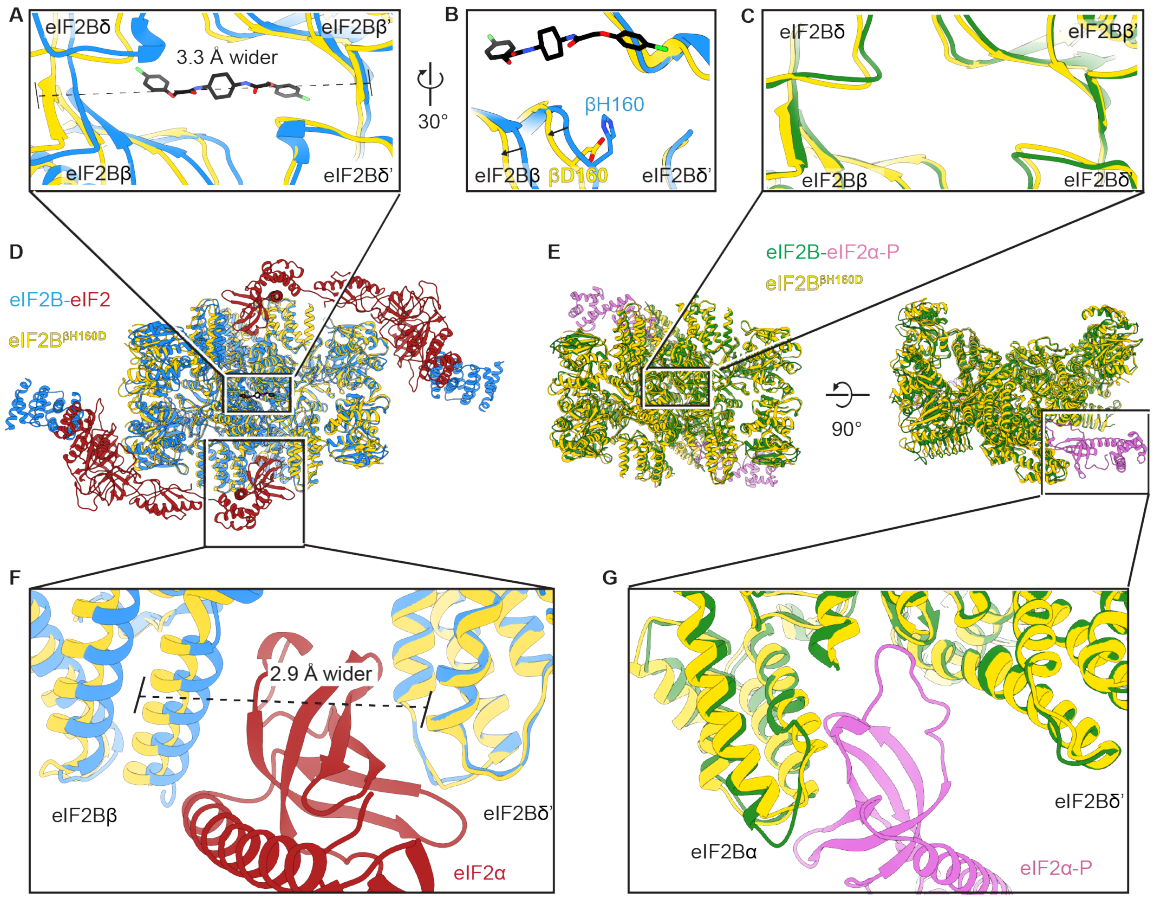

Figure 3.5: The βH160D mutation conformationally diminishes eIF2B activity. **(A)** Overlay of the eIF2B^{βH160D} structure to the eIF2B-eIF2 structure showing a ~ 3 Å lengthening of the ISRIB-binding pocket in the eIF2B^{βH160D} structure. The pocket lengthening is measured between eIF2Bδ and eIF2Bδ' L482; the 'prime' indicates the subunit of the opposing tetramer. ISRIB is shown in stick representation. **(B)** A rotated view of panel (A) showing that in the eIF2B^{βH160D} structure the loop bearing βD160 retracts from the opposite tetramer due loss of some attractive interactions (for details, see Figure 5 – figure supplement 1). **(C)** Overlay of the eIF2B^{βH160D} structure to the eIF2B-eIF2α-P structure showing the similar dimensions of the ISRIB binding pockets. **(D)** Zoom out of the overlay in panels (A), (B), and (F). **(E)** Zoom out of the overlay in panel (C) and (G). **(F)** Overlay of the eIF2-bound eIF2B to eIF2B^{βH160D} showing the 2.9 Å widening of the eIF2α binding pocket induced by the βH160D mutation. The pocket widening is measured between eIF2Bβ E139 and eIF2Bδ' R250. **(G)** Overlay of the eIF2α-P-bound eIF2B to eIF2B^{βH160D} showing the similar dimensions of the eIF2α-P binding pockets. Protein molecules are colored as in Figure 4. ISRIB is colored in CPK.

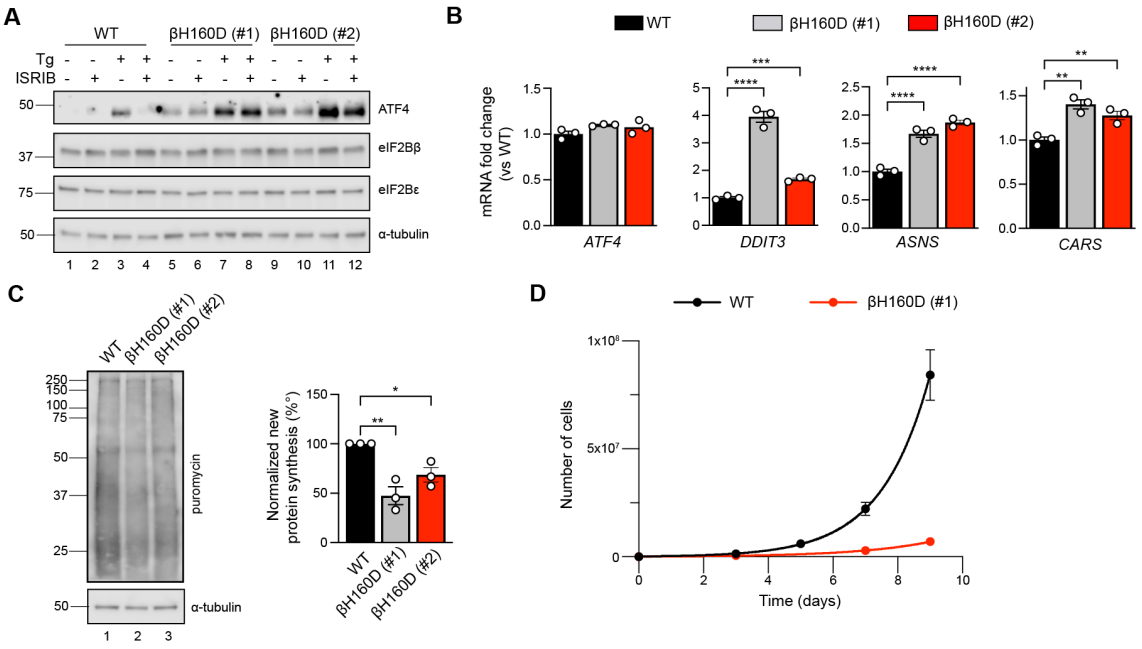

Figure 3.6: The βH160D mutation spontaneously activates the ISR in cells.
(**A**) Western blot of WT vs *EIF2B2*^{H160D} HEK293FTR cell lines (βH160D (#1) and βH160D (#2)) treated with and without stress (10 nM thapsigargin (Tg)) or ISRIB (200 nM) for 1 h. eIF2B subunit levels do not differ between cell lines. ATF4 is constitutively produced in the βH160D cell lines (lanes 5 and 9, compare to lane 1), and its induction is ISRIB-insensitive (lanes 6, 8, 10, 12, compare with lane 4). α-tubulin serves as a loading control. (**B**) RT-qPCR for *ATF4* and *ATF4* transcriptional targets in untreated WT vs. βH160D cell lines. Transcript levels were normalized to *GAPDH* signal and fold changes were calculated with WT level set to 1. While there is no difference in *ATF4* transcript level, the *ATF4* target genes *DDIT3* (CHOP), *ASNS,* and *CARS* are significantly transcriptionally upregulated in the βH160D lines (one-way ANOVA with Dunnett post-hoc tests). (**C**) Puromycin incorporation assay for new protein synthesis. Left panel: representative blot of cell lysates treated with a 10 min puromycin pulse and blotted for puromycin (new protein synthesis) or tubulin (loading control). Right panel: quantification of puromycin incorporation. The puromycin signal is normalized to tubulin levels and set at 100% for WT. Both βH160D cells show a reduction of basal protein translation (one-way ANOVA with Dunnett post-hoc test, p = 0.0026 for WT vs βH160D (#1) and p = 0.0288 for WT vs βH160D (#2)). (**D**) Growth curves showing that βH160D cells grow slower than WT cells (WT doubling time = 25.7 h, s.e.m. = 3.6 h; βH160D doubling time = 38.4 h, s.e.m. = 3.5 h.
All error bars and '±' designations are s.e.m. For (B, D) n = 3 biological replicates. For (C), n = 3 biological replicates, each of which was the average of 3 technical replicate transfers.* p<0.05, **p<0.01, ***p<0.001, ****p<0.0001.

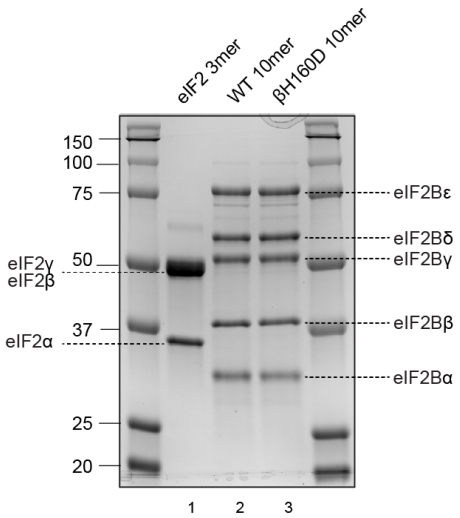

Figure 3.1 – figure supplement 1: Coomassie-stained gel of purified proteins used in this study.
Human eIF2 trimer was purified from mammalian cells (HEK293) (lane 1). WT and βH160D eIF2B decamers (lane 2 and 3, resp.) were assembled from their respective tetramer (eIF2Bβδγε) and α-dimer (eIF2Bα_2), both purified from *E. coli*.

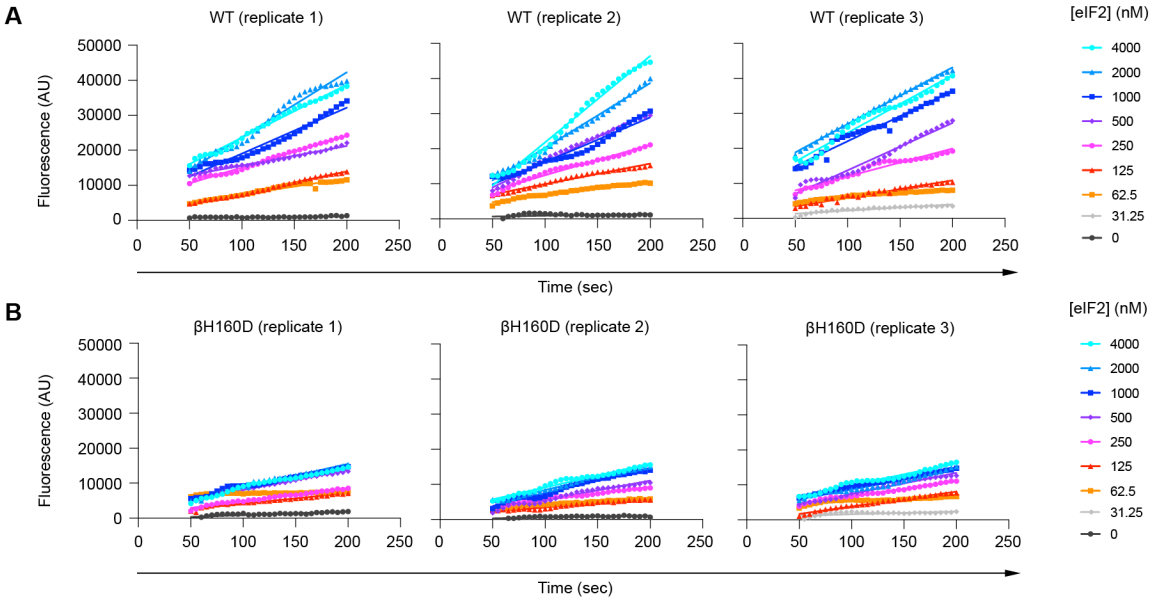

Figure 3.2 – figure supplement 1: The βH160D mutation decreases the initial velocity of eIF2B's guanine nucleotide exchange factor (GEF) activity.
BODIPY-FL-GDP loading onto the eIF2 substrate by (A) WT and (B) βH160D eIF2B decamer at varying eIF2 concentrations. Initial velocity was determined by a linear fit to timepoints acquired from 50 to 200 s after addition of eIF2B. Individual replicates are shown. AU = arbitrary units.

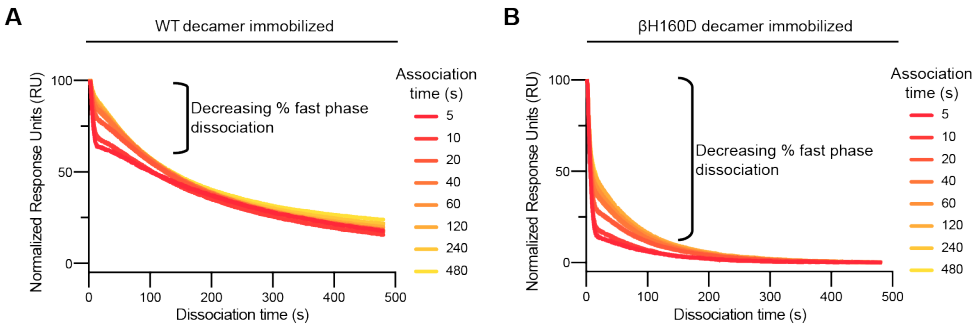

Figure 3.3 – figure supplement 1: The βH160D mutation increases the fraction of eIF2 molecules that bind and then dissociate with fast phase kinetics.
(**A-B**) Representative dissociation phase SPR traces for eIF2 binding to (A) WT eIF2B decamer or (B) βH160D eIF2B decamer after variable association times ranging from 5 to 480 s. Curves were normalized to maximal signal at the beginning of the dissociation phase. For (A-B), n = 3 biological replicates. All error bars and '±' designations are s.e.m.

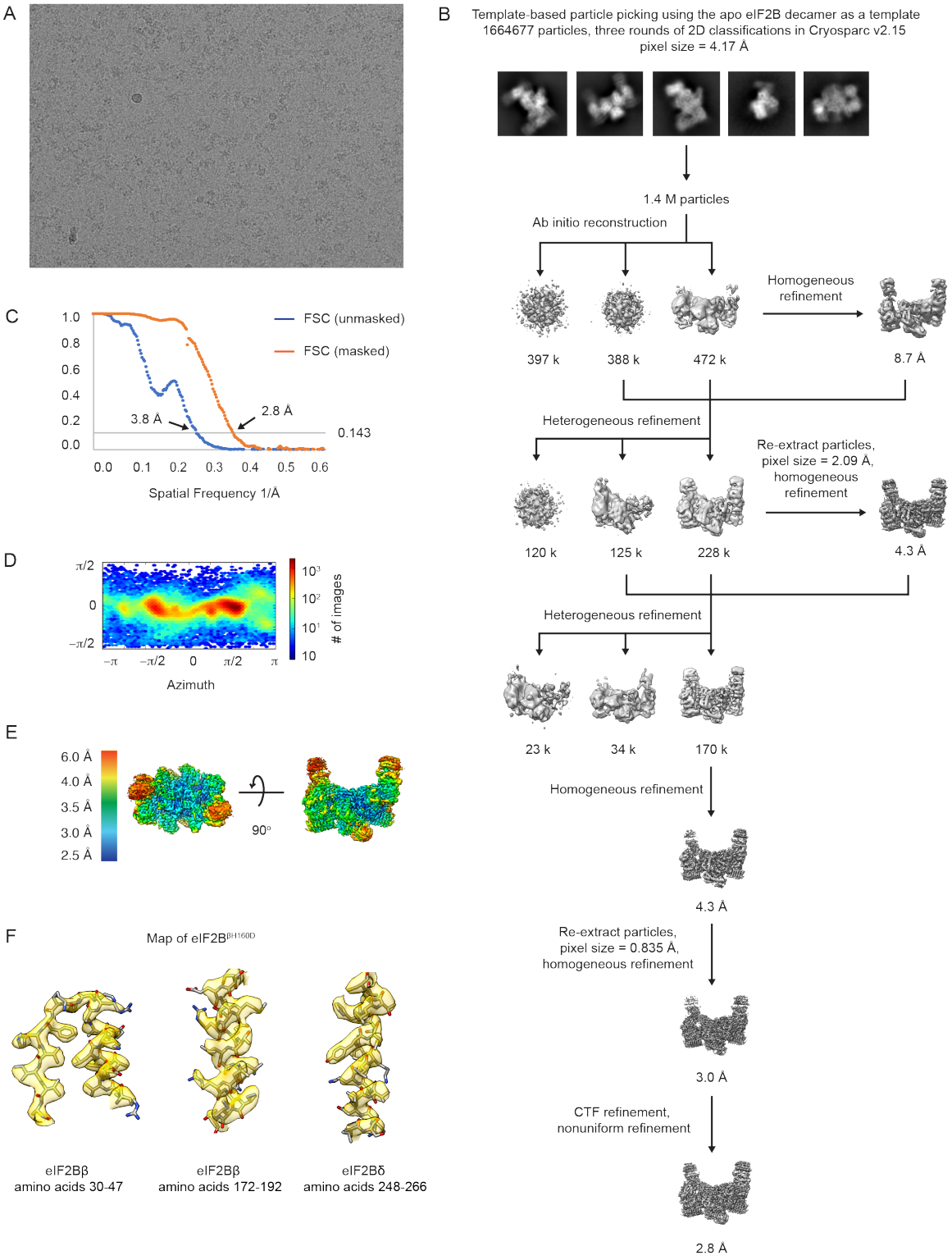

Figure 3.4 – figure supplement 1: Cryo-EM data analysis of the eIF2B^{βH160D} structure. (**A**) Representative micrograph showing the quality of data used for the final reconstruction of the eIF2B^{βH160D} structure. (**B**) Data processing scheme of the eIF2B^{βH160D} structure. (**C**) Fourier shell correlation (FSC) plots of the 3D reconstructions of eIF2B^{βH160D} unmasked (dark blue), masked (orange). (**D**) Orientation angle distribution of the eIF2B^{βH160D} reconstruction. (**E**) Local

resolution map of the eIF2B$^{\beta H160D}$ structure. (**F**) Electron microscopy maps of different regions of the eIF2B$^{\beta H160D}$ structure showing the quality of the data and the fit of the model.

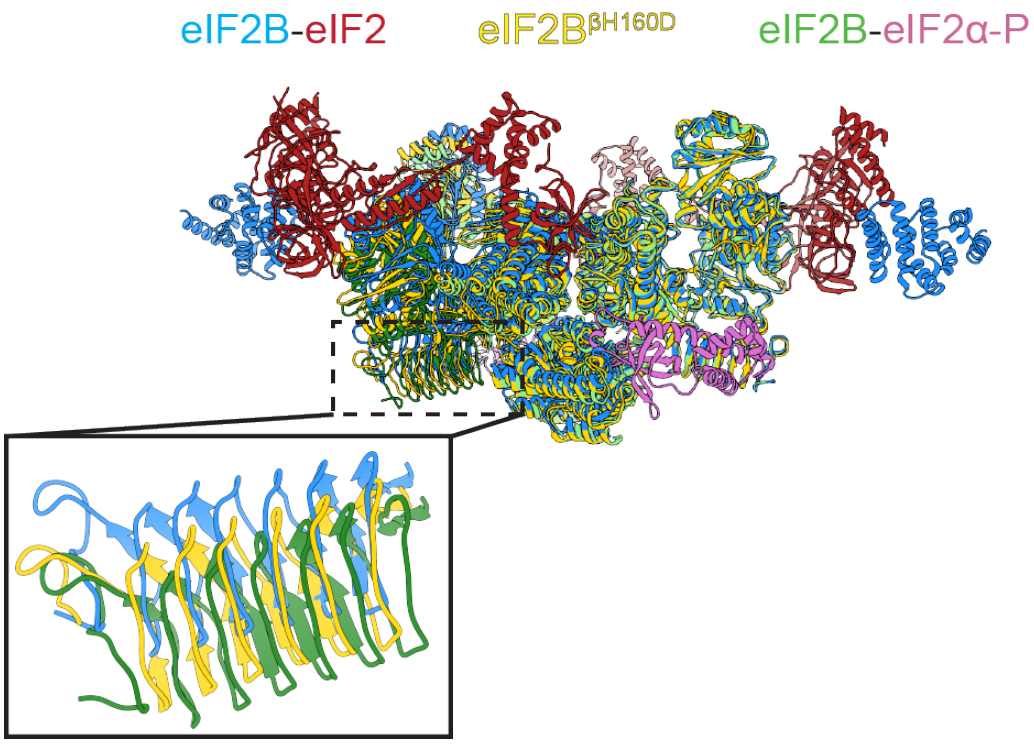

Figure 3.4 – figure supplement 2: Structure overlay of the A and I state models.
Overlay of the A-state model (eIF2-eIF2B complex, PDB ID: 6O81) (blue), the I-State model (eIF2α-P-eIF2B complex, PDB ID: 6O9Z) (green) and the I-State like model (eIF2B^{βH160D}) (yellow) showing the rocking motion between the two tetrameric halves. The inset shows a zoom-in view of the β-solenoid domain (residues 342 to 466) of eIF2Bε. Compared to the βH160D mutation, eIF2α-P binding causes a greater rocking motion in eIF2B.

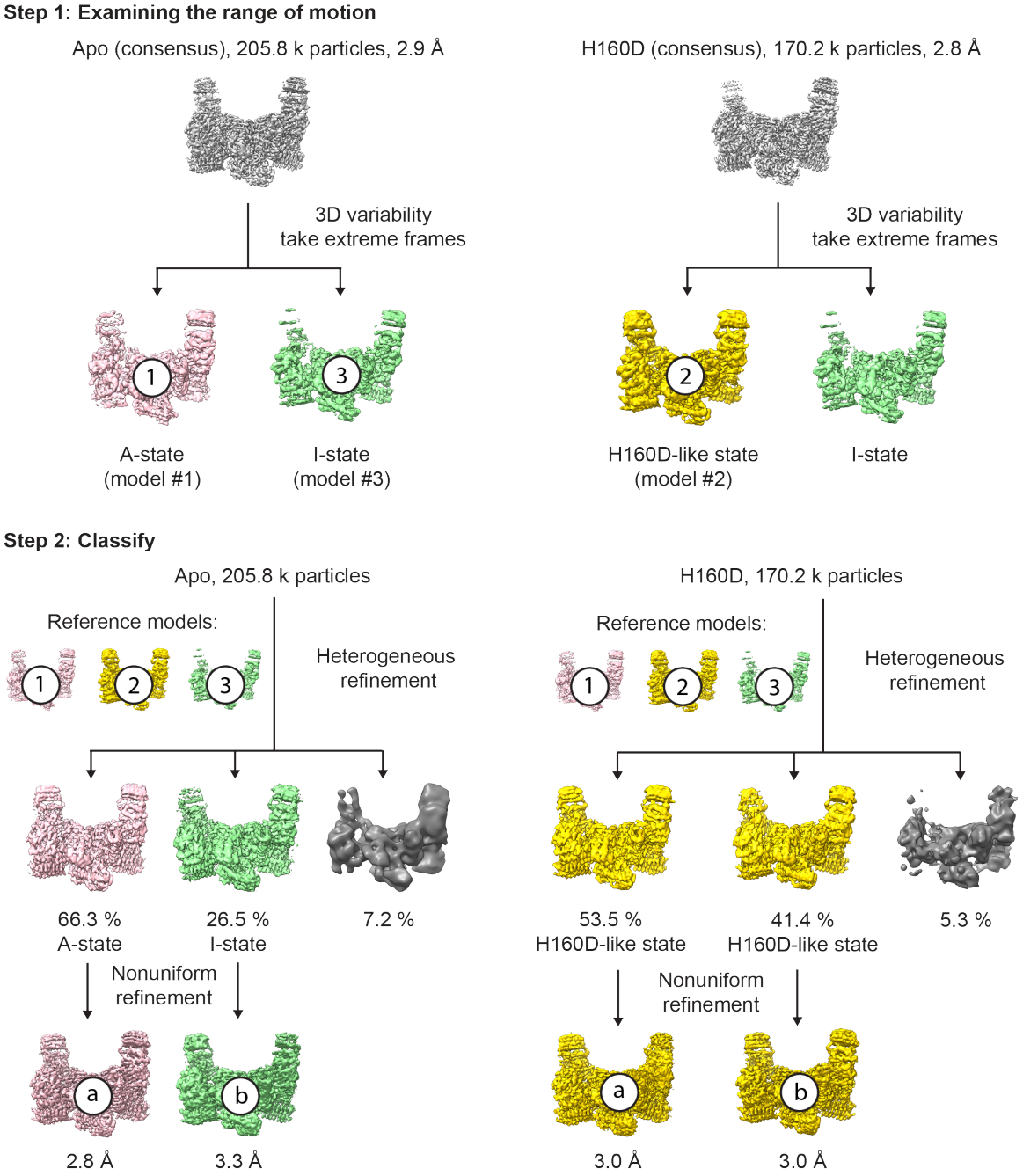

Figure 3.4 – figure supplement 3: Cryo-EM analysis of the conformation and dynamics of the WT decamer and the βH160D decamer – part 1.
To understand how the βH160D mutation affects the conformation and dynamics of the eIF2B decamer, a multi-step analysis of the cryo-EM data was performed to compare the WT apo eIF2B decamer (abbreviated as “apo”; particles are from the consensus apo eIF2B structure (Schoof et al. 2021)) to the βH160D decamer (abbreviated as “H160D”; particles are from the consensus H160D structure in the current study).

In **step 1**, we performed 3D variability analysis in cryoSPARC for the apo versus the H160D to examine the range of rocking motion between the two tetrameric halves. 20 frames were

generated for each structure to represent snapshots of the motion. The first and the last frames represent the two extreme positions of this rocking motion. In the apo structure, the molecule rocks between a state that is very close to the classic A-state (number 1 in the figure) and a classic I-state (number 3 in the figure). In the H160D structure, the molecule rocks between a state that is similar to the consensus H160D state (number 2 in the figure) and a state that is similar to the classic I-state (also similar to the I-state in the apo data). Therefore, H160D and apo both reach similar conformations on the side of the I-state, but apo has a wider range of motion compared to H160D.

Having established the range (by the 3D variability analysis) and the mean position of this motion (the consensus structure) in both apo and H160D, we next determined the particle distribution across these 3 states (1, 2 or 3) in the apo versus the H160D dataset. In **step 2**, we performed heterogeneous refinement of the two datasets separately, using the three models (indicated by numbers 1, 2 and 3 throughout this figure; all maps are low pass filtered to 20 Å) obtained from step 1 as reference models. The apo dataset separated into three classes: 66.3% of all particles went into a class that is similar to the classic A-State (class a), and 26.5 % of all particles went into a class that is similar to the classic I-State (class b), and a small percentage went into a third class that did not result in a high resolution structure. In the H160D dataset, the majority of all particles went into two classes (class a and class b), both of which are similar to the consensus H160D structure.

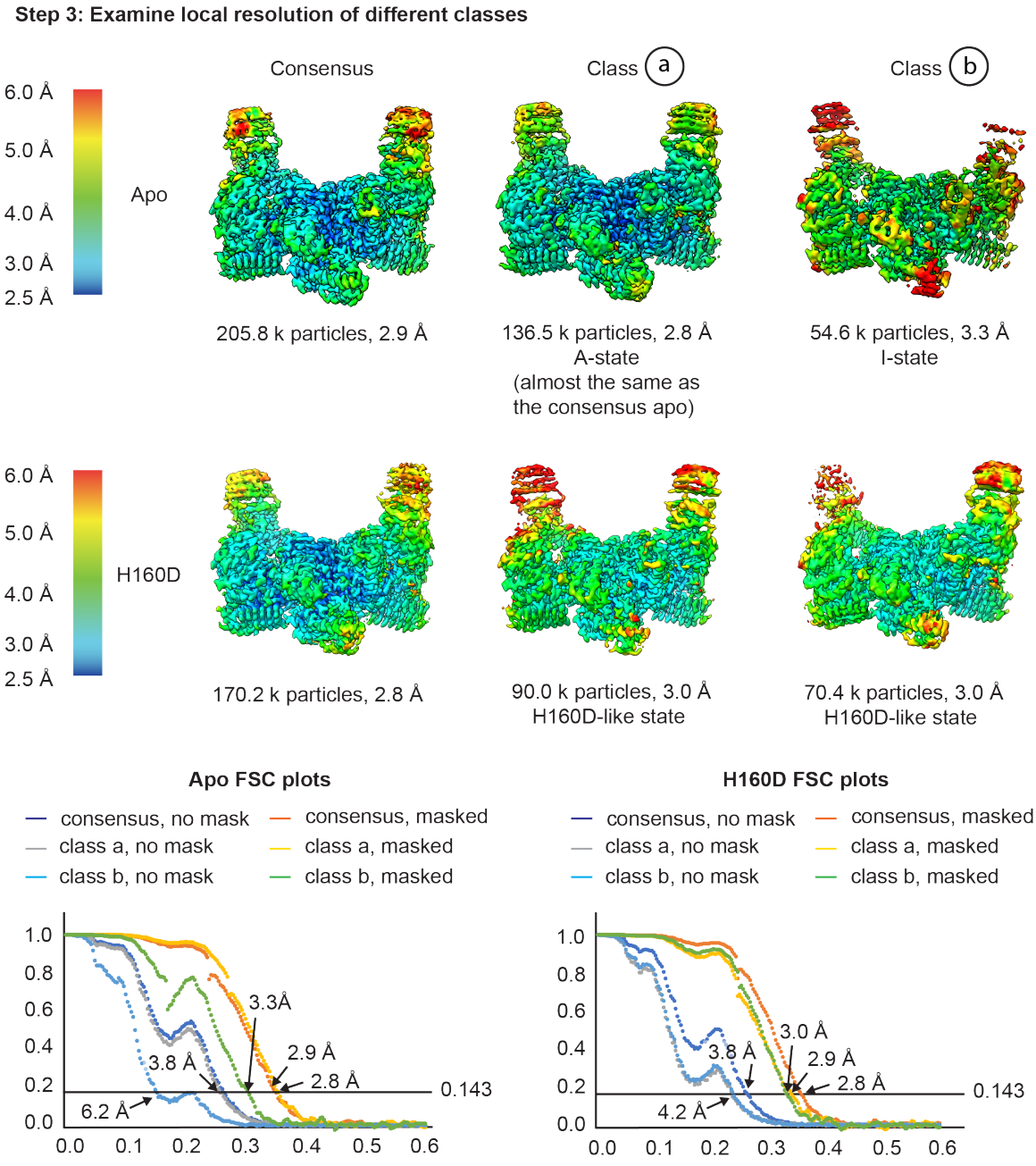

Figure 3.4 – figure supplement 4: Cryo-EM analysis of the conformation and dynamics of the WT decamer and the βH160D decamer – part 2.
Having finished the 3D classification, we then performed local resolution analysis to examine the quality of the density maps in **step 3** to investigate the potential for different subpopulations of particles within each dataset. As shown in **step 3**, in the apo structure, class a showed a slight improvement in overall resolution (2.8 Å for the class and 2.9 Å for the consensus), as well as improvements in local map quality in the flexible regions of the molecule (see the top of the "wings" in both these maps). Class b has a reduced global resolution, local resolution around the flexible regions, as well as a worse FSC profile (see the FSC plots). Class b could therefore either represent particles that are more I-State like that got separated from the consensus structure, or particles that are more damaged (as suggested by the worse FSC profile and the worse map quality in the flexible regions). For the H160D dataset, classification

resulted in two classes that are both similar to the consensus structure (classes a and b) and both classes resulted in worse overall resolution than the consensus (3.0 Å for both classes and 2.8 Å for the consensus). The local resolution of the classes are also worse than the consensus structure in flexible regions. This would suggest that the particles making up the H160D dataset represent a continuous distribution of different conformations, as simply separating them into multiple bins each with fewer particles worsened the map quality of both classes.

Integrating the results from steps 1 to 3, it is likely that the apo dataset mainly consists of A-State particles, and that the H160D mutation shifts the mean conformation of eIF2B towards a state that is I-like. Also, there is no evidence suggesting that the H160D dataset is a mixture of A- and I-State particles, but rather, particles within this dataset most likely follow a continuous distribution.

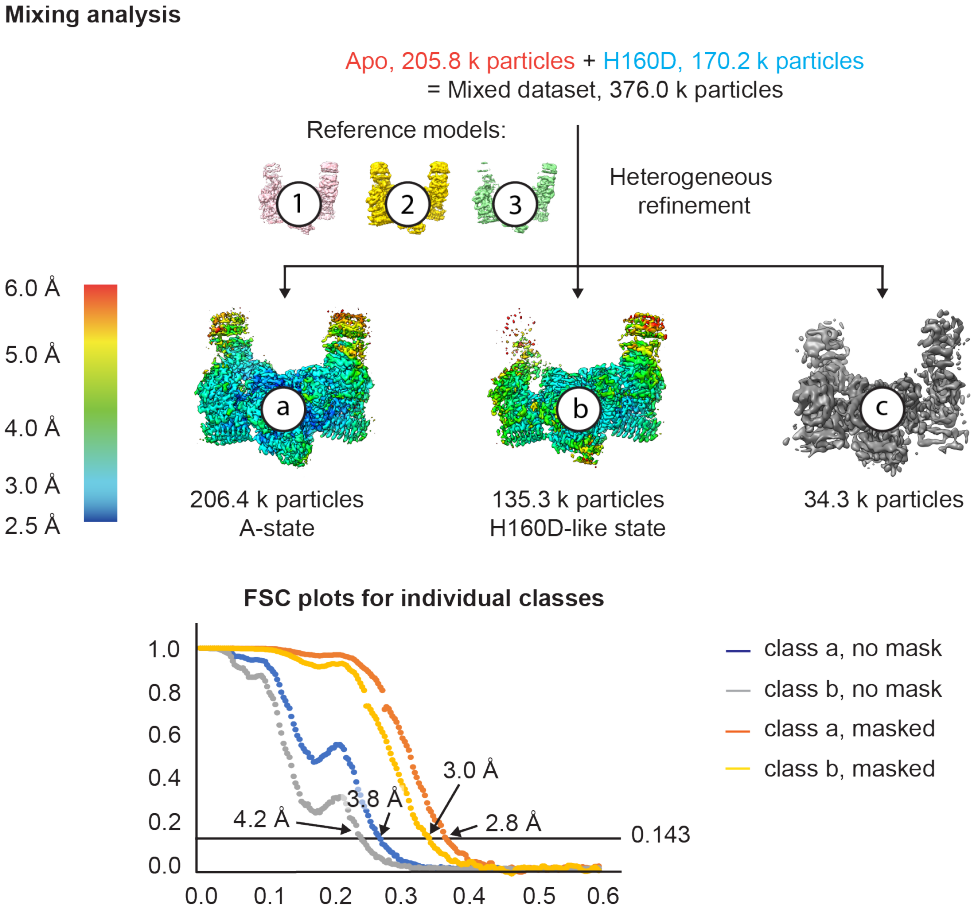

Table Classification result of the mixed dataset

Class	Total number of particles/k	Number of particles from the Apo dataset/k	Percentage of particles from the Apo dataset	Number of particles from the H160D dataset/k	Percentage of particles from the H160D dataset/%
(a)	206.4	156.2	75.9 %	50.3	29.6 %
(b)	135.3	38.2	18.6 %	97.1	57.1 %
(c)	34.3	11.4	5.5 %	22.9	13.5 %

Figure 3.4 – figure supplement 5: Cryo-EM analysis of the conformation and dynamics of the WT decamer and the βH160D decamer – part 3.
Finally, we performed an extra test to make sure that if a dataset is made up of similar conformations, our cryo-EM analysis is indeed able to separate them into two classes. In this test, we combined particle images from the apo dataset and the H160D dataset and performed heterogeneous refinement using models 1, 2 and 3 from step 1. The results show that most of the particles in the mixed dataset went into one of the two following classes: a class that resembles the classic A-State (class a) and another class that resembles the H160D State (class b). As shown in the table, consistent with the heterogeneous classification results described above, 3D classification of the mixed dataset separated the A- from the I-State, with the majority of A-State particles originating from the apo dataset and the majority of the I-State particles originating from the H160D dataset.

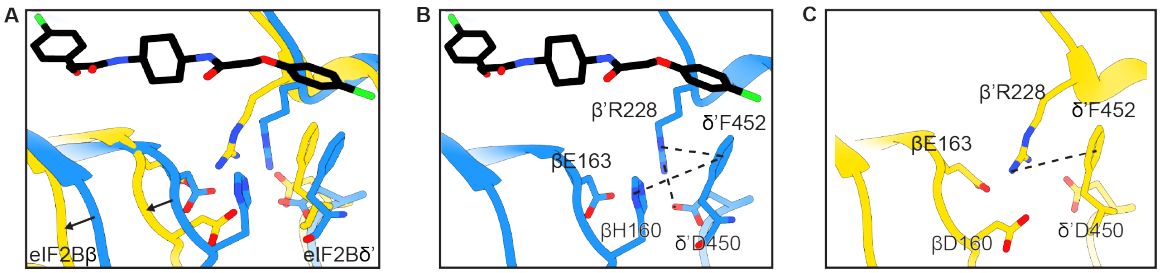

Figure 3.5 – figures supplement 1: Structural details of the symmetry interface of the WT versus βH160D decamer.
(A) Zoomed-in view of the overlay of the eIF2B^{βH160D} structure with the eIF2B-eIF2 structure at the symmetry interface. The βH160D mutation causes the loop bearing βD160 to move away from the opposite tetramer. Black arrows indicate the direction of the movement. (B) Symmetry interface of the eIF2B-eIF2 complex showing the network of interactions. (C) Symmetry interface of the eIF2B^{βH160D} structure showing the local structural rearrangements. Each interaction is denoted with a dashed line. eIF2B in the eIF2B-eIF2 complex is colored blue; eIF2B^{βH160D} is colored in yellow, and ISRIB in CPK.

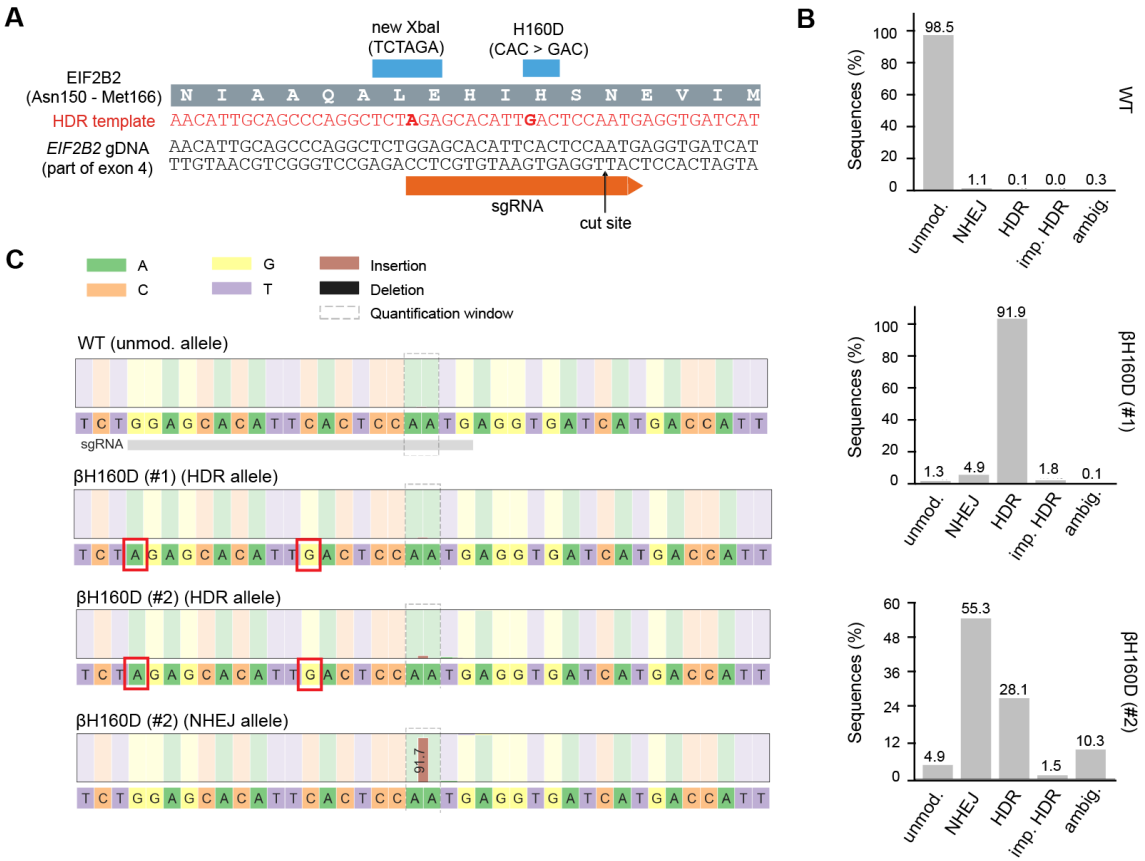

Figure 3.6 – figure supplement 1: CRISPR-Cas9 editing of the endogenous *EIF2B2* gene with the βH160D mutation in HEK293FTR cells.
(**A**) Editing strategy at target locus of exon 4 in *EIF2B2*. The guide RNA (sgRNA) directs Cas9 for cleavage at a site close to the codon coding for H160. The provided homology-directed repair (HDR) template introduces two basepair substitutions: one for the H160D point mutation (CAC > GAC), and one silent mutation for restriction enzyme mediated clone screening (new XbaI site). gDNA = genomic DNA. (**B, C**) Allele frequencies (B) and sequences (C) at the *EIF2B2* target locus in WT cells and two βH160D clones as determined by deep sequencing. For each cell line, 500,000 randomly-selected sequenced reads were analyzed using the CRISPResso2 pipeline. For one clone, βH160D (#1), >90% of reads matched the HDR template, indicating homozygous editing. For the other clone, βH160D (#2), about 1/3 of reads matched the HDR template, and about 2/3 of reads indicated non-homologous end-joining (NHEJ) with a single A-base insertion, leading to a frameshift mutation and premature translation stop. This suggests this clone is triploidic at the target locus, with a single correctly edited allele and two knock-out alleles. Unmod. = unmodified, imp. = imperfect, ambig. = ambiguous.

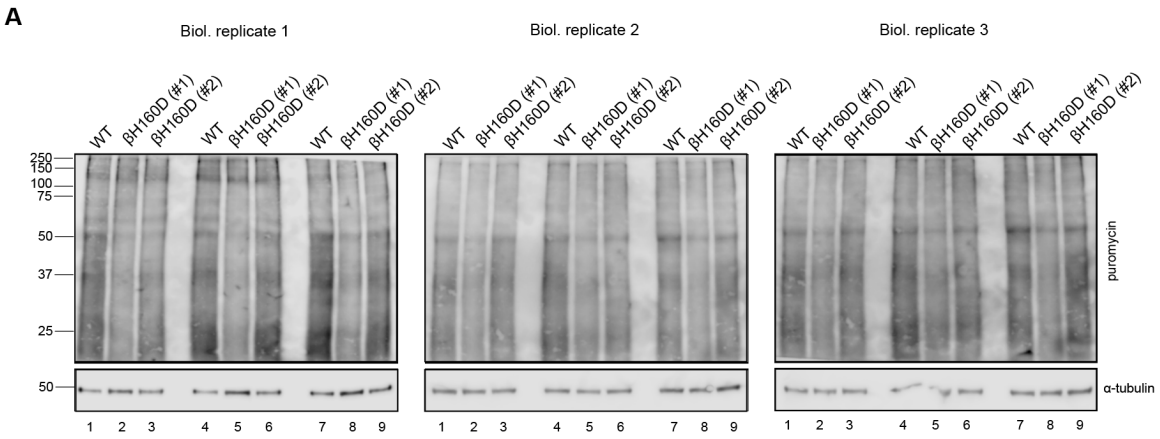

Figure 3.6 – figure supplement 2: Cells with the βH160D mutation in the endogenous *EIF2B2* gene show reduced protein translation.
Cells were treated for 10 min with puromycin and cell extracts analyzed by polyacrylamide electrophoresis followed by blotting and probing with anti-puromycin (new protein synthesis) or anti-tubulin (loading control) antibodies. Each puromycin incorporation blot represents an independent biological replicate loaded in triplicate to correct for efficiency variations during protein transfer. Equal total protein amounts were loaded in each lane.

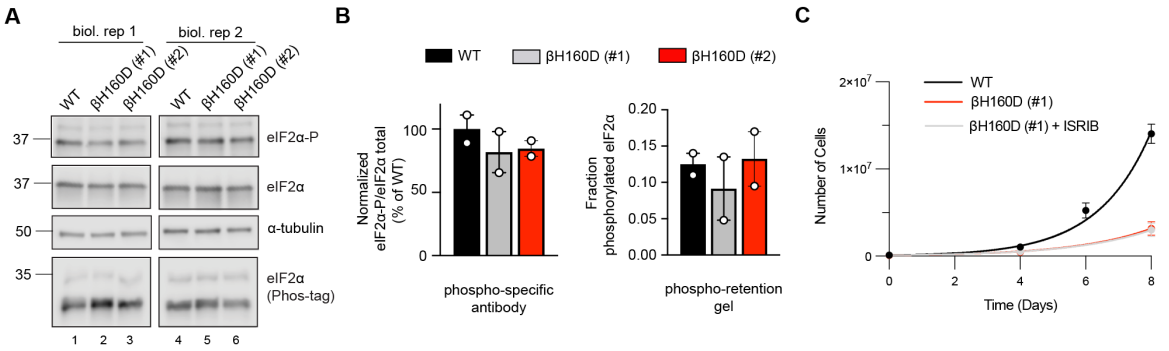

Figure 3.6 – figure supplement 3: The *EIF2B2*-H160D mutation does not alter phosphorylated eIF2α levels and is ISRIB resistant.
(**A**) Western blot of untreated WT vs *EIF2B2*^{H160D} HEK293FTR cell lines (βH160D (#1) and βH160D (#2)), probing for phospho-eIF2α (S51) (upper row), total eIF2α (middle row), and eIF2α on Phos-tag phospho-retention gel (lower row). Both methods (phospho-specific antibody and phospho-retention on Phostag gels) reveal no major difference in basal phosphorylated eIF2 levels between cell lines. (**B**) Quantification of phosphorylated eIF2α on western blots in (A) using a phospho-specific antibody (left) or on a Phostag gel probed with anti-eIF2α antibody (right). Bars of the left graph represent the mean ratio of eIF2α-P/total eIF2α normalized to WT (n = 2), and differences are not significant (one-way ANOVA with Dunnett post-hoc test, p = 0.53 for WT vs βH160D (#1) and p = 0.61 for WT vs βH160D (#2)). Bars on the right graph represent the mean fraction of eIF2α that migrates slower in the Phostag gel (upper band/(upper band + lower band)) (n = 2). Also here, differences are not significant (one-way ANOVA with Dunnett post-hoc test, p = 0.76 for WT vs βH160D (#1) and p = 0.98 for WT vs βH160D (#2)). (**C**) Growth curves showing that the slow growth of βH160D cells cannot be rescued by ISRIB treatment (n = 3 biological replicates); WT doubling time = 26.8 ± 0.4 h; βH160D (#1) doubling time = 39.6 ± 2.7 h; βH160D (#1) + ISRIB doubling time = 40.2 ± 2.7 h). All error bars and '±' designations are s.e.m.

Table 3.1 Summary of SPR kinetics data

	eIF2 binding			eIF2-P binding		
	WT decamer	**βH160D decamer**	**WT tetramer**	**WT decamer**	**βH160D decamer**	**WT tetramer**
k_a ($M^{-1}s^{-1}$)	7.0×10^5	8.6×10^5	1.5×10^6	1.1×10^6	2.1×10^6	No binding
k_d (s^{-1})	slow: 4.2×10^{-3} fast: 0.12	slow: 5.3×10^{-3} fast: 0.12	0.12	1.5×10^{-2}	1.7×10^{-2}	No binding
K_D (nM)	slow: 6.0 fast: 170	slow: 6.1 fast: 140	80	14	8.1	No binding
% slow dissociation	71	33	0	NA	NA	No binding
% fast dissociation	29	67	100	NA	NA	No binding

Table 3.2 Cryo-electron microscopy dataset for eIF2B$^{\beta H160D}$ decamer

Structure	eIF2B$^{\beta H160D}$ (PDB ID: 7TRJ)
Data collection	
Microscope	Titan Krios
Voltage (keV)	300
Nominal magnification	105000x
Exposure navigation	Image shift
Electron dose (e^{-}Å^{-2})	67
Dose rate (e^{-}/pixel/sec)	8
Detector	K3 summit
Pixel size (Å)	0.835
Defocus range (μm)	0.6-2.0
Micrographs	2269
Reconstruction	
Total extracted particles (no.)	1419483
Final particles (no.)	170244
Symmetry imposed	C1
FSC average resolution, masked (Å)	2.8
FSC average resolution, unmasked (Å)	3.8
Applied B-factor (Å)	81.7
Reconstruction package	Cryosparc 2.15
Refinement	
Protein residues	3234
Ligands	0
RMSD Bond lengths (Å)	0.003
RMSD Bond angles (°)	0.838
Ramachandran outliers (%)	0.13
Ramachandran allowed (%)	3.62
Ramachandran favored (%)	96.25
Poor rotamers (%)	6.92
CaBLAM outliers (%)	2.50
Molprobity score	2.40
Clash score (all atoms)	9.59
B-factors (protein)	100.54
B-factors (ligands)	N/A
EMRinger Score	2.52
Refinement package	Phenix 1.17.1-3660-000

Table 3.3 Antibodies and Western blotting conditions

Antibody target	Host	Dilution	Manufacturer	Cat. number	Blocking Conditions
eIF2Bβ	Rabbit	1/1,000	ProteinTech	11034-1-AP	PBS-T + 3% milk
eIF2Bε	Mouse	1/1,000	Santa Cruz Biotechnology	sc-55558	PBS-T + 3% milk
ATF4	Rabbit	1/1,000	Cell Signaling	11815S	PBS-T + 3% milk
α-tubulin	Mouse	1/1,000	Cell Signaling	3873T	PBS-T + 3% milk
Puromycin	Mouse	1/10,000	Millipore	MABE343	PBS-T + 3% milk
eIF2α	rabbit	1/1,000	Cell Signaling	5324S	PBS-T + 3% milk
eIF2α-P (S51)	rabbit	1/1,000	Cell Signaling	9721S	PBS-T + 1% BSA

Table 3.4 Primers, oligos, and guide RNAs

Oligo	Sequence	Target gene
B002_F	TGCACCACCAACTGCTTAGC	*GAPDH*
B002_R	GGCATGGACTGTGGTCATGAG	*GAPDH*
D006_F	ATGACCGAAATGAGCTTCCTG	*ATF4*
D006_R	GCTGGAGAACCCATGAGGT	*ATF4*
D007_F	GGAAACAGAGTGGTCATTCCC	*DDIT3 (CHOP)*
D007_R	CTGCTTGAGCCGTTCATTCTC	*DDIT3 (CHOP)*
D070_F	GGAAGACAGCCCCGATTTACT	*ASNS*
D070_R	AGCACGAACTGTTGTAATGTCA	*ASNS*
D073_F	CCATGCAGACTCCACCTTTAC	*CARS*
D073_R	GCAATACCACGTCACCTTTTTC	*CARS*
C001_F	ACTTTAAGCACATTAACCCTG	*EIF2B2*
C001_R	ACTTGATCTTCTCAGTGTCTC	*EIF2B2*
C015	t*G*CAAAACCGTTCTTACAGAAGGGACAATG GAGAACATTGCAGCCCAGGCTCTAGAGCACA TTGACTCCAATGAGGTGATCATGACCATTGG CTTCTCCCGAACAGT	NA (ssODN)
C034_F	CGCGTAATGTGTGTTTGTGA	
C034_R	GCCTCTACTGTTCGGGAGAA	
C036_F_bc**x**	CAAGCAGAAGACGGCATACGAGAT**xxxxxx**GT GACTGGAGTTCAGACGTGTGCTCTTCCGATC TCGCGTAATGTGTGTTTGTGA	
C036_R	AATGATACGGCGACCACCGAGATCTACACTC TTTCCCTACACGA	
C005_F	acaccgGGAGCACATTCACTCCAATGg	
C005_R	aaaacCATTGGAGTGAATGTGCTCCcg	

* phosphorothioate bond.

x = barcode nucleotide, different for each clone

Materials and Methods

Cloning

eIF2B2 (encoding eIF2Bβ) and *eIF2B4* (encoding eIF2Bδ) had previously been inserted into sites 1 and 2 of pACYCDuet-1 and then further edited to include mNeonGreen and a $(GGGGS)_2$ linker at the C-terminus of *eIF2B2* and mScarlet-i and a $(GGGGS)_2$ linker at the C-terminus of *eIF2B4* (pMS029). In-Fusion HD cloning was used to edit this plasmid further and insert the H160D mutation into *eIF2B2* (pMS114).

For CRISPR editing of the *EIF2B2* gene, guide RNAs were designed using the Benchling CRISPR gRNA Design Tool, selecting the guide with the best on-target and off-target scores, and the H160D mutation within 10 bp of the cut site. Cloning of the guide into the guide expression plasmid (MLM3636, with human U6 promoter) was done as previously described (Kwart et al. 2017). In brief, the guide RNA sequence was synthesized as single stranded DNA oligos (C005_F and C005_R) that were first annealed at 2 µM in 1x annealing buffer (40 mM Tris-HCl pH 8.0, 20 mM $MgCl_2$, 50 mM NaCl, 1 mM EDTA pH 8.0), for 5 min at 95°C followed by gradual decrease of -0.1°C/s to 25°C. The MLM3636 plasmid was digested using BsmBI (NEB) in NEB Buffer 3.1 for 2 h at 55°C, and the 2.2 kb backbone was isolated from a 0.8% agarose gel with 1x SYBR Safe, and purified using the NucleoSpin Gel and PCR cleanup kit (Macherey Nagel). Backbone and annealed guide template were ligated for 1 h at room temperature using T4 DNA Ligase (NEB), 100 ng backbone, 100 nM guide template, and 1x T4 DNA Ligase buffer (NEB).

Purification of human eIF2B subcomplexes

Human eIF2Bα_2 (pJT075), Avi-tagged eIF2Bα_2 (pMS026), WT eIF2B$\beta\gamma\delta\varepsilon$ (pJT073 and pJT074 co-expression), eIF2B$\beta^{H160D}\gamma\delta\varepsilon$ (pJT102 and pJT074), Avi-tagged eIF2B$\beta\gamma\delta\varepsilon$ (pMS001 and pJT074 co-expression), WT eIF2B$\beta\delta\gamma\varepsilon$-F tetramers (pMS029 and pJT074 co-expression), and βH160D eIF2B$\beta\delta\gamma\varepsilon$-F tetramers (pMS114 and pJT074 co-expression) were purified as previously described (Tsai et al. 2018; Schoof et al. 2021).

Purification of heterotrimeric human eIF2

Human eIF2 was purified as previously described (Wong et al. 2018). This material was a generous gift of Calico Life Sciences LLC.

Analytical ultracentrifugation

Analytical ultracentrifugation (sedimentation velocity) experiments were performed as previously described using the ProteomeLab XL-I system (Beckman Coulter) (Tsai et al. 2018). In brief, samples were loaded into cells in a buffer of 20 mM HEPES-KOH, pH 7.5, 150 mM KCl, 1 mM TCEP, and 5 mM $MgCl_2$. A buffer only reference control was also loaded. Samples were then centrifuged in an AN-50 Ti rotor at 40,000 rpm at 20°C and 280 nm absorbance was monitored. Subsequent data analysis was conducted with Sedfit using a non-model-based continuous c(s) distribution.

***In vitro* FRET assays**

In vitro FRET assays were performed as previously described (Schoof et al. 2021).

Guanine nucleotide exchange assay

In vitro detection of GDP binding to eIF2 was performed as described previously (Schoof et al. 2021). As before, we first monitored the loading of fluorescent BODIPY-FL-GDP to eIF2.

Purified human eIF2 (100 nM) was incubated with 100 nM BODIPY-FL-GDP (Thermo Fisher Scientific) in assay buffer (20 mM HEPES-KOH, pH 7.5, 100 mM KCl, 5 mM $MgCl_2$, 1 mM TCEP, and 1 mg/ml BSA) to a volume of 18 µl in 384 square-well black-walled, clear-bottom polystyrene assay plates (Corning). For the assay buffer, TCEP and BSA were always freshly added the day of the experiment. For the tetramer GEF assays, a 10X GEF mix was prepared containing 1 µM eIF2Bβγδε tetramer (WT or βH160D), 2% N-methyl-2-pyrrolidone (NMP), and with or without 10 µM ISRIB, again in assay buffer. For the assay, 2 µl of the 10x GEF mix was spiked into the eIF2::BODIPY-FL-GDP mix, bringing the final concentrations to 100 nM tetramer, 0.2% NMP and with or without 1 µM ISRIB. Fluorescence intensity was recorded every 10 s for 40 s prior to the 10X GEF mix spike, and after the spike for 60 min, using a Clariostar PLUS (BMG LabTech) plate reader (excitation wavelength: 477 nm, bandwidth 14 nm; emission wavelength: 525 nm, bandwidth: 30 nm).

For assays with eIF2B decamers (WT or βH160D), decamers were first assembled by combining eIF2Bβγδε tetramer (WT or βH160D) with $eIF2B\alpha_2$ dimer in a 1:1 molar ratio (a 2-fold excess of $eIF2B\alpha_2$ dimer compared to the number of $eIF2B(\beta\gamma\delta\varepsilon)_2$ octamers) at room temperature for at least 30 min. The 10X GEF mix for decamer assays contained 100 nM $eIF2B(\alpha\beta\gamma\delta\varepsilon)_2$ decamer (WT or βH160D) in assay buffer. The ensuing steps were performed as described for the GEF assays with tetramers. Immediately after the loading assay, in the same wells, we spiked in unlabeled GDP to 1 mM to measure unloading, again recording fluorescence intensities every 10s for 60 min as before. These data were fit to a first-order exponential. For clarity, datapoints were averaged at 1 min intervals and then plotted as single datapoints in Figure 2.

Michaelis-Menten kinetics

The Michaelis-Menten kinetic analysis of eIF2B(αβγδε)$_2$ decamer (WT or βH160D) GEF activity was performed as described previously, with some minor modifications (Schoof et al. 2021). Briefly, BODIPY-FL-GDP loading assays were performed as described above, keeping final decamer concentrations at 10 nM, but varying substrate concentration from 0 nM to 4 µM. BODIPY-FL-GDP concentration was kept at 2 µM final. The initial velocity was determined by a linear fit to timepoints acquired at 5 s intervals from 50 to 200 s after addition of decamer. To convert fluorescence intensities to pmol substrate, the gain in signal after 60 min was plotted against eIF2 concentration for the 31.5 nM – 1 µM concentrations. V_{max} and K_M were determined by fitting the initial velocities as a function of eIF2 concentration to the Michaelis–Menten equation in GraphPad Prism 9. For statistical comparisons of V_{max} and K_M, we used a two-sided t-test with α = 0.05, comparing V_{max} or K_M derived from the individual fit of each replicate experiment.

Affinity determination and variable association analysis by surface plasmon resonance

eIF2 and eIF2-P affinity determination experiments were performed on a Biacore T200 instrument (Cytiva Life Sciences) by capturing the biotinylated WT eIF2B decamer, βH160D eIF2B decamer, and WT eIF2B tetramer at ~50nM on a Biotin CAPture Series S sensor chip (Cytiva Life Sciences) to achieve maximum response (Rmax) of under ~150 response units (RUs) upon eIF2 or eIF2-P binding. eIF2-P was prepared by mixing 5 µM eIF2 in 50-fold excess of 100 nM PERK kinase and with 1 mM ATP. The mixture was incubated at room temperature for 60 min before incubation on ice until dilution into the titration series. 2-fold serial dilutions of purified eIF2 or eIF2-P were flowed over the captured eIF2B complexes at 30 µl / min for 60 seconds followed by 600 seconds of dissociation flow. Following each cycle, the chip surface was regenerated with 3 M guanidine hydrochloride. A running buffer of 20 mM HEPES-KOH, pH 7.5, 100 mM KCl, 5 mM $MgCl_2$, and 1 mM TCEP was used throughout. The resulting

sensorgrams were fit in GraphPad Prism 8.0. Association was fit for all species using the association then dissociation model. For eIF2-P binding this model was used to fit dissociation as well. For eIF2 binding, dissociation was fit using the two phase decay model. For eIF2 binding to WT tetramer the data could be modeled with one phase association, one phase dissociation kinetics by setting the percent fast phase dissociation to 100%. For variable association experiments, WT and βH160D eIF2B decamer was immobilized as described above. A solution containing 62.5 nM eIF2 was flowed over the captured eIF2B for 5-480 s at 30 µl / min to reach the equilibrium of % fast phase dissociation vs % slow phase dissociation. Association was followed by 480 seconds of dissociation flow. The dissociation phase was then fit in GraphPad Prism 8.0 using the two phase decay model as described above.

Generation of endogenous βH160D cells

Editing of the *EIF2B2* gene to introduce the H160D mutation in HEK293Flp-In TRex (HEK293FTR) cells was performed using CRISPR-Cas9 according to a previously published protocol, with some minor modifications (Kwart et al. 2017). Cells were seeded at 250,000 cells/well of a 12-well plate and grown for 24 h prior to transfection with a PAGE-purified, phosphorothioate-protected single-stranded oligonucleotide donor (ssODN) for homologous recombination (C015) (Renaud et al. 2016), a plasmid containing Cas9-GFP, and a plasmid encoding the guide RNA (MLM3636-C005). The 100 nt ssODN was designed to simultaneously introduce the H160D missense mutation (CAC to GAC), to add a silent XbaI restriction site at L156 (TCTGGA to TCTAGA), and to block re-digestion by Cas9 after recombination. Transfection was done with Xtreme Gene9 reagent according to the manufacturer's protocol, using a 3:1 ratio of reagent (µl) to DNA (µg). Reagent-only and pCas9-GFP controls were included. Two days post transfection, cells were trypsinized, washed twice in ice-cold filter-sterilized FACS buffer (25 mM HEPES pH 7.0, 2 mM EDTA, 0.5% v/v fetal bovine serum, in 1x PBS), and resuspended in FACS buffer with 400 ng/ml 7-AAD viability dye (Invitrogen) at

around 1 million cells/ml in filter-capped FACS tubes. Single GFP^+, 7-AAD^- cells were sorted into recovery medium (a 1:1 mix of conditioned medium, and fresh medium with 20% fetal bovine serum, 2 mM L-Glutamine, 1 mM sodium pyruvate, and 1x non-essential amino acids) in single wells of 96-well plates using the Sony SH800 cell sorter. The survival rate was around 2% after 2-3 weeks. Surviving clones were expanded and first screened for correct editing by PCR and XbaI restriction digest. For this, genomic DNA was isolated using the PureLink Genomic DNA mini kit (Invitrogen), and a 473 bp fragment of the *EIF2B2* gene was amplified by PCR using 300 nM forward and reverse primers (C001_F and C001_R), 300 µM dNTPs, 1x HF buffer, 100 ng genomic DNA / 100 µl reaction and 2 U/100 µl reaction of KAPA HiFi polymerase for 3 min at 95°C; and 30 cycles of 98°C for 20 s, 68.9°C for 15 s, 72°C for 15 s, prior to cooling at 4°C. PCR reactions were purified using NucleoSpin Gel and PCR cleanup kit (Macherey Nagel), and HighPrep PCR Cleanup beads (MagBio Genomics) using the manufacturer's instructions. Cleaned up products were digested using XbaI restriction enzyme (NEB) in 1x CutSmart buffer and run on a 1.5% agarose gel with 1x SYBR Safe (Invitrogen) and 100 bp DNA ladder (Promega). Clones with an XbaI restriction site were then deep sequenced to confirm correct editing and zygosity. For this, the *EIF2B2* gene was amplified by PCR using 300 nM forward and reverse primers (C034_F and C034_R), 300 µM dNTPs, 1x HF buffer, 100 ng genomic DNA / 100 µl reaction and 2 U/100 µl reaction of KAPA HiFi polymerase for 3 min at 95°C; and 30 cycles of 98°C for 20 s, 64.9°C for 15 s, 72°C for 15 s, prior to cooling at 4°C. The 196 bp product was purified from a 1.5% agarose gel with 1x SYBR Safe using NucleoSpin Gel and PCR cleanup kit (Macherey Nagel), and HighPrep PCR Cleanup beads (MagBio Genomics) using the manufacturer's instructions. A subsequent second PCR added the Illumina P5/P7 sequences and barcode for deep sequencing. For this, we used 15 ng purified PCR product per 100 µl reaction, 300 nM forward and reverse primer (C036_F_bcx, and C036_R), and 1x KAPA HiFi HotStart mix, for 3 min at 95°C, and 8 cycles of 20 s at 98°C, 15 s at 63.7°C, and 15 s at 72°C prior to cooling on ice. PCR reactions were purified using HighPrep beads (MagBio

Genomics), and amplicon quality and size distribution was checked by chip electrophoresis (BioAnalyzer High Sensitivity kit, Agilent). Samples were then sequenced on an Illumina MiSeq (150 bp paired-end), and results were analyzed with CRISPResso (Pinello et al. 2016). All cell lines were negative for mycoplasma contamination. Amplicon sequencing data was deposited in NCBI's Sequence Read Archive (SRA) under accession number PRJNA821864.

.

Growth Curves

Cells were seeded at 100,000 cells/well of a 6-well plate and grown at 37°C and 5% CO_2. At confluency, cells were trypsinized, expanded into larger plates, and counted. This was repeated until the WT cells reached confluency in a T225 flask. For drug treatment conditions (Figure 6 – figure supplement 3C), we used 500 nM ISRIB with DMSO at a final concentration of 0.1% across conditions.

Western Blotting

Cells were seeded at 400,000 cells/well of a 6-well plate and grown at 37°C and 5% CO_2 for 24 h. For drug treatment, we used 10 nM thapsigargin (Tg) (Invitrogen) and 200 nM ISRIB (made in-house) for 1 h, ensuring the final DMSO concentration was 0.1% across all conditions. For the protein synthesis assay, puromycin was added to a final concentration of 10 µg/ml for 10 min. Plates were put on ice, cells were washed once with ice-cold phosphate-buffered saline (PBS), and then lysed in 150 µl ice-cold lysis buffer (50 mM Tris-HCl pH 7.4, 150 mM NaCl, 1 mM EDTA, 1% v/v Triton X-100, 10% v/v glycerol, 1x cOmplete protease inhibitor cocktail [Roche], and 1x PhosSTOP [Roche]). Cells were scraped off, collected in an eppendorf tube, and put on a rotator for 30 min at 4°C. Debris was pelleted at 12,000 g for 20 min at 4°C, and supernatant was removed to a new tube on ice. Protein concentration was measured using the bicinchonic acid (BCA) assay. Within an experiment, total protein concentration was normalized

to the least concentrated sample (typically all values were within ~10%). A 5x Laemmli loading buffer (250 mM Tris-HCl pH 6.8, 30% glycerol, 0.25% bromophenol blue, 10% SDS, 5% β-mercaptoethanol) was added to each sample to 1x, and samples were denatured at 95°C for 12 min, then cooled on ice. Wells of AnyKd Mini-PROTEAN TGX precast protein gels (AnyKD, Bio-Rad) were loaded with equal amounts of total protein (around 10 µg), in between Precision Plus Dual Color protein ladder (BioRad). After electrophoresis, proteins were transferred onto a nitrocellulose membrane at 4°C, and then blocked for 2 h at room temperature in PBS with 0.1% Tween (PBS-T) + 3% milk (blocking buffer) while rocking. Primary antibody staining was performed with gentle agitation at 4°C overnight using the conditions outlined in Table 3.3. After washing four times in blocking buffer, secondary antibody staining was performed for 1 h at room temperature using anti-rabbit HRP or anti-mouse HRP secondary antibodies (Promega, 1:10,000) in blocking buffer. Membranes were washed 3x in blocking buffer and then 1x in PBS-T without milk. Chemiluminescent detection was performed using SuperSignal West Dura or Femto HRP substrate (Thermo Fisher Scientific), and membranes were imaged on a LI-COR Odyssey gel imager for 0.5–10 min depending on band intensity.

For the phospho-retention blots, equal amounts of total protein lysates (around 10 µg) were loaded on 12.5% Supersep Phos-tag gels (Wako Chemicals) in between Wide-view III protein ladder (Wako Chemicals). After electrophoresis, the gel was washed 3x in transfer buffer with 10 mM EDTA prior to transfer onto nitrocellulose. Blocking, antibody staining and detection was performed as described above.

RT-qPCR

Cells were seeded at 400,000 cells/well of a 12-well plate and grown at 37°C and 5% CO_2 for 24 h. The day of RNA extraction, medium was removed, and cells were lysed in 350 µl TriZOL reagent (Invitrogen). All further handling was done in a fume hood decontaminated for the

presence of RNAses using RNAse ZAP (Invitrogen). Total RNA was isolated using the DirectZOL RNA miniprep kit (Zymo Research), including an on-column DNase digest, according to the manufacturer's instructions. RNA concentration was measured using Nanodrop. cDNA was synthesized using 600 ng input total RNA per 40 µl reaction with the iScript cDNA Synthesis Kit (BioRad), cycling for 5 min at 25°C, 20 min at 46°C, and 1 min at 95°C. Samples were cooled and diluted 1/5 in Rnase-free water. qPCR reactions were set up with final 1x iQ SYBR Green supermix (BioRad), 400 nM each of Fw and Rev QPCR primers (see Table 3.4), 1/5 of the diluted cDNA reaction, and RNAse-free water. No-template and no-reverse transcription reactions were included as controls. Reactions were run in triplicates as 10 µl reactions in 384-well plates on a BioRad CFX384 Thermocycler, for 3 min at 95°C, and then 40 cycles of 95°C for 10 s and 60°C for 30 s, ending with heating from 55°C to 95°C in 0.5°C increments for melting curve generation. C_qs and melting curves were calculated by the BioRad software. C_q values of technical replicates were averaged, and values were calculated with the ΔΔCt method using *GAPDH* for reference gene normalization. Graph points reflect fold changes compared to WT vehicle, with bars being the mean +/- s.e.m. Statistical analysis was done using GraphPad Prism 9 on log-transformed values with ordinary one-way ANOVA and Dunnett's post-hoc test.

Sample preparation for cryo-electron microscopy

Decameric eIF2Bβ^{H160D} was prepared by incubating 16 µM eIF2Bβ^{H160D}γδε with 8.32 µM eIF2Bα$_2$ in a final solution containing 20 mM HEPES-KOH, 200 mM KCl, 5 mM $MgCl_2$, and 1 mM TCEP. This 8 µM eIF2B(αβ^{H160D}γδε)$_2$ sample was further diluted to 750 nM. For grid freezing, a 3 µl aliquot of the sample was applied onto the Quantifoil R 1.2/1/3 400 mesh Gold grid and we waited for 30 s. A 0.5 µl aliquot of 0.1-0.2% Nonidet P-40 substitute was added immediately before blotting. The entire blotting procedure was performed using Vitrobot (FEI) at 10 ºC and 100% humidity.

Electron microscopy data collection

Cryo-EM data was collected on a Titan Krios transmission electron microscope operating at 300 keV. Micrographs were acquired using a Gatan K3 direct electron detector. The total dose was 67 $e^-/ Å^2$, and 117 frames were recorded during a 5.9 s exposure. Data was collected at 105,000 x nominal magnification (0.835 Å/pixel at the specimen level), with a nominal defocus range of -0.6 to -2.0 µm.

Image processing

The micrograph frames were aligned using MotionCor2 (Zheng et al. 2017). The contrast transfer function (CTF) parameters were estimated with GCTF (Zhang 2016). For the decameric $eIF2B^{\beta H160D}$, Particles were picked in Cryosparc v2.15 using the apo eIF2B (EMDB: 23209) as a template (Punjani et al. 2017; Schoof et al. 2021). Particles were extracted using an 80-pixel box size and classified in 2D. Classes that showed clear protein features were selected and extracted for ab initio reconstruction, followed by homogenous refinement. Particles belonging to the best class were then re-extracted with a pixel size of 2.09 Å, and then subjected to homogeneous refinement, yielding a reconstruction of 4.25 Å. These particles were subjected to another round of heterogeneous refinement followed by homogeneous refinement to generate a consensus reconstruction consisting of the best particles. These particles were re-extracted at a pixel size of 0.835 Å. Then, CTF refinement was performed to correct for the per-particle CTF as well as beam tilt. A final round of nonuniform refinement yielded the final structure of 2.8 Å.

Atomic model building, refinement, and visualization

For the decameric $eIF2B^{\beta H160D}$, the previously published apo eIF2B model (PDB ID: 7L70) was used as a starting model (Schoof et al. 2021). Each subunit was docked into the EM density individually and then subjected to rigid body refinement in Phenix (Adams et al. 2010). The

models were then manually adjusted in Coot and then refined in phenix.real_space_refine using global minimization, secondary structure restraints, Ramachandran restraints, and local grid search (Emsley and Cowtan 2004). Then iterative cycles of manual rebuilding in Coot and phenix.real_space_refine were performed. The final model statistics were tabulated using Molprobity (Chen et al. 2010). Distances were calculated from the atomic models using UCSF Chimera (Pettersen et al. 2004). Molecular graphics and analyses were performed with the UCSF Chimera package. UCSF Chimera is developed by the Resource for Biocomputing, Visualization, and Informatics and is supported by NIGMS P41-GM103311. The atomic model is deposited into PDB under the accession code 7TRJ. The EM map is deposited into EMDB under the accession code EMD-26098.

References

Abdulkarim, B., M. Nicolino, M. Igoillo-Esteve, M. Daures, S. Romero, A. Philippi, V. Senée, M. Lopes, D. A. Cunha, H. P. Harding, C. Derbois, N. Bendelac, A. T. Hattersley, D. L. Eizirik, D. Ron, M. Cnop, and C. Julier. 2015. 'A Missense Mutation in PPP1R15B Causes a Syndrome Including Diabetes, Short Stature, and Microcephaly', *Diabetes*, 64: 3951-62.

Adams, P. D., P. V. Afonine, G. Bunkóczi, V. B. Chen, I. W. Davis, N. Echols, J. J. Headd, L. W. Hung, G. J. Kapral, R. W. Grosse-Kunstleve, A. J. McCoy, N. W. Moriarty, R. Oeffner, R. J. Read, D. C. Richardson, J. S. Richardson, T. C. Terwilliger, and P. H. Zwart. 2010. 'PHENIX: a comprehensive Python-based system for macromolecular structure solution', *Acta Crystallogr D Biol Crystallogr*, 66: 213-21.

Adomavicius, T., M. Guaita, Y. Zhou, M. D. Jennings, Z. Latif, A. M. Roseman, and G. D. Pavitt. 2019. 'The structural basis of translational control by eIF2 phosphorylation', *Nat Commun*, 10: 2136.

Algire, M. A., D. Maag, and J. R. Lorsch. 2005. 'Pi release from eIF2, not GTP hydrolysis, is the step controlled by start-site selection during eukaryotic translation initiation', *Mol Cell*, 20: 251-62.

Bogorad, A. M., K. Y. Lin, and A. Marintchev. 2017. 'Novel mechanisms of eIF2B action and regulation by eIF2α phosphorylation', *Nucleic Acids Res*, 45: 11962-79.

Chen, V. B., W. B. Arendall, 3rd, J. J. Headd, D. A. Keedy, R. M. Immormino, G. J. Kapral, L. W. Murray, J. S. Richardson, and D. C. Richardson. 2010. 'MolProbity: all-atom structure validation for macromolecular crystallography', *Acta Crystallogr D Biol Crystallogr*, 66: 12-21.

Chou, A., K. Krukowski, T. Jopson, P. J. Zhu, M. Costa-Mattioli, P. Walter, and S. Rosi. 2017. 'Inhibition of the integrated stress response reverses cognitive deficits after traumatic brain injury', *Proc Natl Acad Sci U S A*, 114: E6420-e26.

Costa-Mattioli, M., and P. Walter. 2020. 'The integrated stress response: From mechanism to disease', *Science*, 368: eaat5314.

Dey, M., C. Cao, A. C. Dar, T. Tamura, K. Ozato, F. Sicheri, and T. E. Dever. 2005. 'Mechanistic link between PKR dimerization, autophosphorylation, and eIF2alpha substrate recognition', *Cell*, 122: 901-13.

Emsley, P., and K. Cowtan. 2004. 'Coot: model-building tools for molecular graphics', *Acta Crystallogr D Biol Crystallogr*, 60: 2126-32.

Gordiyenko, Y., J. L. Llácer, and V. Ramakrishnan. 2019. 'Structural basis for the inhibition of translation through eIF2α phosphorylation', *Nat Commun*, 10: 2640.

Gordiyenko, Y., C. Schmidt, M. D. Jennings, D. Matak-Vinkovic, G. D. Pavitt, and C. V. Robinson. 2014. 'eIF2B is a decameric guanine nucleotide exchange factor with a γ2ε2 tetrameric core', *Nat Commun*, 5: 3902.

Guo, X., G. Aviles, Y. Liu, R. Tian, B. A. Unger, Y. T. Lin, A. P. Wiita, K. Xu, M. A. Correia, and M. Kampmann. 2020. 'Mitochondrial stress is relayed to the cytosol by an OMA1-DELE1-HRI pathway', *Nature*, 579: 427-32.

Hao, Q., J. M. Heo, B. P. Nocek, K. G. Hicks, V. S. Stoll, C. Remarcik, S. Hackett, L. LeBon, R. Jain, D. Eaton, J. Rutter, Y. L. Wong, and C. Sidrauski. 2021. 'Sugar phosphate activation of the stress sensor eIF2B', *Nat Commun*, 12: 3440.

Harding, H. P., I. Novoa, Y. Zhang, H. Zeng, R. Wek, M. Schapira, and D. Ron. 2000. 'Regulated translation initiation controls stress-induced gene expression in mammalian cells', *Mol Cell*, 6: 1099-108.

Harding, H. P., H. Zeng, Y. Zhang, R. Jungries, P. Chung, H. Plesken, D. D. Sabatini, and D. Ron. 2001. 'Diabetes mellitus and exocrine pancreatic dysfunction in perk-/- mice reveals a role for translational control in secretory cell survival', *Mol Cell*, 7: 1153-63.

Hinnebusch, A. G. 2005. 'Translational regulation of GCN4 and the general amino acid control of yeast', *Annu Rev Microbiol*, 59: 407-50.

Hinnebusch, A. G., I. P. Ivanov, and N. Sonenberg. 2016. 'Translational control by 5'-untranslated regions of eukaryotic mRNAs', *Science*, 352: 1413-6.

Kashiwagi, K., M. Takahashi, M. Nishimoto, T. B. Hiyama, T. Higo, T. Umehara, K. Sakamoto, T. Ito, and S. Yokoyama. 2016. 'Crystal structure of eukaryotic translation initiation factor 2B', *Nature*, 531: 122-5.

Kashiwagi, K., T. Yokoyama, M. Nishimoto, M. Takahashi, A. Sakamoto, M. Yonemochi, M. Shirouzu, and T. Ito. 2019. 'Structural basis for eIF2B inhibition in integrated stress response', *Science*, 364: 495-99.

Kashiwagi, K., Y. Shichino, T. Osaki, A. Sakamoto, M. Nishimoto, M. Takahashi, M. Mito, F. Weber, Y. Ikeuchi, S. Iwasaki, and T. Ito. 2021. 'eIF2B-capturing viral protein NSs suppresses the integrated stress response', *Nat Commun,* 12: 7102.

Kenner, L. R., A. A. Anand, H. C. Nguyen, A. G. Myasnikov, C. J. Klose, L. A. McGeever, J. C. Tsai, L. E. Miller-Vedam, P. Walter, and A. Frost. 2019. 'eIF2B-catalyzed nucleotide exchange and phosphoregulation by the integrated stress response', *Science*, 364: 491-95.

Konieczny, A., and B. Safer. 1983. 'Purification of the eukaryotic initiation factor 2-eukaryotic initiation factor 2B complex and characterization of its guanine nucleotide exchange activity during protein synthesis initiation', *J Biol Chem*, 258: 3402-8.

Koromilas, A. E., S. Roy, G. N. Barber, M. G. Katze, and N. Sonenberg. 1992. 'Malignant transformation by a mutant of the IFN-inducible dsRNA-dependent protein kinase', *Science*, 257: 1685-9.

Krukowski, K., A. Nolan, E. S. Frias, M. Boone, G. Ureta, K. Grue, M. S. Paladini, E. Elizarraras, L. Delgado, S. Bernales, P. Walter, and S. Rosi. 2020. 'Small molecule cognitive enhancer reverses age-related memory decline in mice', *Elife*, 9: e62048

Kwart, D., D. Paquet, S. Teo, and M. Tessier-Lavigne. 2017. 'Precise and efficient scarless genome editing in stem cells using CORRECT', *Nat Protoc*, 12: 329-54.

Leegwater, P. A., G. Vermeulen, A. A. Könst, S. Naidu, J. Mulders, A. Visser, P. Kersbergen, D. Mobach, D. Fonds, C. G. van Berkel, R. J. Lemmers, R. R. Frants, C. B. Oudejans, R. B. Schutgens, J. C. Pronk, and M. S. van der Knaap. 2001. 'Subunits of the translation initiation factor eIF2B are mutant in leukoencephalopathy with vanishing white matter', *Nat Genet*, 29: 383-8.

Li, W., X. Wang, M. S. Van Der Knaap, and C. G. Proud. 2004. 'Mutations linked to leukoencephalopathy with vanishing white matter impair the function of the eukaryotic initiation factor 2B complex in diverse ways', *Mol Cell Biol*, 24: 3295-306.

Lu, P. D., H. P. Harding, and D. Ron. 2004. 'Translation reinitiation at alternative open reading frames regulates gene expression in an integrated stress response', *J Cell Biol*, 167: 27-33.

Lu, Y. N., S. Kavianpour, T. Zhang, X. Zhang, D. Nguyen, R. Thombre, L. He, and J. Wang. 2021. 'MARK2 phosphorylates eIF2α in response to proteotoxic stress', *PLoS Biol*, 19: e3001096.

Ma, T., M. A. Trinh, A. J. Wexler, C. Bourbon, E. Gatti, P. Pierre, D. R. Cavener, and E. Klann. 2013. 'Suppression of eIF2α kinases alleviates Alzheimer's disease-related plasticity and memory deficits', *Nat Neurosci*, 16: 1299-305.

Matts, R. L., D. H. Levin, and I. M. London. 1983. 'Effect of phosphorylation of the alpha-subunit of eukaryotic initiation factor 2 on the function of reversing factor in the initiation of protein synthesis', *Proc Natl Acad Sci U S A*, 80: 2559-63.

Nguyen, H. G., C. S. Conn, Y. Kye, L. Xue, C. M. Forester, J. E. Cowan, A. C. Hsieh, J. T. Cunningham, C. Truillet, F. Tameire, M. J. Evans, C. P. Evans, J. C. Yang, B. Hann, C. Koumenis, P. Walter, P. R. Carroll, and D. Ruggero. 2018. 'Development of a stress response therapy targeting aggressive prostate cancer', *Sci Transl Med*, 10: eaar2036

Pettersen, E. F., T. D. Goddard, C. C. Huang, G. S. Couch, D. M. Greenblatt, E. C. Meng, and T. E. Ferrin. 2004. 'UCSF Chimera--a visualization system for exploratory research and analysis', *J Comput Chem*, 25: 1605-12.

Pinello, L., M. C. Canver, M. D. Hoban, S. H. Orkin, D. B. Kohn, D. E. Bauer, and G. C. Yuan. 2016. 'Analyzing CRISPR genome-editing experiments with CRISPResso', *Nat Biotechnol*, 34: 695-7.

Punjani, A., J. L. Rubinstein, D. J. Fleet, and M. A. Brubaker. 2017. 'cryoSPARC: algorithms for rapid unsupervised cryo-EM structure determination', *Nat Methods*, 14: 290-96.

Renaud, J. B., C. Boix, M. Charpentier, A. De Cian, J. Cochennec, E. Duvernois-Berthet, L. Perrouault, L. Tesson, J. Edouard, R. Thinard, Y. Cherifi, S. Menoret, S. Fontanière, N. de Crozé, A. Fraichard, F. Sohm, I. Anegon, J. P. Concordet, and C. Giovannangeli. 2016. 'Improved Genome Editing Efficiency and Flexibility Using Modified Oligonucleotides with TALEN and CRISPR-Cas9 Nucleases', *Cell Rep*, 14: 2263-72.

Rowlands, A. G., R. Panniers, and E. C. Henshaw. 1988. 'The catalytic mechanism of guanine nucleotide exchange factor action and competitive inhibition by phosphorylated eukaryotic initiation factor 2', *J Biol Chem*, 263: 5526-33.

Salimans, M., H. Goumans, H. Amesz, R. Benne, and H. O. Voorma. 1984. 'Regulation of protein synthesis in eukaryotes. Mode of action of eRF, an eIF-2-recycling factor from rabbit reticulocytes involved in GDP/GTP exchange', *Eur J Biochem*, 145: 91-8.

Schoof, M., M. Boone, L. Wang, R. Lawrence, A. Frost, and P. Walter. 2021. 'eIF2B conformation and assembly state regulate the integrated stress response', *Elife*, 10: e65703.

Schoof, M., L. Wang, J. Z. Cogan, R. Lawrence, M. Boone, J. D. Wuerth, A. Frost, and P. Walter. 2021. 'Viral Evasion of the Integrated Stress Response Through Antagonistic eIF2-P Mimicry', *Nat Commun,* 12: 7103.

Sekine, Y., A. Zyryanova, A. Crespillo-Casado, P. M. Fischer, H. P. Harding, and D. Ron. 2015. 'Stress responses. Mutations in a translation initiation factor identify the target of a memory-enhancing compound', *Science*, 348: 1027-30.

Sen, T., R. Gupta, H. Kaiser, and N. Sen. 2017. 'Activation of PERK Elicits Memory Impairment through Inactivation of CREB and Downregulation of PSD95 After Traumatic Brain Injury', *J Neurosci*, 37: 5900-11.

Shi, Y., K. M. Vattem, R. Sood, J. An, J. Liang, L. Stramm, and R. C. Wek. 1998. 'Identification and characterization of pancreatic eukaryotic initiation factor 2 alpha-subunit kinase, PEK, involved in translational control', *Mol Cell Biol*, 18: 7499-509.

Sidrauski, C., D. Acosta-Alvear, A. Khoutorsky, P. Vedantham, B. R. Hearn, H. Li, K. Gamache, C. M. Gallagher, K. K. Ang, C. Wilson, V. Okreglak, A. Ashkenazi, B. Hann, K. Nader, M. R. Arkin, A. R. Renslo, N. Sonenberg, and P. Walter. 2013. 'Pharmacological brake-release of mRNA translation enhances cognitive memory', *Elife*, 2: e00498.

Sidrauski, C., J. C. Tsai, M. Kampmann, B. R. Hearn, P. Vedantham, P. Jaishankar, M. Sokabe, A. S. Mendez, B. W. Newton, E. L. Tang, E. Verschueren, J. R. Johnson, N. J. Krogan, C. S. Fraser, J. S. Weissman, A. R. Renslo, and P. Walter. 2015. 'Pharmacological dimerization and activation of the exchange factor eIF2B antagonizes the integrated stress response', *Elife*, 4: e07314.

Siekierka, J., L. Mauser, and S. Ochoa. 1982. 'Mechanism of polypeptide chain initiation in eukaryotes and its control by phosphorylation of the alpha subunit of initiation factor 2', *Proc Natl Acad Sci U S A*, 79: 2537-40.

Tsai, J. C., L. E. Miller-Vedam, A. A. Anand, P. Jaishankar, H. C. Nguyen, A. R. Renslo, A. Frost, and P. Walter. 2018. 'Structure of the nucleotide exchange factor eIF2B reveals mechanism of memory-enhancing molecule', *Science*, 359: eaaq0939.

van der Knaap, M. S., P. A. Leegwater, A. A. Könst, A. Visser, S. Naidu, C. B. Oudejans, R. B. Schutgens, and J. C. Pronk. 2002. 'Mutations in each of the five subunits of translation initiation factor eIF2B can cause leukoencephalopathy with vanishing white matter', *Ann Neurol*, 51: 264-70.

Vattem, K. M., and R. C. Wek. 2004. 'Reinitiation involving upstream ORFs regulates ATF4 mRNA translation in mammalian cells', *Proc Natl Acad Sci U S A*, 101: 11269-74.

Welsh, G. I., and C. G. Proud. 1993. 'Glycogen synthase kinase-3 is rapidly inactivated in response to insulin and phosphorylates eukaryotic initiation factor eIF-2B', *Biochem J*, 294: 625-9.

Wong, Y. L., L. LeBon, R. Edalji, H. B. Lim, C. Sun, and C. Sidrauski. 2018. 'The small molecule ISRIB rescues the stability and activity of Vanishing White Matter Disease eIF2B mutant complexes', *Elife*, 7: e32733.

Wortham, N. C., M. Martinez, Y. Gordiyenko, C. V. Robinson, and C. G. Proud. 2014. 'Analysis of the subunit organization of the eIF2B complex reveals new insights into its structure and regulation', *Faseb j*, 28: 2225-37.

Wortham, N. C., J. D. Stewart, S. Harris, M. J. Coldwell, and C. G. Proud. 2016. 'Stoichiometry of the eIF2B complex is maintained by mutual stabilization of subunits', *Biochem J*, 473: 571-80.

Zhang, K. 2016. 'Gctf: Real-time CTF determination and correction', *J Struct Biol*, 193: 1-12.

Zheng, S. Q., E. Palovcak, J. P. Armache, K. A. Verba, Y. Cheng, and D. A. Agard. 2017. 'MotionCor2: anisotropic correction of beam-induced motion for improved cryo-electron microscopy', *Nat Methods*, 14: 331-32.

Zyryanova, A. F., K. Kashiwagi, C. Rato, H. P. Harding, A. Crespillo-Casado, L. A. Perera, A. Sakamoto, M. Nishimoto, M. Yonemochi, M. Shirouzu, T. Ito, and D. Ron. 2021. 'ISRIB Blunts the Integrated Stress Response by Allosterically Antagonising the Inhibitory Effect of Phosphorylated eIF2 on eIF2B', *Mol Cell*, 81: 88-103.e6.

Zyryanova, A. F., F. Weis, A. Faille, A. A. Alard, A. Crespillo-Casado, Y. Sekine, H. P. Harding, F. Allen, L. Parts, C. Fromont, P. M. Fischer, A. J. Warren, and D. Ron. 2018. 'Binding of ISRIB reveals a regulatory site in the nucleotide exchange factor eIF2B', *Science*, 359: 1533-36.

Chapter 4

An ultra-potent synthetic nanobody neutralizes SARS-CoV-2 by stabilizing inactive Spike

Summary

The SARS-CoV-2 virus enters host cells via an interaction between its Spike protein and the host cell receptor angiotensin converting enzyme 2 (ACE2). By screening a yeast surface-displayed library of synthetic nanobody sequences, we developed nanobodies that disrupt the interaction between Spike and ACE2. Cryogenic electron microscopy (cryo-EM) revealed that one nanobody, Nb6, binds Spike in a fully inactive conformation with its receptor binding domains (RBDs) locked into their inaccessible down-state, incapable of binding ACE2. Affinity maturation and structure-guided design of multivalency yielded a trivalent nanobody, mNb6-tri, with femtomolar affinity for Spike and picomolar neutralization of SARS-CoV-2 infection. mNb6-tri retains function after aerosolization, lyophilization, and heat treatment, which enables aerosol-mediated delivery of this potent neutralizer directly to the airway epithelia.

Introduction

Over the last two decades, three zoonotic β-coronaviruses have entered the human population, causing severe respiratory symptoms with high mortality (Ksiazek et al. 2003; Zaki et al. 2012; Zhou et al. 2020). The COVID-19 pandemic is caused by SARS-CoV-2, the most readily transmissible of these three coronaviruses (Chan et al. 2020; Huang et al. 2020; Wu et al. 2020; Zhu et al. 2020). No preventive treatment has been approved for any coronavirus to date, and the although vaccine development and rollout has seen great success, waning of vaccine efficacy, low booster adoption, and poor vaccine access in developing nations remain serious issues. The development of novel therapeutic and prophylactic approaches thus remains essential.

Coronavirus virions are bounded by a membrane that contains the homotrimeric transmembrane glycoprotein Spike responsible for virus entry into the host cell (Ke et al. 2020; Turonova et al. 2020). The surface-exposed portion of Spike is composed of two domains, S_1 and S_2 (Bosch et al. 2003). S_1 binds the host cell receptor angiotensin converting enzyme 2 (ACE2), while S_2 catalyzes fusion of the viral and host cell membranes (Cai et al. 2020; Wang et al. 2020; Yan et al. 2020). Contained within S_1 is the receptor binding domain (RBD), which directly binds to ACE2, and the N terminal domain (NTD). The RBD is attached to the body of Spike by a flexible region and can exist in an inaccessible down-state or an accessible up-state (Walls et al. 2020; Wrapp, Wang, et al. 2020). Binding to ACE2 requires the RBD in the up-state and enables cleavage by host proteases, triggering a conformational change in S_2 required for viral entry (Hoffmann et al. 2020). In SARS-CoV-2 virions, Spike exchanges between an active, open conformation with at least one RBD in the up-state and an inactive, closed conformation with all RBDs in the down-state (Ke et al. 2020; Turonova et al. 2020).

Results

We isolated single domain antibodies (nanobodies) that neutralize SARS-CoV-2 by screening a yeast surface-displayed library of >$2x10^9$ synthetic nanobody sequences for binders to the Spike ectodomain (McMahon et al. 2018). We used a mutant form of SARS-CoV-2 Spike ($Spike^{S2P}$) as the antigen (Wrapp, Wang, et al. 2020). $Spike^{S2P}$ lacks one of the two proteolytic cleavage sites between the S_1 and S_2 domains and introduces two mutations and a trimerization domain to stabilize the pre-fusion conformation. We labeled $Spike^{S2P}$ with biotin or with fluorescent dyes and selected nanobody-displaying yeast over multiple rounds, first by magnetic bead binding and then by fluorescence-activated cell sorting (Figure 4.1A).

Three rounds of selection yielded 21 unique nanobodies that bound $Spike^{S2P}$ and showed decreased binding in the presence of a dimeric construct of the ACE2 extracellular domain (ACE2-Fc). These nanobodies fall into two classes. Class I binds the RBD and competes directly with ACE2-Fc (Figure 4.1B). A prototypical example of this class is nanobody Nb6, which binds to $Spike^{S2P}$ and to RBD alone with a K_D of 210nM and 41nM, respectively (Figure 4.1C; Table 4.1). Class II, exemplified by nanobody Nb3, binds to $Spike^{S2P}$ (K_D=61nM), but displays no binding to RBD alone (Figure 4.1C, Table 4.1). In the presence of excess ACE2-Fc, binding of Nb6 and other Class I nanobodies is blocked entirely, whereas binding of Nb3 and other Class II nanobodies is moderately decreased (Figure 4.1B). These results suggest that Class I nanobodies target the RBD to block ACE2 binding, whereas Class II nanobodies target other epitopes. Indeed, surface plasmon resonance (SPR) experiments demonstrate that Class I and Class II nanobodies can bind $Spike^{S2P}$ simultaneously (Figure 4.1D).

Class I nanobodies show a consistently faster association rate constant (k_a) for nanobody binding to the isolated RBD than to $Spike^{S2P}$ (Table 4.1), which suggests that RBD accessibility

influences the K_D. We next tested the efficacy of Class I and Class II nanobodies to inhibit binding of fluorescently labeled Spike^{S2P} to ACE2-expressing HEK293 cells (Figure 4.1E; Table 4.1). Class I nanobodies Nb6 and Nb11 emerged as two of the most potent clones with IC_{50} values of 370 and 540nM, respectively. Class II nanobodies showed little to no activity in this assay. We prioritized two Class I nanobodies, Nb6 and Nb11, that combine potent Spike^{S2P} binding with relatively small differences in k_a between binding to Spike^{S2P} or RBD. For Class II nanobodies, we prioritized Nb3 because of its relative yield during purification (Table 4.1).

To define the binding sites of Nb6 and Nb11, we determined their cryogenic electron microscopy (cryo-EM) structures bound to Spike^{S2P} (Figure 4.2A-B; Figure 4.2 – figure supplement 1-3; Table 4.1 and 4.2). Both nanobodies recognize RBD epitopes that overlap the ACE2 binding site (Figure 4.2E). For Nb6 and Nb11, we resolved nanobody binding to both the open and closed conformations of Spike^{S2P}. We obtained a 3.0Å map of Nb6 bound to closed Spike^{S2P}, which enabled modeling of the Nb6-Spike^{S2P} complex (Figure 4.2A), including the complementarity determining regions (CDRs). We also obtained lower resolution maps for Nb6 bound to open Spike^{S2P} (3.8Å), and Nb11 bound to open and closed Spike^{S2P} (4.2Å, and 3.7Å, respectively). For these lower resolution maps, we could define the nanobody's binding orientation but not accurately model the CDRs.

Nb6 bound to closed Spike^{S2P} straddles the interface between two adjacent RBDs. The majority of the contacting surfaces are contributed by CDR1 and CDR2 of Nb6 (Figure 4.2C). CDR3 contacts the adjacent RBD positioned counterclockwise when viewed from the top (Figure 4. 2C). The binding of one Nb6 therefore stabilizes two adjacent RBDs in the down-state and likely pre-organizes the binding site for a second and third Nb6 molecule to stabilize the closed Spike conformation. By contrast, Nb11 bound to down-state RBDs only contacts a single RBD (Figure 4.2D).

The structure of Nb6 bound to closed Spike^{S2P} enabled us to engineer bivalent and trivalent nanobodies predicted to lock all RBDs in the down-state. We inserted flexible Gly-Ser linkers of either 15 or 20 amino acids to span the 52Å distance between adjacent Nb6 monomers bound to down-state RBDs in closed Spike^{S2P} (Figure 4.2 – figure supplement 4). These linkers are too short to span the 72Å distance between Nb6 molecules bound to open Spike. Moreover, steric clashes would prevent binding of three RBDs in open Spike with a single up-state RBD even with longer linker length (Figure 4.2 – figure supplement 4). By contrast, the minimum distance between adjacent Nb11 monomers bound to either open or closed Spike^{S2P} is 68Å. We predicted that multivalent binding by Nb6 constructs would display significantly slowed dissociation rates due to enhanced avidity.

In SPR experiments, both bivalent Nb6 with a 15 amino acid linker (Nb6-bi) and trivalent Nb6 with two 20 amino acid linkers (Nb6-tri) dissociate from Spike^{S2P} in a biphasic manner. The dissociation phase can be fitted to two components: a fast phase with kinetic rate constants k_{d1} of $2.7\text{x}10^{-2}\text{s}^{-1}$ for Nb6-bi and $2.9\text{x}10^{-2}\text{s}^{-1}$ for Nb6-tri, which are close to that observed for monovalent Nb6 (k_d=$5.6\text{x}10^{-2}\text{s}^{-1}$) and a slow phase that is dependent on avidity (k_{d2}=$3.1\text{x}10^{-4}\text{s}^{-1}$ for Nb6-bi and k_{d2}<$1.0\text{x}10^{-6}\text{s}^{-1}$ for Nb6-tri, respectively) (Figure 4.3A). The relatively similar k_d for the fast phase suggests that a fraction of the observed binding for the multivalent constructs is nanobody binding to a single Spike^{S2P} RBD. By contrast, the slow dissociation phase of Nb6-bi and Nb6-tri indicates engagement of two or three RBDs. We observed no dissociation for the slow phase of Nb6-tri over 10 minutes, indicating an upper boundary for k_{d2} of $1\text{x}10^{-6}\text{s}^{-1}$ and subpicomolar affinity. This measurement remains an estimate because the measurement is limited by the intrinsic dissociation rate of Spike^{S2P} from the SPR chip imposed by the chemistry used to immobilize Spike^{S2P}.

Biphasic dissociation could be explained by a slow interconversion between up- and down-state RBDs, with conversion to the more stable down-state required for multivalent binding: a single domain of Nb6-tri engaged with an up-state RBD would dissociate rapidly. The system would then re-equilibrate as the RBD flips into the down-state, eventually allowing Nb6-tri to trap all RBDs in closed Spike^{S2P}. To test this directly, we varied the association time for Nb6-tri binding to Spike^{S2P}. Indeed, we observed an exponential decrease in the percent fast-phase with a $t_{1/2}$ of 65s (Figure 4.3B), which, we surmise, reflects the timescale of conversion between the RBD up- and down-states in Spike^{S2P}. Taken together, dimerization and trimerization of Nb6 afforded 750-fold and >200,000-fold gains in K_D, respectively.

Unable to determine the binding site of Nb3 by cryo-EM, we turned to radiolytic hydroxyl radical footprinting. Apo or Nb3-bound Spike^{S2P} was exposed to synchrotron X-ray radiation to label solvent-exposed amino acids with hydroxyl radicals, which were subsequently quantified by mass spectrometry of protease digested Spike^{S2P} (Gupta et al. 2007). Two neighboring surface residues on the S_1 N-terminal domain of Spike (M177 and H207) were protected in the presence of Nb3 at a level consistent with prior observations of antibody-antigen interactions by hydroxyl radical footprinting (Figure 4.2 – figure supplement 5) (Zhang et al. 2017). Previously discovered coronavirus neutralizing antibodies bind an epitope within the N-terminal domain of Spike with Fab fragments that are non-competitive with the host cell receptor (Chi et al. 2020; Zhou et al. 2019). Further SPR experiments demonstrated that Nb3 can bind Spike^{S2P} simultaneously with monovalent ACE2 (Figure 4.3 – figure supplement 1A). We hypothesized that multivalent display of Nb3 on the surface of yeast may account for the partial decrease in Spike^{S2P} binding observed in the presence of ACE2-Fc. Indeed, a trivalent construct of Nb3 with 15 amino acid linkers (Nb3-tri) inhibited Spike^{S2P} binding to ACE2 cells with an IC_{50} of 41nM (Figure 4.3 – figure supplement 1B). How Nb3-tri disrupts Spike-ACE2 interactions remains unclear.

We next tested the neutralization activity of monovalent and trivalent versions of our top Class I (Nb6 and Nb11) and Class II (Nb3) nanobodies against SARS-CoV-2 pseudotyped lentivirus using a previously described assay (Crawford et al. 2020). Nb6 and Nb11 inhibited pseudovirus infection with IC_{50} values of 2.0μM and 2.4μM, respectively. Nb3 inhibited pseudovirus infection with an IC_{50} of 3.9μM (Figure 4.3C, Table 4.1). Nb6-tri shows a 2000-fold enhancement of inhibitory activity, with an IC_{50} of 1.2nM, whereas trimerization of Nb11 and Nb3 resulted in more modest gains of 40- and 10-fold (51nM and 400nM), respectively (Figure 4.3C). We confirmed these neutralization activities with a viral plaque assay using live SARS-CoV-2 virus infection of VeroE6 cells. Here, Nb6-tri proved exceptionally potent, neutralizing SARS-CoV-2 with an average IC_{50} of 160pM (Figure 4.3D). Nb3-tri neutralized SARS-CoV-2 with an average IC_{50} of 140nM (Figure 4.3D).

We further optimized the potency of Nb6 by selecting a saturation mutagenesis library targeting all three CDRs. Two rounds of selection identified high-affinity clones with two penetrant mutations: I27Y in CDR1 and P105Y in CDR3. We incorporated these mutations into Nb6 to generate matured Nb6 (mNb6), which binds with 500-fold increased affinity to $Spike^{S2P}$ (Figure 4.4A). mNb6 inhibits both pseudovirus and live SARS-CoV-2 infection with low nanomolar potency, a ~200-fold improvement compared to Nb6 (Figure 4.4B; Table 4.1).

A 2.9Å cryo-EM structure shows that mNb6 binds to closed $Spike^{S2P}$ (Figure 4.4C; Figure 4.4 – figure supplement 1). mNb6 induces a slight rearrangement of the down-state RBDs as compared to $Spike^{S2P}$ bound to Nb6, inducing a 9° rotation of the RBD away from the central three-fold symmetry axis. This deviation likely arises from a different interaction between CDR3 and $Spike^{S2P}$, which nudges the RBDs into a new resting position (Figure 4.4D). While the I27Y substitution optimizes local contacts between CDR1 in its original binding site on the RBD, the P105Y substitution leads to a marked rearrangement of CDR3 in mNb6 (Figure 4.4E-F). This

conformational change yields a different set of contacts between mNb6 CDR3 and the adjacent RBD. An X-ray crystal structure of mNb6 alone revealed dramatic conformational differences in CDR1 and CDR3 between free and Spike^{S2P}-bound mNb6 (Figure 4.4G; Table 4.3). Although differences in loop conformation in the crystal structure may arise from crystal lattice contacts, they are suggestive of conformational heterogeneity for unbound mNb6 and induced-fit rearrangements upon binding to Spike^{S2P}.

The binding orientation of mNb6 is similar to that of Nb6, suggesting that multivalent design would likewise enhance binding affinity. Unlike Nb6-tri, trivalent mNb6 with a 20 amino acid linker (mNb6-tri) bound to Spike^{S2P} with no observable fast-phase dissociation and no measurable dissociation over ten minutes, yielding an upper bound for the dissociation rate constant k_d of $1.0 \times 10^{-6} s^{-1}$ ($t_{1/2}$>8 days) and a K_D of <1pM (Figure 4.4A). mNb6-tri displays further gains in potency in both pseudovirus and live SARS-CoV-2 infection assays with IC_{50} values of 120 pM (5.0ng/mL) and 54pM (2.3ng/mL), respectively (Figure 4.4B, Table 4.1). Given the sub-picomolar affinity observed by SPR, it is likely that these viral neutralization potencies reflect the lower limit of the assays. mNb6-tri is therefore an exceptionally potent SARS-CoV-2 neutralizing molecule.

We next tested whether viral neutralization by the Class I nanobody mNb6 is potentially synergistic with the Class II nanobody Nb3-tri. In pseudovirus neutralization assays, we observed an additive effect when combining Nb3-tri with mNb6 (Figure 4.5 – figure supplement 1). However, the potency for mNb6 viral neutralization was unchanged with increasing concentrations of Nb3-tri, suggesting minimal synergy between these two nanobodies.

We next tested Nb6 and its derivatives for stability. Circular dichroism revealed melting temperatures of 66.9, 62.0, 67.6, and 61.4°C for Nb6, Nb6-tri, mNb6 and mNb6-tri, respectively

(Figure 4.5 – figure supplement 2). Moreover, mNb6 and mNb6-tri were stable to lyophilization and to aerosolization, showing no aggregation by size exclusion chromatography and preserved high affinity binding to Spike^{S2P} (Figure 4.5A-B and Figure 4.5 – figure supplement 2). Finally, mNb6-tri retains potent inhibition of pseudovirus infection after aerosolization, lyophilization, or heat treatment for 1 hour at 50°C (Figure 4.5C).

Discussion

Strategies to prevent SARS-CoV-2 entry into the host cell aim to block the ACE2-RBD interaction. Although high-affinity monoclonal antibodies are leading the way as potential therapeutics (Baum et al. 2020; Cao et al. 2020; Chi et al. 2020; Ju et al. 2020; Liu et al. 2020; Pinto et al. 2020; Rogers et al. 2020; Zost et al. 2020; Tortorici et al. 2020), they are expensive to produce by mammalian cell expression and need to be intravenously administered by healthcare professionals (Ledford 2020). Large doses are needed for prophylactic use, as only a small fraction of systemic antibodies cross the epithelial cell layers lining the airways (Leyva-Grado et al. 2015). By contrast, nanobodies can be inexpensively produced in bacteria or yeast. The inherent stability of nanobodies enables aerosolized delivery directly to the nasal and lung epithelia (Detalle et al. 2016). Indeed, aerosol delivery of a trimeric nanobody targeting respiratory syncytial virus (ALX-0171) was recently demonstrated to be effective in substantially decreasing measurable viral load in hospitalized infants (Cunningham et al. 2020). Finally, potential immunogenicity of camelid-derived nanobodies can be mitigated by established humanization strategies (Vincke et al. 2009).

Nanobody multimerization has been shown to improve target affinity by avidity (Detalle et al. 2016; Wrapp, De Vlieger, et al. 2020). In the case of Nb6 and mNb6, structure-guided design of a multimeric construct that simultaneously engages all three RBDs yielded profound gains in potency. Furthermore, because RBDs must be in the up-state to engage with ACE2, conformational control of RBD accessibility serves as an added neutralization mechanism (Tortorici et al. 2020). Indeed, when mNb6-tri engages with Spike, it prevents ACE2 binding by both directly occluding the binding site and by locking the RBDs into an inactive conformation.

Our discovery of Class II neutralizing nanobodies demonstrates potentially novel mechanisms of disrupting Spike function. Pairing of Class I and Class II nanobodies in a prophylactic or therapeutic cocktail could provide both potent neutralization and prevention of escape variants (Baum et al. 2020). The combined stability, potency, and diverse epitope engagement of our anti-Spike nanobodies therefore provide a unique potential prophylactic and therapeutic strategy to limit the continued toll of the COVID-19 pandemic.

Figures

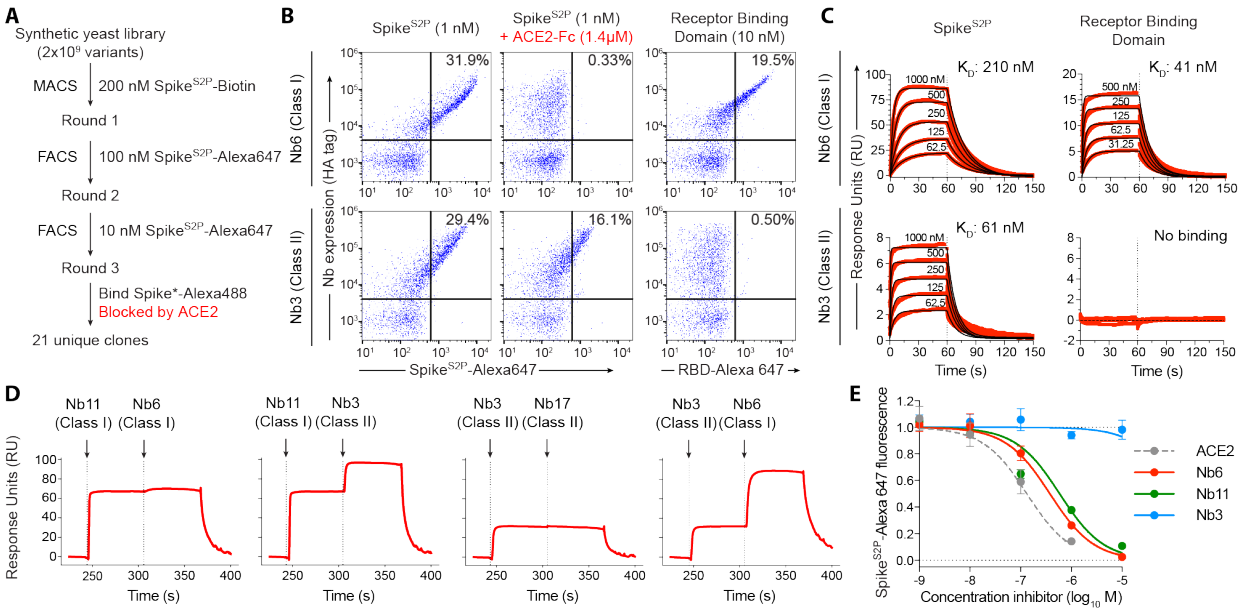

Figure 4.1: Discovery of two distinct classes of anti-Spike nanobodies.
A, Selection strategy for identification of anti-Spike nanobodies that disrupt Spike-ACE2 interactions using magnetic bead selections (MACS) or fluorescence activated cell sorting (FACS). **B,** Flow cytometry of yeast displaying Nb6 (a Class I nanobody) or Nb3 (a Class II nanobody). Nb6 binds Spike^{S2P}-Alexa 647 and receptor binding domain (RBD-Alexa 647). Nb6 binding to Spike^{S2P} is completely disrupted by an excess (1.4 μM) of ACE2-Fc. Nb3 binds Spike^{S2P}, but not the RBD. Nb3 binding to Spike^{S2P} is partially decreased by ACE2-Fc. **C,** SPR of Nb6 and Nb3 binding to either Spike^{S2P} or RBD. Red traces are raw data and global kinetic fits are shown in black. Nb3 shows no binding to RBD. **D,** SPR experiments with immobilized Spike^{S2P} show that Class I and Class II nanobodies can bind Spike^{S2P} simultaneously. By contrast, two Class I nanobodies or Class II nanobodies do not bind simultaneously. **E,** Nanobody inhibition of 1 nM Spike^{S2P}-Alexa 647 binding to ACE2 expressing HEK293T cells. n = 3 (ACE2, Nb3) or 5 (Nb6, Nb11) biological replicates. All error bars represent s.e.m.

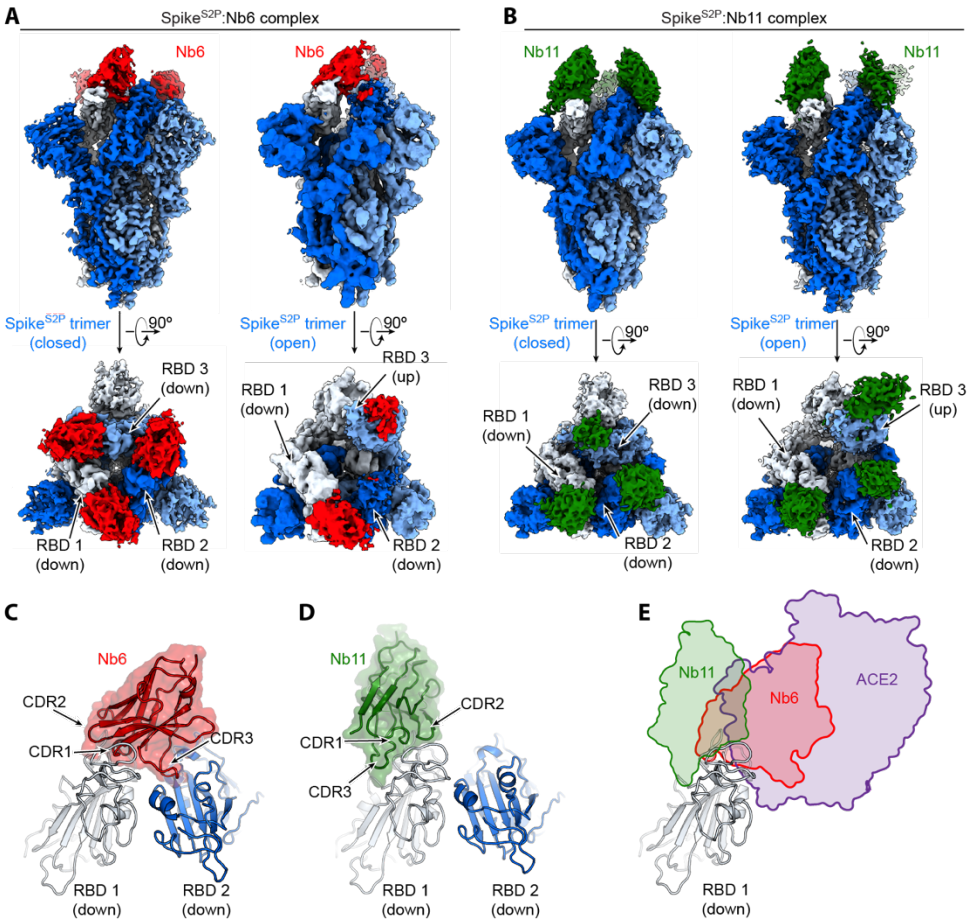

Figure 4.2: Cryo-EM structures of Nb6 and Nb11 bound to Spike.
A, Cryo-EM maps of Spike^{S2P}-Nb6 complex in either closed (left) or open (right) Spike^{S2P} conformation. **B,** Cryo-EM maps of Spike^{S2P}-Nb11 complex in either closed (left) or open (right) Spike^{S2P} conformation. The top views show receptor binding domain (RBD) up- or down-states. **C,** Nb6 straddles the interface of two down-state RBDs, with CDR3 reaching over to an adjacent RBD. **D,** Nb11 binds a single RBD in the down-state (displayed) or similarly in the up-state. No cross-RBD contacts are made by Nb11 in either RBD up- or down-state. **E,** Comparison of RBD epitopes engaged by ACE2 (purple), Nb6 (red), or Nb11 (green). Both Nb11 and Nb6 directly compete with ACE2 binding.

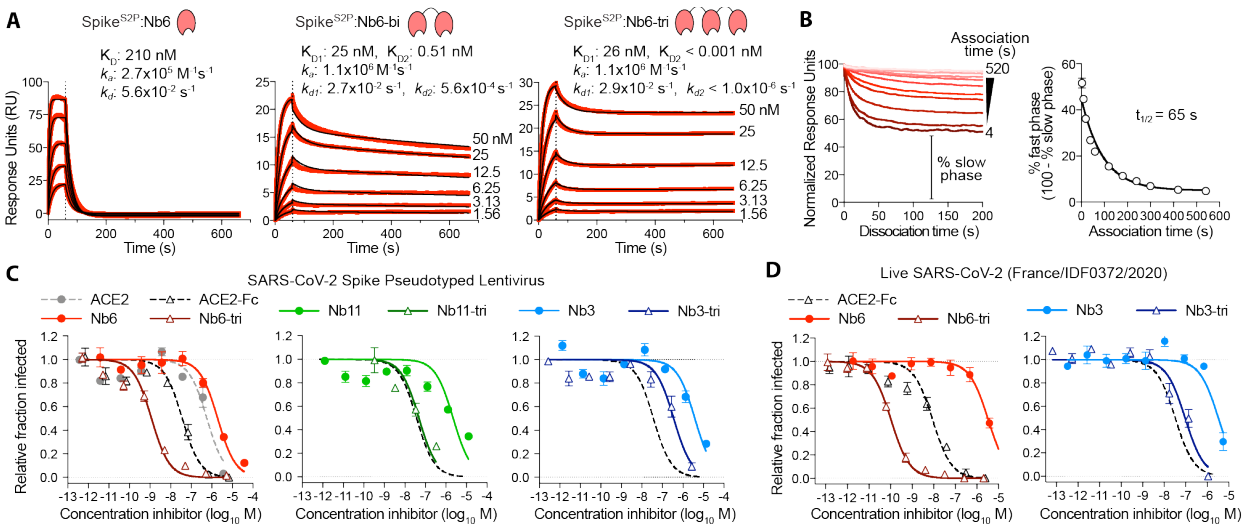

Figure 4.3: Multivalency improves nanobody affinity and inhibitory efficacy.
A, SPR of Nb6 and multivalent variants. Red traces show raw data and black lines show global kinetic fit for Nb6 and independent fits for association and dissociation phases for Nb6-bi and Nb6-tri. **B,** Dissociation phase SPR traces for Nb6-tri after variable association time ranging from 4 to 520 s. Curves were normalized to maximal signal at the beginning of the dissociation phase. Percent fast phase is plotted as a function of association time (right) with a single exponential fit. n = 3 independent biological replicates. **C,** Inhibition of pseudotyped lentivirus infection of ACE2 expressing HEK293T cells. n = 3 biological replicates for all but Nb11-tri (n = 2) **D,** Inhibition of live SARS-CoV-2 virus. Representative biological replicate with n = 3 (right panel) or 4 (left panel) technical replicates per concentration. n = 3 biological replicates for all but Nb3 and Nb3-tri (n = 2). All error bars represent s.e.m.

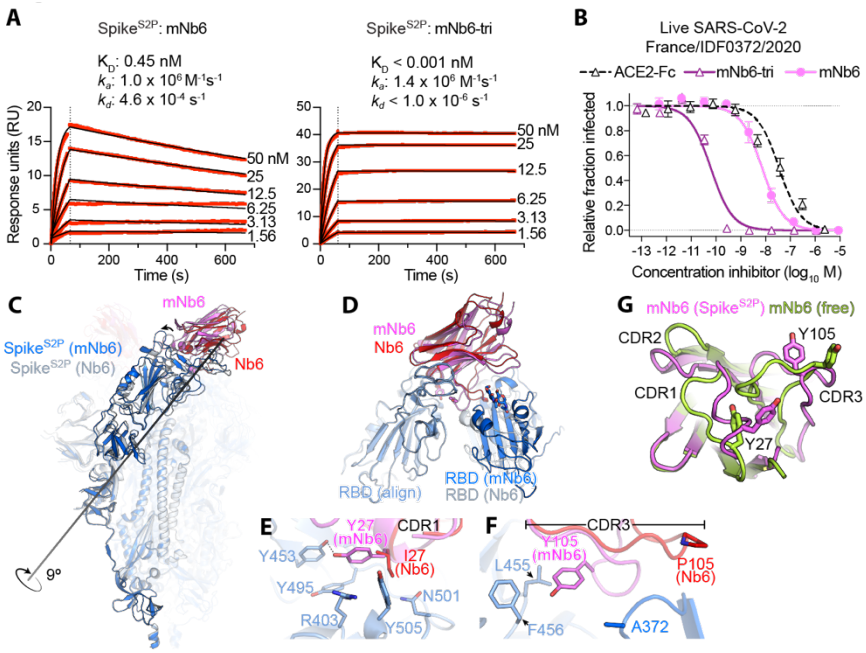

Figure 4.4: Affinity maturation of Nb6 yields a picomolar SARS-CoV-2 neutralizing molecule. **A,** SPR of mNb6 and mNb6-tri binding to immobilized Spike^{S2P}. Red traces show raw data and black lines show global kinetic fit. No dissociation was observed for mNb6-tri over 10 minutes. **B,** mNb6 and mNb6-tri inhibit SARS-CoV-2 infection of VeroE6 cells in a plaque assay. Representative biological replicate with n = 4 technical replicates per concentration. n = 3 biological replicates for all samples. All error bars represent s.e.m. **C,** Comparison of closed Spike^{S2P} bound to mNb6 and Nb6. Rotational axis for RBD movement is highlighted. **D,** Comparison of receptor binding domain (RBD) engagement by Nb6 and mNb6. One RBD was used to align both structures (RBD align), demonstrating changes in Nb6 and mNb6 position and the adjacent RBD**. E,** CDR1 of Nb6 and mNb6 binding to the RBD. As compared to I27 in Nb6, Y27 of mNb6 hydrogen bonds to Y453 and optimizes pi-pi and pi-cation interactions with the RBD. **F,** CDR3 of Nb6 and mNb6 binding to the RBD demonstrating a large conformational rearrangement of the entire loop in mNb6. **G,** Comparison of mNb6 complementarity determining regions in either the cryo-EM structure of the Spike^{S2P}-mNb6 complex or an X-ray crystal structure of mNb6 alone.

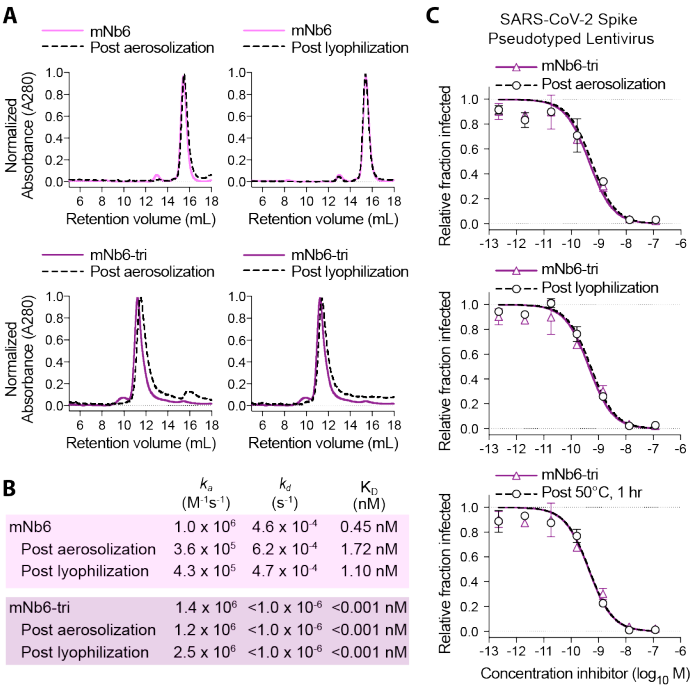

B

	k_a ($M^{-1}s^{-1}$)	k_d (s^{-1})	K_D (nM)
mNb6	1.0×10^6	4.6×10^{-4}	0.45 nM
Post aerosolization	3.6×10^5	6.2×10^{-4}	1.72 nM
Post lyophilization	4.3×10^5	4.7×10^{-4}	1.10 nM
mNb6-tri	1.4×10^6	$<1.0 \times 10^{-6}$	<0.001 nM
Post aerosolization	1.2×10^6	$<1.0 \times 10^{-6}$	<0.001 nM
Post lyophilization	2.5×10^6	$<1.0 \times 10^{-6}$	<0.001 nM

Figure 4.5: mNb6 and mNb6-tri retain activity after aerosolization, lyophilization, and heat treatment.
A, Size exclusion chromatography of nanobodies after lyophilization or aerosolization. **B,** Summary table of SPR kinetics data and affinities for aerosolized or lyophilized mNb6 and mNb6-tri. **C,** Inhibition of pseudotyped lentivirus infection of ACE2 expressing HEK293T cells by mNb6-tri after aerosolization, lyophilization, or heat treatment at 50°C for 1 hour.

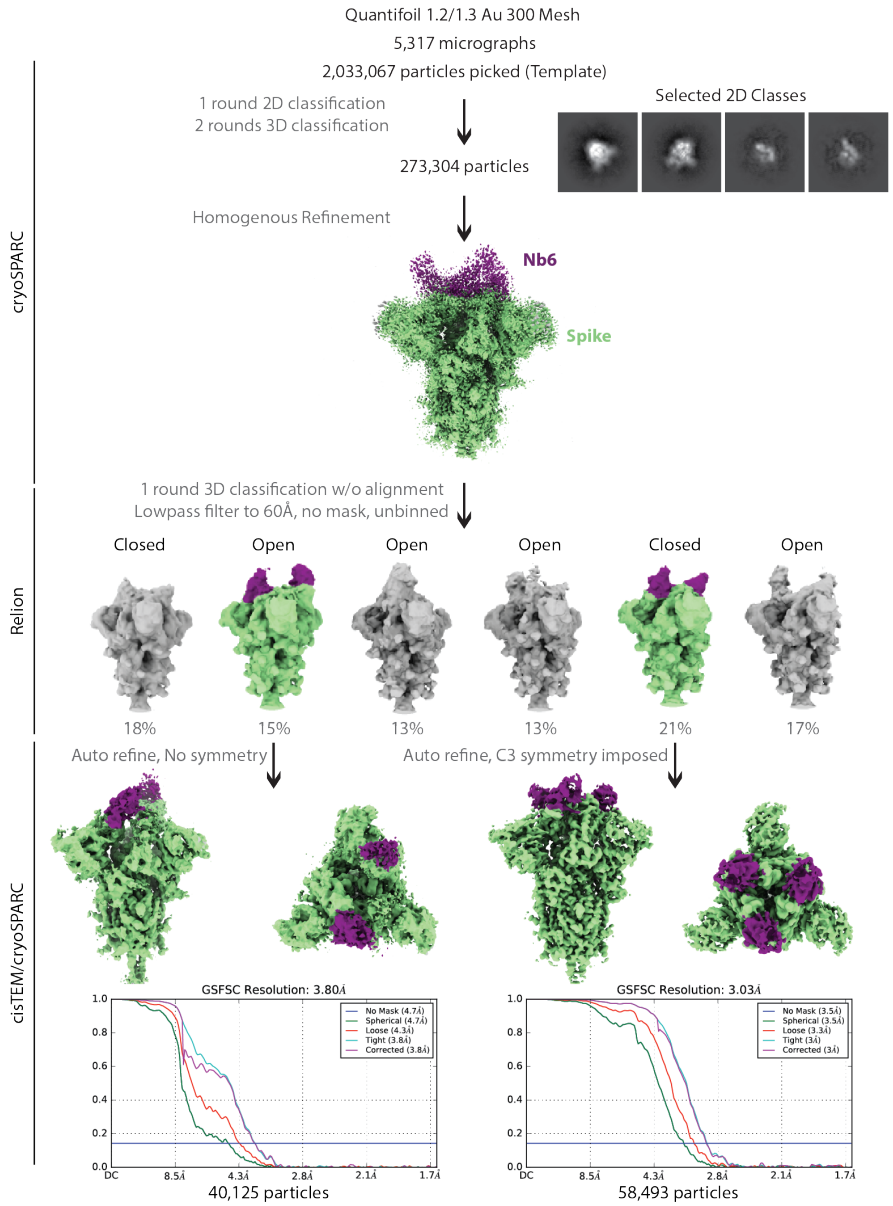

Figure 4.2 – figure supplement 1: Cryo-EM workflow for Nb6
A flowchart representation of the classification workflow for Spike^{S2P}-Nb6 complexes yielding open and closed Spike^{S2P} conformations. From top to bottom, particles were template picked with a set of 20 Å low-pass filtered 2D backprojections of apo-Spike^{S2P} in the closed conformation. Extracted particles in 2D classes suggestive of various Spike^{S2P} views were subject to a round of heterogenous refinement in cryoSPARC with two naïve classes generated from a truncated *Ab initio* job, and a 20 Å low-pass filtered volume of apo-Spike^{S2P} in the closed conformation. Particles in the Spike^{S2P} 3D class were subject to 25 iterations of 3D classification into 6 classes without alignment in RELION, using the same input volume from cryoSPARC 3D classification, low pass filtered to 60 Å, T = 8. Particles in classes representing the open and closed Spike^{S2P} conformations were imported into cisTEM for automatic refinement. Half maps from refinement were imported into cryoSPARC for local resolution estimation.

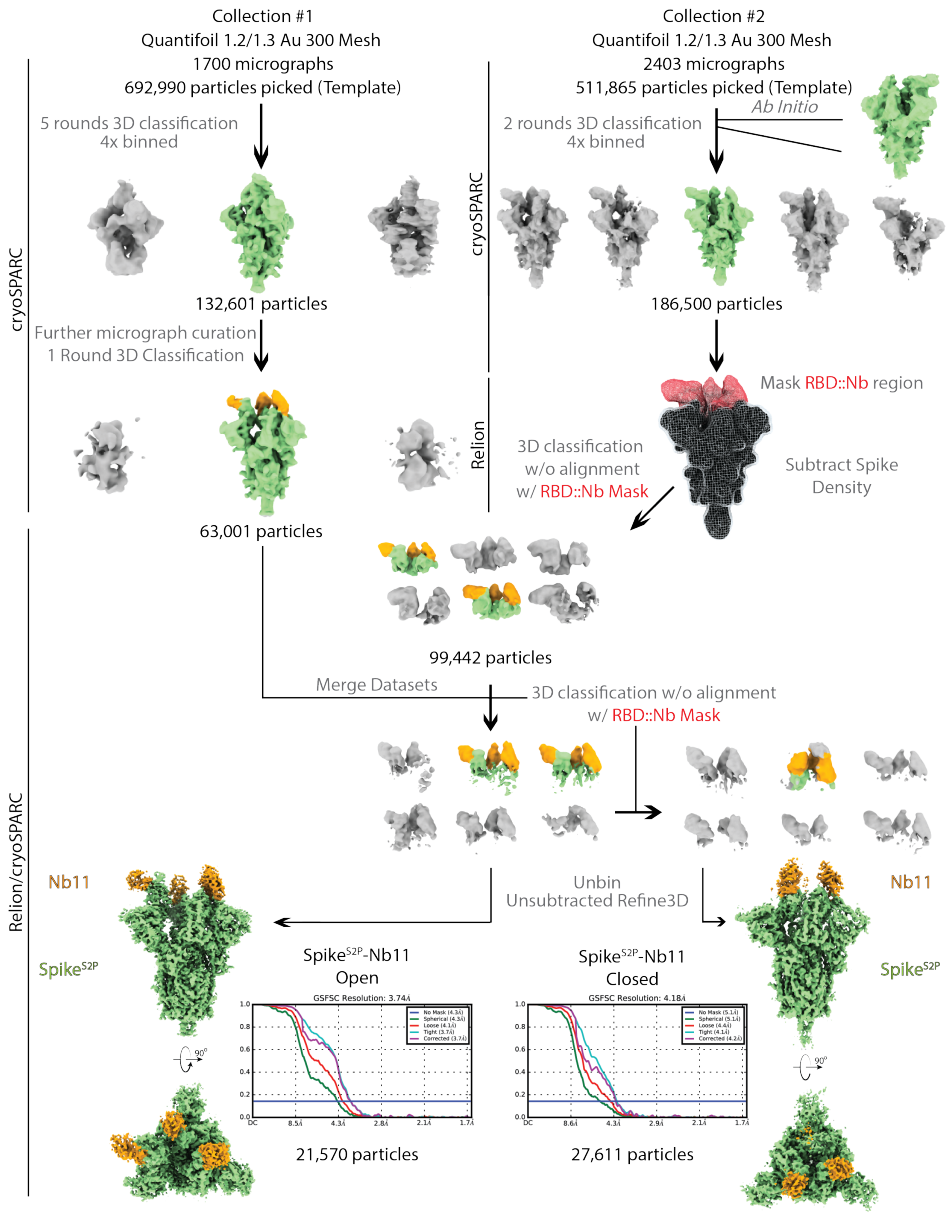

Figure 4.2 – figure supplement 2: Cryo-EM workflow for Nb11

A flowchart representation of the classification workflow for Spike^{S2P}-Nb11 complexes yielding open and closed Spike^{S2P} conformations. From top to bottom, particles were template picked from two separate collections with a set of 20 Å low-pass filtered 2D backprojections of apo-Spike^{S2P} in the closed conformation. Extracted particles were Fourier cropped to 128 pixels prior to extensive heterogenous refinement in cryoSPARC, using a 20 Å low-pass filtered volume of apo-Spike^{S2P} in the closed conformation and additional naïve classes for removal of non-Spike^{S2P} particles. After cryoSPARC micrograph curation and heterogenous refinement, Spike^{S2P} density corresponding to all regions outside of the ACE2 RBD::Nanobody interface were subtracted. A mask around the ACE2 RBD::Nanobody interface was generated, and used for multiple rounds of 3D classification without alignment in RELION. Particles in classes representing open and closed Spike^{S2P} conformations were selected, unsubtracted and

unbinned prior to refinement in RELION. Half maps from refinement were imported into cryoSPARC for local resolution estimation.

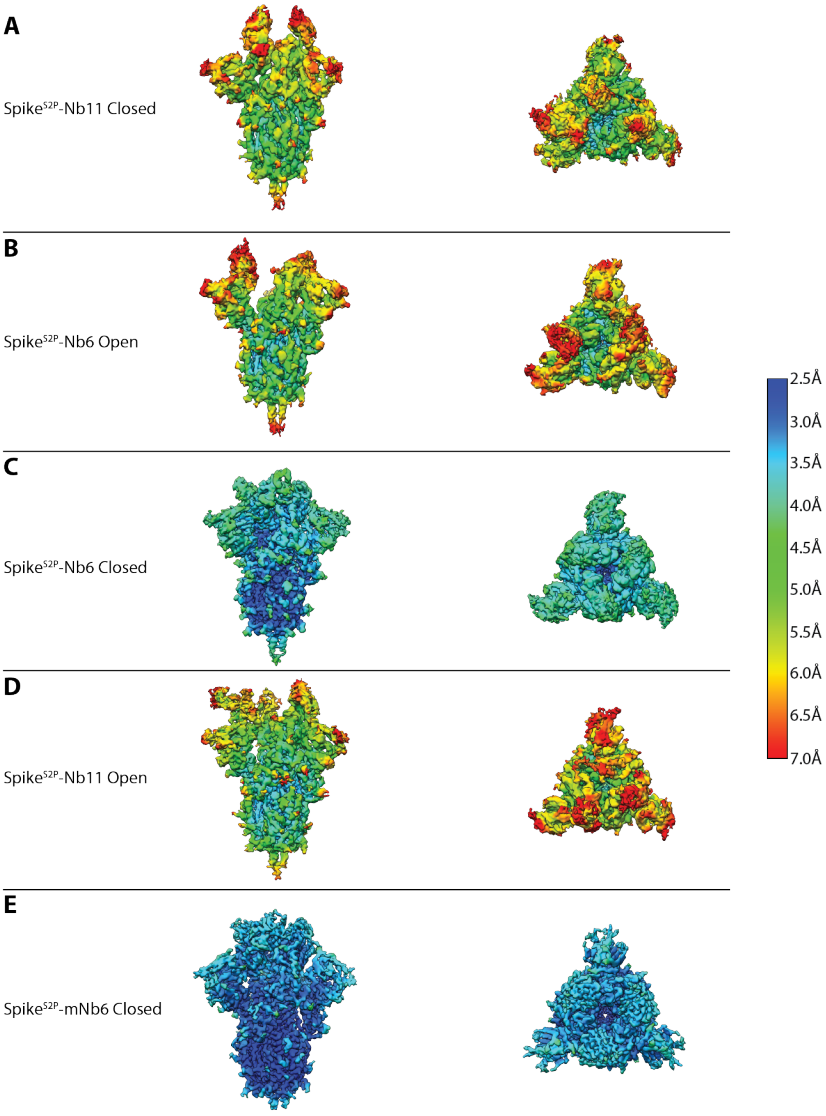

Figure 4.2 – figure supplement 3: Local resolution of cryo-EM maps
Local resolution estimates of Spike^{S2P} complexes with A-B) Nb6, C-D) Nb11, and E) mNb6 as generated in cryoSPARC. All maps (except mNb6) are shown with the same enclosed volume. All maps are colored on the same scale, as indicated.

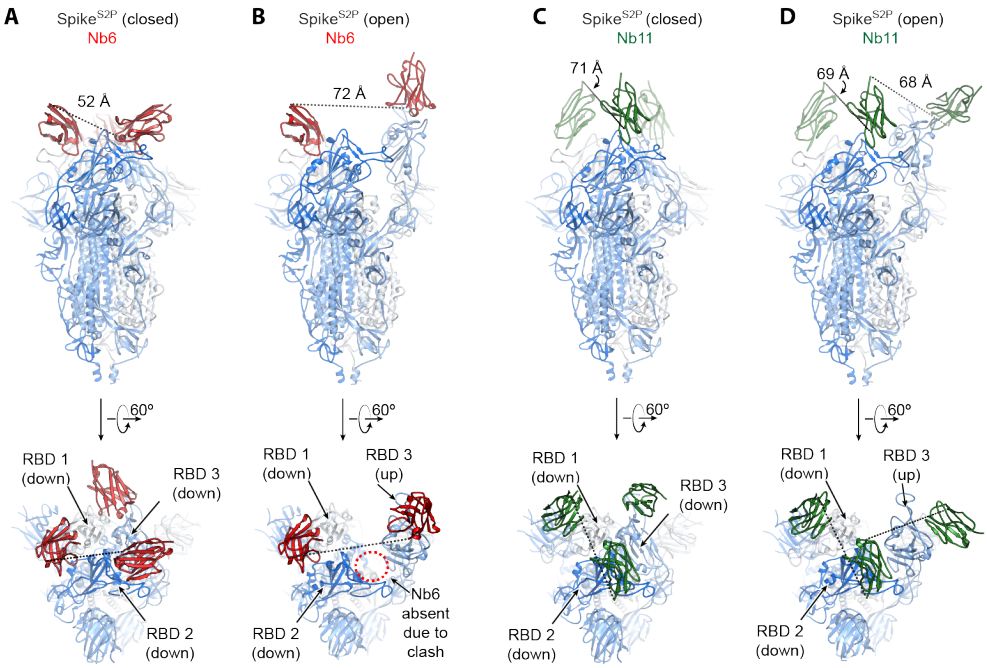

Figure 4.2 – figure supplement 4: Modeling of distances for multimeric nanobody design. **A,** Model of Spike^{S2P}:Nb6 complex in the closed state. The minimal distance between adjacent Nb6 N- and C-termini is 52 Å (dashed line). **B,** Model of Spike^{S2P}:Nb6 complex in the open state with Nb6 docked into the cryo-EM density for up-state RBD. Minimal distance between N- and C-termini of both nanobodies is 72 Å**.** Nb6 cannot bind RBD2 in open Spike^{S2P}, as this would sterically clash with RBD3. **C,** Model of Spike^{S2P}:Nb11 complex in the closed state. The minimal distance between adjacent Nb6 N- and C-termini is 71 Å (dashed line). **D,** Model of Spike^{S2P}:Nb11 complex in the open state. The minimal distance between adjacent Nb6 N- and C-termini is 68 Å between Nb11 bound to RBD2 in the down-state and RBD3 in the up-state. For B, the model of Nb6 from A was docked into the cryo-EM map to enable modeling of distance between N- and C-termini. For C and D, a generic nanobody was docked into cryo-EM maps to model the distance between N- and C-termini.

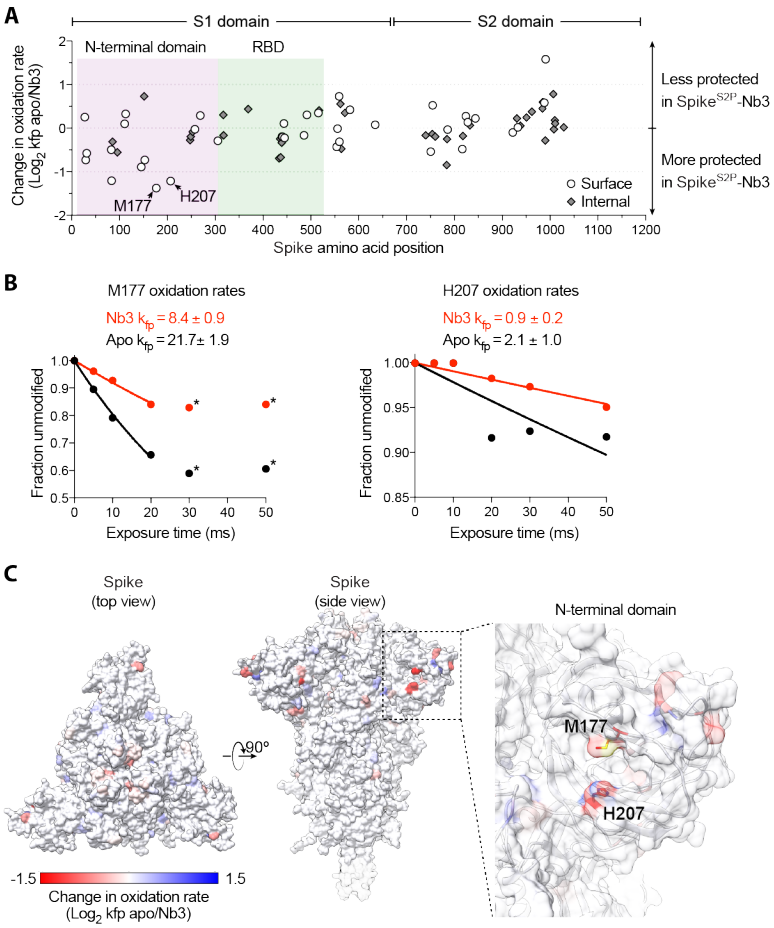

Figure 4.2 – figure supplement 5: Radiolytic hydroxyl radical footprinting of Spike^{S2P}. **A,** Change in oxidation rate between Spike^{S2P} and Nb3-Spike^{S2P} complexes at all residues. A cluster of highly protected residues in the Spike^{S2P}-Nb3 complex is observed in the N-terminal domain. **B,** Oxidation rate plots of the two (M177, H207) most heavily protected residues upon Nb3 binding to Spike^{S2P}. Data points labeled with an asterisk are excluded from rate calculations as these values fall outside of the first order reaction, likely due to extensive oxidation-mediated damage. **C,** Change in oxidation rate mapped onto Spike in the all RBD down conformation.

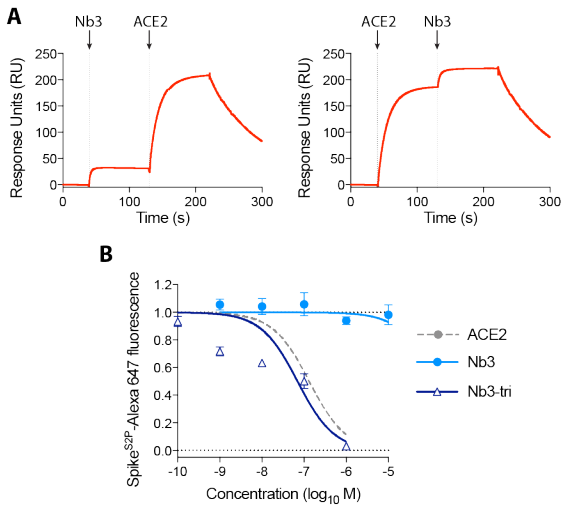

Figure 4.3 – figure supplement 1: Multivalent Nb3 construct inhibits Spike^{S2P}:ACE2 interaction.
A, SPR experiments with immobilized Spike^{S2P} show that Nb3 and monovalent ACE2 can bind Spike^{S2P} simultaneously. The order of Nb3 and monovalent ACE2 does not affect the binding of the second reagent. Nb3 therefore does not inhibit Spike^{S2P} binding to monovalent ACE2. **B,** Nanobody inhibition of 1 nM Spike^{S2P}-Alexa 647 binding to ACE2 expressing HEK293T cells by either monovalent or trivalent Nb3. n = 2 biological replicates for Nb3-tri. All error bars represent s.e.m.

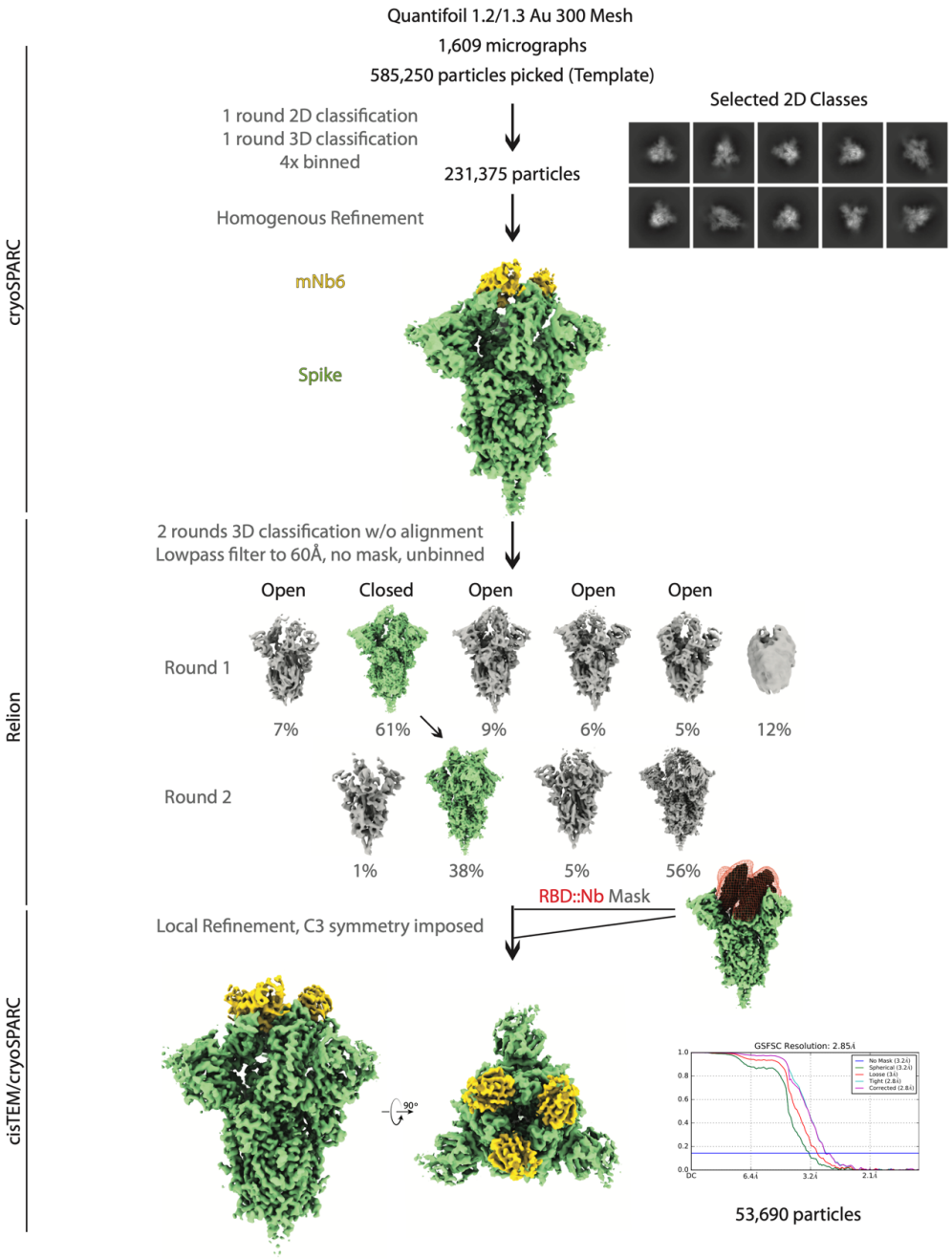

Figure 4.3 – figure supplement 2: CryoEM workflow for mNb6
A flowchart representation of the classification workflow for the Spike^{S2P}-mNb6 complex yielding a closed Spike^{S2P} conformation. From top to bottom, particles were template picked from two separate collections with a set of 20Å low-pass filtered 2D backprojections of apo-Spike^{S2P} in the closed conformation. Extracted particles were Fourier cropped to 96 pixels prior to 2D classification. Particles in Spike^{S2P} 2D classes were selected for a round of heterogeneous refinement in cryoSPARC using a 20 Å low-pass filtered volume of apo-Spike^{S2P} in the closed conformation and additional naïve classes for removal of non-Spike^{S2P} particles. In RELION, particles in the Spike^{S2P} 3D class were subject to two rounds of 3D classification without alignment into 6 classes using the same input volume from cryoSPARC 3D classification, low pass filtered to 60 Å, T = 8. Unbinned particles in the Spike^{S2P}-closed conformation were

exported into cisTEM for automatic refinement, followed by local refinement using a mask around the RBD::Nanobody interface. Half maps from refinement were imported into cryoSPARC for local resolution estimation.

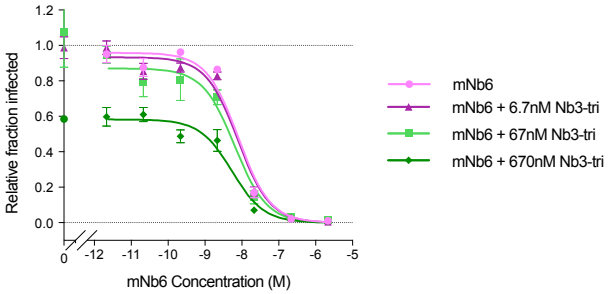

Figure 4.5 – figure supplement 1: mNb6 and Nb3-tri are additive for viral neutralization. Inhibition of pseudotyped lentivirus infection of ACE2 expressing HEK293T cells by mNb6 with increasing concentrations of Nb3-tri. mNb6 neutralization is additive with Nb3-tri, as demonstrated by inhibitory activity at a sub-saturating dose of Nb3-tri. However, the potency of mNb6 is unchanged by Nb3-tri, suggesting no synergistic effect on viral neutralization.

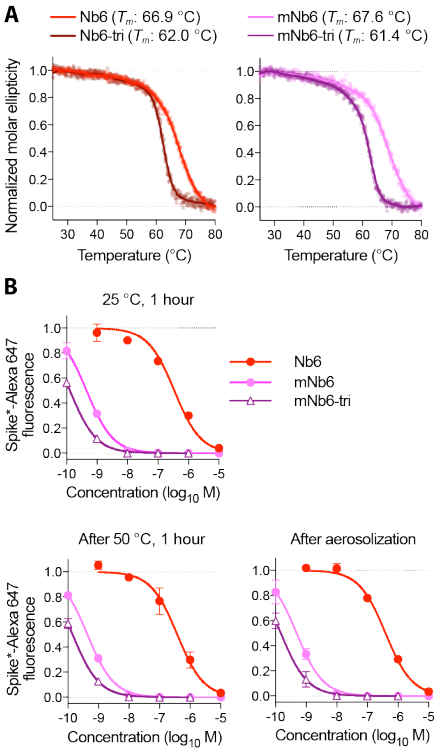

Figure 4.5 – figure supplement 2: Stability of Nb6 and its derivatives.
A, Thermal denaturation of nanobodies assessed by circular dichroism measurement of molar ellipticity at 204 nm. Apparent melting temperatures (T_m) for each nanobody are indicated. **B,** Nanobody inhibition of 1 nM Spike^{S2P}-Alexa 647 binding to ACE2 expressing HEK293T cells after incubation at either 25 °C or 50 °C for 1 hour or after aerosolization.

Table 4.1. Anti-Spike nanobody affinity and neutralization potency

Nanobody	Class	Spike^{S2P} Binding			RBD Binding			Spike^{S2P} Competition IC_{50} (s.e.m) (M)[a]	SARS-CoV-2 Pseudovirus IC_{50} (s.e.m.) (M)[b]	Live SARS-CoV-2 IC_{50} (s.e.m.) (M)[c]
		k_a ($M^{-1}s^{-1}$)	k_d (s^{-1})	K_D (M)	k_a ($M^{-1}s^{-1}$)	k_d (s^{-1})	K_D (M)			
Nb2	I	$9.0x10^{5}$	$5.3x10^{-1}$	$5.9x10^{-7}$	$1.0x10^{6}$	$9.9x10^{-1}$	$9.7x10^{-7}$	$8.3x10^{-6}$ ($1.7x10^{-6}$)	NP	NP
Nb3[d]	II	$1.8x10^{6}$	$1.1x10^{-1}$	$6.1x10^{-8}$	NB			NC	$3.9x10^{-6}$ ($7.9x10^{-7}$)	$3.0x10^{-6}$ ($3.2x10^{-7}$)
Nb6	I	$2.7x10^{5}$	$5.6x10^{-2}$	$2.1x10^{-7}$	$2.1x10^{6}$	$8.7x10^{-2}$	$4.1x10^{-8}$	$3.7x10^{-7}$ ($4.9x10^{-8}$)	$2.0x10^{-6}$ ($3.5x10^{-7}$)	$3.3x10^{-6}$ ($7.2x10^{-7}$)
Nb8	I	$1.4x10^{5}$	$8.1x10^{-1}$	$5.8x10^{-6}$	$6.6x10^{5}$	$3.3x10^{-1}$	$5.1x10^{-7}$	$4.8x10^{-6}$ ($4.9x10^{-7}$)	NP	NP
Nb11	I	$1.2x10^{6}$	$1.6x10^{-1}$	$1.4x10^{-7}$	$3.2x10^{6}$	$2.4x10^{-1}$	$7.6x10^{-8}$	$5.4x10^{-7}$ ($1.2x10^{-7}$)	$2.4x10^{-6}$ ($5.4x10^{-7}$)	NP
Nb12	I	$1.2x10^{2}$	$2.0x10^{-4}$	$1.6x10^{-6}$	Biphasic	Biphasic	Biphasic	$2.5x10^{-7}$ ($5.5x10^{-8}$)	$1.2x10^{-6}$ ($9.0x10^{-7}$)	NP
Nb15	I	$1.7x10^{5}$	$2.3x10^{-1}$	$1.3x10^{-6}$	$6.0x10^{5}$	$2.2x10^{-1}$	$3.6x10^{-7}$	$2.2x10^{-6}$ ($2.5x10^{-7}$)	$6.7x10^{-6}$ ($3.6x10^{-6}$)	NP
Nb16	I	$1.1x10^{5}$	$1.3x10^{-1}$	$1.3x10^{-6}$	NP			$9.5x10^{-7}$ ($1.1x10^{-7}$)	NP	NP
Nb17[d]	II	$7.3x10^{5}$	$2.0x10^{-1}$	$2.7x10^{-7}$	NB			NC	$7.6x10^{-6}$ ($1.0x10^{-6}$)	NP
Nb18[d]	II	$1.4x10^{5}$	$6.4x10^{-3}$	$4.5x10^{-8}$	NB			$5.2x10^{-5}$ ($1.5x10^{-5}$)	NP	NP
Nb19	I	$2.4x10^{4}$	$1.1x10^{-1}$	$4.5x10^{-6}$	$1.0x10^{5}$	$8.9x10^{-2}$	$8.8x10^{-7}$	$4.1x10^{-6}$ ($4.9x10^{-7}$)	$2.4x10^{-5}$ ($7.7x10^{-6}$)	NP
Nb24	I	$9.3x10^{5}$	$2.7x10^{-1}$	$2.9x10^{-7}$	$2.4x10^{6}$	$3.5x10^{-1}$	$1.5x10^{-7}$	$7.5x10^{-7}$ ($1.0x10^{-7}$)	NP	NP
ACE2	N/A	$2.7x10^{5}$	$1.2x10^{-2}$	$4.4x10^{-8}$	NP	NP	NP	$1.7x10^{-7}$ ($6.6x10^{-8}$)	$6.2x10^{-7}$ ($1.7x10^{-7}$)	NP
mNb6	I	$1.0x10^{6}$	$4.5x10^{-4}$	$4.5x10^{-10}$	$1.1x10^{6}$	$6.4x10^{-4}$	$5.6x10^{-10}$	$1.3x10^{-9}$ ($4.1x10^{-10}$)	$6.3x10^{-9}$ ($1.6x10^{-9}$)	$1.2x10^{-8}$ ($2.5x10^{-9}$)
Nb3-bi	II	NP	NP	NP	NP	NP	NP	NP	$3.6x10^{-7}$ ($1.5x10^{-7}$)	$1.8x10^{-7}$ ($1.2x10^{-8}$)
Nb3-tri	II	Biphasic	Biphasic	Biphasic	NP	NP	NP	$4.1x10^{-8}$ ($1.6x10^{-8}$)	$4.0x10^{-7}$ ($1.6x10^{-7}$)	$1.4x10^{-7}$ ($4.9x10^{-8}$)
Nb6-bi	I	$1.1x10^{6}$	$2.7x10^{-2}$ $5.6x10^{-4}$	$2.5x10^{-8}$ $5.1x10^{-10}$	NP	NP	NP	NP	$6.3x10^{-8}$ ($1.5x10^{-8}$)	NP
Nb6-tri (15 aa)	I	$1.2x10^{6}$	$2.1x10^{-2}$ $<1.0x10^{-6}$	$1.8x10^{-8}$ $<1.0x10^{-12}$	NP	NP	NP	$8.6x10^{-10}$ ($1.8x10^{-10}$)	$1.0x10^{-9}$ ($1.9x10^{-10}$)	NP
Nb6-tri (20 aa)	I	$1.1x10^{6}$	$2.9x10^{-2}$ $<1.0x10^{-6}$	$2.6x10^{-8}$ $<1.0x10^{-12}$	NP	NP	NP	$1.5x10^{-9}$ ($5.2x10^{-10}$)	$1.2x10^{-9}$ ($2.5x10^{-10}$)	$1.6x10^{-10}$ ($2.6x10^{-11}$)
Nb11-tri	I	Biphasic	Biphasic	Biphasic	NP	NP	NP	NP	$5.1x10^{-8}$ ($1.6x10^{-8}$)	NP
ACE2-Fc	N/A	NP	NP	NP	NP	NP	NP	$5.3x10^{-9}$ ($2.5x10^{-9}$)	$4.0x10^{-8}$ ($8.8x10^{-9}$)	$2.6x10^{-8}$ ($8.5x10^{-9}$)
mNb6-tri (15 aa)	I	$1.6x10^{6}$	$<1.0x10^{-6}$	$<1.0x10^{-12}$	NP	NP	NP	$4.3x10^{-10}$ ($1.4x10^{-10}$)	$2.9x10^{-10}$ ($4.2x10^{-11}$)	NP
mNb6-tri (20 aa)	I	$1.4x10^{6}$	$<1.0x10^{-6}$	$<1.0x10^{-12}$	NP	NP	NP	$4.0x10^{-10}$ ($1.7x10^{-10}$)	$1.2x10^{-10}$ ($2.8x10^{-11}$)	$5.4x10^{-11}$ ($1.0x10^{-11}$)

[a]Average values from n = 5 biological replicates for Nb6, Nb11, Nb15, Nb19 are presented, all others were tested with n = 3 biological replicates.
[b]Average values from n = 2 biological replicates for Nb12, Nb17, and Nb11-tri are presented, all others were tested with n = 3 biological replicates.
[c]Average values from n = 2 biological replicates for Nb3, Nb3-bi, and Nb3-tri. n = 3 biological replicates for all others.
[d]Nb3, Nb17, and Nb18 expresses at 41.3, 4.0, and 2.2 milligrams per liter of *E. coli* culture, respectively. Nb3 is monodisperse on size exclusion chromatography over a GE S200 Increase 10x300 column, while Nb17 and Nb18 are polydisperse.
NB – no binding
NC – no competition
NP – not performed

Table 4.2. Cryo-electron microscopy datasets for Spike-Nanobody complexes

Sample:	**Spike^{S2P}-Nb6**		**Spike^{S2P}-Nb11**		**Spike^{S2P}-mNb6**
Spike^{S2P} conformation:					
EMDB:	Open	Closed	Open	Closed	Closed
PDB:	XXXX	XXXX XXXX	XXXX	XXXX	XXXX XXXX
Data collection and processing					
Microscope/Detector	Titan Krios/Gatan K3 with Gatan Bioquantum Energy Filter				
Imaging software and collection	SerialEM, 3x3 image shift				
Magnification	105,000				
Voltage (kV)	300				
Electron exposure (e–/Å^2)	66				
Dose rate (e–/pix/sec)	8				
Frame exposure (e–/Å^2)	0.55				
Defocus range (μm)	-0.8 to -2.0				
Pixel size (Å)	0.834 (physical)				
Micrographs	5,317		4,103		1,609
Reconstruction					
Autopicked particles (template-based in cryosparc)	2,033,067		1,204,855		585,250
Particles in final refinement	40,125 (cisTEM)	58,493 (cisTEM)	21,570 (cisTEM)	27,611 (RELION)	53,690 (cisTEM)
Symmetry imposed	C1	C3	C1	C1	C3
Map sharpening *B* factor (Å^2)		-90			-140
Map resolution, global FSC (Å)					
FSC 0.5, unmasked/masked	7.8/4.6	4.1/3.4	7.0/4.4	7.6/5.3	3.9/3.3
FSC 0.143, unmasked/masked	4.7/3.8	3.5/3.0	4.3/3.7	5.1/4.2	3.2/2.9
Refinement					
Initial model used (PDB code)		6VXX, 3P0G			6VXX, 3P0G
Model resolution (Å)					
FSC 0.5, unmasked/masked		3.5/3.2			3.2/2.9
Model composition					
Non-hydrogen atoms		26871			27024
Protein residues		3360			3360
Glycans (NAG)		54			63
B factors (Å^2)					
Protein		93.3			62.3
Ligand		76.9			88.2
R.m.s. deviations					
Bond lengths (Å)		0.020			0.020
Bond angles (°)		1.702			1.636
Validation					
MolProbity score		0.72			0.76
Clashscore		0.66			0.83
Poor rotamers (%)		0.21			0.41
EMRinger score		3.30			4.22
CaBLAM score		2.31			1.85
Ramachandran plot					
Favored (%)		98.15			98.55
Allowed (%)		1.85			1.45
Disallowed (%)		0			0

Table 4.3. X-ray data collection and refinement statistics

	mNb6 (PDB XXXX)
Data collection	
Space group	$P2_1$
Cell dimensions	
a, *b*, *c* (Å)	44.56, 71.25, 46.43
α, β, γ (°)	90.0, 114.93, 90.0
Molecules in asymmetric unit	2
Resolution (Å)	71.25 - 2.05 (2.09 - 2.05)[a]
R_{sym} or R_{merge}	0.13 (0.94)[b]
$I / \sigma I$	7.2 (0.9)
Completeness (%)	97.8 (96.6)
Redundancy	6.4 (5.7)
CC (1/2) (%)	99.8 (64.4)
Refinement	
Resolution (Å)	71.25 – 2.05
No. reflections	104195
R_{work} / R_{free} (%)	21.16 / 24.75
No. atoms	
Protein	1798
Ligand/ion	21
Water	131
B-factors	
Protein	33.1
Ligand/ion	76.1
Water	42.2
R.m.s. deviations	
Bond lengths (Å)	0.07
Bond angles (°)	0.826
Ramachandran plot	
Allowed (%)	99.06
Generous (%)	0.94
Disallowed (%)	0

[a] Values in parentheses correspond to the highest resolution shell.

[b] $R_{merge} = \Sigma|I - \langle I \rangle|/\Sigma I$

Table 4.4. Nanobody expression plasmids

Plasmid	Nanobody	Plasmid backbone	Resistance Marker
pPW3544	Nb2	pet-26b(+)	kanamycin
pPW3545	Nb3	pet-26b(+)	kanamycin
pPW3546	Nb6	pet-26b(+)	kanamycin
pPW3547	Nb8	pet-26b(+)	kanamycin
pPW3548	Nb11	pet-26b(+)	kanamycin
pPW3549	Nb12	pet-26b(+)	kanamycin
pPW3550	Nb15	pet-26b(+)	kanamycin
pPW3551	Nb16	pet-26b(+)	kanamycin
pPW3552	Nb17	pet-26b(+)	kanamycin
pPW3553	Nb18	pet-26b(+)	kanamycin
pPW3554	Nb19	pet-26b(+)	kanamycin
pPW3555	Nb24	pet-26b(+)	kanamycin
pPW3557	Trivalent Nb6, 20AA length GS linker	pet-26b(+)	kanamycin
pPW3558	Trivalent Nb3, 15AA length GS linker	pet-26b(+)	kanamycin
pPW3559	Trivalent Nb11, 15AA length GS linker	pet-26b(+)	kanamycin
pPW3560	Bivalent Nb3, 15AA length GS linker	pet-26b(+)	kanamycin
pPW3561	Bivalent Nb6, 15AA length GS linker	pet-26b(+)	kanamycin
pPW3563	Trivalent mNb6, 20AA length GS linker	pet-26b(+)	kanamycin
pPW3564	mNb6	pet-26b(+)	kanamycin

Materials and Methods

Expression and purification of SARS-CoV-2 Spike, RBD, and ACE2.

We used a previously described construct to express and purify the pre-fusion SARS-CoV-2 Spike ectodomain ($Spike^{S2P}$) (Wrapp, Wang, et al. 2020). ExpiCHO or Expi293T cells (ThermoFisher) were transfected with the $Spike^{S2P}$ construct per the manufacturer's instructions for the MaxTiter protocol and harvested between 3-9 days after transfection. Clarified cell culture supernatant was loaded onto Ni-Excel beads (Cytiva) followed by extensive washes in 20 mM HEPES pH 8.0, 200 mM sodium chloride, and 10 mM imidazole and elution in the same buffer supplemented with 500 mM imidazole. $Spike^{S2P}$ was concentrated using a 100 kDa MWCO spin concentrator (Millipore) and further purified by size exclusion chromatography over a Superose 6 Increase 10/300 column (GE Healthcare) in 20 mM HEPES pH 8.0 and 200 mM sodium chloride. All purification steps were performed at room temperature. The resulting fractions for trimeric $Spike^{S2P}$ were pooled and either used directly for cryo-EM studies or concentrated and flash frozen in liquid nitrogen with 15% glycerol for other biochemical studies.

We used a previously described construct to express and purify the SARS-CoV-2 Receptor binding domain (RBD) (Stadlbauer et al. 2020). Expi293T cells (ThermoFisher) were transfected with the RBD construct per the manufacturer's instructions and harvested between 3-6 days after transfection. Clarified cell culture supernatant was loaded onto Ni-Excel beads (Cytiva) or a His-Trap Excel column (GE Healthcare) followed by washes in 20 mM HEPES pH 8.0, 200 mM sodium chloride, and 10 mM imidazole and elution using the same buffer supplemented with 500 mM imidazole. RBD was concentrated using a 30 kDa MWCO spin concentrator (Millipore) and further purified by size exclusion chromatography over a Superdex 200 Increase 10/300 GL column (GE Healthcare) in 20 mM HEPES pH 8.0 and 200 mM sodium chloride. The resulting fractions were pooled, concentrated, and flash frozen in liquid nitrogen with 10% glycerol.

For biochemical and yeast display experiments, Spike^{S2P} and RBD were labeled with freshly prepared stocks of Alexa 647-NHS, Alexa 488-NHS, or Biotin-NHS (ThermoFisher) with a 5-fold stoichiometry for 1 hour at room temperature followed by quenching of NHS with 10 mM Tris pH 8.0 for 60 minutes. Labeled proteins were further purified by size exclusion chromatography, concentrated using a spin concentrator (Millipore), and flash frozen in liquid nitrogen with 10-15% glycerol.

We used an ACE2-ECD (18-614) Fc fusion expression plasmid to express and purify Fc tagged ACE2-ECD (Lui et al. 2020). Expi293T cells (ThermoFisher) were transfected with the ACE2-Fc construct per the manufacturer's instructions and harvested between 5-7 days after transfection. Clarified cell culture supernatant was loaded onto a MabSelect Pure 1 mL Column (GE Healthcare). Column was washed with Buffer A (20 mM HEPES pH 7.5, 150 mM NaCl) and protein was eluted with Buffer B (100 mM Sodium Citrate pH 3.0, 150 mM NaCl) into a deep well block containing 1 M HEPES pH 7.5 to neutralize the acidic elution. ACE2-Fc was concentrated using a 30 kDa MWCO spin concentrator (Millipore) and further purified by size exclusion chromatography over a Superdex 200 Increase 10/300 GL column (GE Healthcare) in SEC Buffer (20 mM HEPES pH 7.5, 150 mM NaCl, 5% v/v Glycerol). The resulting fractions were pooled, concentrated, and flash frozen in liquid nitrogen. To obtain monomeric ACE2, 1:50 (w/w) His-tagged TEV protease was added to ACE2-Fc and incubated at 4 °C overnight. This mixture was then purified by size exclusion chromatography in SEC Buffer. Monomeric ACE2 fractions were pooled and washed with His-resin (1 mL of 50% slurry) to remove excess TEV. The resulting supernatant was pooled, concentrated, and flash frozen in liquid nitrogen.

Identification of anti SARS-CoV2 Spike nanobodies

To identify nanobodies against the SARS-CoV-2 Spike ECD, we used a yeast surface displayed library of synthetic nanobody sequences that recapitulate amino acid position specific-variation in natural llama immunological repertoires. This library encodes a diversity of >$2x10^9$ variants, and uses a synthetic stalk sequence for nanobody display, as described previously in a modified vector encoding nourseothricin (NTC) resistance (McMahon et al. 2018). For the first round of selection, $2x10^{10}$ yeast induced in YPG (Yeast Extract-Peptone-Galactose) supplemented with NTC were washed repeatedly in selection buffer (20 mM HEPES, pH 7.5, 150 mM sodium chloride, 0.1% (w/v) low biotin bovine serum albumin, BSA) and finally resuspended in 10 mL of selection buffer containing 200 nM biotinylated-Spike^{S2P}. Yeast were incubated for 30 minutes at 25 °C, then washed repeatedly in cold selection buffer, and finally resuspended in 10 mL of cold selection buffer containing 200 µL of Miltenyi anti-Streptavidin microbeads. After 30 minutes of incubation at 4 °C, yeast were again washed with cold selection buffer. Spike^{S2P} binding yeast were captured on a Miltenyi MACS LS column and recovered in YPD (Yeast Extract-Peptone-Dextrose) medium supplemented with NTC.

For round 2, $4x10^8$ induced yeast from Round 1 were incubated with 100 nM Spike^{S2P} labeled with Alexa647 in 1 mL of selection buffer for 1 hr at 25 °C. After extensive washes with cold selection buffer, Spike^{S2P} binding yeast were isolated by fluorescence activated cell sorting (FACS) on a Sony SH800 instrument. A similar approach was used for round 3, with substitution of 10 nM Spike^{S2P} labeled with Alexa647. Post round 3 yeast were plated on YPD+NTC solid media and 768 individual colonies were induced with YPG+NTC media in 2 mL deep well plates. Each individual clone was tested for binding to 4 nM Spike^{S2P}-Alexa488 by flow cytometry on a Beckman Coulter Cytoflex. To identify nanobodies that disrupt Spike-ACE2 interactions, Spike^{S2P} binding was repeated in the presence of 0.5-1 µM ACE2-Fc. Out of 768 clones, we identified 21 that strongly bind Spike^{S2P} and are competitive with ACE2 (Table 4.4).

Expression and purification of nanobodies

Nanobody sequences were cloned into the pET26-b(+) expression vector using In-Fusion HD cloning (Takara Bio), transformed into BL21(DE3) *E. coli*, grown in Terrific Broth at 37 °C until OD 0.7-0.8, followed by gene induction using 1 mM IPTG for 18-22 hours at 25°C. *E. Coli* were harvested and resuspended in SET Buffer (200 mM Tris, pH 8.0, 500 mM sucrose, 0.5 mM EDTA, 1X cOmplete protease inhibitor (Roche)) for 30 minutes at 25 °C before a 45 minute osmotic shock with a two-fold volume addition of water. NaCl, MgCl2, and imidazole were added to the lysate to 150 mM, 2 mM, and 40 mM respectively before centrifugation at 17-20,000xg for 15 minutes to separate cell debris from the periplasmic fraction. For every liter of bacterial culture, the periplasmic fraction was then incubated with 4 mL of 50% HisPur Ni-NTA resin (Thermo Scientific) which had been equilibrated in Nickel Wash Buffer (20 mM HEPES, pH 7.5, 150 mM NaCl, 40 mM imidazole). This mixture was incubated for 1 hr with rotation at RT before centrifugation at 50xg to collect the resin. The resin was then washed with 5 volumes of Nickel Wash buffer 3 times, each time using centrifugation to remove excess wash buffer. Bound proteins were then eluted using three washes with Elution Buffer (20 mM HEPES, pH 7.5, 150 mM NaCl, 500 mM imidazole). The eluted protein was concentrated using a 3.5 kDa MWCO centrifugal filter unit (Amicon) before injection onto a Superdex 200 Increase 10/300 GL column equilibrated with 20 mM HEPES, pH 7.5, 150 mM NaCl. Nanobody constructs were concentrated again using a 3.5k MWCO centrifugal filter unit, and flash frozen in liquid nitrogen.

Affinity determination by surface plasmon resonance

Nanobody (Nb) affinity determination experiments were performed on Biacore T200 and 8K instruments (Cytiva Life Sciences) by capturing the StreptagII-tagged Spike^{S2P} at 10 µg/mL on a StreptactinXT-immobilized (Iba Life Sciences) CM5 Series S sensor chip (Cytiva Life Sciences) to achieve maximum response (Rmax) of approximately 30 response units (RUs) upon

nanobody binding. 2-fold serial dilutions of purified nanobody from 1 μM to 31.25 nM (for monovalent constructs) or from 50 nM to 1.56 nM (for affinity matured and multimeric constructs) were flowed over the captured Spike^{S2P} surface at 30 μL/minute for 60 seconds followed by 600 seconds of dissociation flow. Following each cycle, the chip surface was regenerated with 3 M guanidine hydrochloride.

Separately, biotinylated SARS-CoV-2 RBD at 8 μg/mL was loaded onto a preconditioned Series S Sensor Chip CAP chip (Cytiva Life Sciences) to achieve an Rmax of approximately 60 RUs upon nanobody binding. 2-fold serial dilutions in the same running buffer and sample series (parent or affinity matured clone) as the Spike^{S2P} runs were flowed over the RBD surface at 30 μL/minute for 60 seconds followed by 600 seconds of dissociation flow. Chip surface regeneration was performed with a guanidine hydrochloride/sodium hydroxide solution.

The resulting sensorgrams for all monovalent clones were fit to a 1:1 Langmuir binding model using the Biacore Insight Evaluation Software (Cytiva Life Sciences) or the association/dissociation model in GraphPad Prism 8.0. For determination of kinetic parameters for Nb6-bi and Nb6-tri binding, the dissociation phase was fit to a biexponential decay constrained to two dissociation rate constants shared between each concentration. The association phase was fit separately using an association kinetics model simultaneously fitting the association rate constant for each concentration.

For nanobody competition experiments, Spike^{S2P} was loaded onto a StreptactinXT-immobilized CM5 sensor chip as previously described. As in the kinetics experiments, the primary nanobody was flowed over the captured Spike^{S2P} surface for 60 seconds at 30 μL/minute to achieve saturation. Immediately following this, a second injection of a mixture of primary and variable nanobody at the same concentration as in the primary injection was performed.

ACE2 cellular surface binding competition assays

A dilution series of nanobody was generated in PBE (PBS + 0.5% (w/v) BSA + 2 mM EDTA and mixed with Spike^{S2P}-Alexa647 or RBD-Alexa647. ACE2 expressing HEK293T cells were dissociated with TrypLE Express (ThermoFisher) and resuspended in PBE (Crawford et al. 2020). The cells were mixed with the Spike^{S2P}-nanobody solution and incubated for 45 minutes, washed in PBE, and then resuspended in PBE. Cell surface Alexa647 fluorescence intensity was assessed on an Attune Flow Cytometer (ThermoFisher).

Affinity maturation of Nb6

A site saturation mutagenesis library of Nb6 was generated by assembly PCR of overlapping oligonucleotides encoding the Nb6 sequence. Individual oligos for each position in CDR1, CDR2, and CDR3 were designed with the degenerate “NNK” codon. The assembled gene product was amplified with oligonucleotides with overlapping ends to enable homologous recombination with the yeast surface display vector as previously described and purified with standard silica-based chromatography (McMahon et al. 2018). The resulting insert DNA was transformed into *Saccharomyces cerevisiae* strain BJ5465 along with the yeast display vector pYDS2.0 to generate a library of $2x10^8$ transformants. After induction in YPD+NTC medium at 20 °C for 2 days, $2x10^9$ yeast were washed in selection buffer (20 mM HEPES, pH 8.0, 150 mM sodium chloride, 0.1% (w/v) low biotin BSA) and incubated with 1 nM biotin-Spike^{S2P} for 1 hour at 25 °C. Yeast were subsequently washed in selection buffer, resuspended in 1 mL selection buffer, and incubated with 10 µL streptavidin microbeads (Miltenyi) for 15 min. at 4 °C. Yeast were washed again with cold selection buffer and Spike^{S2P}-binding yeast were isolated by magnetic separation using an LS column (Miltenyi). Recovered yeast were grown in YPD+NTC at 37 °C and induced in YPG+NTC at 20 °C. A second round of selection was performed as above, substituting 100 pM RBD-Alexa647 as the antigen. Yeast displaying high affinity clones

were selected by magnetic separation using Anti-Cy5 microbeads (Miltenyi) and an LS column. Analysis of the library after the second round of selection revealed a population of clones with clear binding of 10 pM RBD-Alexa647. Therefore, 96 individual clones were screened for binding to 10 pM RBD-Alexa647 by flow cytometry. Sequence analysis of eight clones that showed robust binding to 10 pM RBD-Alexa647 revealed two consensus mutations, I27Y and P105Y, which were used to generate the affinity matured clone mNb6.

Structures of Spike-nanobody complexes by cryo-EM

Sample preparation and microscopy

To prepare Spike^{S2P}-nanobody complexes, each nanobody was incubated on ice at a 3-fold molar excess to Spike^{S2P} at 2.5 μM for 10 minutes. 3 μL of Spike^{S2P}-nanobody complex was added to a 300 mesh 1.2/1.3R Au Quantifoil grid previously glow discharged at 15 mA for 30 seconds. Blotting was performed with a blot force of 0 for 4 seconds at 4°C and 100% humidity in a FEI Vitrobot Mark IV (ThermoFisher) prior to plunge freezing into liquid ethane.

For each complex, 120-frame super-resolution movies were collected with a 3x3 image shift collection strategy at a nominal magnification of 105,000x (physical pixel size: 0.834 Å/pix) on a Titan Krios (ThermoFisher) equipped with a K3 camera and a Bioquantum energy filter (Gatan) set to a slit width of 20 eV. Collection dose rate was 8 e^-/pixel/second for a total dose of 66 e^-/Å^2. Each collection was performed with semi-automated scripts in SerialEM (Mastronarde 2005).

Image Processing

For all datasets, dose fractionated super-resolution movies were motion corrected with MotionCor2 (Zheng et al. 2017). Contrast transfer function determination was performed with

cryoSPARC patch CTF (Punjani et al. 2017). Particles were picked with a 20 Å low-pass filtered apo Spike 2D templates generated from a prior data collection.

Nb6-Spike^{S2P} and mNb6-Spike^{S2P} particles were extracted with a 384 pixel box, binned to 96 pixels and subject to single rounds of 2D and 3D classification prior to unbinning for homogenous refinement in cryoSPARC. Refined particles were then imported into Relion3.1 for 3D classification without alignment using the input refinement map low pass filtered to 40 Å (Zivanov et al. 2018). Particles in classes representing the closed conformation of Spike were imported into cisTEM and subject to autorefinement followed by local refinement within a RBD::nanobody masked region (Grant, Rohou, and Grigorieff 2018). Following local refinement, a new refinement package symmetrized to the C3 axis was created for a final round of local refinement without masking. Final particle counts for each map are as follows: Nb6-Open: 40,125, Nb6-Closed: 58,493, mNb6: 53,690.

Nb11-Spike^{S2P} particles were extracted with a 512 pixel box, binned to 128 pixels for multiple rounds of 3D classification as described in Figure 4.2 – figure supplement 2. Following homogenous refinement, particles were exported to Relion3.1. Particle density roughly corresponding to RBD-nanobody complexes was retained post-particle subtraction. 3D classification without alignment was performed on the particle subtracted stacks. Particles in classes with robust RBD-nanobody density were selected, unsubtracted and refined in Relion followed by post-processing. 21,570 particles contributed to the final maps. Final particle counts for each map are as follows: Nb11-Open: 21,570, Nb11-Closed: 27,611. For all maps, final local resolution estimation and GSFSC determination was carried out in cryoSPARC.

Structure modeling

Models of Nb6-Spike^{S2P} and mNb6-Spike^{S2P} were built using a previously determined structure of closed Spike^{S2P} (PDB: 6VXX) (Walls et al. 2020). A composite model incorporating resolved regions of the RBD was made using a previously determined X-ray crystal structure of the SARS-CoV-2 RBD (PDB: 6M0J) (Lan et al. 2020). For Nb6, the beta2-adrenergic receptor nanobody Nb80 (PDB: 3P0G) was used as a template to first fit the nanobody into the cryo-EM density map for the Nb6-Spike^{S2P} complex (Rasmussen et al. 2011). Complementarity determining loops were then truncated and rebuilt using RosettaES (Frenz et al. 2017). The final structure was inspected and manually adjusted in COOT and ISOLDE, followed by real space refinement in PHENIX (Adams et al. 2010; Croll 2018; Emsley and Cowtan 2004). The higher resolution structure of mNb6 enabled manual building of nanobody CDR loops *de novo*, and therefore the Rosetta-based approach was not used for modeling. Conformational outliers were manually inspected and rebuilt in COOT. Final refinement was done using the Rosetta Glycan Relax application, which utilizes CHI (CarboHydrate Intrinsic) energy term and backbone dihedral sampling. Glycans were validated using the Privateer software package distributed under CCP4 (Agirre et al. 2015; Winn et al. 2011).

Final models were analyzed in PHENIX, with statistics reported in Table 4.2.

For models of Nb11-Spike^{S2P} complexes presented here, the closest nanobody by sequence in the PDB (beta2-adrenergic receptor Nb60, PDB ID: 5JQH) was fit by rigid-body refinement in COOT into the cryo-EM density map using only the framework regions (Staus et al. 2016). While the lower resolution of these maps precluded confident assignment of loop conformations, the overall orientation of Nb11 relative to Spike^{S2P} was well constrained, enabling accurate modeling of distances between the N- and C- termini of two Nb11 molecules bound to Spike^{S2P}.

Radiolytic hydroxyl radical footprinting and mass-spectrometry of apo and Nb3-bound Spike^{S2P}

Spike^{S2P} and Nb3 samples were buffer exchanged into 10 mM phosphate buffer (pH 7.4) by extensive dialysis at 25 °C. A 1.5-fold molar excess of Nb3 was added to 5 μM Spike^{S2P} and the complex was incubated for >24 hr at 25 °C. For radiolytic footprinting, protein concentrations and beam parameters were optimized using an Alexa-488 fluorophore assay (Gupta et al. 2007). Apo Spike^{S2P} and Spike^{S2P}-Nb3 complex at concentrations of 1-3 μM were exposed to a synchrotron X-ray white beam at 6 timepoints between 0-50 ms at beamline 3.2.1 at the Advanced Light Source in Berkeley, CA and were quenched with 10 mM methionine amide immediately post-exposure. Glycans were removed by treatment with 5% SDS, 5 mM DTT at 95 °C for five minutes and subsequent PNGase (Promega) digestion at 37°C for 2 hours. Samples were buffer exchanged into ammonium bicarbonate (ABC) buffer (pH 8.0) using ZebaSpin columns (Thermo Fisher). Alkylation of cysteines was achieved by treatment with 8 M urea and 5 mM DTT at 37°C for 30 minutes followed by an incubation with 15 mM iodoacetamide at 25 °C in the dark for 30 minutes. All samples were further buffer exchanged to ABC pH 8.0 using ZebaSpin columns and digested with either Trypsin/Lys-C or Glu-C (Promega) at an enzyme:protein ratio of 1:20 (w/w) at 37 °C for 8 hours.

Samples were lyophilized and resuspended in 1% formic acid at 200 fmol/μL concentration. For each MS analysis, 1 μL of sample was injected onto a 5 mm Thermo Trap C18 cartridge, and then separated over a 15 cm column packed with 1.9 μm Reprosil C18 particles (Dr. Maisch HPLC GmbH) by a nanoElute HPLC (Bruker). Separation was performed at 50 °C and a flow rate of 400 μL/min by the following gradient in 0.1% formic acid: 2% to 17% acetonitrile from 0 to 20 min, followed by 17% to 28% acetonitrile from 20 to 40 min. The eluent was electrospray ionized into a Bruker timsTOF Pro mass spectrometer and data was collected using data-dependent PASEF acquisition. Database searching and extraction of MS1 peptide abundances

was performed using the FragPipe platform with either trypsin or GluC enzyme specificity, and all peptide and protein identifications were filtered to a 1% false-discovery rate (Yu et al. 2020). Searches were performed against a concatenated protein database of the Spike protein, common contaminant proteins, and the *Saccharomyces cerevisiae* proteome (downloaded July 23, 2020). Note, the *Saccharomyces cerevisiae* proteome was included to generate a sufficient population of true negative identifications for robust false discovery rate estimation of peptide and protein identifications. Lastly, the area under the curve MS1 intensities reported from FragPipe were summarized for each peptide species using MSstats (Choi et al. 2014).

The peak areas of extracted ion chromatograms and associated side-chain modifications were used to quantify modification at each timepoint. Increasing beamline exposure time decreases the fraction of unmodified peptide and can be represented as a site-specific dose-response plot. The rate of hydroxyl radical reactivity (k_{fp}) is dependent on both the intrinsic reactivity of each residue and its solvent accessibility and was calculated by fitting the dose-response to a pseudo-first order reaction scheme in Graphpad Prism Version 8. The ratio of k_{fp} between apo Spike^{S2P} and the Spike-Nb3 complex at specific residues gave information on solvent accessibility changes between the two samples. These changes were mapped onto the SARS-CoV-2 Spike (PDB 6XR8) (Cai et al. 2020). In some cases, heavily modified residues show a flattening of dose-response at long exposures which we interpret as radical induced damage. These over-exposed timepoints were excluded from the calculation of k_{fp}.

mNb6 crystallography and structure determination

Purified mNb6 was concentrated to 18.7 mg/mL and filtered using 0.1 µm hydrophilic PVDF filters (Millipore). mNb6 crystal screens were set up in 96 well plates in hanging drop format at 2:1 protein:reservoir in Index and AmSO4 screens (Hampton Research, Aliso Viejo, CA). Crystals in over 60 different screening conditions with various morphologies appeared overnight

at ambient temperature and were obtained directly from the screens without further optimization. The crystals were cryoprotected by quick dipping in a solution containing 80% reservoir and 20% PEG400 or 20% Glycerol, then mounted in CrystalCap HT Cryoloops (Hampton Research, Aliso Viejo, CA) and flash cooled in a cryogenic nitrogen stream (100 K). All data were collected at the Advanced Light Source (Berkeley, CA) beam line 8.3.1. A single crystal of mNb6 that grew in 0.1 M Tris.HCl pH 8.5, 1.0 M Ammonium sulfate diffracted to 2.05 Å. Integration, and scaling were performed with Xia2, using XDS for indexing and integration and XSCALE for scaling and merging (Kabsch 1993). The structure was solved molecular replacement using PHASER using the structure of nanobody, Nb.b201 (PDB 5VNV) as search model (McCoy et al. 2007; McMahon et al. 2018). Model building was performed with COOT and refined with PHENIX and BUSTER (Adams et al. 2010; Bricogne G. and Roversi P 2017; Emsley and Cowtan 2004).

Pseudovirus assays for nanobody neutralization

ZsGreen SARS-CoV-2-pseudotyped lentivirus was generated according to a published protocol (Crawford et al. 2020). The day before transduction, 50,000 ACE2 expressing HEK293T cells were plated in each well of a 24-well plate. 10-fold serial dilutions of nanobody were generated in complete medium (DMEM + 10% FBS + PSG) and pseudotyped virus was added to a final volume of 200 µL. Media was replaced with nanobody/pseudotyped virus mixture for four hours, then removed. Cells were washed with complete medium and then incubated in complete medium at 37 °C. Three days post-transduction, cells were trypsinized and the proportion of ZsGreen+ cells was measured on an Attune flow cytometer (ThermoFisher).

Authentic SARS-CoV-2 neutralization assay

SARS-CoV-2, isolate France/IDF0372/2020, was supplied by the National Reference Centre for Respiratory Viruses hosted by Institut Pasteur (Paris, France) and headed by Pr. Sylvie van der

Werf. Viral stocks were prepared by propagation in Vero E6 cells in Dulbecco's modified Eagle's medium (DMEM) supplemented with 2% (v/v) fetal bovine serum (FBS, Invitrogen). Viral titers were determined by plaque assay. All plaque assays involving live SARS-CoV-2 were performed at Institut Pasteur Paris (IPP) in compliance with IPP's guidelines following Biosafety Level 3 (BSL-3) containment procedures in approved laboratories. All experiments were performed in at least three biologically independent samples.

Neutralization of infectious SARS-CoV-2 was performed using a plaque reduction neutralization test in Vero E6 cells (CRL-1586, ATCC). Briefly, nanobodies (or ACE2-Fc) were eight-fold serially diluted in DMEM containing 2% (v/v) FBS and mixed with 50 plaque forming units (PFU) of SARS-CoV-2 for one hour at 37°C, 5% CO_2. The mixture was then used to inoculate Vero E6 cells seeded in 12-well plates, for one hour at 37 °C, 5% CO2. Following this virus adsorption time, a solid agarose overlay (DMEM, 10% (v/v) FBS and 0.8% agarose) was added. The cells were incubated for a further 3 days prior to fixation using 4% formalin and plaques visualized by the addition of crystal violet. The number of plaques in quadruplicate wells for each dilution was used to determine the half maximal inhibitory concentrations (IC_{50}) using 3-parameter logistic regression (GraphPad Prism version 8).

Nanobody stability studies

Nanobody thermostability by circular dichroism was assessed using a Jasco J710 CD spectrometer equipped with a Peltier temperature control. Individual nanobody constructs were diluted to 5 µM in phosphate buffered saline. Mollar ellipticity was measured at 204 nm (2 nm bandwidth) between 25 °C and 80 °C with a 1 °C/min heating rate. The resulting molar ellipticity values were normalized and plotted in GraphPad Prism 8.0 after applying a nearest neighbor smoothing function.

For nanobody competition experiments on ACE2 expressing HEK293T cells, nanobodies were incubated at either 25°C or 50°C for one hour. Alternatively, each nanobody was aerosolized with a portable mesh nebulizer producing 2-5 μm particles at a final concentration of 0.5 mg/mL. The resulting aerosol was collected by condensation into a 50 mL tube cooled on ice. Samples were then treated as indicated above to determine IC50 values for binding to $Spike^{S2P}$-Alexa647 or used for pseudovirus neutralization studies as described above.

Further experiments assessing mNb6 and mNb6-tri stability to aerosolization and lyophilization used a starting concentration of 0.5 mg/mL of each construct. Aerosolization was performed as described above. For lyophilization, nanobodies were first flash frozen in liquid nitrogen and the solution was dried to completion under vacuum. The resulting dried material was resuspended in 20 mM HEPES pH 7.5, 150 mM NaCl. Size exclusion chromatography of the unstressed, post-aerosolization, and post-lyophilization samples were performed an a Superdex 75 Increase 10/300 column in 20 mM HEPES pH 7.5, 150 mM NaCl. SPR experiments to assess binding to $Spike^{S2P}$ were performed as described above.

References

Adams, P. D., P. V. Afonine, G. Bunkóczi, V. B. Chen, I. W. Davis, N. Echols, J. J. Headd, L. W. Hung, G. J. Kapral, R. W. Grosse-Kunstleve, A. J. McCoy, N. W. Moriarty, R. Oeffner, R. J. Read, D. C. Richardson, J. S. Richardson, T. C. Terwilliger, and P. H. Zwart. 2010. 'PHENIX: a comprehensive Python-based system for macromolecular structure solution', *Acta Crystallogr D Biol Crystallogr*, 66: 213-21.

Agirre, J., J. Iglesias-Fernandez, C. Rovira, G. J. Davies, K. S. Wilson, and K. D. Cowtan. 2015. 'Privateer: software for the conformational validation of carbohydrate structures', *Nat Struct Mol Biol*, 22: 833-4.

Baum, Alina, Benjamin O. Fulton, Elzbieta Wloga, Richard Copin, Kristen E. Pascal, Vincenzo Russo, Stephanie Giordano, Kathryn Lanza, Nicole Negron, Min Ni, Yi Wei, Gurinder S. Atwal, Andrew J. Murphy, Neil Stahl, George D. Yancopoulos, and Christos A. Kyratsous. 2020. 'Antibody cocktail to SARS-CoV-2 spike protein prevents rapid mutational escape seen with individual antibodies', *Science*.

Bosch, Berend Jan, Ruurd van der Zee, Cornelis A. M. de Haan, and Peter J. M. Rottier. 2003. 'The coronavirus spike protein is a class I virus fusion protein: structural and functional characterization of the fusion core complex', *J. Virol.*, 77: 8801-11.

Bricogne G., Blanc E., Brandl M., Flensburg C., Keller P., Paciorek W.,, and Sharff A. Roversi P, Smart O.S., Vonrhein C., Womack T.O. . 2017. 'BUSTER version 1.10.0. ', *Cambridge, United Kingdom: Global Phasing Ltd.*

Cai, Yongfei, Jun Zhang, Tianshu Xiao, Hanqin Peng, Sarah M. Sterling, Richard M. Walsh, Jr., Shaun Rawson, Sophia Rits-Volloch, and Bing Chen. 2020. 'Distinct conformational states of SARS-CoV-2 spike protein', *Science*.

Cao, Yunlong, Bin Su, Xianghua Guo, Wenjie Sun, Yongqiang Deng, Linlin Bao, Qinyu Zhu, Xu Zhang, Yinghui Zheng, Chenyang Geng, Xiaoran Chai, Runsheng He, Xiaofeng Li, Qi

Lv, Hua Zhu, Wei Deng, Yanfeng Xu, Yanjun Wang, Luxin Qiao, Yafang Tan, Liyang Song, Guopeng Wang, Xiaoxia Du, Ning Gao, Jiangning Liu, Junyu Xiao, Xiao-Dong Su, Zongmin Du, Yingmei Feng, Chuan Qin, Chengfeng Qin, Ronghua Jin, and X. Sunney Xie. 2020. 'Potent Neutralizing Antibodies against SARS-CoV-2 Identified by High-Throughput Single-Cell Sequencing of Convalescent Patients' B Cells', *Cell*, 182: 73-84.e16.

Chan, J. F., S. Yuan, K. H. Kok, K. K. To, H. Chu, J. Yang, F. Xing, J. Liu, C. C. Yip, R. W. Poon, H. W. Tsoi, S. K. Lo, K. H. Chan, V. K. Poon, W. M. Chan, J. D. Ip, J. P. Cai, V. C. Cheng, H. Chen, C. K. Hui, and K. Y. Yuen. 2020. 'A familial cluster of pneumonia associated with the 2019 novel coronavirus indicating person-to-person transmission: a study of a family cluster', *Lancet*, 395: 514-23.

Chi, Xiangyang, Renhong Yan, Jun Zhang, Guanying Zhang, Yuanyuan Zhang, Meng Hao, Zhe Zhang, Pengfei Fan, Yunzhu Dong, Yilong Yang, Zhengshan Chen, Yingying Guo, Jinlong Zhang, Yaning Li, Xiaohong Song, Yi Chen, Lu Xia, Ling Fu, Lihua Hou, Junjie Xu, Changming Yu, Jianmin Li, Qiang Zhou, and Wei Chen. 2020. 'A neutralizing human antibody binds to the N-terminal domain of the Spike protein of SARS-CoV-2', *Science*.

Choi, M., C. Y. Chang, T. Clough, D. Broudy, T. Killeen, B. MacLean, and O. Vitek. 2014. 'MSstats: an R package for statistical analysis of quantitative mass spectrometry-based proteomic experiments', *Bioinformatics*, 30: 2524-6.

Crawford, K. H. D., R. Eguia, A. S. Dingens, A. N. Loes, K. D. Malone, C. R. Wolf, H. Y. Chu, M. A. Tortorici, D. Veesler, M. Murphy, D. Pettie, N. P. King, A. B. Balazs, and J. D. Bloom. 2020. 'Protocol and Reagents for Pseudotyping Lentiviral Particles with SARS-CoV-2 Spike Protein for Neutralization Assays', *Viruses*, 12.

Croll, T. I. 2018. 'ISOLDE: a physically realistic environment for model building into low-resolution electron-density maps', *Acta Crystallogr D Struct Biol*, 74: 519-30.

Cunningham, S., P. A. Piedra, F. Martinon-Torres, H. Szymanski, B. Brackeva, E. Dombrecht, L. Detalle, C. Fleurinck, and Respire study group. 2020. 'Nebulised ALX-0171 for respiratory syncytial virus lower respiratory tract infection in hospitalised children: a double-blind, randomised, placebo-controlled, phase 2b trial', *Lancet Respir Med*.

Detalle, L., T. Stohr, C. Palomo, P. A. Piedra, B. E. Gilbert, V. Mas, A. Millar, U. F. Power, C. Stortelers, K. Allosery, J. A. Melero, and E. Depla. 2016. 'Generation and Characterization of ALX-0171, a Potent Novel Therapeutic Nanobody for the Treatment of Respiratory Syncytial Virus Infection', *Antimicrob Agents Chemother*, 60: 6-13.

Emsley, P., and K. Cowtan. 2004. 'Coot: model-building tools for molecular graphics', *Acta Crystallogr D Biol Crystallogr*, 60: 2126-32.

Frenz, B., A. C. Walls, E. H. Egelman, D. Veesler, and F. DiMaio. 2017. 'RosettaES: a sampling strategy enabling automated interpretation of difficult cryo-EM maps', *Nat Methods*, 14: 797-800.

Grant, T., A. Rohou, and N. Grigorieff. 2018. 'cisTEM, user-friendly software for single-particle image processing', *Elife*, 7.

Gupta, S., M. Sullivan, J. Toomey, J. Kiselar, and M. R. Chance. 2007. 'The Beamline X28C of the Center for Synchrotron Biosciences: a national resource for biomolecular structure and dynamics experiments using synchrotron footprinting', *J Synchrotron Radiat*, 14: 233-43.

Hoffmann, Markus, Hannah Kleine-Weber, Simon Schroeder, Nadine Krüger, Tanja Herrler, Sandra Erichsen, Tobias S. Schiergens, Georg Herrler, Nai-Huei Wu, Andreas Nitsche, Marcel A. Müller, Christian Drosten, and Stefan Pöhlmann. 2020. 'SARS-CoV-2 Cell Entry Depends on ACE2 and TMPRSS2 and Is Blocked by a Clinically Proven Protease Inhibitor', *Cell*, 181: 271-80.e8.

Huang, C., Y. Wang, X. Li, L. Ren, J. Zhao, Y. Hu, L. Zhang, G. Fan, J. Xu, X. Gu, Z. Cheng, T. Yu, J. Xia, Y. Wei, W. Wu, X. Xie, W. Yin, H. Li, M. Liu, Y. Xiao, H. Gao, L. Guo, J. Xie,

G. Wang, R. Jiang, Z. Gao, Q. Jin, J. Wang, and B. Cao. 2020. 'Clinical features of patients infected with 2019 novel coronavirus in Wuhan, China', *Lancet*, 395: 497-506.

Ju, Bin, Qi Zhang, Jiwan Ge, Ruoke Wang, Jing Sun, Xiangyang Ge, Jiazhen Yu, Sisi Shan, Bing Zhou, Shuo Song, Xian Tang, Jinfang Yu, Jun Lan, Jing Yuan, Haiyan Wang, Juanjuan Zhao, Shuye Zhang, Youchun Wang, Xuanling Shi, Lei Liu, Jincun Zhao, Xinquan Wang, Zheng Zhang, and Linqi Zhang. 2020. 'Human neutralizing antibodies elicited by SARS-CoV-2 infection', *Nature*.

Kabsch, W. 1993. 'Automatic processing of rotation diffraction data from crystals of initially unknown symmetry and cell constants', *Journal of Applied Crystallography*, 26: 795-800.

Ke, Z., J. Oton, K. Qu, M. Cortese, V. Zila, L. McKeane, T. Nakane, J. Zivanov, C. J. Neufeldt, B. Cerikan, J. M. Lu, J. Peukes, X. Xiong, H. G. Krausslich, S. H. W. Scheres, R. Bartenschlager, and J. A. G. Briggs. 2020. 'Structures and distributions of SARS-CoV-2 spike proteins on intact virions', *Nature*.

Ksiazek, Thomas G., Dean Erdman, Cynthia S. Goldsmith, Sherif R. Zaki, Teresa Peret, Shannon Emery, Suxiang Tong, Carlo Urbani, James A. Comer, Wilina Lim, Pierre E. Rollin, Scott F. Dowell, Ai-Ee Ling, Charles D. Humphrey, Wun-Ju Shieh, Jeannette Guarner, Christopher D. Paddock, Paul Rota, Barry Fields, Joseph DeRisi, Jyh-Yuan Yang, Nancy Cox, James M. Hughes, James W. LeDuc, William J. Bellini, Larry J. Anderson, and Sars Working Group. 2003. 'A novel coronavirus associated with severe acute respiratory syndrome', *N. Engl. J. Med.*, 348: 1953-66.

Lan, J., J. Ge, J. Yu, S. Shan, H. Zhou, S. Fan, Q. Zhang, X. Shi, Q. Wang, L. Zhang, and X. Wang. 2020. 'Structure of the SARS-CoV-2 spike receptor-binding domain bound to the ACE2 receptor', *Nature*, 581: 215-20.

Ledford, H. 2020. 'Antibody therapies could be a bridge to a coronavirus vaccine - but will the world benefit?', *Nature*.

Leyva-Grado, V. H., G. S. Tan, P. E. Leon, M. Yondola, and P. Palese. 2015. 'Direct administration in the respiratory tract improves efficacy of broadly neutralizing anti-influenza virus monoclonal antibodies', *Antimicrob Agents Chemother*, 59: 4162-72.

Liu, Lihong, Pengfei Wang, Manoj S. Nair, Jian Yu, Micah Rapp, Qian Wang, Yang Luo, Jasper F. W. Chan, Vincent Sahi, Amir Figueroa, Xinzheng V. Guo, Gabriele Cerutti, Jude Bimela, Jason Gorman, Tongqing Zhou, Zhiwei Chen, Kwok-Yung Yuen, Peter D. Kwong, Joseph G. Sodroski, Michael T. Yin, Zizhang Sheng, Yaoxing Huang, Lawrence Shapiro, and David D. Ho. 2020. 'Potent neutralizing antibodies directed to multiple epitopes on SARS-CoV-2 spike', *Nature*.

Lui, Irene, Xin X. Zhou, Shion A. Lim, Susanna K. Elledge, Paige Solomon, Nicholas J. Rettko, Beth Shoshana Zha, Lisa L. Kirkemo, Josef A. Gramespacher, Jia Liu, Frauke Muecksch, Julio Cesar Cetrulo Lorenzi, Fabian Schmidt, Yiska Weisblum, Davide F. Robbiani, Michel C. Nussenzweig, Theodora Hatziioannou, Paul D. Bieniasz, Oren S. Rosenburg, Kevin K. Leung, and James A. Wells. 2020. 'Trimeric SARS-CoV-2 Spike interacts with dimeric ACE2 with limited intra-Spike avidity', *bioRxiv*: 2020.05.21.109157.

Mastronarde, D. N. 2005. 'Automated electron microscope tomography using robust prediction of specimen movements', *J Struct Biol*, 152: 36-51.

McCoy, A. J., R. W. Grosse-Kunstleve, P. D. Adams, M. D. Winn, L. C. Storoni, and R. J. Read. 2007. 'Phaser crystallographic software', *J Appl Crystallogr*, 40: 658-74.

McMahon, Conor, Alexander S. Baier, Roberta Pascolutti, Marcin Wegrecki, Sanduo Zheng, Janice X. Ong, Sarah C. Erlandson, Daniel Hilger, Søren G. F. Rasmussen, Aaron M. Ring, Aashish Manglik, and Andrew C. Kruse. 2018. 'Yeast surface display platform for rapid discovery of conformationally selective nanobodies', *Nat. Struct. Mol. Biol.*, 25: 289-96.

Pinto, Dora, Young-Jun Park, Martina Beltramello, Alexandra C. Walls, M. Alejandra Tortorici, Siro Bianchi, Stefano Jaconi, Katja Culap, Fabrizia Zatta, Anna De Marco, Alessia Peter,

Barbara Guarino, Roberto Spreafico, Elisabetta Cameroni, James Brett Case, Rita E. Chen, Colin Havenar-Daughton, Gyorgy Snell, Amalio Telenti, Herbert W. Virgin, Antonio Lanzavecchia, Michael S. Diamond, Katja Fink, David Veesler, and Davide Corti. 2020. 'Cross-neutralization of SARS-CoV-2 by a human monoclonal SARS-CoV antibody', *Nature*, 583: 290-95.

Punjani, A., J. L. Rubinstein, D. J. Fleet, and M. A. Brubaker. 2017. 'cryoSPARC: algorithms for rapid unsupervised cryo-EM structure determination', *Nat Methods*, 14: 290-96.

Rasmussen, S. G., H. J. Choi, J. J. Fung, E. Pardon, P. Casarosa, P. S. Chae, B. T. Devree, D. M. Rosenbaum, F. S. Thian, T. S. Kobilka, A. Schnapp, I. Konetzki, R. K. Sunahara, S. H. Gellman, A. Pautsch, J. Steyaert, W. I. Weis, and B. K. Kobilka. 2011. 'Structure of a nanobody-stabilized active state of the β(2) adrenoceptor', *Nature*, 469: 175-80.

Rogers, Thomas F., Fangzhu Zhao, Deli Huang, Nathan Beutler, Alison Burns, Wan-Ting He, Oliver Limbo, Chloe Smith, Ge Song, Jordan Woehl, Linlin Yang, Robert K. Abbott, Sean Callaghan, Elijah Garcia, Jonathan Hurtado, Mara Parren, Linghang Peng, Sydney Ramirez, James Ricketts, Michael J. Ricciardi, Stephen A. Rawlings, Nicholas C. Wu, Meng Yuan, Davey M. Smith, David Nemazee, John R. Teijaro, James E. Voss, Ian A. Wilson, Raiees Andrabi, Bryan Briney, Elise Landais, Devin Sok, Joseph G. Jardine, and Dennis R. Burton. 2020. 'Isolation of potent SARS-CoV-2 neutralizing antibodies and protection from disease in a small animal model', *Science*.

Stadlbauer, Daniel, Fatima Amanat, Veronika Chromikova, Kaijun Jiang, Shirin Strohmeier, Guha Asthagiri Arunkumar, Jessica Tan, Disha Bhavsar, Christina Capuano, Ericka Kirkpatrick, Philip Meade, Ruhi Nichalle Brito, Catherine Teo, Meagan McMahon, Viviana Simon, and Florian Krammer. 2020. 'SARS-CoV-2 Seroconversion in Humans: A Detailed Protocol for a Serological Assay, Antigen Production, and Test Setup', *Curr. Protoc. Microbiol.*, 57: e100.

Staus, D. P., R. T. Strachan, A. Manglik, B. Pani, A. W. Kahsai, T. H. Kim, L. M. Wingler, S. Ahn, A. Chatterjee, A. Masoudi, A. C. Kruse, E. Pardon, J. Steyaert, W. I. Weis, R. S. Prosser, B. K. Kobilka, T. Costa, and R. J. Lefkowitz. 2016. 'Allosteric nanobodies reveal the dynamic range and diverse mechanisms of G-protein-coupled receptor activation', *Nature*, 535: 448-52.

Tortorici, M. A., M. Beltramello, F. A. Lempp, D. Pinto, H. V. Dang, L. E. Rosen, M. McCallum, J. Bowen, A. Minola, S. Jaconi, F. Zatta, A. De Marco, B. Guarino, S. Bianchi, E. J. Lauron, H. Tucker, J. Zhou, A. Peter, C. Havenar-Daughton, J. A. Wojcechowskyj, J. B. Case, R. E. Chen, H. Kaiser, M. Montiel-Ruiz, M. Meury, N. Czudnochowski, R. Spreafico, J. Dillen, C. Ng, N. Sprugasci, K. Culap, F. Benigni, R. Abdelnabi, S. C. Foo, M. A. Schmid, E. Cameroni, A. Riva, A. Gabrieli, M. Galli, M. S. Pizzuto, J. Neyts, M. S. Diamond, H. W. Virgin, G. Snell, D. Corti, K. Fink, and D. Veesler. 2020. 'Ultrapotent human antibodies protect against SARS-CoV-2 challenge via multiple mechanisms', *Science*.

Turonova, B., M. Sikora, C. Schurmann, W. J. H. Hagen, S. Welsch, F. E. C. Blanc, S. von Bulow, M. Gecht, K. Bagola, C. Horner, G. van Zandbergen, J. Landry, N. T. D. de Azevedo, S. Mosalaganti, A. Schwarz, R. Covino, M. D. Muhlebach, G. Hummer, J. Krijnse Locker, and M. Beck. 2020. 'In situ structural analysis of SARS-CoV-2 spike reveals flexibility mediated by three hinges', *Science*.

Vincke, C., R. Loris, D. Saerens, S. Martinez-Rodriguez, S. Muyldermans, and K. Conrath. 2009. 'General strategy to humanize a camelid single-domain antibody and identification of a universal humanized nanobody scaffold', *J Biol Chem*, 284: 3273-84.

Walls, Alexandra C., Young-Jun Park, M. Alejandra Tortorici, Abigail Wall, Andrew T. McGuire, and David Veesler. 2020. 'Structure, Function, and Antigenicity of the SARS-CoV-2 Spike Glycoprotein', *Cell*, 181: 281-92.e6.

Wang, Qihui, Yanfang Zhang, Lili Wu, Sheng Niu, Chunli Song, Zengyuan Zhang, Guangwen Lu, Chengpeng Qiao, Yu Hu, Kwok-Yung Yuen, Qisheng Wang, Huan Zhou, Jinghua

Yan, and Jianxun Qi. 2020. 'Structural and Functional Basis of SARS-CoV-2 Entry by Using Human ACE2', *Cell*, 181: 894-904.e9.

Winn, M. D., C. C. Ballard, K. D. Cowtan, E. J. Dodson, P. Emsley, P. R. Evans, R. M. Keegan, E. B. Krissinel, A. G. Leslie, A. McCoy, S. J. McNicholas, G. N. Murshudov, N. S. Pannu, E. A. Potterton, H. R. Powell, R. J. Read, A. Vagin, and K. S. Wilson. 2011. 'Overview of the CCP4 suite and current developments', *Acta Crystallogr D Biol Crystallogr*, 67: 235-42.

Wrapp, Daniel, Dorien De Vlieger, Kizzmekia S. Corbett, Gretel M. Torres, Nianshuang Wang, Wander Van Breedam, Kenny Roose, Loes van Schie, Vib-Cmb Covid- Response Team, Markus Hoffmann, Stefan Pöhlmann, Barney S. Graham, Nico Callewaert, Bert Schepens, Xavier Saelens, and Jason S. McLellan. 2020. 'Structural Basis for Potent Neutralization of Betacoronaviruses by Single-Domain Camelid Antibodies', *Cell*, 181: 1004-15.e15.

Wrapp, Daniel, Nianshuang Wang, Kizzmekia S. Corbett, Jory A. Goldsmith, Ching-Lin Hsieh, Olubukola Abiona, Barney S. Graham, and Jason S. McLellan. 2020. 'Cryo-EM structure of the 2019-nCoV spike in the prefusion conformation', *Science*, 367: 1260-63.

Wu, F., S. Zhao, B. Yu, Y. M. Chen, W. Wang, Z. G. Song, Y. Hu, Z. W. Tao, J. H. Tian, Y. Y. Pei, M. L. Yuan, Y. L. Zhang, F. H. Dai, Y. Liu, Q. M. Wang, J. J. Zheng, L. Xu, E. C. Holmes, and Y. Z. Zhang. 2020. 'A new coronavirus associated with human respiratory disease in China', *Nature*, 579: 265-69.

Yan, Renhong, Yuanyuan Zhang, Yaning Li, Lu Xia, Yingying Guo, and Qiang Zhou. 2020. 'Structural basis for the recognition of SARS-CoV-2 by full-length human ACE2', *Science*, 367: 1444-48.

Yu, F., S. E. Haynes, G. C. Teo, D. M. Avtonomov, D. A. Polasky, and A. I. Nesvizhskii. 2020. 'Fast quantitative analysis of timsTOF PASEF data with MSFragger and IonQuant', *Mol Cell Proteomics*.

Zaki, Ali M., Sander van Boheemen, Theo M. Bestebroer, Albert D. M. E. Osterhaus, and Ron A. M. Fouchier. 2012. 'Isolation of a novel coronavirus from a man with pneumonia in Saudi Arabia', *N. Engl. J. Med.*, 367: 1814-20.

Zhang, Y., A. T. Wecksler, P. Molina, G. Deperalta, and M. L. Gross. 2017. 'Mapping the Binding Interface of VEGF and a Monoclonal Antibody Fab-1 Fragment with Fast Photochemical Oxidation of Proteins (FPOP) and Mass Spectrometry', *J Am Soc Mass Spectrom*, 28: 850-58.

Zheng, S. Q., E. Palovcak, J. P. Armache, K. A. Verba, Y. Cheng, and D. A. Agard. 2017. 'MotionCor2: anisotropic correction of beam-induced motion for improved cryo-electron microscopy', *Nat Methods*, 14: 331-32.

Zhou, H., Y. Chen, S. Zhang, P. Niu, K. Qin, W. Jia, B. Huang, S. Zhang, J. Lan, L. Zhang, W. Tan, and X. Wang. 2019. 'Structural definition of a neutralization epitope on the N-terminal domain of MERS-CoV spike glycoprotein', *Nat Commun*, 10: 3068.

Zhou, P., X. L. Yang, X. G. Wang, B. Hu, L. Zhang, W. Zhang, H. R. Si, Y. Zhu, B. Li, C. L. Huang, H. D. Chen, J. Chen, Y. Luo, H. Guo, R. D. Jiang, M. Q. Liu, Y. Chen, X. R. Shen, X. Wang, X. S. Zheng, K. Zhao, Q. J. Chen, F. Deng, L. L. Liu, B. Yan, F. X. Zhan, Y. Y. Wang, G. F. Xiao, and Z. L. Shi. 2020. 'A pneumonia outbreak associated with a new coronavirus of probable bat origin', *Nature*, 579: 270-73.

Zhu, Na, Dingyu Zhang, Wenling Wang, Xingwang Li, Bo Yang, Jingdong Song, Xiang Zhao, Baoying Huang, Weifeng Shi, Roujian Lu, Peihua Niu, Faxian Zhan, Xuejun Ma, Dayan Wang, Wenbo Xu, Guizhen Wu, George F. Gao, Wenjie Tan, Investigating China Novel Coronavirus, and Team Research. 2020. 'A Novel Coronavirus from Patients with Pneumonia in China, 2019', *N. Engl. J. Med.*, 382: 727-33.

Zivanov, J., T. Nakane, B. O. Forsberg, D. Kimanius, W. J. Hagen, E. Lindahl, and S. H. Scheres. 2018. 'New tools for automated high-resolution cryo-EM structure determination in RELION-3', *Elife*, 7.

Zost, Seth J., Pavlo Gilchuk, James Brett Case, Elad Binshtein, Rita E. Chen, Joseph P. Nkolola, Alexandra Schäfer, Joseph X. Reidy, Andrew Trivette, Rachel S. Nargi, Rachel E. Sutton, Naveenchandra Suryadevara, David R. Martinez, Lauren E. Williamson, Elaine C. Chen, Taylor Jones, Samuel Day, Luke Myers, Ahmed O. Hassan, Natasha M. Kafai, Emma S. Winkler, Julie M. Fox, Swathi Shrihari, Benjamin K. Mueller, Jens Meiler, Abishek Chandrashekar, Noe B. Mercado, James J. Steinhardt, Kuishu Ren, Yueh-Ming Loo, Nicole L. Kallewaard, Broc T. McCune, Shamus P. Keeler, Michael J. Holtzman, Dan H. Barouch, Lisa E. Gralinski, Ralph S. Baric, Larissa B. Thackray, Michael S. Diamond, Robert H. Carnahan, and James E. Crowe, Jr. 2020. 'Potently neutralizing and protective human antibodies against SARS-CoV-2', *Nature*.

Publishing Agreement

It is the policy of the University to encourage open access and broad distribution of all theses, dissertations, and manuscripts. The Graduate Division will facilitate the distribution of UCSF theses, dissertations, and manuscripts to the UCSF Library for open access and distribution. UCSF will make such theses, dissertations, and manuscripts accessible to the public and will take reasonable steps to preserve these works in perpetuity.

I hereby grant the non-exclusive, perpetual right to The Regents of the University of California to reproduce, publicly display, distribute, preserve, and publish copies of my thesis, dissertation, or manuscript in any form or media, now existing or later derived, including access online for teaching, research, and public service purposes.

DocuSigned by:
Michael Schoof
AD12FFDD95EC436...
Author Signature

4/20/2022
Date